MODELLING OF EVANESCENT FIELD IMMUNOSENSORS

Sarah Margaret Keating

University College London

Submitted for the degree of Doctor of Philosophy

ProQuest LLC
789 East Eisenhower Parkway
P.O. Box 1346
Ann Arbor, MI 48106-1346

Abstract

Several factors affect the viability of biosensor design. This thesis presents the development of a computer-based model that will enable the sources and effects of noise and variations in concentrations within an evanescent field immunosensor to be analysed.

The model was developed as a series of modules, each representing one aspect of the sensor, which when linked provide a simulation of the whole sensor. A complete solution of the complex biochemical reactions involved in the immunoassay module was achieved using a Markov chain approach. More traditional methods of solving sets of equations, such as optimisation, genetic algorithms and simulated annealing, all failed to produce satisfactory results. Two alternative assays, a sandwich and a competitive assay, are presented. The light module details the modelling of the coupling into a planar monomode waveguide and calculation of fluorescence excited by the resulting evanescent field using standard electromagnetic formulae. However, both beam divergence and scattering from the immobilised antibody layer were incorporated into the model. Two alternative coupling techniques were modelled, prism coupling and coupling through a "resonant mirror" multilayer. The detection system modelled the amplification of the fluorescence by a photomultiplier tube.

The resulting model represents the most rigorous modelling undertaken in this area and the potential applications and benefits of such a model were detailed. Analysis of noise within the sensor allowed the impact of variation in the physical parameters defining the sensor to be determined and compared. The model was used to compare different protocols and confirmed that the sandwich assay produced the more sensitive device. A study of the kinetic response of the assay determined that measurements could be performed at half the time taken to reach equilibrium without significant loss of sensitivity. An analysis of the effect of scattering at the waveguide surface showed this to be significant noise factor. An initial study of the impact of the humectant layer illustrated that this is an issue that merits further consideration.

I would like to acknowledge the help and support of the following people:

Dr Mick Flanagan (My supervisor)
for everything, particularly going out of his way on occasion

Professor John O'Reilly
for his interest and useful discussions

My family:
Sandy & Mike Keating (My parents)

Jake & Alex Coombes (My sons)

and all the others
Liz, Pat, Bethany, Ben, Niamh,
Bernie, Paul, Luan, Muirin, Odie,
Cath & Ben.

(They all know what they did!)

Contents

List of tables

Chapter 1

Introduction

Simulation, the mimicking of the operation of a real system that gives information about the system being investigated, is currently developing as a means of experimentation. The complexity and interactions of the factors affecting the practicality of a biosensor have hindered their development in the traditional experimental environment. This thesis presents the development of a computer-based model, i.e. a simulation, of a biosensor that will enable the sources and effect of noise and variability within the sensor to be analysed and allow comparisons between different sensor arrangements to be made, thus providing the basis for a design tool to facilitate biosensor research and development.

1.1 Evanescent field immunosensor

A biosensor is a portable chemical sensor, which combines the selectivity and sensitivity of a biological molecule with the processing power of microelectronics to produce a powerful analytical tool for determining the presence and/or quantity of a particular substance, the analyte, in a biological sample. The molecule used is selected for its specificity to the analyte in question and incorporated within a physical transducer to produce a signal that can be detected. Figure 1.1 shows the schematic of a biosensor, illustrating the variety of biological recognition systems that have been combined with various different transducers in the production of biosensors [1].

A biosensor employing an antibody as the recognition molecule is designated an immunosensor and an evanescent field immunosensor is a device in which the physico-chemical response is probed within the evanescent field e.g. a device where the signal is produced by detecting the fluorescence emitted from a fluorophore labelled molecule excited by the evanescent field above a guiding waveguide.

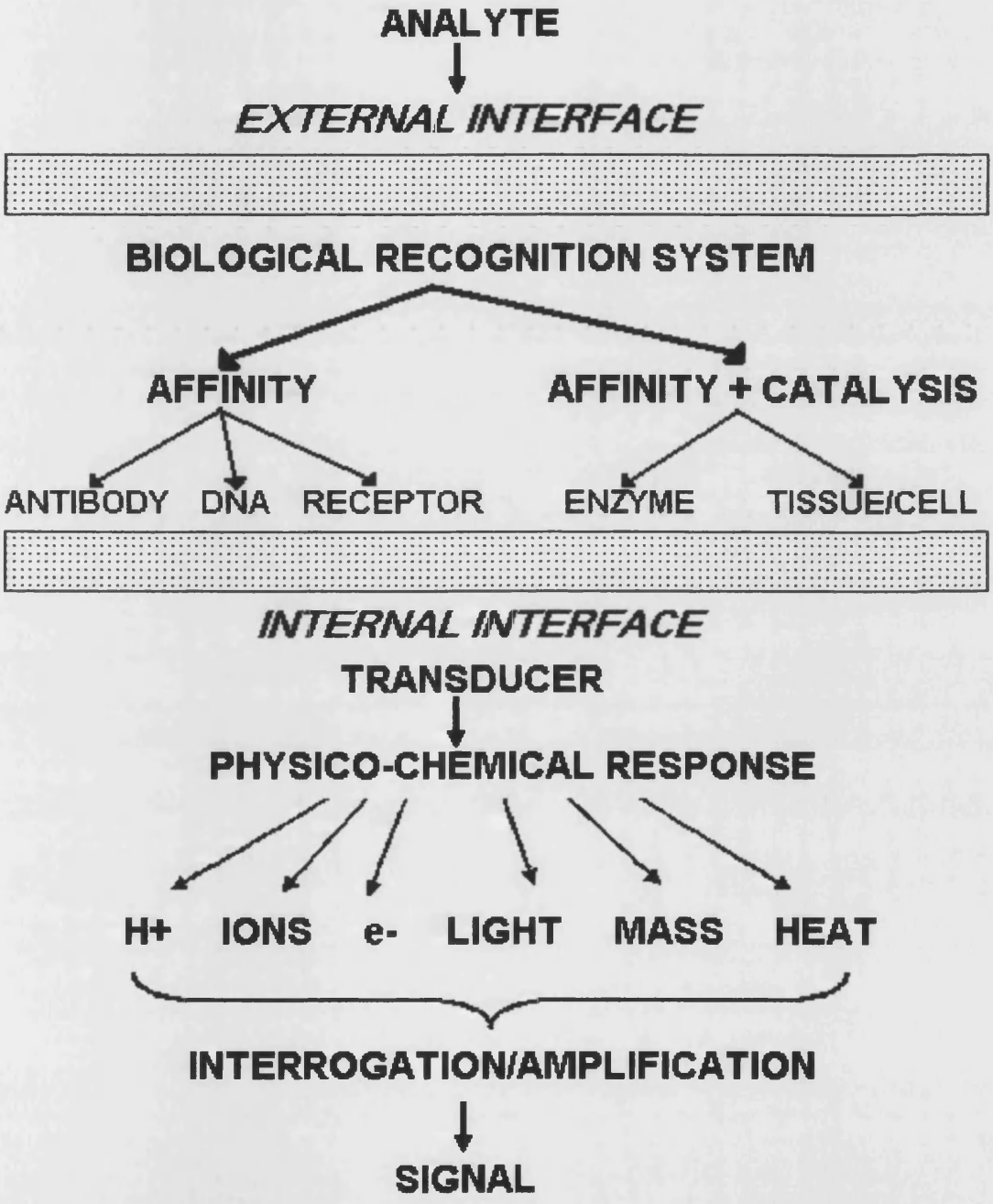

***Figure 1.1**: Schematic diagram of possible biosensor design*

1.2 Applications

The potential of biosensors has been recognised since the early seventies and applications have been identified in a number of areas (Table 1.1). Despite a significant research effort to exploit this potential, few biosensors have been developed that satisfy all the requirements of a commercially viable product [2]. The acknowledged exception is the blood glucose monitor for diabetics, patented by MediSense® in 1984 [3] and currently available worldwide. The less demanding category of biosensor, the qualitative biosensor, has achieved slightly more success. In this category, the biochemical reactions involved cause an observable colour change or employ a chemiluminescent label to indicate whether or not the analyte is present. There are a number of qualitative biosensors available of which the most widely recognised is the CLEARBLUE pregnancy test [4].

Table 1.1: Biosensors applications

Area	Application	Example
Medicine [5]	Diagnostic tool	blood sugar monitoring
Veterinary science [6]	Drug testing	detection of steroids
Environmental monitoring [7]	Pollution control	organic pollutant detection
Process control [8]	Fermentation	yeast quantity monitoring
Food and drink [9]	Microbe detection	salmonella
Military [10]	Explosives detection	TNT

1.3 Design criteria

Several factors affect the viability of biosensor design. The device must be capable of producing reliable results at the sensitivity necessary for the particular analyte. In order for the device to be easily used it must require addition of the sample only, with no further reagent addition or washing steps [11]. Any reagents incorporated within the device must have a realistic shelf life. The device must be self-calibrating, with the inclusion of either a calibration channel within the sensor [12] or with a user-friendly means of calibrating the device for a fixed number of uses, as employed by the glucose

monitor [13]. Finally, as a part disposable device, it needs to be cost effective both to manufacture and to use.

The number of design factors that need to be considered and the resulting complexity and interplay of these factors has impeded progress in the area of biosensors. The miniaturisation and lack of automation necessary to produce a portable, easy to use device have dramatically reduced the sensitivities achieved with immunosensors from those achieved by performing the immunoassay, the biochemical aspect of the sensor, within a laboratory environment. Non-specific binding contributions and variation in biomolecular immobilisations within the immunoassay; manufacturing tolerances within the sensor and noise within the detection elements may all contribute to unreliable results [14] and thus a reduction in the sensitivity achieved.

1.4 Aims of the project

The underlying aim of this project is to develop a computer model of an evanescent field immunosensor, which can be used to analyse the various design criteria in a manner that cannot be achieved experimentally, thus providing a more rational design strategy for biosensor fabrication.

In order to achieve this underlying aim, the first objective of the project is to rigorously model each component of this type of immunosensor, that is, to produce an accurate model of

i) the light source;
ii) the propagation of light through the system;
iii) the complex biochemical reactions that occur when an analyte is present;
iv) the amount and detection of the resulting fluorescence and
v) the transformation of the detected signal into a readable output.

Once each component of the immunosensor has been modelled and verified against experimental data, the second objective is to build a complete model of the immunosensor. This model will be implemented in such a way to enable different

aspects of the system to be studied and to allow the effect of noise within the system to be analysed. Thus the second objective of the project is to

i) implement a full model of an immunosensor;
ii) use the model to investigate certain design issues in biosensor development e.g. the time required to produce a reliable result and
iii) use the model to investigate some of the sources and effects of noise within the sensor.

The third objective of the project is to use the application of the full, rigorously tested model of an immunosensor to demonstrate the advantages of this type of modelling and the potential for such a model to become the basis of a design tool. Thus the third objective of the project is to

i) use the model to compare different protocols e.g. assays;
ii) use the model to study the effect of varying different parameters within the system e.g. the concentration of labelled molecule initially added;
iii) apply the model to a recently published configuration for an evanescent field optical immunosensor and to use the model to investigate the practicality of this arrangement and
iv) use the model to analyse aspects of the system for which experimental data cannot be generated e.g. the effect of a humectant layer on the thermodynamics of the biochemical reactions.

Briefly the three objectives of the project are to

i) model the components of an evanescent field immunosensor;
ii) implement a full model and use it to study the sensor implemented and
iii) demonstrate the potential of the model as a design tool.

References

[1] Vadgama P & Crump PW, Biosensors: Recent Trends A Review, *Analyst*, **117**, 1657-1670, 1992.

[2] Baird CL & Myszka DG, Current and emerging commercial optical biosensors, *Journal of Molecular Recognition*, **14**, 261-268, 2001.

[3] Medisense, Medisense Facts, Available via the World Wide Web at http://www.medisense.co.uk/pages/medisensefacts.cfm

[4] Unipath, ClearBlue UK Index, Available via the World Wide Web at http://www.clearblue.org.uk

[5] Bluestein BI, Walczak IM and Chen S-Y, *TIBTECH*, **8**, 161-168, 1990.

[6] Elliott CT, Baxter GA, Hewitt SA, Arts CJM, van Baak M, Hellenas KE & Johannson A, *Analyst*, **123**, 2469-2473, 1998.

[7] Boisde G & Harmer A, *Chemical and Biochemical Sensing With Optical Fibers and Waveguides*, (Norwood MA: Artec House, Inc.) pp 339 – 347, 1996.

[8] Eggins B, *Biosensors An Introduction*, (Chichester UK: John Wiley & Sons Ltd.), pp 11-13, 1996.

[9] Richter ER, *Journal of Dairy Science*, **76**, 3114-3117, 1993.

[10] Narang U, Gauger PR & Ligler FS, *Analytical Chemistry*, **69**, 2779-2785, 1997.

[11] Robinson GA, Optical immunosensing systems – meeting the market needs, *Biosensors & Bioelectronics*, **6**, 183-191, 1991.

[12] Private communication between MT Flanagan and the Food and Drug Administration.

[13] Bier FF, Stocklein W, Bocher M, Bilitewski U & Schmid RD, *Sensors and Actuators*, **B7**, 509-512, 1992.

[14] Luppa PB, Sokoll LJ & Chan DW, Immunosensors – principles and applications to clinical chemistry, *Clinica Chimica Acta*, **314**, 1 – 26, 2001.

Chapter 2

Evanescent field immunosensors

2.1 Historical evolution

2.1.1 The Clark electrode

In 1962 Clark & Lyons presented the development of an enzyme electrode based glucose sensor [1], which could provide a measurement of the amount of glucose in a blood sample without the need to send the sample for laboratory analysis. Their device, originally known as the oxygen electrode, was the first example of a device that we now know as a biosensor.

The oxygen electrode determined the concentration of glucose in a sample by using an electrode to monitor the decrease in the amount of oxygen due to the reaction between oxygen and glucose catalysed by the presence of glucose oxidase. The original technique proved problematic due to the need to control the ambient level of oxygen and the high reduction potential needed for the reaction to occur. However the possibilities for point of care analysis were immediately recognised and research in the area of biosensors began. The electrochemical detection of glucose went through a number of developmental stages. The second generation of glucose sensors replaced oxygen with a mediator, a chemical whose concentration was easier to control and requiring lower redox potentials [2]. Further progress was made with a technique that stabilised the electrode surface to enzymes, by incorporating a charge transfer complex, and produced directly coupled enzyme electrodes [3].

In 1984, MediSense® patented a portable glucose sensor based on this technique. This sensor and its derivatives have become an acknowledged success and are currently used worldwide for blood glucose monitoring [4]. The stability of the enzyme based amperometric sensor together with the relatively high concentration of glucose in human blood and the clear market niche for glucose sensors directed the major focus of biosensor research to the arena of glucose sensing.

2.1.2 Antibodies

The biological recognition molecule used in a biosensor determines the specificity of the device and the concentration of analyte that it is possible to measure. The use of enzymes in biosensors, as in the Clark oxygen electrode, became well established due to their fast acting catalysing effect. However, enzymes can be expensive to extract and it is difficult to modify their selectivity [5].

Antibodies are extremely versatile and can be raised to be selective to a huge variety of antigens. Antibodies bind very strongly with their specific antigen and the addition of a second reactant in the form of a labelled molecule can be used to determine the amount of antigen in the resulting compound. This process, known as an immunoassay, has been used as clinical diagnostic technique since Yalow & Berson [6] proposed the first radio-immunoassay in 1959. The subsequent development of fluorescent dyes provided a safer means of labelling molecules, with labels that could be detected using light.

Whilst there is no direct comparison between antibody and enzyme catalysed reactions, each can be characterised by a transfer function from which a half saturation value may be determined. This value, i.e. the affinity constant, for an antibody-antigen reaction is typically 10^7 M^{-1}, whereas for an enzyme reaction the value, i.e. the Michaelis constant, is typically 10^3 M^{-1}. Given that both these constants can be related to the concentrations of the species involved, it can be seen that the antibody-antigen reactions can be used to determine much lower concentrations of analytes than can be determined using enzymes.

2.1.3 Optical transducers

In the early sixties conventional waveguides consisted of hollow metal conductors and could be used to transmit electromagnetic waves in the microwave region between parts of a circuit. However, conventional guided wave transmission gave way to the new advances in optical communication systems. The optical fibre, proposed in 1966 [7], and the dielectric film waveguide provided a cheap, efficient means of guiding light, a potential that was recognised by the biosensor industry and a number of

techniques evolved that used a combination of immunoassay with a means of using light to detect a change in adsorption, fluorescence, luminescence, scatter or refractive index caused by addition of the analyte. In 1973 Kronick & Little [8] suggested the exploitation of the evanescent field as a means of interrogating an immunoassay situated above a waveguide and the first evanescent field immunosensors began to appear.

2.2 Evanescent field techniques

2.2.1 Evanescent field

The power of an electromagnetic wave guided within a waveguide is not totally constrained within the waveguide but extends into the region beyond the boundaries. Figure 2.1 shows a typical distribution for a monomode waveguide. The evanescent field decays exponentially with increased distance from the boundary but the propagation of the wave is in the z-direction only.

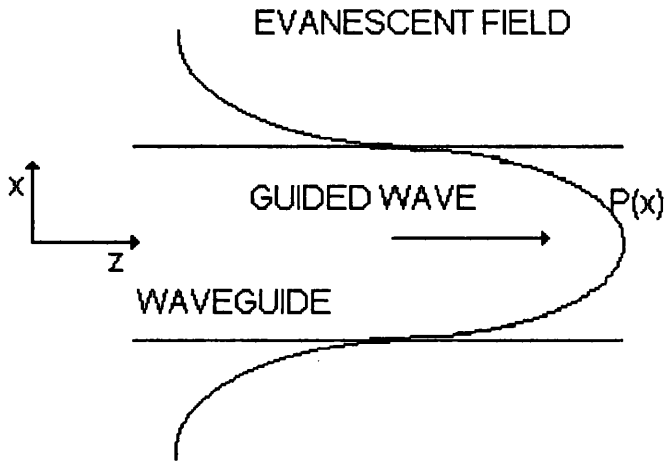

***Figure 2.1**: Power distribution for an electromagnetic wave guided within a monomode waveguide. The evanescent field is the exponentially decaying energy within the region beyond the waveguide boundaries.*

2.2.2 Surface Plasmon Resonance

Surface plasmons are charge density waves that propagate along the surface of a metal. It is possible to couple light into surface plasmons by depositing a thin metal layer onto the surface of a prism. Light is then directed through the prism, hitting the prism – metal interface at an angle greater than the critical angle. Total internal reflection occurs and the resulting evanescent wave propagates through the metal film exciting the surface plasmons at the surface of the metal, which is immersed in some liquid (Figure 2.2). Surface plasmon resonance (SPR) occurs when the component of the light wave vector matches the wave vector of the surface plasmon. At this point there is a dramatic drop in the reflected light intensity.

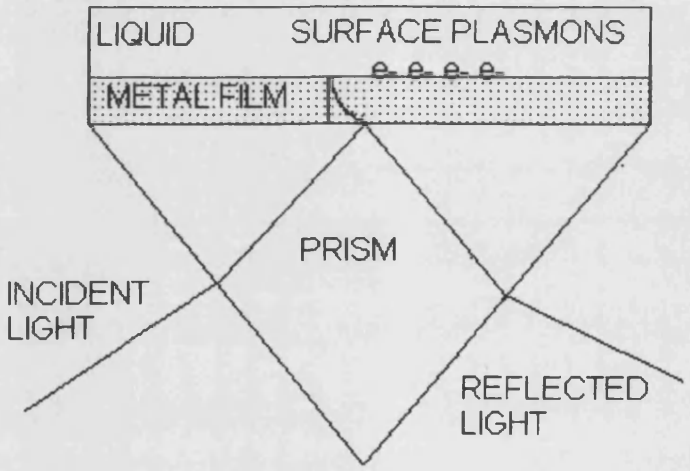

***Figure 2.2**: Surface plasmons excited at the metal surface by the evanescent field propagating in the thin metal layer.*

The frequency of incident light or the angle of incidence at which resonance occurs is extremely sensitive to the refractive index of the liquid above the metal. Thus if an immunoassay takes place within the liquid, performing an angle scan and noting the position of the SPR before and after the addition of a sample can be used to determine information relating to the sample and reactions occurring within it [9].

2.2.3 Resonant Mirror

An adaptation of SPR involves a device known as a resonant mirror [10]. As with SPR light is coupled into the system via a prism. However, two layers have replaced the metal layer (Figure 2.3); a very thin layer of high refractive index – the resonant layer, which is separated from the prism by a thicker layer of lower refractive index. This layer is thin enough for light to be coupled into the resonant layer via the evanescent field. Efficient coupling into this layer is dependent on the incident angle and is once again very sensitive to changes in the layer above. Thus shifts in the angle of incidence at which resonance occurs can be used to study reactions occurring in the sample.

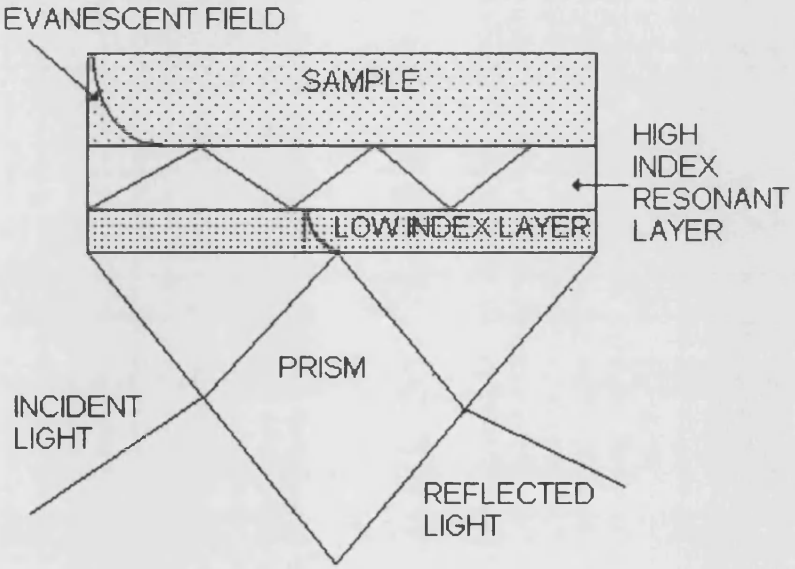

***Figure 2.3**: Resonant mirror configuration. The evanescent field in the low index layer couples light into the higher index resonant layer. This coupling achieves a maximum at a particular angle of incidence – the resonant angle.*

Research has recently suggested an improvement to the resonant mirror using a technique known as asymmetric anti-resonant reflecting optical waveguides [11]. This technique suggests the inclusion of a porous polymer layer above the resonant layer, into which the immunoassay has diffused. This layer has a higher refractive index than the sample and thus the guided wave becomes trapped in this layer, allowing more effective monitoring of the changes in refractive index caused by the biochemical reactions.

2.2.4 Commercially available devices

In the early nineties BIAcore™ produced the first in their range of instruments [12] using SPR. They had not achieved the miniaturisation necessary to become portable diagnostic devices but were immediately recognised as being ideal analytical tools for the analysis of kinetic reactions [13], determination of constants associated with reactions [14] and the study of molecular interactions [15].

BIAcore™ instruments cornered the market in this area and have maintained their role as the market leader in analytical tools for the study of molecular interactions, with 98% of the relevant literature published in 1998 using their instruments for analytical purposes [16]. The remaining 2% use the IAsys™, a resonant mirror device produced by Affinity Sensors [17]. A small number of companies produce comparable instruments, whilst others report devices under development [18]. Texas Instruments have a SPR device that is reported to be hand-held [18], but is not yet commercially available [19].

In terms of commercially available portable clinical diagnostic devices, the market has changed little in the past 10 years. There are currently a number of testing kits available that can be used to detect the presence of particular substances e.g. cocaine, cannabis etc. These operate in a similar fashion to a pregnancy test indicating only the presence, not the quantity of the particular analyte. A small number of "health check" kits are also available giving a colour-coded determination of the state of liver, kidney function etc. However, the vision of devices available in doctor's surgeries for routine screening, in the home for drug level monitoring or in ambulances for emergency diagnosis has not been realised.

2.3 Design criteria.

A commercially viable biosensor needs to meet a number of criteria. It must be a sensitive, reliable device that is easy to use and self-calibrating. It must have a realistic shelf life and be cost effective to manufacture and therefore to supply. In the sense that portability is inherent in the definition a biosensor, it must be small enough to be used

outside a laboratory. Table 2.1 lists the different criteria and their corresponding market requirements [20]. The number of design factors and the interactions between them has certainly contributed to the lack of commercially available biosensors [21].

Table 2.1: Design criteria and market requirements for biosensors

Criteria	Requirement
Sensitivity	Must be appropriate to analyte e.g. 1mM for glucose
Assay time	1 – 2 minutes
Instrumentation	Small, dedicated, low cost
Calibration	At least dual channel for calibration
Assay protocol	No reagent addition or washing necessary
Operator interface	No skill required
Sample	No preparation required
Sample addition	No measurement required
Shelf life	Minimum 6 months at room temperature (20° C)

Progress in each of the different areas represented by the design criteria varies according to the criteria and the sensing technique used. Since the field of biosensors is large, the number of variants in both biological recognition molecules and transducer techniques represents a vast array of different devices. Thus this review will confine itself to the particular arena of optical immunosensors.

2.3.1 Sensitivity

Sensitivity, that is the lowest detectable concentration of an analyte distinguishable from measurements made with no analyte present, is of prime importance in determining the viability of a biosensor. In the medical arena sensitivities range from concentrations of 1 mM (e.g. glucose [22]) to 1 pM (e.g. hCG [23]).

During the seventies the definition of the sensitivity of an immunoassay was the cause of much debate. Berson & Yalow defined sensitivity as the slope of the dose-response curve [24]. However, Ekins argued that if this were the case then the sensitivity would be dependant on the frame of reference used to plot the response curve. He further

argued that it was the signal-to-noise ratio that was the major factor in determining assay sensitivity [25]; a view currently accepted by the biosensor community.

The development and refinement of different techniques have produced the sensitivities reported in Table 2.2, although it must be stressed that in the majority of cases these remain results achieved in the laboratory and not those achieved using a successful commercial device. When detecting analytes in human serum, immunosensors are still at least one magnitude less sensitive than immunoassay analysers [26], large laboratory based devices that use immunoassay techniques for the detection of analytes in samples.

Table 2.2: Sensitivities reported using optical immunosensors

Analyte	**Sensitivity**		**Technique**
	Quoted	**Molar**	
Cocaine [27]	0.5 nM	0.5 nM	Spectrophotometer
hCG [28] (human chorionic gonadatrophin)	6.25×10^{-6} IU	17.25 fM	Chemiluminescent
M3G [29] (Morphine metabolite)	0.2 ng/mL	40.9 nM	Fibre-optic fluorescence
IgG [30] (Immunoglobulin)	6.3 nM	6.3 nM	Fibre-optic fluorescence
PSA [31] (Prostate-specific antigen)	4 – 10 ng/ml	11.8 – 29.4 nM	Fluorescence capillary fill device

Noise within the sensor and detection elements of an immunosensor has a significant effect on the concentrations that can be detected. In 1983 Jackson and Ekins [32] showed that the detection limit of an immunoassay system is directly proportional to the relative error in the signal, supporting the by then accepted theory that noise played a crucial role in limiting the sensitivity of an immunosensor.

Within an immunoassay there is often a disparity between the theoretically predicted sensitivity and that achieved experimentally [33], suggesting that there is a degree of

variation or "noise" within the immunoassay itself. Sources of noise in this element of the sensor are likely to occur due to the effects of the surface immobilisation necessary to secure the antibody to the surface that forms part of the physical transducer e.g. a waveguide in some optical immunosensors.

The optimum density and ideal orientation of the antibodies are of paramount importance as these can affect both the kinetic parameters of the assay and the amount of non-specific binding that is likely to occur [34]. Several approaches to immobilisation have been investigated, in many cases involving linking to an intermediate molecule [35, 36].

2.3.2 User Interface

Immunoassay traditionally requires skilled technicians in a clean laboratory environment. The sample needs to be prepared prior to analysis and accurate measurements of concentrations and volumes are often required. Although modern immunoassay analysis has been automated to a certain extent, such automation itself requires the investment, space and skilled maintenance available within a laboratory installation.

It is normal procedure to determine results from an immunoassay once chemical equilibrium has been achieved and any unbound elements have been removed by washing. However, some immunoassays take as long as 20 minutes to reach equilibrium, an excessive time if one is sitting waiting for a result.

An ideal biosensor would be available in a doctor's surgery, an ambulance or even at home. Thus it must be possible for an unskilled person to use the device given minimal instruction. In order to facilitate this, the sample must require no preparation i.e. the sample must use the whole blood or urine with no cleaning or removal of components necessary. It must be easy to add the sample to the sensor, with no accurate measurements necessary. Thus adding a drop of blood to a plate or point on a sensor is ideal. If the immunoassay requires any further reagents, e.g. a labelled component, they must be packaged within the system, making it appear reagent-less and the device

should produce results within a couple of minutes. Techniques that exploit the evanescent field above a waveguide to excite a labelled component within the immunoassay have been used to provide sensor systems that address some or all of these requirements. In particular, the capillary-fill device has been developed to produce a user-friendly approach to immunoassay.

2.3.3 Fluorescence evanescent field techniques

An evanescent field immunosensor consists of an immunoassay where the capture antibody has been immobilised on the upper surface of a waveguide, either planar or fibre. One of the molecules taking part in the biochemical reactions has been labelled, for example with a fluorophore. The evanescent field produced by light propagating within the waveguide decays into the region above the waveguide, thus exciting those fluorophores that are bound near the surface and not those still free in the solution beyond the evanescent field. This exploitation of the evanescent field eliminates the need for washing away any unbound solution. The resulting fluorescence is proportional to the amount of analyte and the detected fluorescence can be used to determine the concentration of analyte present in the sample.

Recent studies have begun to look at methods of enhancing the evanescent field and thus producing stronger signals using this technique. Reverse-symmetry waveguides have been suggested [37], where the substrate material has a lower refractive index than the medium above the waveguide; thus allowing deeper penetration into this layer.

2.3.4 Capillary fill device

The capillary fill device (CFD) invented by Professor Shanks at Unilever and developed by Serono [38] exploits the evanescent field whilst seeking to address some of the design issues relating to the easy of use of the device. This device consists of two layers of glass with a narrow (approximately 100 microns) gap between them creating a cell of known volume. On the lower surface of the cell a waveguide has been deposited and on top of this the capture antibody of the immunoassay has been immobilised. A fluorescent-labelled antibody is trapped within a water-soluble polymer inside the top

surface of the cell. The addition of the sample causes this polymer to dissolve, thus adding the labelled molecule to the immunoassay without the need for any action on the part of the user. Thus, to the user, the device appears reagent-less. The sample to be tested is added at the end of the device, which fills due to capillary action. This eliminates any need for preparation or measurement of the sample. The addition of the sample causes the release of the labelled antibody and the biochemical reactions between the capture antibody, the analyte and the labelled antibody occur. Light is then coupled into the waveguide, producing an evanescent field that excites the bound fluorophores (Figure 2.4). The resulting fluorescence can be detected and used to determine the quantity of analyte present in the sample.

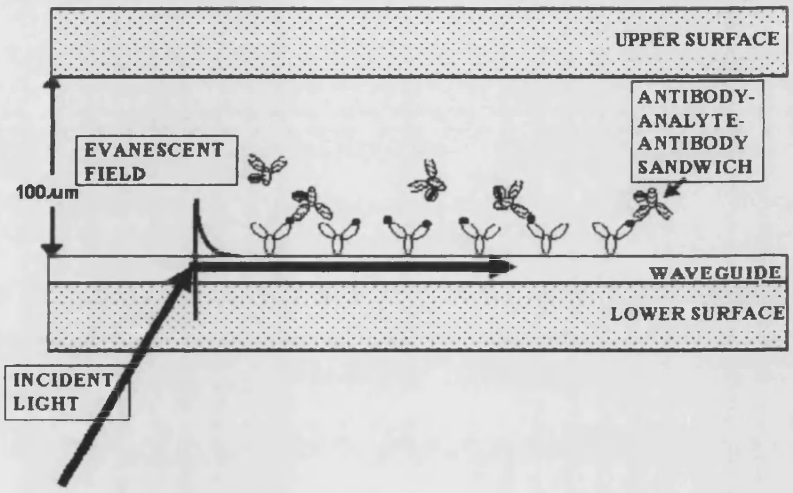

***Figure 2.4**: Capillary fill device with immunoassay immobilised to lower surface. Guided light in the waveguide produces an evanescent field that excites the fluorophores close to the surface i.e. those that are bound.*

2.3.5 Manufacturing criteria

The diagnostic market is bound by clearly defined standards, with comprehensive regulations being set and enforced by government institutions e.g. Food and Drug Administration [39]. Before a medical device can be marketed it must be fully tested and classified by the appropriate authority. In the case of an immunosensor, the major requirements are that the device is non-harmful, sensitive, and reliable and has a satisfactory means of calibration.

The issue of calibration within a portable device is one of the most stringent requirements that must be satisfied if an immunosensor is to become commercially successful. Calibration may be achieved by including a separate calibration channel within the sensor [40]. This would allow a calibration to be performed with each use. Planar waveguide sensors with multiple channels are under development [41], offering the potential for both within sensor calibration and multi-analyte detection. Alternatively an adaptation of the calibration technique employed by the MediSense® glucose sensor, i.e. calibrating the device for a fixed number of uses [4], must be established.

Any product seeking commercial success needs to consider manufacturing costs. The device must be manufactured at such a cost that its purchase price is realistic for the intended market. Classical integrated optics involves the use of Titanium indiffused waveguides fabricated in crystal materials such as Lithium Niobate. Sloper & Flanagan [42] developed a cheaper means of fabricating thin film metal phosphate waveguides for use in immunosensors. Developers are currently looking at fabricating waveguides out of polymers [37] or using a conducting oxide layer [43] as further means of producing inexpensive waveguide immunosensors.

2.4 Modelling

Early computer models of biosensors were developed involving a combination of two models: the physico-chemical model of the immunoassay and an error model representing the errors incurred in the measurement of the assay response [44]. However, these received only limited application, which Ekins [44] ascribed to the experimentalists reluctance to dissect their assay systems in order to identify the sources of error.

The emergence of Systems Biology as a field of research in the last couple of years has provided experimentalists with tools to facilitate the production and exchange of models [45] and there are a growing number of simulation packages available. The continued development of such tools is likely to produce an increase in the amount of modelling of biological and biochemical systems.

Ezan & Grassi [46] attributed the lack of exploitation of computer models in biosensor development to the fact that such models are complex, do not easily take into account common features of assays or information on assay parameters and thus do not reflect reality. A review of the small amount of literature devoted to biosensor modelling confirms this view. Several attempts have been made to produce a mathematical model to determine output [47], sensitivity [48] or the detection limit [49] of different types of optical immunosensor. Holt et al. [50] acknowledged the potential benefit of modelling to biosensor design and produced a model of a continuous flow displacement immunosensor that they used to optimise certain parameters. However, the common feature of these publications is either the gross simplification involved when including the immunoassay element of the sensor or the complete absence of any attempt to model this aspect of the sensor. The intention of this project is to develop a model that tackles this failing i.e. a model that can be used to determine accurate values for assay parameters and takes into account the full complexity of the immunoassay.

References

[1] Clark LC & Lyons C, Electrode systems for continuous monitoring in cardiovascular surgery, *Ann. N. Y. Acad Sci*, **102**, 29 - 45 ,1962.

[2] Cass AEG, Davis G, Francis GD, Hill HAO, Aston WJ, Higgins IJ, Plotkin EV, Scott LDL & Turner APF, Ferrocene-mediated enzyme electrode for amperometric determination of glucose, *Analytical Chemistry*, **56**, 6567 – 6571, 1984.

[3] Albery WJ & Cranston DH, Amperometric enzyme electrodes In *Biosensors: Fundamentals and Applications* Eds Turner APF, Karube I & Wilson GS (Oxford UK: Oxford University Press) pp 180 – 210, 1987.

[4] Medisense, Medisense Facts, Available via the World Wide Web at http://www.medisense.co.uk/pages/medisensefacts.cfm

[5] Eggins BR, *Chemical Sensors and Biosensors*, (Chichester UK: John Wiley & Sons, Ltd) pp 89 – 154, 2002.

[6] Yalow RS & Berson SA, Assay of plasma insulin in human subjects by immunological methods, *Nature*, **184**, 1648-1649, 1959.

[7] O'Reilly JJ, *Telecommunication Principles*, 2nd edition, (London UK: Chapman & Hall) pp 7 – 8, 1989.

[8] Kronick MN & Little AW, *Bull. Am. Phys. Soc.*, **18**, 782 – 790, 1973.

[9] Liedberg B, Nylander C & Lundstrom I, Biosensing with surface-plasmon resonance – how it all started, *Biosensors & Bioelectronics*, **10**, R1 – R9 FAL, 1995.

[10] Cush R, Cronin JM, Stewart WJ, Maule CH, Molloy J & Goddard NJ, The resonant mirror: a novel optical biosensor for direct sensing of biomolecular interactions, *Biosensors & Bioelectronics*, **8**, 347-353, 1993.

[11] Goddard NJ, Hulme J, Malins C, Singh K & Fielden PR, Asymmetric anti-resonant reflecting optical waveguides (arrow) as chemical sensors, *Analyst*, **127**, 378-382, 2002.

[12] Biacore Home, Available via the World Wide Web at http://www.biacore.com

[13] Vancott TC, Loomis LD, Redfield RR et al, Real-time biospecific interaction analysis of antibody reactivity to peptides from the envelope glycoprotein, GP160, of HIV-I, *Journal of Immunological Methods*, **146** (2), 163 – 175, 1992.

[14] Altschuh D, Dubs MC. Weiss E et al, Determination of kinetic constants for the interaction between a monoclonal antibody and peptides using surface plasmon resonance, *Biochemistry – US*, **31** (27), 6298 – 6304, 1992.

[15] Dubs MC, Altschuh D & VanRegenmortel MHV, Mapping of viral epitopes with conformationally specific monoclonal-antibodies using biosensor technology, *Journal of Chromotography*, **597** (1-2), 391 – 396, 1992.

[16] Myszka DG, Survey of the 1998 optical biosensor literature, *Journal of Molecular Recognition*, **12**, 390-408, 1999.

[17] Affinity Sensors Online, Available via the World Wide Web at http://www.affinity-sensors.com

[18] Baird CL & Myszka DG, Current and emerging commercial optical biosensors, *Journal of Molecular Recognition*, **14**, 261-268, 2001.

[19] Spreeta Technology at TI, Available via the World Wide Web at http://www.ti.com/sc/docs/product/msp/control/spreeta.htm

[20] Robinson GA, Optical immunosensing systems – are they meeting the market needs?, *Biosensors & Bioelectronics*, **8**, xli – xliv, 1993.

[21] Robinson GA, Optical immunosensing systems – meeting the market needs, *Biosensors & Bioelectronics*, **6**, 183 – 191, 1991.

[22] Jaffe BM & Behrman HR (Eds) *Methods of hormone radioimmunoassay,* (London: Academic Press Inc.) 2nd edition, pp 1008, 1979.

[23] Bier FF, Stocklein W, Bocher M, Bilitewski U & Schmid RD, *Sensors and Actuators*, **B7**, 509-512, 1992.

[24] Berson SA & Yalow RS, Measurements of hormones – Radio-immunoassay in *Methods in Investigative and Diagnostic Endocrinology* vol 2A Berson SA & Yalow RS (Eds) (Elsevier/North Holland, Amsterdam) pp 84 – 135, 1973.

[25] Ekins RP, Assay design and quality control, In *Radioimmunoassay*, Bizollon CA (Ed) (Elsevier/North Holland, Amsterdam) pp 239 – 255, 1979.

[26] Kubitschko S, Spinke J, Bruckner T, Pohl S & Oranth N, Sensitivity enhancement of optical immunosensors with nanoparticles, *Anal Biochem*, **253**, 112-122, 1997.

[27] Eremenko AV, Bauer CG, Makower A, Kanne B, Baumgarten H & Scheller FW, The development of a non-competitive immunoenzymometric assay of cocaine, *Analytica Chimica Acta*, **358**, 5-13, 1998.

[28] Sasamoto H, Maeda M, Tsuji A & Manita H, Highly sensitive immunological assays for human chorionic gonadotrophin and prostatic acid-phosphatase using phenacyl phosphate as a chemiluminescent label, *Analytica Chimica Acta*, **309**, 221-225, 1995.

[29] Eldefrawi ME, Azer NL, Nath N, Anis NA, Bagalore MS, O'Conell KP, Schwartz RP & Wrigth J, A sensitive solid-phase fluorimmmunoassay for detection of opiates in urine, *Applied Biochemistry and Biotechnology*, **87**, 23-35, 2000.

[30] Vidal M, Prata M, Santos S, Tavares T, Hossfield J, Preininger C & Oliva A, Fluorescence IgG immunosensor based on micro flow cell containing controlled pore glass as immobilisation support, *Analyst*, **125**, 1387-1391, 2000.

[31] O'Neill PM, Fletcher JE, Stafford CG, Daniels PB & Bacarese-Hamilton T, Use of an optical biosensor to measure prostate-specific antigen in whole blood, *Sensors and Actuators*, **B29**, 79-83, 1995.

[32] Jackson TM & Ekins PR, Theoretical limitations on immunoassay sensitivity: Current practice and potential advantages of fluorescent Eu^{3+} chelates as non-radioactive tracers, *Journal of Immunological Methods*, **87**, 13-20, 1983.

[33] Davies C, Introduction to Immunoassay Principles in *The Immunoassay Handbook*, Wild D (Ed) (London UK: Nature Publishing Group) pp 3 – 40, 2001.

[34] Luppa PB, Sokoll LJ & Chan DW, Immunosensors – principles and applications to clinical chemistry, *Clinica Chimica Acta*, **314**, 1 – 26, 2001.

[35] Gopel W & Heiduschka P, Interface analysis in biosensor design, *Biosensors & Bioelectronics*, **10**, 853-883, 1995.

[36] Cass T & Ligler FS (Eds), *Immobilised Biomolecules in Analysis A Practical Approach*, (Oxford UK: Oxford University Press), 1998.

[37] Horvath R, Lindvold LR & Larsen NB, Reverse-symmetry waveguides: theory and fabrication, *Appl. Phys. B*, **74**, 383-393, 2002.

[38] Robinson GA, Attridge JW, Deacon JK & Whitely SC, The fluorescent capillary fill device, *Sensors and Actuators*, **B11**, 235-238, 1993.

[39] Laws Enforced by the Food and Drug Administration and Related Statutes, Available via the World Wide Web at http://www.fda.gov/opacom/laws/lawtoc.htm

[40] Private communication between MT Flanagan and the Food and Drug Administration.

[41] Ligler FS, Breimer M, Golden JP, Nivens DA, Dodson JP, Green TM, Haders DP & Sadik OA, Integrating Waveguide Biosensor, *Anal. Chem.*, **74**, 713-719, 2002.

[42] Sloper AN & Flanagan MT, Metal phosphate planar waveguides for biosensors, *Applied Optics*, **33**, 4230-4240, 1994.

[43] Liron Z, Tender LM, Golden JP & Ligler FS, Voltage-induced inhibition of antigen-antibody binding at conducting optical waveguides, *Biosensors & Bioelectronics*, **17**, 489-494, 2002.

[44] Ekins R, Immunoassay design and optimisation In *Principles and Practice of Immunoassay* Eds Price CP & Newman DJ, (NY: Stockton Press) pp 96-153, 1991.

[45] Hucka M, Finney A, Sauro HM, Bolouri H, Doyle JC, Kitano H & SBML Forum, The systems biology markup language (SBML): a medium for representation and exchange of biochemical network models, *Bioinformatics*, **19**, 524-531, 2003.

[46] Ezan E & Grassi J Optimization In *Immunoassays* Ed. Gosling JP, (Oxford: Oxford University Press) pp 187 - 210, 2000.

[47] Saracoglu OG & Ozsoy S, Simple equation to estimate the output power of an evanescent field absorption-based fiber sensor, *Opt. Eng.*, **41**, 598-600, 2002.

[48] Sotsky AB, Primak IU, Khomchenko AV & Tomov AV, Sensitivity of integrated optical sensors based on a prism coupler, *Optical and Quantum Electronics*, **31**, 191-200, 1999.

[49] O'Connor T & Gosling JP, The dependence of radioimmunoassay detection limits on antibody affinity, *Journal of Immunological Methods*, **208**, 181-189, 1997.

[50] Holt DB, Kusterbeck AW & Ligler FS, Continuous Flow Displacement Immunosensors: A Computational Study, *Analytical Biochemistry*, **287**, 234-242, 2000.

Chapter 3

Overview of model

There are a number of biosensor techniques being used or at various stages of development. The model implemented during this project represents the initial stages in the development of a design tool that could provide an inexpensive way of studying and comparing different approaches to biosensing. However, in order to establish the reliability and usefulness of such a model, it is important that the data generated using the model is closely related to data obtained experimentally. Thus, the initial modelling is based on experimental evanescent field immunosensors previously studied in this group. Models of these systems can be readily tested and verified against existing experimental data.

3.1 Experimental model

The experimental evanescent field immunosensors previously studied [1,2] are based on the capillary fill device (CFD) invented by Professor Shanks at Unilever, developed by Serono [3] and described in chapter 2. This device consists of two layers of glass with a narrow (approximately 100 microns) gap between them.

Two variations of the device have been modelled. In the first, an indium phosphate waveguide has been deposited directly onto the lower glass surface of the CFD [4]. Light is coupled into the waveguide using a prism and the resulting evanescent field excites the fluorophore label of the immunoassay on the waveguide surface (Figure 3.1a overleaf). The second variation involves a resonant mirror type coupling into the waveguide (Figure 3.1b overleaf). A buffer layer has been deposited onto the lower glass surface, with an iron phosphate waveguide deposited on top. Light is evanescently coupled into the waveguide through the buffer layer, coupling that achieves a maximum at a particular incident angle, the resonant angle. Guided light in the waveguide produces an evanescent field, once again exciting the bound fluorophore.

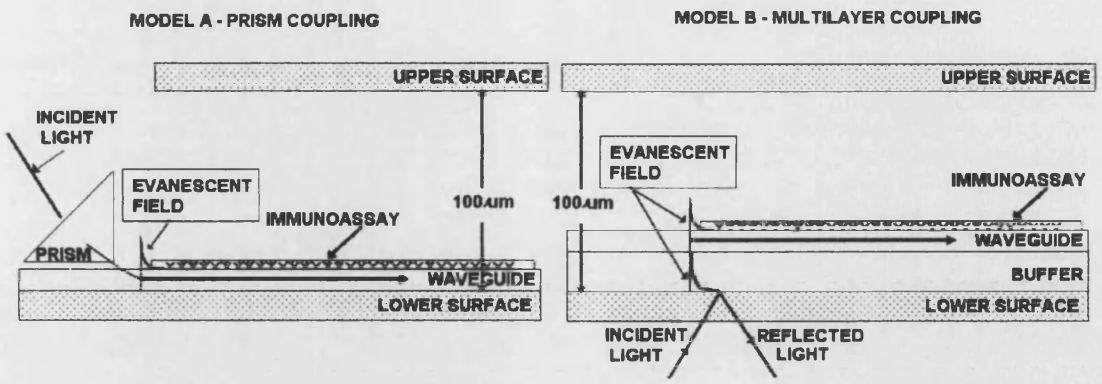

Figure 3.1 *A capillary fill device used as an immunosensor*
Model A - Light is coupled into the waveguide using a prism
Model B - Light is coupled through multiple layers c.f. resonant mirror

The CFD requires an exciting light and some means of detecting the resulting fluorescence. Several alternatives have been suggested e.g. Helium-Neon or semi-conductor laser as light sources and photomultiplier tubes or avalanche photodiodes as the means of detection. The light source and detection system modelled in this project reflect the experimental apparatus previously used by Sloper [1] and Pampapathi [2] to generate data pertaining to the use of a CFD as a biosensor (Figure 3.2), data that has been used to verify the model.

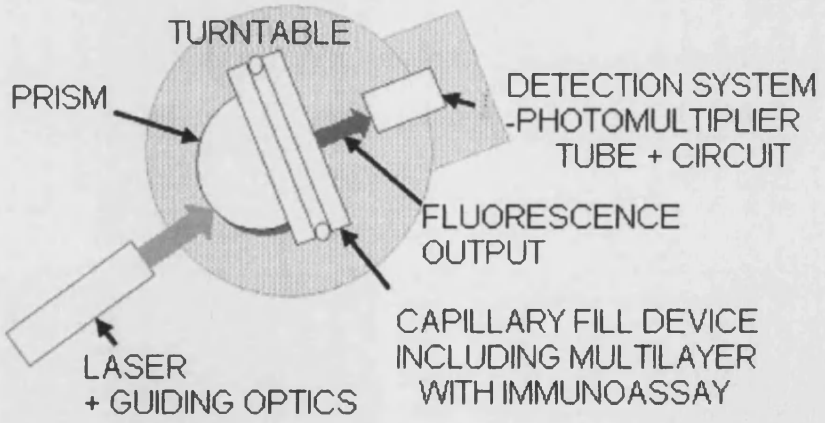

Figure 3.2*: Experimental set-up of a fluorescent evanescent field immunosensor. In the particular case illustrated the exciting light was provided by a Helium-Neon laser and the output fluorescence was detected using a photomultiplier tube.*

3.2 Specification of requirements

The specification of requirements when developing a piece of software is an accurate determination of what the software should achieve and the type of interaction between the user and the software that will be appropriate and necessary.

The primary requirement of this particular model is that it provides an accurate means of reproducing the output from an evanescent field immunosensor. In order to do this it must accurately model the following components:

i) light source;
ii) propagation of light through the system;
iii) immunoassay i.e. the biochemical reactions;
iv) resulting fluorescence;
v) detection system.

The model will enable the user to study the effect of varying different parameters within the system by allowing the user to assign values to certain parameters. Each of the components listed have a number of parameters that may effect the functionality of the overall sensor e.g. wavelength of light source, refractive indices, thickness of any materials etc. A comprehensive list of the parameters that can be varied is given in the chapters relating to the development of the model of each of the relevant components.

Developing the model to allow the analysis of the noise within the system requires the facility for the user to assign a variance to the value of certain parameters and the model to determine both the output from the sensor and the error in this output caused by the specified variances. This will allow the sensitivity of the specified device to be calculated, a key factor in establishing the viability of a sensor.

One of the potential benefits of the model is that it will allow the impact of certain characteristics within the system to be studied, e.g. scattering of light. It must therefore be possible to examine data at various key points within the model.

It will be possible to use the model to compare different protocols by allowing the user to replace a particular component with an alternative variant of that component without the remainder of the system being altered e.g. coupling might be via a prism or the multilayer. Thus, where a number of variants are available, the user must be able to specify the required variant.

In summary, the model should

i) allow the user to specify the design of the system:
   a) choose component variants where available
      e.g. prism or multilayer coupling;
   b) assign values and variances to certain design parameters,
      discussed in detail in Chapters 4 - 6;
   c) choose the point in the model at which to output intermediate data.

ii) accurately calculate the output and corresponding variance where necessary, at the point specified given the parameters entered.

A model that meets these requirements will demonstrate the potential of this type of modelling to the field of biosensor design and allow data pertaining to some elements of the system that cannot be produced experimentally to be generated and analysed.

3.3 System analysis and design

The analysis and design of a piece of software involves precise determination of the functionality of the system and decisions regarding how this functionality and the requirements specified can be implemented [5].

3.3.1 Overall model

In the case of the immunosensor model, analysis suggested that the best approach to modelling would be to divide the system into a number of modules each representing one component of the system e.g. the immunoassay element. Each module could then be modelled separately, providing the opportunity for testing each component

independently and the potential for analysis of data from within a particular element of the sensor.

Linking the modules together provides a model of the sensor in its entirety, which can then be used to study the overall effect of changing any particular parameter. Figure 3.3 illustrates the modules, the possible variants and the flow of data through the model. Substitution of modules will facilitate the direct comparison of different variants of each component, although not all of the variants shown have been modelled.

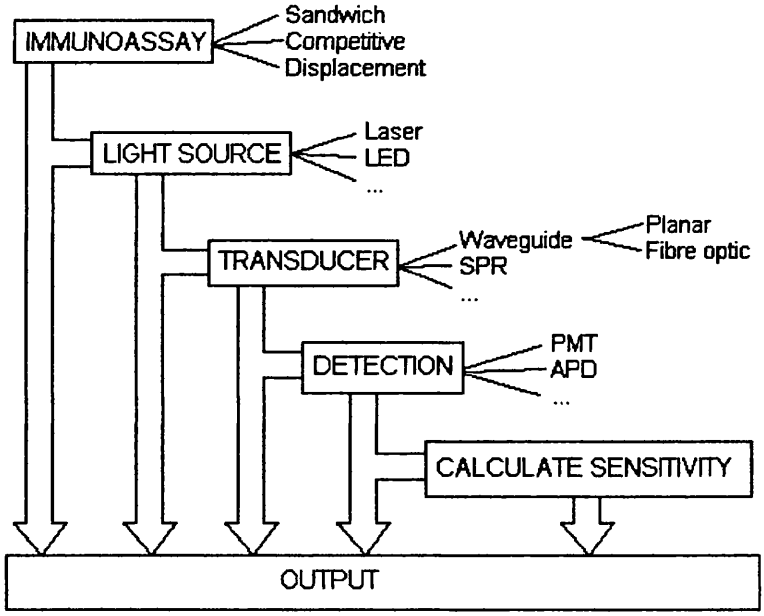

***Figure 3.3**: Data flow through the computer model of the immunosensor.*
The blocks denote each module representing a component of the sensor, with the module variants listed to the right.
Data from each module can be output or fed into the next module in the sensor model.

3.3.2 Modules within the model

Analysis of each particular module required the development of a mathematical model that accurately represented the physical system being described. Once the mathematical model had been established, it was possible to identify both parameters that could be variable and points at which useful intermediate data could be accessed. This enabled decisions regarding how to proceed with the implementation to be taken.

3.4 Implementation

3.4.1 Timescale

Software development can be time consuming and it is necessary to closely monitor the time spent on any one aspect of the development to avoid becoming trapped within an infinite loop of writing and testing code which will never produce a satisfactory result. Figure 3.4 illustrates the time scale for development of the immunosensor model.

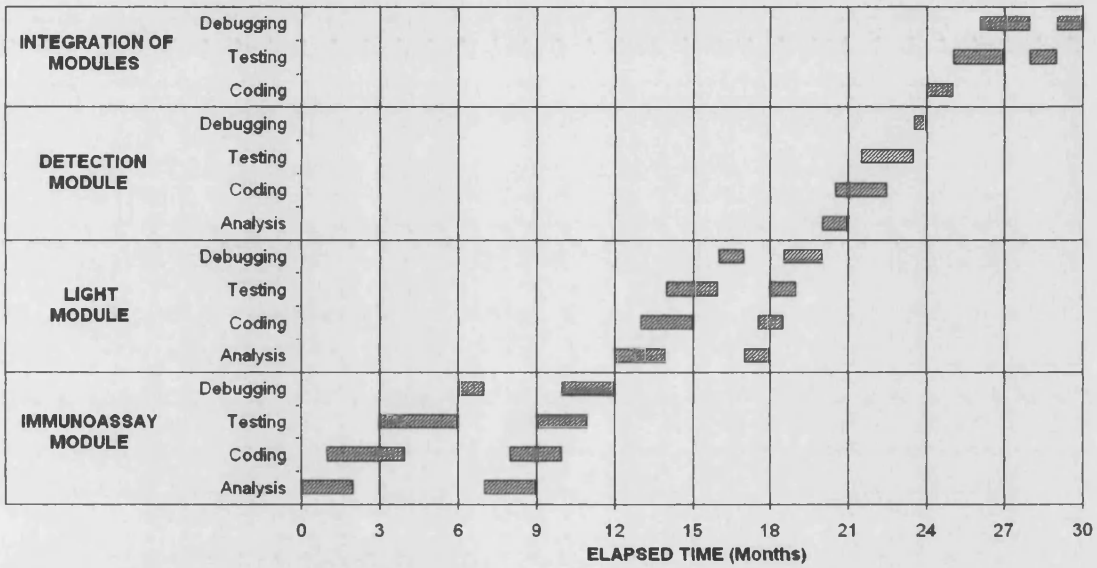

***Figure 3.4**: Time scale for the development of the immunosensor model. It should be noted that in the case of the immunoassay and light models the repetition of the process refers to the two variants of each of this modules.*

Development of each module of the immunosensor consisted of four main aspects. The first stage is the analysis of the module described above (3.3.2). Once analysis has begun, it is sensible to start writing code as soon as possible. Thus any immediate pitfalls of translating a particular mathematical model into computer code should be established. Testing can begin before the code is completely finished. It is often desirable to test functions separately and independently of the overall program. Once testing is complete the process of debugging, i.e. correcting any of the problems identified can be started. It is common practice amongst commercial software developers to separate the testing and debugging processes completely, as it is sometimes easier to isolate a bug in code with which a developer is not completely familiar.

3.4.2 Simple overview of C++

The object oriented language C++ has been used to implement the model, as it is particularly appropriate for the modelling approach adopted. In C++ it is possible to create new data types i.e. classes, that encapsulate all the information and capabilities of the data type into a single entity. Object orientation enables the developer to create instances of the new class with which to interact. A simple example would be a class Animal. An Animal may contain information such as Weight and Age (the variables) and have the capability to Walk or Speak (the methods). In order to interact with an Animal the developer creates an instance of the Animal i.e. Animal Fang (the object), to which a Weight and Age can be assigned. It is also possible to get Fang to Walk or Speak.

Inheritance in C++ allows further classes to be derived from a base class. A developer might wish to have a class Dog. Since a Dog is also an Animal and will have several attributes and methods in common with an Animal, it is possible to derive a class Dog from the base class Animal. An instance of the class Dog will automatically have a Weight and Age and be able to Walk and Speak. Similarly a Cat class may also be derived. The polymorphism of C++ means that a pointer to an instance of class Animal can be assigned to any of its derived class i.e. either Dog or Cat.

It is possible to change the functionality of a method from the base class by declaring the method to be virtual. Thus if the Speak method is declared virtual in the Animal base class and Speak is redefined for both a Dog and a Cat then a call to the Speak method could output "Woof!" if the object is a Dog and "Meow" if it is a Cat.

3.4.3 Physical objects in the immunosensor model

Application of an object oriented approach to the immunosensor model allowed a basic set of data and functions to be determined for each component of the model and developed as a base class representing that particular component. Each base class was extended and customised for each particular variant of the module e.g. an immunoassay base class with derived classes for each of the immunoassay types. This facilitates the substitution of module variants.

In some cases the main class is composed of a number of instances of other classes. A class detailing its physical properties represents each biochemical species. A second class representing a chemical reaction includes the rate constants governing the particular reaction and three instances of the species class, referring to the constituent and product species involved. The immunoassay class contains arrays of both the species and reactions relevant to the particular assay. Figure 3.5 illustrates part of the composition of the immunoassay class and its relation to the physical assay object.

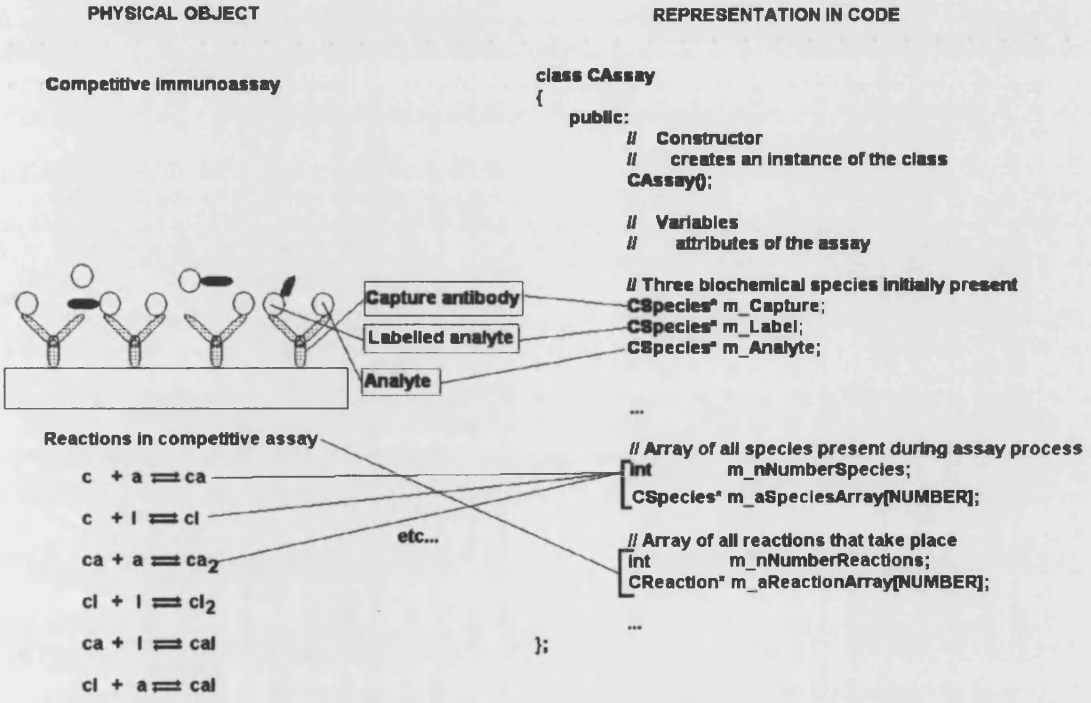

***Figure 3.5**: Illustration of a competitive assay as a physical object and its corresponding implementation as a C++ class.*

3.4.4 Mathematical objects

In addition to creating classes that represent physical objects, it is also possible to develop classes to represent mathematical objects. Two mathematical classes of particular use in the immunosensor model were a complex class; a type consisting of two variables representing the real and imaginary parts of a complex number; and an error class; a type consisting of two variables, one representing a measured or calculated value, the other an estimate of its associated variance. The development of

these classes facilitated the development of a "complex_error" class, a type representing complex numbers were both the real and imaginary parts had a value and an associated variance.

3.4.4.1 Operator overloading

Operator overloading in C++ facilitates the use of mathematical classes such as the complex and error classes described above. Code can be written that allows the functionality of the arithmetic operators to be reassigned when applied to the developed class e.g. the code for overloading the '+' operator for the error class is:

```
CError::CError operator + (CError & rhs)
{
        newValue = value + rhs.getValue();
        newError = square_root( square(error) + square(rhs.getError()) );
        return CError(newValue, newError);
}
```

Thus, applied to the line of code

Error3 = Error1 + Error2

value represents the measurement of object Error1
error represents the error associated with Error1
rhs refers to the object Error2 of type error
getValue() accesses the value variable within the error class
getError() accesses the error variable within the error class
and Error3 is the returned object of type error with variables newValue and newError as calculated within the function.

The overloading of the arithmetic operators within the error class allows the propagation of errors through a module to be accomplished with minimal effort. Any parameters that have an associated variance and any calculated values are declared to

be of type Error. The code is unchanged from the code in which all values are real, but the end result is of type Error and therefore has a value and a variance. Figure 3.6 shows the declaration of the class Error and illustrates the full range of operator overloaded functions.

```
class Error
{
public:  // constructor & destructor
                Error();
                Error(double, double);
                ~Error();
        // functions to get values
                double getValue();
                double getError();
                void            Initialise(double, double);
        // arithmetic operators
                Error operator+ (Error &);
                Error operator+ (const double &);
                Error operator- (Error &);
                Error operator- (const double &);
                Error operator* (Error &);
                Error operator* (const double &);
                Error operator/ (Error &);
                Error operator/ (const double &);
        // assignment operators
                Error& operator= (Error & );
                Error& operator+= (Error &);
                Error& operator+= (const double &);
                Error& operator-= (Error &);
                Error& operator-= (const double &);
                Error& operator*= (Error &);
                Error& operator*= (const double &);
                Error& operator/= (Error &);
                Error& operator/= (const double &);
        // output functions
                void Print();
                void Print(ofstream&);
        // friend functions
                friend Error operator+ (const double, Error);
                friend Error operator- (const double, Error);
                friend Error operator* (const double, Error);
                friend Error operator/ (const double, Error);
private:
                double value;
                double error;
};
```

Figure 3.6: *Error class member variables and functions*

Similarly a complex class consisting of two variables, one representing the real part and the other the imaginary part, facilitates the use of complex numbers, necessary for

modelling of light through absorbing materials. The complex_error class allows variances to be assigned to both the real and imaginary parts of any complex number and the calculations to proceed with only a change in the data type of certain variables necessary.

3.4.5 Monte Carlo simulation

> "Stochastic methods attempt to mimic or replicate the behaviour of a system by exploiting randomness to obtain a statistical sample of possible outcomes."
> Heath [6]

A Monte Carlo procedure is a stochastic procedure in which random sampling is used to generate mean and standard deviation values that are difficult to determine analytically [7]. Whilst error propagation could be used to determine deviations in parts of the model, other parts, in particular the optimisation methods used to determine the concentrations of biochemicals within the immunoassay module, described in detail in Chapter 4, did not provide suitable procedures within which to apply the propagation of error technique. Thus, in order to determine values for the errors in these parts of the model a Monte Carlo simulation was adopted.

3.4.5.1 Details of Monte Carlo procedure

In order to determine a mean and standard deviation of the output from a particular element of the model a value and associated error must be determined for each of the input variables. An array of normally deviated random numbers, using the desired value as mean and the error as standard deviation was generated for each variable concerned. The simulation could then be performed for each combination of array values and the mean and standard deviation of the output results calculated.

3.4.5.2 Random Numbers

A computer must use some sort of algorithm to produce a supposedly random number. These random number generators have merited much discussion [8] and the general conclusion is that the majority of standard number generating functions produce sequences that are pseudo-random at best, totally inadequate at worst.

Random numbers generated for use within the Monte Carlo procedures were generated using a Knuth algorithm [9]. This subtractive method produced a set of random deviates between zero and one. These numbers were then corrected to normal deviates for a Gaussian distribution of zero mean and unit standard deviation using a Box-Muller transform [9]. The resulting sequence was then scaled to the required mean and standard deviation.

Any random number generator uses a seed to produce the sequence of numbers. Use of the same seed will produce the same set of numbers. Thus, to further randomise the process, the number used to seed the random number generator was produced using the C++ time function and was therefore variable. In addition, the first 1000 numbers generated were discarded before a final set of random numbers was produced.

3.4.6 Integration of modules

Each module within the immunosensor model was implemented as a stand-alone program using a class defining the module and a test routine. The classes were linked together to produce a model of a complete evanescent field immunosensor with the resulting class structure as shown in Figure 3.7.

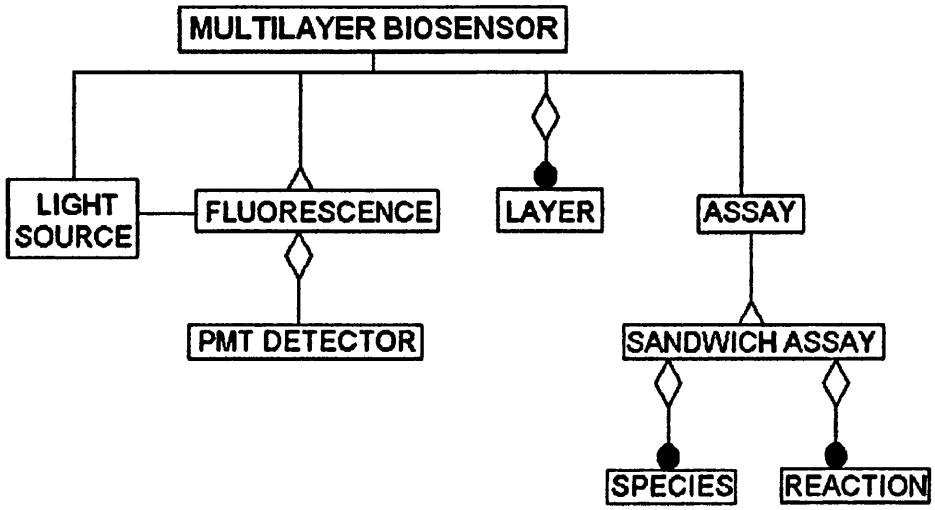

Figure 3.7: *Structure diagram of the full model of the multilayer coupled capillary fill device containing a sandwich immunoassay.*

3.5 Testing and verification

"Bugs lurk in corners and congregate at boundaries."

Beizer [10]

Testing and verification play a crucial role in the development of any software. Not only is it vital to check that the resulting software meets the user requirements specified, but it is also important to check that the code is functioning correctly for a range of situations, including those that are outside the intended use of the software. For example, if the software expects the user to enter a number and he enters a letter a good software implementation would inform the user of his mistake and request an appropriate entry.

3.5.1 White box testing

Testing involves the systematic checking of all algorithms, interfaces, data handling and error trapping within the computer code, a process that is usually more time consuming than the original implementation. Testing at this level is known as white box testing i.e. the testing of the internal computer code. It should ensure that all statements within the code are executed, thus eliminating redundant code. Both paths of any logical test should be checked to ensure that the output is valid. Any loops should be tested both within the loop and at their boundary conditions and all internal data should be validated to ensure that accidental stack overwriting does not occur.

Testing of the code implemented in the development of the immunosensor model followed a procedure known as "basic path testing" [11]. This involves producing a low level flow chart of the route that is taken through a particular piece of code. Analysis of this flow chart enables all the possible routes to be identified and test cases involving both the acceptable and non-acceptable routes can then be derived. These test cases are then used to test the code within and at the extremes of its operating limits. Figure 3.8 shows an example of the flow chart for a particular piece of code.

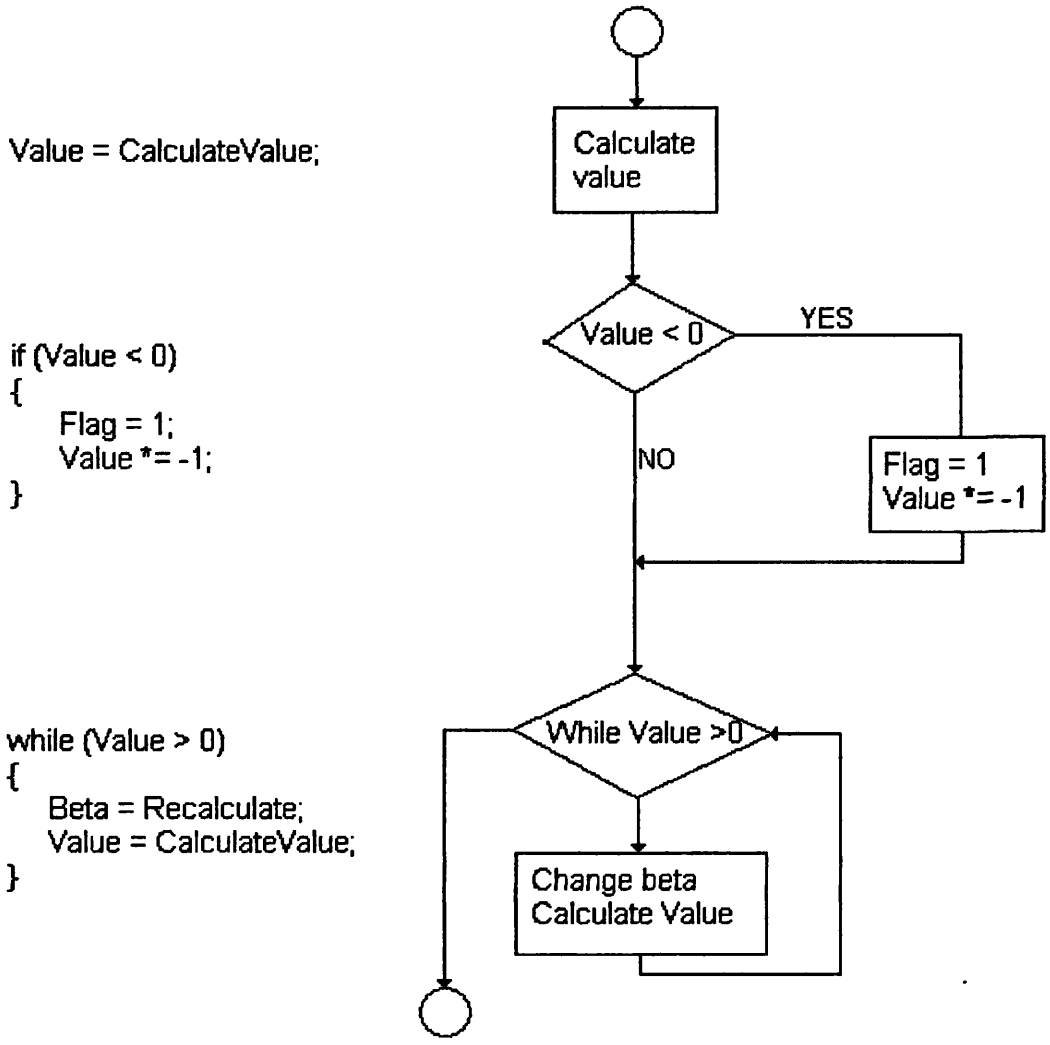

***Figure 3.8**: Flow chart illustrating the basic paths through the code for calculating the propagation constant of the guided light within the waveguide. Code includes both an 'if' statement (logical decision) and a while loop.*

3.5.2 Black box testing

Verification refers to the process of determining whether the output of the software is as expected for a particular input and is known as black-box testing [12], a process that has no interest in the internal workings of the software. Verification of the model of the immunosensor includes fitting the model to experimental data in order to determine whether the output from the model is equivalent to the output generated by experiment. Details of the verification process are included in the relevant chapter for each component of the model.

References

[1] Sloper AN, *PhD Thesis University of London*, ppl - 5, 1991.

[2] Pampapathi VKM, *PhD Thesis University of London*, pp30 – 32, 1994.

[3] Robinson GA, Attridge JW, Deacon JK & Whitely SC, The fluorescent capillary fill device, *Sensors and Actuators*, **B11**, 235-238, 1993.

[4] Sloper AN & Flanagan MT, Scattering in planar surface waveguide immunosensors, *Sensors and Actuators*, **B11**, 537-542, 1993.

[5] Pressman RS, *Software Engineering A Beginner's Guide*, (NY: McGraw-Hill, Inc), pp 53-93, 1988.

[6] Heath MT, *Scientific Computing An Introductory Survey*, (NY: McGraw-Hill), pp374 – 380, 1997.

[7] Moran PAP, *An introduction to probability theory*, (Oxford, UK: Oxford University Press), pp 43 -46, 1968.

[8] Yakowitz SJ, *Computational Probability and Simulation. Applied Mathematics and Computation No12*, (Addison-Wesley Publishing Company, Inc), pp 2 – 5, 1997.

[9] Press WH, Teukolsky SA, Vetterling WT & Flannery BP, *Numerical Recipes in C*, 2nd Edition (Cambridge University Press) pp 274 - 284, 1992.

[10] Beizer B, *Software Testing Techniques*, (Van Nostrand-Reinhold), 1983.

[11] McCabe T, *Structured Testing*, IEEE Computer Society, 1982.

[12] Bouzeghoub M, Gardarin G & Valduriez P *Object Technology Concepts and Methods* (I T P), pp 106 – 113, 1997.

Chapter 4

Immunoassay module

4.1 Immunoassay

Immunotechniques provide sophisticated biochemical tools that can be used to investigate and manipulate minute concentrations of complex molecules [1]. One example, the immunoassay, allows the concentrations of biochemicals to be determined. The majority of immunoassay techniques involve an antibody chosen for it's specificity to the substance to be detected, the analyte. This antibody, known as the capture antibody, is usually immobilised on a surface. The sample containing the analyte is added to the capture antibody, together with a second antibody/analyte that has been labelled with a molecule that can be used to generate a signal e.g. a radioactive isotope or a fluorophore. Following the biochemical reactions, the signal generated can be used to determine the quantity of analyte present in the sample. Immunosensors have incorporated competitive (Figure 4.1) [2], displacement [3] and sandwich [4] immunoassays.

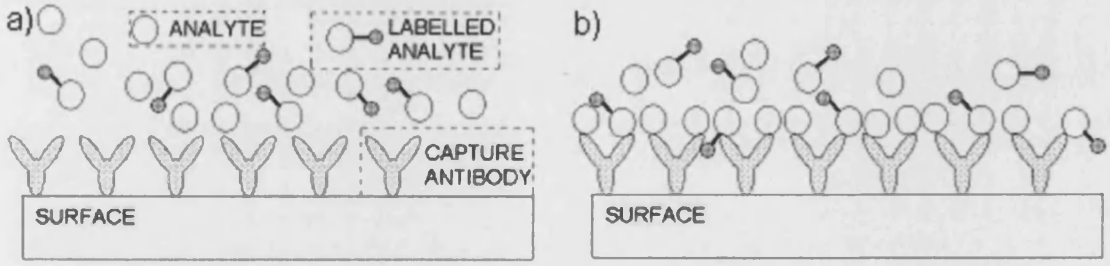

Figure 4.1: *Competitive assay*
a) sample containing the analyte and the labelled analyte is added to the capture antibody immobilised on a surface
b) at equilibrium

4.1.1 Competitive assay

In a competitive assay the sample added contains the analyte to be detected and a known quantity of the analyte that has been labelled with, for example, a fluorophore (Figure 4.1). The analyte and the labelled analyte compete for the antibody binding sites as the system comes to equilibrium. Thus, the bound analyte is inversely

proportional to the amount of bound labelled analyte and can be measured by detecting the light emitted by the fluorescent label.

4.1.2 Displacement assay

A displacement assay involves a capture antibody that has already been exposed to a known concentration of labelled analyte. The sample containing the analyte is added and this analyte once again competes with the labelled analyte for the binding sites, in this case displacing some of the previously bound labelled analyte. At equilibrium the displacement assay (Figure 4.2) resembles the competitive assay and the amount of bound analyte can be determined by measuring the reduction in signal resulting from addition of the sample.

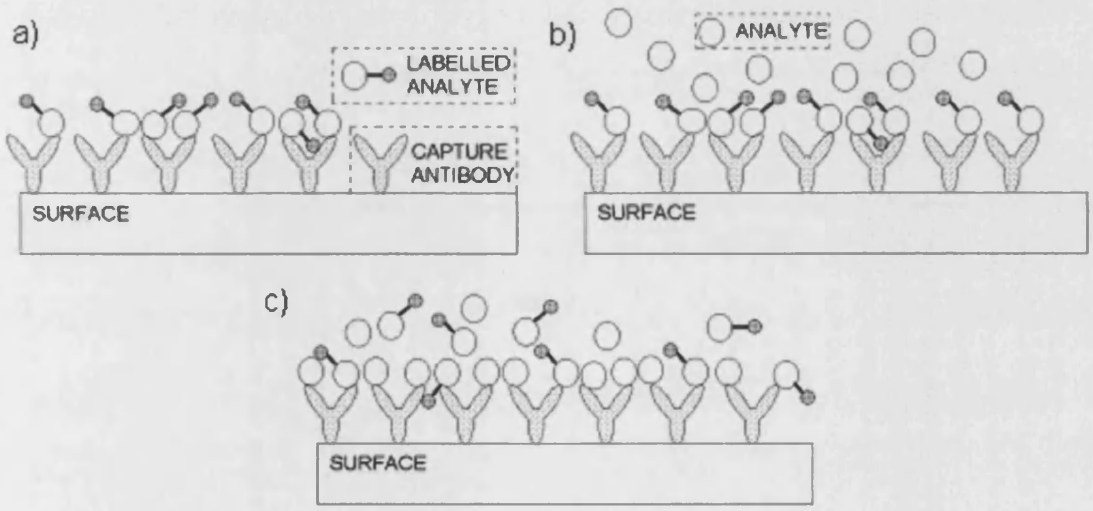

***Figure 4.2**: Displacement assay*
a) capture antibody is bound with a known concentration of labelled analyte
b) the sample containing the analyte is added
c) at equilibrium

4.1.3 Sandwich assay

A sandwich or immunometric assay involves a capture antibody, the analyte and a labelled antibody. The analyte may bind with the capture antibody, the labelled antibody or both and thus becomes bound within an antibody-analyte-labelled antibody sandwich. The bound analyte is proportional to the bound labelled antibody and can thus be measured by detecting the amount of bound label e.g. the light emitted by a

fluorescent label. Figure 4.3 illustrates a sandwich immunoassay being performed within a capillary-fill device (CFD).

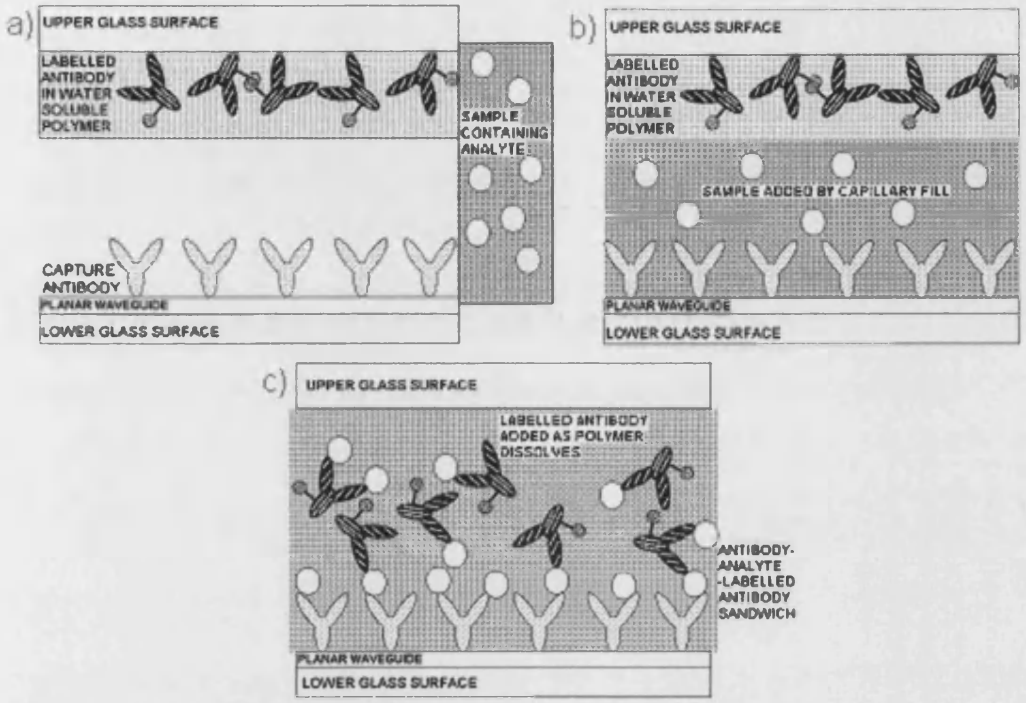

Figure 4.3: *Sandwich assay inside a capillary fill device*

a) Capture antibody immobilised on lower surface; labelled antibody trapped within water soluble polymer on upper surface; analyte in sample placed at end of capillary

b) Sample added by capillary action

c) Polymer dissolves adding labelled antibody and sandwich assay reactions occur

4.1.4 Immunoassay within an evanescent field immunosensor

Traditionally the bound label has been separated from the unbound label by washing any excess solution from the assay. Development of a biosensor requires the elimination of this washing step. Optical sensors that utilise the effects of the evanescent field provide a means of probing the immunoassay without the removal of the unbound label i.e. the washing step becomes unnecessary. The capture antibody is immobilised onto a waveguide into which light is coupled. The light within the evanescent field excites the fluorophores. The rapid decay of this field away from the surface ensures that the fluorophores excited are predominately those that are bound, hence eliminating the need for washing. This technique has been further adapted by

incorporating the immunoassay into the lower surface of a capillary-fill device [5]. This provides a means by which the amount of label and solution containing analyte may be controlled without the need for specialist equipment or experience.

4.1.5 Modelling considerations

Initial biosensor modelling concentrated on the radioimmunoassay, an immunoassay in which the molecule used as the label was a radioisotope, and established that using a sandwich assay produced a more sensitive device than one using a competitive assay [6]. Current practice has replaced the radioisotope labels with fluorescent labels and the need to perform a washing step with the exploitation of the evanescent field. However, no in depth modelling has been undertaken to establish whether the sandwich assay is still superior in this type of system.

Figures 4.1 – 4.3 illustrate different immunoassay techniques where the size of the analyte shown is small compared to the size of the antibody. However, in reality this is often not the case and it is obvious that should a large molecule become bound to an antibody this may hinder the binding of a second molecule. The amount by which binding is prevented is known as steric hindrance and may range in value from 0 - 1, where a value of 0 indicates that no hindrance occurs and a value of 1 indicates that there is total steric hindrance (Figure 4.4). The model needs to take account of such steric hindrance.

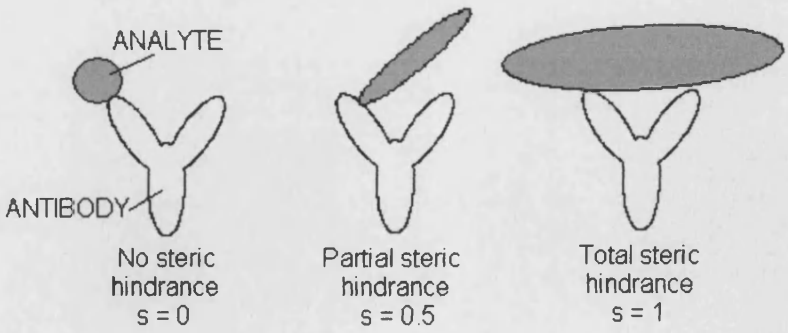

Figure 4.4: *A single molecule bound to an antibody may interfere with the binding of a second molecule. This phenomenon is known as steric hindrance (s); where s may take values between 0 (no steric hindrance) and 1 (total steric hindrance).*

The time required for the immunoassay to come to equilibrium, typically 10 – 15 minutes, is often greater than the acceptable operation time of a biosensor [7]. Few appointments with a doctor would allow time for a test that required 10 minutes of waiting time. Thus, it has become necessary for the biosensor industry to explore the feasibility of determining results during the kinetic phase of the immunoassay. Modelling provides the ideal vehicle with which to undertake preliminary studies. Therefore the model of the immunoassay element of the biosensor will need to establish both the equilibrium and transient concentrations of each of the species involved.

4.2 Optimisation applied to immunoassay

The equilibrium equations that characterise a competitive assay are listed in Table 4.1. In order to determine the concentrations of each of the species present at equilibrium it is necessary to solve the set of equilibrium equations. There are no good, general methods for solving systems of more than one non-linear equation [8]. The most common approach is to cast the equations into a form that allows an optimisation procedure to be used. The function derived below is applicable to any set of reactions although will be exemplified in relation to a competitive assay.

Table 4.1: Equilibria for a competitive assay.

	Equilibrium equation	Forward rate equation	$[A_i]$	$[B_i]$	$[AB_i]$
1	$c + a \rightleftarrows ca$	$d[ca]/dt = k_1[c][a] - k_{-1}[ca]$	c	a	ca
2	$ca + a \rightleftarrows ca_2$	$d[ca_2]/dt = k_2[ca][a] - k_{-2}[ca_2]$	ca	a	ca_2
3	$c + l \rightleftarrows cl$	$d[cl]/dt = k_3[c][l] - k_{-3}[cl]$	c	l	cl
4	$cl + l \rightleftarrows cl_2$	$d[cl_2]/dt = k_4[cl][l] - k_{-4}[cl_2]$	cl	l	cl_2
5	$ca + l \rightleftarrows cal$	$d[cal]/dt = k_5[ca][l] - k_{-5}[cal]$	ca	l	cal
6	$cl + a \rightleftarrows cal$	$d[cal]/dt = k_6[cl][a] - k_{-6}[cal]$	cl	a	cal

Each equation produces both forward (shown) and reverse rate equations; with rate constants for creation (k_{+i}) and depletion (k_{-i}) of each species.
At equilibrium the rate of change in concentration is zero and the association constant $K_i = k_i/k_{-i} = [AB_i]/[A_i][B_i]$ can be derived.
c – capture antibody; a – analyte; l – labelled analyte

4.2.1 Optimisation function

Each equilibrium equation has a corresponding association constant, K_i, defined by

$$K_i = \frac{[AB_i]}{[A_i][B_i]}$$

where i denotes the equation

$[X_i]$ denotes the concentration of species X_i

and [XY] denotes a compound species.

Rearranging produces a set of equations

$$f_i = s_i K_i [A_i][B_i] - [AB_i] \qquad (4.1)$$

where all $f_i = 0$ at equilibrium

and s_i is a steric hindrance factor.

The concentrations of the initial species are limited by the equality constraints imposed by mass conservation. In the case of the competitive assay the mass conservation equations are

$$\begin{aligned} g_1 &= [c]_0 - [c] - [ca] - [ca_2] - [cl] - [cl_2] - [cal] \\ g_2 &= [a]_0 - [ca] - 2[ca_2] - [cal] \\ g_3 &= [l]_0 - [cl] - 2[cl_2] - [cal] \end{aligned} \qquad (4.2)$$

where $[X_i]_0$ is the initial concentration of species X_i

and all $g_i = 0$ at equilibrium.

The concentrations of the all other species are limited in that they cannot exceed an amount dictated by the constraints of mass conservation e.g.

$$0 \le [\mathrm{ca}] \le Min([\mathrm{c}]_0, [\mathrm{a}]_0)$$

where *Min*(a,b) is the minimum value of a and b.

The standard method of recasting to a single sum of squares was adopted and the optimisation function, F, which could be minimised to determine the concentration values at equilibrium, was developed.

$$\begin{aligned} F &= \sum_{i=1}^{N} f_i^2 \\ &+ \sum_{i=1}^{M} \lambda_i g_i^2 \\ &+ \sum_{i=1}^{L} h(\theta_{\min,i} - \theta_i)\gamma_i(\theta_{\min,i} - \theta_i)^2 \\ &+ \sum_{i=1}^{L} h(\theta_{\max,i} - \theta_i)\gamma_i(\theta_{\max,i} - \theta_i)^2 \end{aligned} \quad . \qquad (4.3)$$

where f_i as defined by equation (4.1)

g_i as defined by equation (4.2)

λ_i are the Lagrangian multipliers

h() is the Heaviside function

γ_i are the weighting factors

θ_i are the concentrations of species X_i

$\theta_{\min,i}$ are the minimum allowed concentration values of species X_i

$\theta_{\max,i}$ are the maximum allowed concentration values of species X_i

N is the number of equilibrium equations

M is the number of initial species

and L is the number of species created by the reactions.

4.2.1.1 Lagrangian multipliers

A common technique for imposing equality constraints on the optimisation of a function is to introduce a Lagrangian multiplier [9]. In a simple two variable system a typical Lagrange equation would be of the form

$$A(x,y)-\lambda(C-B(x,y))$$

where A(x,y) is the function to be optimised
B(x,y) = C is the constraint
and λ is the Lagrangian multiplier.

Differentiating the Lagrange equation with respect to x, y and λ produces a set of simultaneous equations which can be solved for x and y, and also as a by-product of the procedure, λ. The complexity of equation (4.3) means that the values of λ_i cannot be established in this fashion. However, by including the Lagrangian multipliers as variables within the optimisation, it is possible to impose the equality constraints necessary to conserve mass within an immunoassay system.

4.2.1.2 Penalty functions

Penalty functions provide an ideal method of imposing inequality constraints within an optimisation procedure [10]. A penalty function erects a barrier within the search surface that forces the optimisation to return to the realistic parameter space. A constant, with a value large enough to be beyond the possible scope of the function being optimised, is used as a multiplier with the Heaviside function

$$h(x)=\begin{matrix}0 & x<0\\ 1 & x\geq 0\end{matrix}$$

and added to the optimisation function. Thus, variables values exceeding the limits imposed by the inequality should quickly be abandoned by the optimisation procedure.

4.2.1.3 Search surface

Inspection of equation (4.3) indicates that the surface, F, over which an optimisation search is to be performed, has a large dimensionality and is likely to be complex. This suggests that the optimisation may be troubled by the well-known problems of ill-conditioning and false minima, with consequent difficulties in choosing initial estimates.

The search surface described by F for a competitive assay has at least 8 dimensions and is obviously difficult to visualise. A subsystem of chemical reactions

$$a + l \rightleftarrows al$$

$$al + a \rightleftarrows a_2l$$

was considered and an examination of the surface represented by the function, F, was undertaken for this subsystem. The functions f_i for this subsystem are

$$f_1 = s_1K_1[a][l] - [al]$$
$$f_2 = s_2K_2[al][a] - [a_2l]$$

The mass conservation equations, g_i, are

$$g_1 = [a]_0 - [a] - [al] - 2[a_2l]$$
$$g_2 = [l]_0 - [al] - [a_2l]$$

Assuming values for the initial concentrations of

$$[a]_0 = 10 \text{ nM}$$
$$[l]_0 > 10 \text{ nM}$$

the inequality constraints on the species produced within the system are

$$0 \leq [al] \leq 10$$
$$0 \leq [a_2l] \leq 5$$

Figure 4.5 shows the surface calculated for all pairs of values of al and a_2l, using equation (4.3), in which both g_i were included, all γ_i were set equal to zero and all λ_i were set to equal to unity, i.e. one in which the conservation equations are included within the optimisation but the inequality constraints have been excluded. A long valley around the minimum, typical of ill conditioning can be seen, thus indicating that it is necessary to impose the inequality constraints within the optimisation.

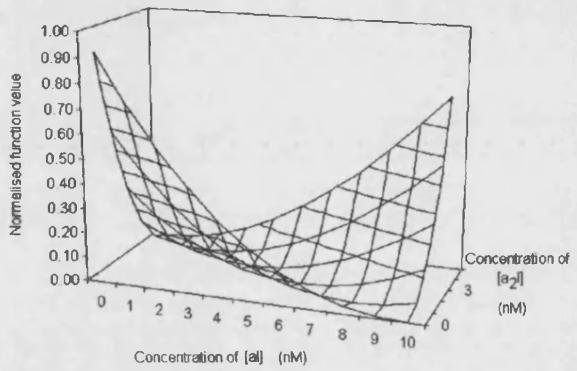

***Figure 4.5**: Optimisation search surface (F) plotted for the subsystem of equilibrium equations $a + l \rightleftarrows al$ and $al + a \rightleftarrows a_2l$ for all pairs of values of [al] and $[a_2l]$*
$N = M = L = 2$; $\lambda_i = 1$ and $\gamma_i = 0$ for all i in equation (4.3)

Figure 4.6 illustrates the search surface for F in which the weighting factors, γ_i, are set equal to a constant large value i.e. in which penalty functions have been used to impose the inequality constraints on the species concentrations. Figure 4.6 now represents a correctly constrained surface but one in which there are several comparable local minima, a consequence of collapsing a set of non-linear equations into a single function [8].

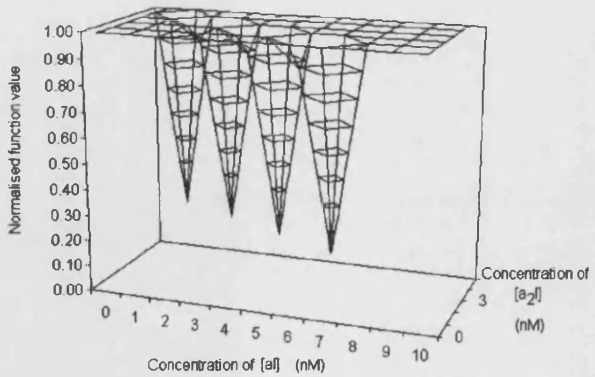

***Figure 4.6**: Optimisation search surface (F) plotted for the subsystem of equilibrium equations $a + l \rightleftarrows al$ and $al + a \rightleftarrows a_2l$ for all pairs of values of [al] and $[a_2l]$*
$N = M = L = 2$; $\lambda_i = 1$ and $\gamma_i = 1 \times 10^{80}$ for all i in equation (4.3)

A review of Table 4.1 shows there to be one redundant equation, i.e. both equations numbered 5 and 6 lead to the production of the species cal, and therefore one may be eliminated. The choice of the set of equilibrium equations to be used will not alter the global minimum but may affect the surface, F, over which the optimisation search is operating. The equations describing the subsystem were reviewed and whilst neither of the equilibrium conditions is redundant it was found that if the second mass conservation equation, g_2, was removed from the calculation a much better conditioned search surface was achieved (Figure 4.7). It should be noted that removing one of the conservation equations adds another variable to the optimisation procedure and the search surface is now three-dimensional. Figure 4.7 represents a two-dimensional snap-shot for a fixed value of the concentration of species a.

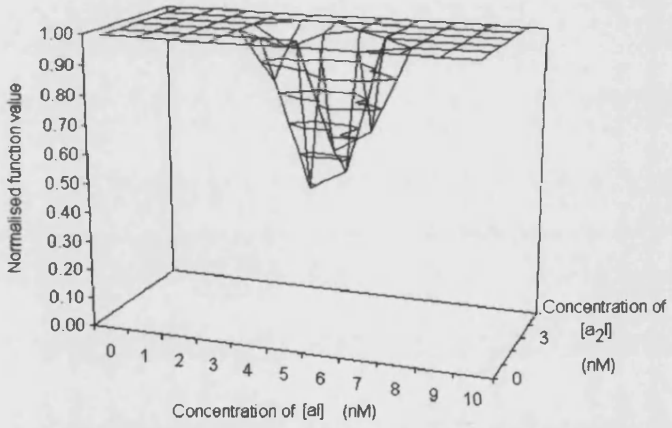

Figure 4.7: *Optimisation search surface (F) plotted for the subsystem of equilibrium equations* $a + l \rightleftarrows al$ *and* $al + a \rightleftarrows a_2l$ *for all pairs of values of [al] and* $[a_2l]$
$N = L = 2$; $M = 1$; $\lambda_1 = 1$; $\gamma_i = 1e80$ *for all i and* $[a] = 1e\text{-}13$ *M in equation (4.3)*

4.2.2 Optimisation techniques

Optimisation techniques vary in the methodology used to find a solution. Given the complexity of the immunoassay equations and the resulting search surface, two classes of optimisation, classical regression and intelligent optimisation techniques, were implemented in an attempt to calculate the concentrations of the species X_i at equilibrium. As this calculation may be repeated many times both accuracy and speed of computation are major determinants of the most appropriate method.

4.2.2.1 Classical regression techniques

Preliminary work on all major regression procedures identified three that proved most promising when applied to an immunoassay; the simplex method of Nelder-Mead [11], the secant method of Broyden [12] and the quasi-Newton method of Davidon-Fletcher-Powell [13]. These techniques vary slightly in their approach to the minimisation of a particular function. The simplex method of Nelder-Mead expands and then contracts the region of search until it converges onto the minimum. This approach, whilst robust can be time consuming. Broyden's secant method avoids the need for determining the partial derivatives of the function by using an approximation to the Jacobian matrix and deriving a formula that uniquely determines the change in this matrix resulting from a multidimensional "step" towards the minimum. Davidon-Fletcher-Powell's quasi-Newton method does require the first derivatives of the function but then uses an approximation to the inverse Hessian matrix that ensures that this matrix remains symmetric and positive definite. This matrix is then updated to the point where it converges to the true inverse Hessian and a solution is found. These three methods were fully implemented.

4.2.2.2 Intelligent optimisation techniques

Intelligent optimisations, those that can make decisions about the validity of a solution, are often considered to be better at finding a global minimum than are the classical procedures [8]. Simulated annealing is a general optimisation method, which stochastically simulates the slow cooling of a physical system. A cost function defines a value that establishes the state of the system at a particular point or "temperature". The algorithm works by iteratively changing the temperature, and hence the state of the system, and either accepting or rejecting each change according to the resulting cost. A simulated annealing procedure with a stepwise cooling schedule [14] was implemented to determine the equilibrium concentrations of the immunoassay.

A genetic algorithm is an optimisation technique that uses an algorithm that is analogous to the genetic selection of nature. A set of solutions i.e. a population is proposed and each is allocated a fitness value. New solutions are generated by selecting members of the previous generation based on their fitness and reproducing a

new population by crossing these members. A small amount of mutation is also allowed. Selection, reproduction and mutation of each population should result in a population that has the highest fitness value, i.e. the optimum solution. A genetic algorithm was implemented to optimise the function, F (equation 4.3) using a combination of elitist and steady state selection [15]. The encoding of multiple floating-point numbers as bit strings was compared with the approach of Davis [16] using real numbers in a hybrid genetic algorithm.

4.2.3 Application to a competitive assay

Although this multidimensional problem cannot be graphed in the same way as illustrated above for the subsystem (Figures 4.5 – 4.7), varying the choice of redundant equation to eliminate from the search function F demonstrated a similar pattern when applied to a competitive assay. This and the dependence of the regression techniques on a suitable starting point indicate the importance of good initial estimates.

4.2.3.1 Initial estimates

The technique developed by Flanagan *et al* [17] for simpler multiple antibody-hapten equilibria was considered. This involved starting with the lowest analyte concentration and making all initial complex concentration estimates zero. The results for each analyte concentration were then used as the estimates for the next highest analyte concentration. Unfortunately no such simple technique could be found that would work with the competitive assay reactions (Table 4.2).

Table 4.2: Reactions within a competitive assay

Index	Reaction
1	$c + a \rightleftarrows ca$
2	$ca + a \rightleftarrows ca_2$
3	$c + l \rightleftarrows cl$
4	$cl + l \rightleftarrows cl_2$
5	$ca + l \rightleftarrows cal$
6	$cl + a \rightleftarrows cal$

The technique adopted for calculating the initial estimates of the concentrations within a competitive assay, where the reaction number and index of K refer to Table 4.2, was

i) assume that species c will be distributed between ca and cl in proportion to the ratio of the rate constant for each reaction over the sum of the rate constants for the two reactions:

i.e. $[c]_1 = [c]_0 \frac{K_1}{K_1 + K_3}$ and $[c]_2 = [c]_0 \frac{K_3}{K_1 + K_3}$

ii) calculate [ca] resulting from reaction 1 using

$$K_1 = \frac{[\mathrm{ca}]}{[\mathrm{c}]_1[\mathrm{a}]_0}$$

iii) calculate [cl] resulting from reaction 3 using

$$K_3 = \frac{[\mathrm{cl}]}{[\mathrm{c}]_2[\mathrm{l}]_0}$$

iv) calculate concentrations of a and l remaining after reactions 1 and 3 have occurred using

$$[a] = [a]_0 - [ca] \text{ and } [l] = [l]_0 - [cl]$$

v) divide the concentrations of a, l, cl and ca in the ratio of the rate constants of their subsequent reactions

e.g. divide [ca] in the ratio K_2:K_5 to get $[ca]_2$ and $[ca]_5$

divide [cl] in the ration K_4:K_6 etc...

vi) calculate concentrations resulting from remaining reactions assuming that the concentrations calculated in (v) are the initial concentrations for these reactions

e.g. $[cal]_{5\_new} = K_5[ca]_5[l]_5$

and $[l]_{5\_new} = [l]_5 - [cal]_{5\_new}$ etc..

vii) total the concentration values for each species from each of the reactions

e.g. $[\mathrm{cal}] = [\mathrm{cal}]_{5\_new} + [\mathrm{cal}]_{6\_new}$.

Table 4.3: Equilibria for a sandwich assay

	Equilibrium equation	**Forward rate equation**
1	$c + a \rightleftarrows ca$	$d[ca]/dt = k_1[c][a] - k_{-1}[ca]$
2	$l + a \rightleftarrows al$	$d[al]/dt = k_2[l][a] - k_{-2}[al]$
3	$c + al \rightleftarrows cal$	$d[cal]/dt = k_3[c][al] - k_{-3}[cal]$
4	$ca + l \rightleftarrows cal$	$d[cal]/dt = k_4[ca][l] - k_{-4}[cal]$
5	$ca + a \rightleftarrows ca_2$	$d[ca_2]/dt = k_5[ca][a] - k_{-5}[ca_2]$
6	$a + al \rightleftarrows a_2l$	$d[a_2l]/dt = k_6[a][al] - k_{-6}[a_2l]$
7	$ca + al \rightleftarrows ca_2l(1)$	$d[ca_2l(1)]/dt = k_7[ca][al] - k_{-7}[ca_2l(1)]$
8	$ca + al \rightleftarrows ca_2l(2)$	$d[ca_2l(2)]/dt = k_8[ca][al] - k_{-8}[ca_2l(2)]$
9	$c + a_2l \rightleftarrows ca_2l(2)$	$d[ca_2l(2)]/dt = k_9[c][a_2l] - k_{-9}[ca_2l(2)]$
10	$ca_2 + l \rightleftarrows ca_2l(1)$	$d[ca_2l(1)]/dt = k_{10}[ca_2][l] - k_{-10}[ca_2l(1)]$
11	$ca_2l(1) + l \rightleftarrows ca_2l_2$	$d[ca_2l_2]/dt = k_{11}[ca_2l(1)][l] - k_{-11}[ca_2l_2]$
12	$cal + a \rightleftarrows ca_2l(1)$	$d[ca_2l(1)]/dt = k_{12}[cal][a] - k_{-12}[ca_2l(1)]$
13	$cal + a \rightleftarrows ca_2l(2)$	$d[ca_2l(2)]/dt = k_{13}[cal][a] - k_{-13}[ca_2l(2)]$
14	$ca + a_2l \rightleftarrows ca_3l$	$d[ca_3l]/dt = k_{14}[ca][a_2l] - k_{-14}[ca_3l]$
15	$cal + al \rightleftarrows ca_2l_2$	$d[ca_2l_2]/dt = k_{15}[cal][al] - k_{-15}[ca_2l_2]$
16	$ca_2 + al \rightleftarrows ca_3l$	$d[ca_3l]/dt = k_{16}[ca_2][al] - k_{-16}[ca_3l]$
17	$ca_2l(1) + al \rightleftarrows ca_3l_2$	$d[ca_3l_2]/dt = k_{17}[ca_2l(1)][al] - k_{-17}[ca_3l_2]$
18	$ca_2l(2) + al \rightleftarrows ca_3l_2$	$d[ca_3l_2]/dt = k_{18}[ca_2l(2)][al] - k_{-18}[ca_3l_2]$
19	$cal + a_2l \rightleftarrows ca_3l_2$	$d[ca_3l_2]/dt = k_{19}[cal][a_2l] - k_{-19}[ca_3l_2]$
20	$ca_2l(2) + a_2l \rightleftarrows ca_4l_2$	$d[ca_4l_2]/dt = k_{20}[ca_2l(2)][a_2l] - k_{-20}[ca_4l_2]$
21	$ca_2l_2 + a \rightleftarrows ca_3l_2$	$d[ca_3l_2]/dt = k_{21}[ca_2l_2][a] - k_{-21}[ca_3l_2]$
22	$ca_3l + l \rightleftarrows ca_3l_2$	$d[ca_3l_2]/dt = k_{22}[ca_3l][l] - k_{-22}[ca_3l_2]$
23	$ca_3l + al \rightleftarrows ca_4l_2$	$d[ca_4l_2]/dt = k_{23}[ca_3l][al] - k_{-23}[ca_4l_2]$
24	$ca_3l_2 + a \rightleftarrows ca_4l_2$	$d[ca_4l_2]/dt = k_{24}[ca_3l_2][a] - k_{-24}[ca_4l_2]$
25	$ca_2l(1) + a \rightleftarrows ca_3l$	$d[ca_3l]/dt = k_{25}[ca_2l(1)][a] - k_{-25}[ca_3l]$
26	$ca_2l(2) + a \rightleftarrows ca_3l$	$d[ca_3l]/dt = k_{26}[ca_2l(2)][a] - k_{-26}[ca_3l]$

Each equation produces both forward (shown) and reverse rate equations; with rate constants for creation (k_{+i}) and depletion (k_{-i}) of each species. These equations can be combined to produce an overall rate of change equation for each species involved.
At equilibrium the rate of change in concentration is zero and the association constant $K_i = k_i/k_{-i}$ can be derived.
c – capture antibody; a – analyte; l – labelled antibody

4.2.4 Application to a sandwich assay

The equilibrium equations describing a sandwich assay are listed in Table 4.3. Comparison of the complexity of these with the corresponding competitive assay equations (Table 4.1) indicates that the demands on an optimisation procedure will be greatly increased for the sandwich assay. The competitive assay has six equilibrium equations compared with the twenty-six that describe a sandwich assay. All the reactions within a competitive assay occur at the surface, whilst within the sandwich assay it is possible for the analyte to bind to the labelled antibody while in the solution above the surface. The fourteen species that may occur during the sandwich assay reactions dictate that the search surface F, (equation 4.3), for a sandwich assay optimisation procedure has at least fourteen dimensions.

Early investigation showed that finding an optimisation technique that would produce an accurate result from a set of crude initial estimates was unlikely in the case of a sandwich assay. Analysis indicated that the optimisation could be simplified into a number of stages that would each provide an initial estimate for the subsequent stage.

Initially the equilibrium concentrations within the solution containing only analyte and labelled antibody were easily calculated by applying the optimisation procedure to the subsystem of equations:

$$\mathrm{a} + \mathrm{l} \rightleftarrows \mathrm{al}$$

$$\mathrm{al} + \mathrm{a} \rightleftarrows \mathrm{a_2l}.$$

The resulting concentrations of a, l, al and a_2l could then be divided between double the capture antibody concentration assuming each capture antibody to be monovalent, i.e. a situation with twice as many antibodies each having only a single binding site which preserves the number of binding sites available. Thus concentrations for c, ca, cal and ca_2l assuming monovalent capture antibodies were calculated.

For each of these species the ratio of the number of binding sites occupied by the species to the total number of binding sites available was calculated e.g.

$$[ca]:2[c]_0$$

where $[c]_0$ is the actual concentration of bivalent capture antibodies.

A nearest neighbour analysis was then used to estimate concentrations for the bivalent species. The analysis is detailed for the species ca_2l which is formed from a monovalent ca and a monovalent cal. The probability of a bivalent capture antibody being found in the form ca_2l is given by

$$p(ca_2l) = 2\frac{[ca]}{2[c]_0}\frac{[cal]}{2[c]_0} = \frac{[ca][cal]}{2[c]_0^2}$$

where [cX] is the concentration of [cX] calculated for monovalent c (above)
and $[c]_0$ is the actual concentration of bivalent capture antibodies.

The estimated concentration of ca_2l is thus

$$[ca_2l] = p(ca_2l)[c]_0 = \frac{[ca][cal]}{2[c]_0}$$

Similar calculations were made for each of the species possibly present within a sandwich immunoassay and these concentrations provided an initial estimate for the optimisation procedure.

In summary, the process of optimising a sandwich immunoassay involved

i) calculating the equilibrium of the solution containing only the analyte and the labelled antibody
ii) distributing the resulting species assuming monovalent capture antibodies, i.e. only one-site capture
iii) performing a nearest neighbour statistical analysis to estimate concentrations of the bivalent antibody species

iv) using these values as the initial estimate for the optimisation of the equations that describe a full sandwich immunoassay.

The process is illustrated by Figure 4.8.

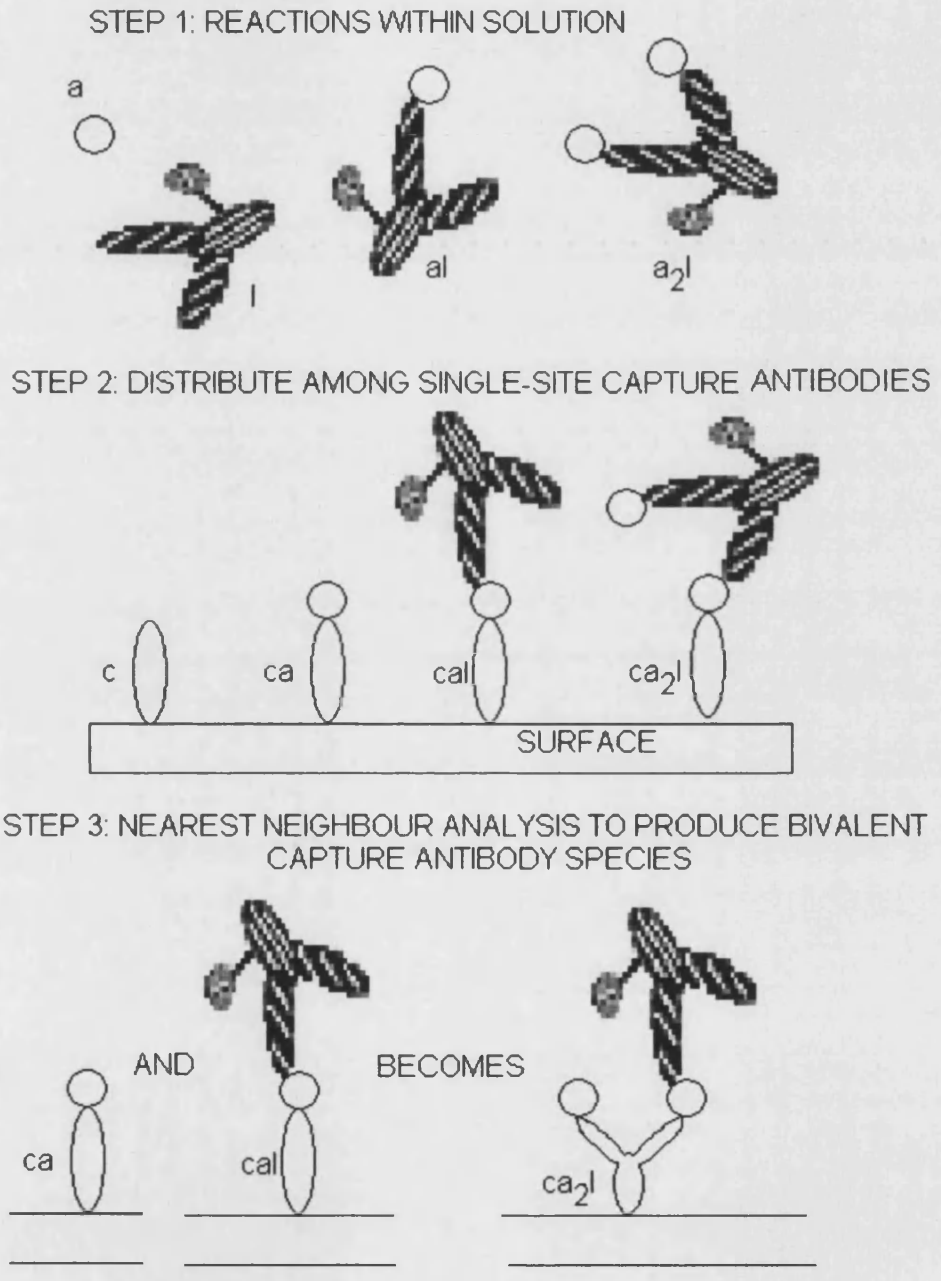

Figure 4.8: *Three steps identified as a means of approaching the optimisation of a sandwich assay*

4.3 Markov chains applied to immunoassay

The application of optimisation techniques to the modelling of the immunoassay proved problematic. Collapsing the multiple equilibrium equations into a single function produced surfaces that were ill conditioned and the optimisation results were extremely sensitive to the initial estimates, indicating the presence of several local minima. In addition the approach offered no possibility for modelling the transient response of the chemical reactions. Consequently a second approach, one using an adaptation of Markov chains, was explored. Analogous to the optimisation model, the model presented is applicable to any set of chemical reactions but is illustrated using the equilibrium equations describing a competitive assay as previously listed in Table 4.1.

4.3.1 Markov chains

A stochastic process $\{X(t), t \in T\}$ is a Markov process if, for any set of s+1 values $t_1 < t_2 < \ldots < t_s < t_{s+1} \in T$ with corresponding set of states $\{x_1, x_2, \ldots, x_s, x_{s+1}\}$, the probability that the process is in state x_{s+1} depends only on state x_s i.e. the next state that the process will enter depends only on it's current state and not on the previous history of the process [18].

Considering a discrete time set

$$T = \{0, 1, 2, 3, \ldots\}$$

with positive integer states X_i

$$i = \{1, 2, 3, \ldots, S\}$$

the transition probabilities can be defined as

$$q_{ij} = P\left[X_{s+1} = j \middle| X_s = i\right]$$

where q_{ij} is the probability that if the process is in state i the next state will be state j.

The probability of the process being in state j at stage s+1 becomes

$$p_j(s+1) = \sum_i p_i(s) q_{ij}(s).$$

Thus the set of equations for each state can be expressed in matrix form as

$$\mathbf{p}(s+1) = \mathbf{p}(s)\mathbf{Q}(s) \qquad (4.4)$$

where **p**(s) is the probability vector

and **Q**(s) is an s x s matrix with elements q_{ij},
known as the transition probability matrix.

4.3.2 Application to immunoassay

Too et al [19] proposed that Markov chains could be applied to the chemical reactions in continuous flow reactors by considering the number of molecules of each chemical species present during the reactions to be a state of the process. Antia and Lee [20] showed that for this application to be successful the Markov process had to be modified to maintain mass conservation. Such stochiometric considerations dictate that the sum of the row elements in the transition probability matrix need not equal unity. The number of molecules of a species at any stage can then be calculated using equation (4.4), where **p**(s) becomes the vector representing the number of molecules of each species.

The immunoassay reactions are more complex than those considered by Antia and Lee but their similar general form suggests that a comparable modified Markov chain approach may be applicable. The probability that a number of molecules of a species occurs at stage s+1 (**p**(s+1))can be written in terms of the number of molecules of each species at stage s (**p**(s))and the rate at which each reaction is progressing (**Q**(s)).

The number of molecules of a species X is given by

$$n_X = [X]VN_{Avagadro}$$

where [X] is the concentration of species X

V is the volume in which the concentration is present

and $N_{Avadagro}$ is Avagadro's constant.

Since the volume of the capillary fill cell in which the immunoassay is performed is fixed then the concentration of a species is the number of molecules divided by a constant. Thus it is possible to consider the concentrations of the species to be the states of the process and for a competitive assay (Table 4.4), the "probability vector" is

$$\mathbf{p(s)} = ([c]\ \ [a]\ \ [l]\ \ [ca]\ \ [cl]\ \ [ca_2]\ \ [cl_2]\ \ [cal])$$

where [X] represents the concentration of species X.

Table 4.4: Equilibria for a competitive assay

	Equilibrium equation	Forward rate equation
1	$c + a \rightleftarrows ca$	$d[ca]/dt = k_1[c][a] - k_{-1}[ca]$
2	$ca + a \rightleftarrows ca_2$	$d[ca_2]/dt = k_2[ca][a] - k_{-2}[ca_2]$
3	$c + l \rightleftarrows cl$	$d[cl]/dt = k_3[c][1] - k_{-3}[cl]$
4	$cl + l \rightleftarrows cl_2$	$d[cl_2]/dt = k_4[cl][l] - k_{-4}[cl_2]$
5	$ca + l \rightleftarrows cal$	$d[cal]/dt = k_5[ca][l] - k_{-5}[cal]$
6	$cl + a \rightleftarrows cal$	$d[cal]/dt = k_6[cl][a] - k_{-6}[cal]$

Part of Table 4.1 reproduced for reference

The rate equations are combined to produce an equation that describes the rate of change in concentration of each of the species involved. This equation involves addition of all the terms relating to the production of the species and subtraction of all the terms relating to its depletion. The case of the species ca is illustrated.

The reactions in a competitive assay involving ca (Table 4.4) are:

$$c + a \rightleftarrows ca$$
$$ca + a \rightleftarrows ca_2$$
$$ca + l \rightleftarrows cal$$

with corresponding rate equations

$$d[ca]/dt = k_1[c][a] - k_{-1}[ca]$$
$$d[ca_2]/dt = k_2[ca][a] - k_{-2}[ca_2]$$
$$d[cal]/dt = k_5[ca][l] - k_{-5}[cal]$$

Combining these produces an equation that describes the rate of change of the concentration of the species ca.

$$\frac{d[ca]}{dt} = k_1[c][a] - k_{-1}[ca] - k_2[ca][a] + k_{-2}[ca_2] - k_5[ca][l] + k_{-5}[cal]$$

Thus, if [X] refers to the concentration of species X at stage s and the transition to stage s+1 occurs in a time period Δt, the concentration of ca at stage s+1 will be

$$[ca]^{new} = [ca](1 - \beta_{-1} - \beta_2[a] - \beta_5[l]) + \beta_1[c][a] + \beta_{-2}[ca_2] + \beta_{-5}[cal]$$

where $\beta_i = \Delta t k_i$

Similar equations can be derived for each of the species involved and the transition probability matrix describing the system can be written as **Q**(s).

Q(s) =

	c	**a**	**l**	**ca**	**cl**	**ca_2**	**cl_2**	**cal**
c	$1 - \beta_1[a] - \beta_3[l]$	0	0	$\frac{1}{2}\beta_1[a]$	$\frac{1}{2}\beta_3[l]$	0	0	0
a	0	$1 - \beta_1[c] - \beta_2[ca] - \beta_5[cl]$	0	$\frac{1}{2}\beta_1[c]$	0	$\frac{1}{2}\beta_2[ca]$	0	$\frac{1}{2}\beta_5[cl]$
l	0	0	$1 - \beta_3[c] - \beta_4[cl] - \beta_6[ca]$	0	$\frac{1}{2}\beta_3[c]$	0	$\frac{1}{2}\beta_4[cl]$	$\frac{1}{2}\beta_6[ca]$
ca	β_{-1}	β_{-1}	0	$1 - \beta_{-1} - \beta_2[a] - \beta_6[l]$	0	$\frac{1}{2}\beta_2[a]$	0	$\frac{1}{2}\beta_6[l]$
cl	β_{-3}	0	β_{-3}	0	$1 - \beta_{-3} - \beta_4[l] - \beta_5[a]$	0	$\frac{1}{2}\beta_4[l]$	$\frac{1}{2}\beta_5[a]$
ca_2	0	β_{-2}	0	β_{-2}	0	$1 - \beta_{-2}$	0	0
cl_2	0	0	β_{-4}	0	β_{-4}	0	$1 - \beta_{-4}$	0
cal	0	β_{-5}	β_{-6}	β_{-6}	β_{-5}	0	0	$1 - \beta_{-5} - \beta_{-6}$

Equation (4.5)

The introduction of the ½ reflects the stochiometry of the reactions. Steric hindrance is included as a factor multiplying the value of the association constant prior to calculating the rate constants. Repeated application of equation (4.4) using the vector and matrix defined for the assay allows the calculation of the number of molecules and

hence concentration of each of the species at successive intervals throughout the reaction; thus allowing both the transient and equilibrium values to be determined.

4.4 Diffusion included within immunoassay module

The models considered above assume that all the species involved in the immunoassay reactions are physically present at the capture antibody surface. Use of the CFD implies that this will not actually be the case; the analyte and labelled component must diffuse through the solution in the cell in order to reach this surface.

Diffusion of the molecules in solution can be described using a finite element approach [21]. The capillary fill cell is divided into N+1 elements of height Δx (Figure 4.9). The initial concentration of analyte and labelled molecule are equally distributed throughout the cell.

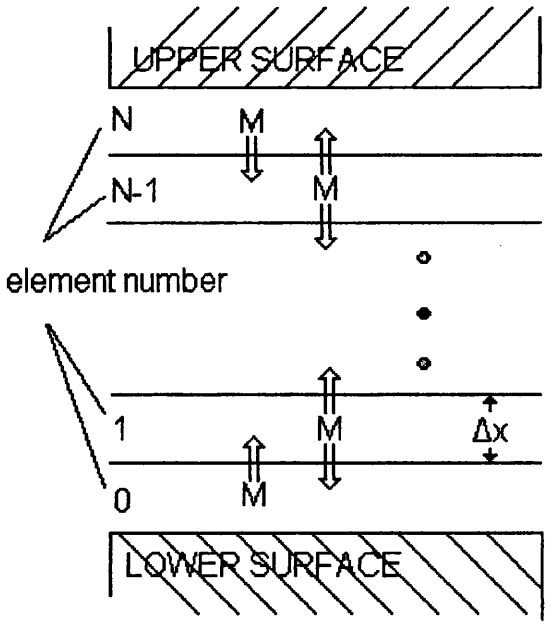

***Figure 4.9**: Finite element approach to the modelling of diffusion. The distance between the two surfaces is divided into N+1 elements of height Δx. M represents the diffusing molecule.*

The concentration of each species within each element due to diffusion is calculated according to (see Appendix A):

$$[X]_k^{new} = \begin{cases} [X]_k^{old} + \dfrac{D\Delta t}{(\Delta x)^2}\left([X]_{k+1}^{old} - [X]_k^{old}\right) & k = 0 \\ [X]_k^{old} + \dfrac{D\Delta t}{(\Delta x)^2}\left([X]_{k+1}^{old} - 2[X]_k^{old} + [X]_{k-1}^{old}\right) & 1 \le k \le N-1 \\ [X]_k^{old} + \dfrac{D\Delta t}{(\Delta x)^2}\left(-[X]_k^{old} + [X]_{k-1}^{old}\right) & k = N \end{cases} \quad (4.6)$$

where $[X]_k$ is the concentration of species X in element k

D is the diffusion coefficient

Δt is the change in time

and Δx is the height of the element.

The modified Markov model is then used to calculate the concentrations within each element resulting from any reactions. The bound species are converted from surface concentrations to volumetric concentrations for the purposes of implementing the reaction equations. In the case of a competitive assay, reactions will occur in element 0 only, i.e. at the surface, but in a sandwich assay the analyte and labelled antibody may react in solution before reaching the surface.

4.4.1 Calculation of Δx

The factor $\dfrac{D\Delta t}{(\Delta x)^2}$ in equation (4.6) is known as the model diffusion coefficient D_m. It is obvious that the larger the value of D_m, the smaller the value of Δx and hence the more accurate the model. However, it also necessary to consider computation time and memory allocation when specifying Δx; an unnecessarily small value will be expensive in terms of computer resources. Thus it is normal to fix D_m and calculate the corresponding Δx.

The usual choice is a value $D_m = 0.45$ [21] and Δx is calculated as

$$\Delta x = \left(\frac{\overline{D}\Delta t}{D_m} \right)^{1/2} \qquad (4.7)$$

where $\overline{D}$ is the average diffusion coefficient

$D_m = 0.45$

and Δt calculated below (Section 4.4.2).

4.4.2 Calculation of Δt

The value of Δt is of paramount importance within the finite element model. It must reflect both the diffusion of the molecules and the reaction rates of the initial surface reactions, these being the fastest reactions within the system. The value of Δt used must be small enough so that when the free species arrive at the capture antibody surface the reactions that occur are within the physical constraints of the system.

In the case of the competitive assay, when the analyte and labelled analyte arrive at the surface, reactions 1 and 3 in Table 4.4 take place with the resulting concentrations

$$[ca] = \Delta t k_1 [c][a]$$
$$[cl] = \Delta t k_3 [c][l]$$

These concentrations are constrained such that

$$\frac{[ca]}{[a]} = \Delta t k_1 [c] \leq 1$$
$$\frac{[cl]}{[l]} = \Delta t k_3 [c] \leq 1 \qquad (4.8)$$

In the capillary fill cell the capture antibody concentration is given as a surface concentration and converted to a volumetric concentration for the purposes of reaction with other free species. Thus

$$[c] = \frac{A_I}{A_T \Delta x}[c]_{surface} \qquad (4.9)$$

where A_I is the area of the surface covered by immobilised antibody

A_T is the total area of the lower surface of the cell

Δx is the height of the finite elements calculated above (Section 4.4.1)

and $[c]_{surface}$ is the surface concentration of c

Substituting for [c] (4.9) and Δx (4.7) in equation (4.8) and rearranging leads to

$$\Delta t \leq \frac{\overline{D}}{D_m}\left(\frac{A_T}{A_I[c]_{surface} MAX(k_1, k_3)}\right)^2 \qquad (4.10)$$

where $\overline{D}$ is the average diffusion coefficient

$D_m = 0.45$

A_T is the total area of the lower surface of the cell

A_I is the area of the surface covered by immobilised antibody

$[c]_{surface}$ is the surface concentration of c

and $MAX(k_1,k_3)$ is the maximum forward rate constant.

A similar formula, which includes the maximum forward rate constant of the four possible initial reactions, can be derived for a sandwich assay.

4.4.3 Diffusion coefficients within the cell

The diffusion process within the cell may be complicated by the presence of other chemicals, namely the humectant layer used to preserve the capture antibody. The humectant layer is an additional substance e.g. sucrose that is used to coat the capture antibody layer. This preserves the activity of the antibody and hence the shelf life of the device.

Once the sample is added and the solution fills the capillary fill cell, the humectant layer will dissolve thus altering the viscosity of the solution and therefore the diffusion

coefficients of the molecules. The diffusion of the humectant layer into the solution and the resulting effect on the diffusion coefficients of the molecules must therefore be accommodated within the model. The most time efficient method of considering the changes in diffusion coefficients was to write a set of two-dimensional look-up tables for each of the molecules concerned.

4.4.3.1 Diffusion coefficient lookup tables

The lookup tables provided the diffusion coefficients of the molecules within the assay as a function of elapsed time and distance from the surface. Values of Δt and Δx could be small and therefore a complete table, one including a value for all values of t and x, would be excessive. Also, for a given elapsed time large parts of the table would contain identical values. Thus the tables were written with varying values of elapsed time and distance which reflected the diffusion of the humectant layer into the whole capillary fill cell. A bicubic spline interpolation could then be used to determine the diffusion coefficients within a particular element at a particular elapsed time.

4.4.4 Calculation of concentrations

The concentrations of each species at a time T after addition of the sample containing the analyte are calculated as follows:

i) calculate Δt;

ii) calculate Δx;

iii) determine the transition probability matrix based on the reactions involved at the surface;

iv) determine the vector of initial concentrations at the surface;

v) determine the initial concentrations within each element;

vi) calculate the diffusion of the humectant layer into the solution and determine at which point in time equilibrium occurs (t_{eq})

vii) calculate the diffusion coefficients of the analyte and labelled molecules (and any complex of these) within each element as a function of time until t_{eq}

viii) iterate
   a. if $t < t_{eq}$ calculate diffusion coefficients
   b. calculate concentrations in each element resulting from diffusion
   c. calculate concentrations in each element resulting from reactions
   d. apply equation (4.4) to the surface reactions

   required number of times to reach time T.

The physical parameters of the system that may effect the resulting concentrations are:

i) the initial concentrations of capture, analyte and labelled molecule and
ii) the intrinsic association constants for the reactions.

4.5 Verification of model

It is vital, with any model, to establish that the model is producing results that are an accurate representation of the system being modelled. In the case of the immunoassay module verification involves establishing that the concentrations returned by the model, given an initial set of concentrations and association constants for the reactions, are the concentrations that would be achieved by performing the immunoassay experimentally.

4.5.1 Optimisation model

In order to consider the accuracy of the optimisation model it was necessary to consider the composition of the optimisation function F to determine which, if any, of the redundant equations should be ignored in order to produce a well-conditioned search surface.

Initially the three classical regression procedures were applied to a competitive assay for the protein IgG. The initial concentrations for the assay were

$$[a]_0 = 20 \times 10^{-9}\ M$$
$$[c]_0 = 12.5 \times 10^{-9}\ M$$
$$[l]_0 = 45 \times 10^{-9}\ M$$

the association constants were

capture – analyte $K_C = 5.67 \times 10^9\ M^{-1}$

capture – labelled analyte $K_L = 2.63 \times 10^8\ M^{-1}$

and all steric hindrance values were set equal to 0, i.e. steric hindrance was ignored.

Table 4.5 shows the association constants and forward and reverse rate constants used in the model. The association of the capture antibody with the analyte, IgG, was assumed to be diffusion controlled and thus the forward rate constants k_i were calculated by the standard procedure used for diffusion controlled chemical reactions [22]. The association constants shown are derived statistically from the intrinsic values quoted above (see Appendix B).

Table 4.5: Values of the rate constants used in the competitive assay model.

Equilibrium equation	**Association constant** $K_i\ (M^{-1})$	**Values used in model** $k_i\ (M^{-1}\ s^{-1})$	$k_{-i}\ (s^{-1})$
$c + a \rightleftarrows ca$	$2K_C$	3.23×10^7	2.85×10^{-3}
$ca + a \rightleftarrows ca_2$	$\frac{1}{2}K_C$	1.83×10^7	6.43×10^{-3}
$c + l \rightleftarrows cl$	$2K_L$	3.23×10^7	6.14×10^{-2}
$cl + l \rightleftarrows cl_2$	$\frac{1}{2}K_L$	1.64×10^8	1.25
$ca + l \rightleftarrows cal$	K_L	6.57×10^8	1.16×10^{-1}
$cl + a \rightleftarrows cal$	K_C	1.83×10^7	6.94×10^{-2}

Forward rates calculated as diffusion limited rate
Backward rates from $K_i = k_i/k_{-i}$.
$K_C = 5.67 \times 10^9\ M^{-1}$ and $K_L = 2.63 \times 10^8\ M^{-1}$.

Figure 4.10 illustrates the results when all the equations are included within the optimisation. The differing results indicate that this search surface is ill-conditioned, as was the case for an optimisation function including all equations for the subsystem discussed in Section 4.2.1.3.

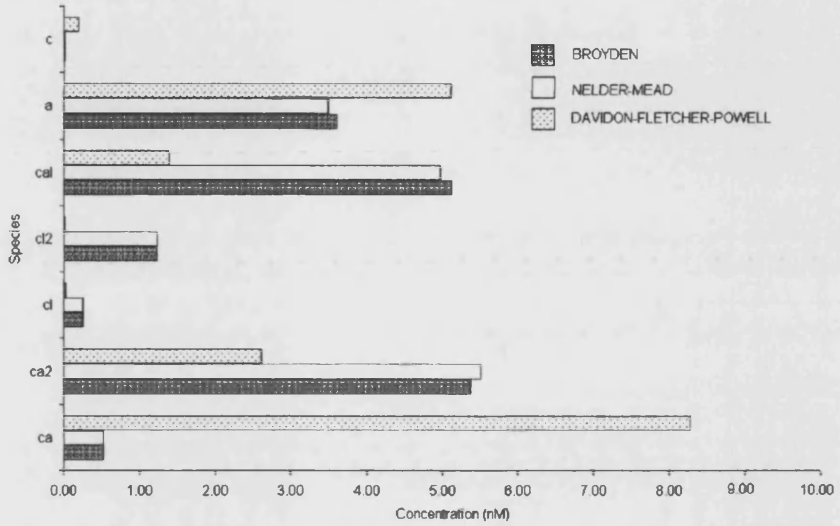

Figure 4.10: *Comparison of the concentration values returned by three classical regression techniques applied to the optimisation of F (4.3) for a competitive assay*
N = 6; M = 3; L = 8 ; γ_i = 1e80 for all i and λ_i – Lagrangian multipliers
Initial analyte concentration = 20 nM,
effective capture antibody concentration = 12.5 nM,
initial labelled analyte concentration = 45 nM.

Figure 4.11 illustrates the results achieved using the three different techniques in the case where one redundant equation has been removed from the optimisation function.

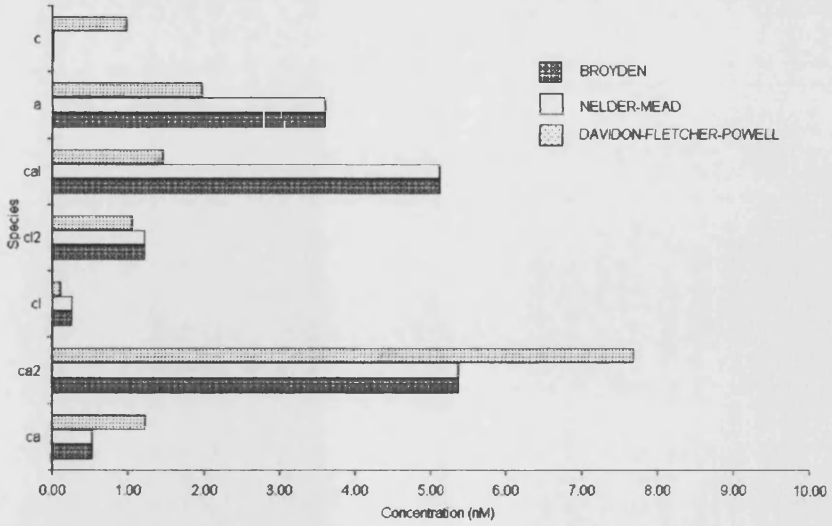

Figure 4.11: *Comparison of the concentration values returned by three classical regression techniques applied to the optimisation of F for the competitive assay described in Figure 4.10*
N = 6; M = 2; L = 8 ; γ_i = 1e80 for all i and λ_i – Lagrangian multipliers

It can be seen that the Nelder-Mead procedure and the Broyden procedure, despite its record of failure if started away from the global minimum, give consistent results for both approaches but that the Davidon-Fletcher-Powell procedure is unreliable with either approach. The Davidon-Fletcher-Powell is considered a robust procedure [8,9], however it can prove problematic in situations were the scaling of the data is variable; a situation which is evident in the case of an immunoassay.

Comparison of Figures 4.10 and 4.11 shows that in the case illustrated by Figure 4.11, i.e. with one redundant equation removed, the Broyden and Nelder-Mead methods converge to an identical solution. However, application of these procedures to the more complex sandwich assay failed to produce consistent results, with the optimisation remaining extremely sensitive to the initial estimates.

Extending the comparison to include the intelligent optimisation methods produced a similar result i.e. equilibrium values for the competitive assay could be established but those for the sandwich assay could not. As the calculation is to be included within a procedure to fit to experimental data the speed of the calculation was a vital factor in determining the optimisation method to be used. Table 4.6 shows the times taken by the different techniques and indicates that the Broyden regression procedure would be the most appropriate.

Table 4.6: Comparison of performance time and minimum achieved by three types of optimisation procedure.

Procedure	**Time Taken**	**Function value at minimum**
Genetic algorithm[1]	7.91 s	3.35×10^{-13}
Simulated annealing	16.20s	2.03×10^{-16}
Broyden	< 1 ms	8.09×10^{-23}

[1]No significant difference in performance on changing encoding procedure

The failure of the genetic algorithm to produce a global minimum for the sandwich assay optimisation indicates that the surface is prone to local minima and as the equation describing the sandwich assay has at least 14 dimensions it would seem impossible to isolate and eliminate this problem.

4.5.2 Markov model

The modified Markov approach was applied to the competitive assay of IgG previously described. Figure 4.12 illustrates the concentration of each species as a function of time obtained by repeated application of equation (4.4) with a time interval, Δt, of 0.1 s, an initial vector $\mathbf{p}(0) = \left([c]_0 \quad [a]_0 \quad [l]_0 \quad 0 \quad 0 \quad 0 \quad 0 \quad 0\right)$ and $\mathbf{Q}(s)$ as in equation (4.5).

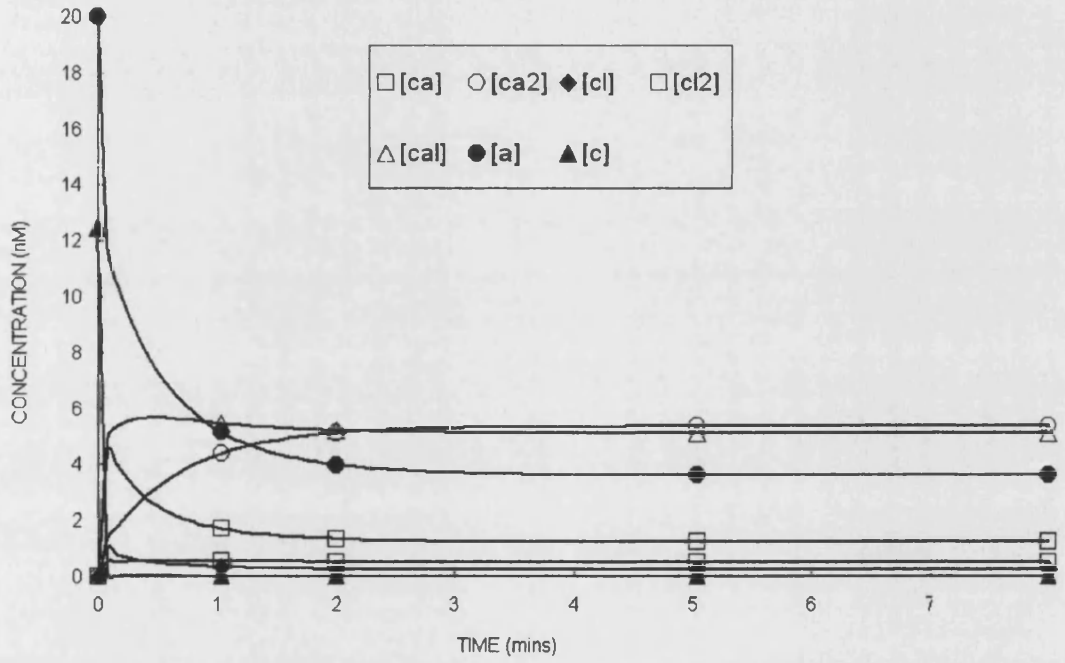

Figure 4.12: *The transient response for the competitive assay for IgG calculated using the modified Markov approach.*
Analyte concentration = 20 nM,
effective capture antibody concentration = 12.5 nM,
labelled analyte = 45 nM.

4.5.2.1 Equilibrium values

Figure 4.13 shows the concentrations of the species for the competitive assay at equilibrium obtained using this modified Markov approach, i.e. after 7 minutes. The results are compared with those obtained from the classical regression procedures that were found to be reliable i.e. the Broyden and Nelder-Mead procedures and shows excellent agreement.

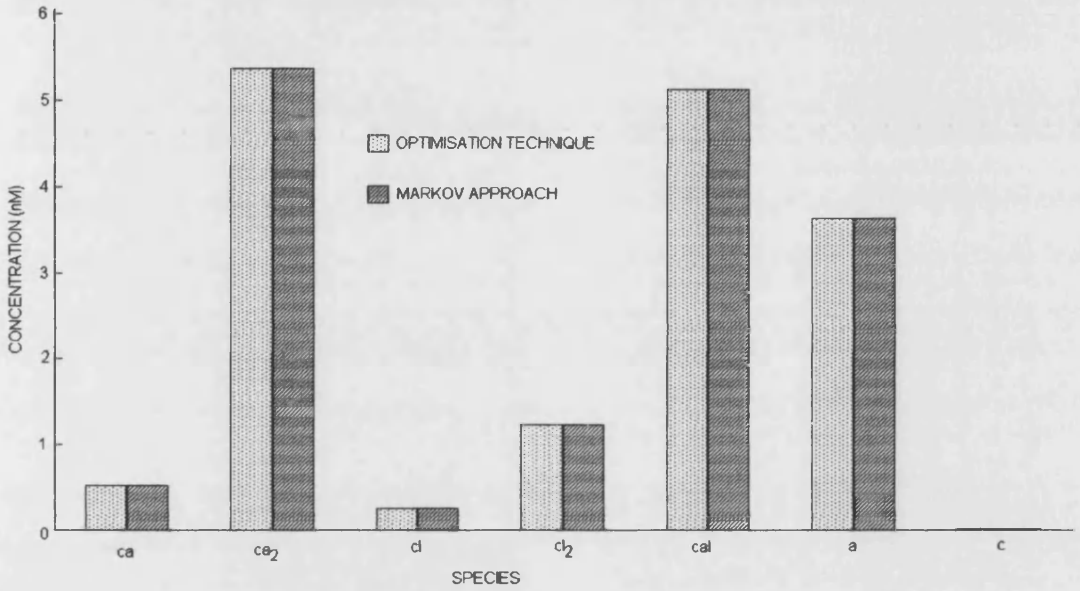

Figure 4.13: *The comparison of equilibrium values calculated using modified Markov approach and classical regression techniques for the competitive assay for IgG*
Analyte concentration = 20 nM,
effective capture antibody concentration = 12.5 nM,
labelled analyte = 45 nM.

4.5.2.2 Transient response

The advantage of the modified Markov approach to modelling the immunoassay is the fact that the search pathway to equilibrium appears to mimic the transient response of the reactions. Analytical solutions are not available for the full immunoassay reaction set but are available for subsets, e.g. the individual reactions in Tables 4.1 and 4.3. The transient concentrations of the species associated with any of these, e.g. $c + a \rightleftarrows ca$, were calculated using the modified Markov approach. These were compared with the results of the analytical solution of this simpler reaction equation (see Appendix C):

$$[ca] = \frac{(\beta+q)(\beta-q)\left(1-e^{-k_{-1}qt}\right)}{2K\left((\beta+q)e^{-k_{-1}qt}-\beta+q\right)}$$

$$[c] = [c]_0 - [ca]$$

$$[a] = [a]_0 - [ca]$$

where $[X]_0$ is the initial concentration of species X

[X] is the concentration of species X at time t

k_1 is the forward rate constant

k_{-1} is the backward rate constant

$K = \frac{k_1}{k_{-1}}$ is the association constant

$\beta = -(K[a]_0 + K[c]_0 + 1)$

$q = \sqrt{(\beta^2 - 4K\gamma)}$

and $\gamma = K[a]_0[c]_0$

The results were found to be in agreement as shown in Figure 4.14.

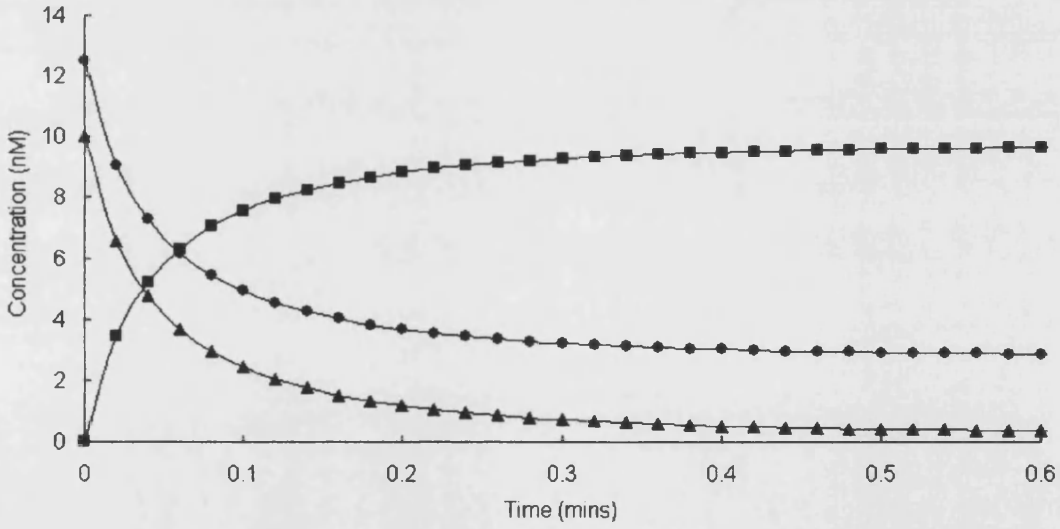

***Figure 4.14**: The transient response of the reaction $c + a \rightleftarrows ca$ calculated both analytically (continuous line) and using the modified Markov approach (symbols). Initial concentrations: $[c]_0 = 12.5$ nM (circles), $[a]_0 = 10$ nM (triangles), and $[ca]_0 = 0$ nM (squares). Rate constants: $k_1 = 3.23 \times 10^7\ M^{-1}\ s^{-1}$ and $k_{-1} = 2.85 \times 10^{-3}\ s^{-1}$.*

Variants of the Runge-Kutta method are commonly used to solve the differential equations describing the kinetics of a chemical reaction for which no analytical solution is available [23, 8]. Comparison of a fourth order Runge-Kutta solution with a solution determined using the modified Markov method for the competitive assay for IgG showed that both methods produced identical results. Whilst the Runge-Kutta method proved slightly more robust, producing accurate results for $\Delta t < 0.16$s compared to $\Delta t < 0.13$s for the modified Markov approach, it was computationally more expensive in terms of elapsed time (Table 4.7).

Table 4.7: Time taken to produce results for the transient concentration values of the competitive assay for IgG using the two approaches

Δt (secs)	***Elapsed time (secs)***	
	Markov	***Runge-Kutta***
0.1	< 1ms	0.06
0.01	< 1 ms	0.16
0.001	0.16	1.54
0.0001	1.21	10.76
0.00001	7.91	102.98

Both techniques were then extended to the more complex sandwich assay described by Table 4.3. Similarly to the competitive assay results were in agreement and although the Runge-Kutta method was slightly more robust, producing results for $\Delta t = 0.1$ s, the modified Markov approach was again superior in terms of time taken (Table 4.8).

Table 4.8: Time taken to produce results for the transient concentration values of the sandwich assay for IgG using the two approaches

Δt (secs)	**Elapsed time (secs)**	
	Markov	**Runge-Kutta**
0.1	FAILED	0.06
0.01	0.06	0.33
0.001	0.33	2.15
0.0001	2.25	16.86
0.00001	17.52	163.73

4.5.3 Finite element diffusion model

4.5.3.1 Humectant diffusion

The diffusion model was applied to a capillary fill cell with a sucrose humectant layer and the following initial values

CFD thickness $= 97 \times 10^{-6}$ m

Humectant layer thickness $= 10 \times 10^{-6}$ m

Temperature = 293 K.

The concentration of the humectant within the elements as a function of time is shown in Figure 4.15. This verifies that the humectant is diffusing to a constant gradient as expected.

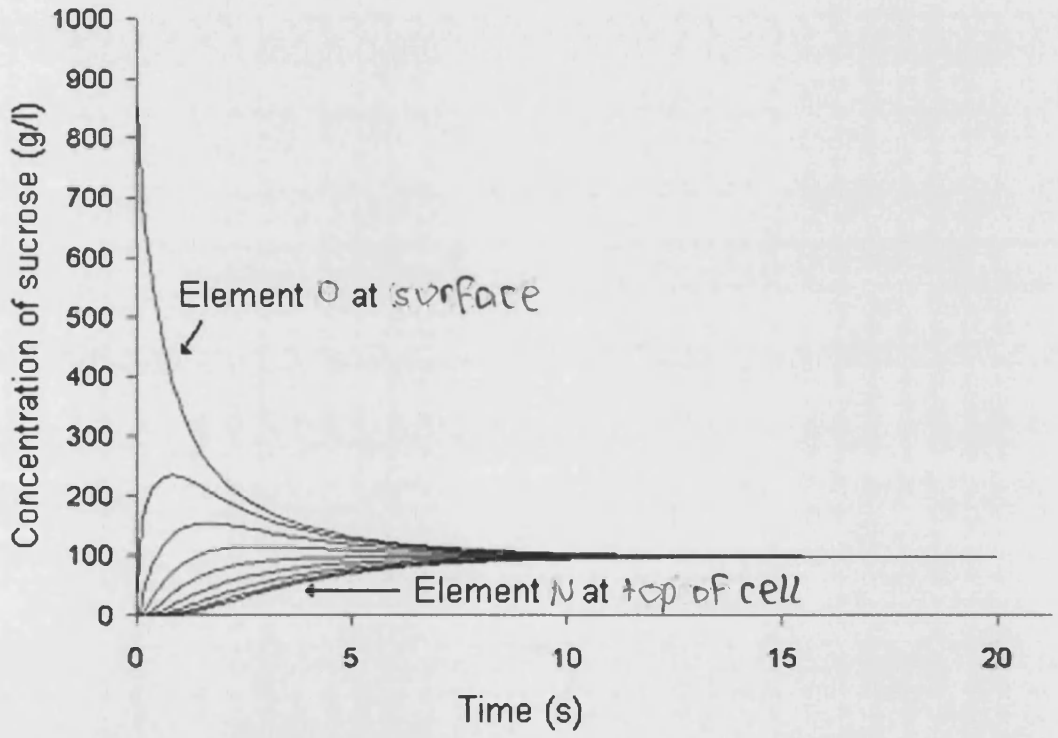

***Figure 4.15**: The diffusion of the humectant through the capillary fill cell. Different lines relate to different elements within the finite element analysis, ranging from the element closest to the surface to that furthest away.*

4.5.3.2 Application to an immunoassay

The finite element diffusion model was applied to a capillary fill device that included the competitive assay for IgG described above. An equilibrium solution was determined and found to be in total agreement with the equilibrium achieved when considering the immunoassay without diffusion. A similar result was achieved for a sandwich assay. Obviously the amount of calculation involved when considering the diffusing system greatly extends the computation time involved. Table 4.9 shows the time taken to perform a full analysis of the immunoassay.

Table 4.9: Characteristics and time taken to perform the finite element diffusion model of immunoassay

Assay	Δt (s)	No. finite elements	Time taken (s)
Competitive	0.021978	56	59.26
Sandwich	0.002614	175	591.11

4.5.4 Results of verification

A review of the verification of the immunoassay model indicates that the equilibrium concentrations of the less complex competitive assay can be calculated using the standard optimisation technique of collapsing the equations to a single equation which is then minimised using an optimisation procedure. The most effective procedure in terms of computation time was the secant regression technique of Broyden. However optimisation failed to produce reliable results for the more complex sandwich assay.

Equilibrium concentrations for the competitive assay calculated using the modified Markov approach showed good agreement with those achieved using the regression technique. This approach also produced results for the equilibrium concentrations of the sandwich assay, not achieved using regression techniques. The advantage of this approach was that no initial estimates were needed.

Comparison of the transient response calculated using the modified Markov approach with the analytical solution of a single reaction showed good agreement. The classic Runge-Kutta technique for solving differential equations was applied to the rate equations and the results were in agreement with those generated using the modified Markov approach. Although slightly less robust than the Runge-Kutta solution the modified Markov approach proved significantly superior in terms of computation time.

Inclusion of a finite element analysis of diffusion within the capillary fill cell provided a successful means of incorporating both the diffusion and the reactions within the model. Equilibrium concentrations calculated using this full model were in total agreement with those calculated using an analysis of the immunoassay only.

4.6 Comparison with experiment

The modified Markov approach was incorporated into a Nelder-Mead optimisation in order to fit a set of experimental data available from work previously undertaken within the group [24]. The assay was a sandwich assay for human chorionic gonadatrophin (hCG) with initial concentrations

$$[c]_0 = 30.9 \times 10^{-9}\ M$$
$$[l]_0 = 250 \times 10^{-9}\ M$$

The variables used for fitting were the

i) capture-analyte intrinsic association constant
ii) analyte-label intrinsic association constant
iii) steric hindrance factor between capture antibody and analyte
iv) steric hindrance factor between labelled antibody and analyte

Figure 4.16 illustrates the results of the fitting with the values for the factors shown in Table 4.10. The values established for the association constants indicate that the immobilisation process or the addition of a label alter the rates at which antibodies react within the immunoassay. Noting that hCG is a large molecule the steric hindrance factors were as expected i.e. total steric hindrance occurs, demonstrating the importance of the inclusion of this factor within the model.

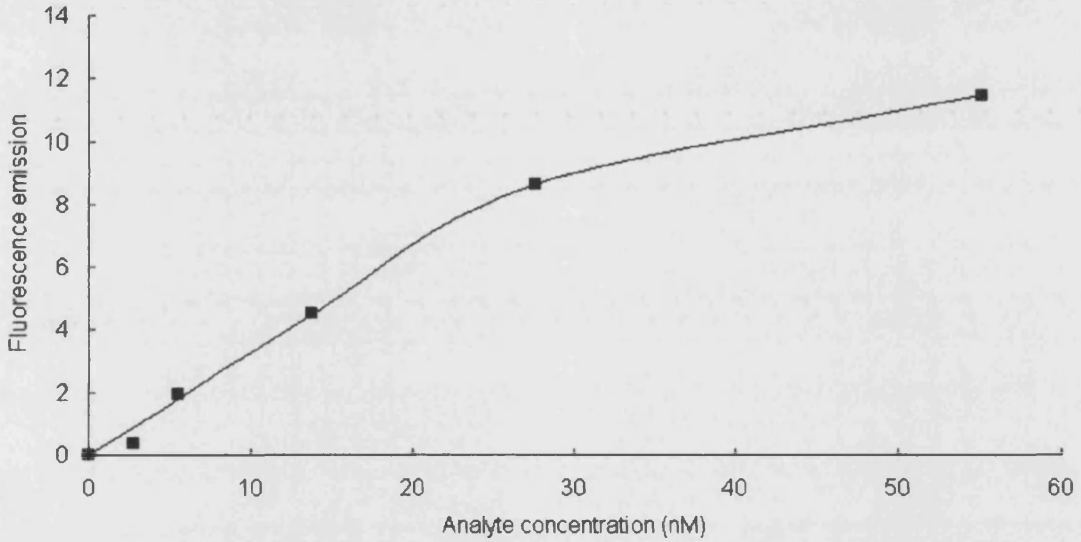

***Figure 4.16**: Results of using the modified Markov approach to fit equilibrium data for the sandwich assay for hCG.*
Squares – experimental data points
Smooth line – fitted curve

Table 4.10: Values of factors determined using the modified Markov approach to fit experimental data for the sandwich assay of hCG

Factor	**Manufacturers value**	**Value established**
Capture association constant	6×10^{10} M^{-1}	2.2×10^{9} M^{-1}
Label association constant	2×10^{11} M^{-1}	4.1×10^{10} M^{-1}
Steric hindrance a - c		0.99
Steric hindrance a - 1		1.0

References

[1] Davies C, Introduction to Immunoassay principles, **In** *The Immunoassay Handbook* 2nd Edition, Ed Wild D (London: Nature Publishing Group 2001) pp 3 – 40, 2001.

[2] Tromberg BJ, Sepaniak MJ, Vo-Dinh T and Griffin GD, *Anal. Chem.* **59,** 1226 – 1230, 1987.

[3] Sapsford KE, Charles PT, Patterson CH & Ligler FS, Demonstration of Four Immunoassay Formats Using the Array Biosensor, *Anal. Chem.*, **74,** 1061-1068, 2002.

[4] Sloper AN, Deacon JK and Flanagan MT, *Sensors and Actuators*, **B1**, 589-591, 1989.

[5] Robinson GA, Attridge JW, Deacon JK & Whitely SC, The fluorescent capillary fill device, *Sensors and Actuators*, **B11**, 235-238, 1993.

[6] Ekins R, Immunoassay design and optimisation **In** *Principles and Practice of Immunoassay* Eds Price C. P. and Newman D. J. (NY: Stockton Press) pp 96-153, 1991.

[7] Robinson GA, Optical immunosensing systems – meeting the market needs, *Biosensors & Bioelectronics*, **6,** 183 – 191, 1991.

[8] Press WH, Teukolsky SA, Vetterling WT & Flannery BP, *Numerical Recipes in C*, 2nd Edition (Cambridge University Press) pp 379 – 455, 1992.

[9] Constrained optimisation, Available via the World Wide web at: http://www.lmu.ac.uk/lbs/epia/people/beachill/quants/quantch7.doc

[10] Greig DM, *Optimisation* (New York, NY: Longman Group Limited) pp 150 – 163, 1980.

[11] Nelder JA & Mead R, *Comp. J.*, **7,** 308 – 313, 1965.

[12] Broyden CG, *Mathematics of Computation,* **19,** 577 – 593, 1965.

[13] Fletcher R & Powell MJD, *Comp. J.*, **6,** 163 – 168, 1963.

[14] Pham DT & Karaboga D, *Intelligent Optimisation Techniques: Genetic Algorithms, Tabu Search, Simulated Annealing and Neural Networks* (London: Springer-Verlag Limited) pp 1 – 15, 2000.

[15] Goldberg DE *Genetic Algorithms in Search, Optimization and Machine Learning* (USA: Addison Wesley Longman, Inc.) pp 54 – 60, 1989.

[16] Davis L *Handbook of Genetic Algorithms* (New York, NY: Van Nostrand Reinhold) pp 59 – 86, 1991.

[17] Flanagan MT, Tattam FG & Green NM, *Immunochemistry,* **15,** 261 – 267, 1978.

[18] O'Reilly JJ, Markov Chains **In** *Problems of Randomness in Communication Engineering* Eds. Cattermole KW & O'Reilly JJ (Plymouth, UK: Pentech Press) pp 38 - 63, 1984.

[19] Too JR, Fan LT & Nassar R, *Computers and Chemical Engineering,* **7,** 1-12, 1983.

[20] Antia FD & Lee S, *Chemical Engineering Science,* **40,** 1969 – 1971, 1985.

[21] Bard AJ & Faulkner LR, *Electrochemical Methods, Fundamentals and Applications*, (New York, USA: John Wiley and Sons) pp 676 - 678, 1980.

[22] Weston RE & Schwartz HA, *Chemical Kinetics*, (New Jersey: Prentice-Hall Inc.) pp 152-158, 1972.

[23] Holt DB, Kusterbeck AW & Ligler FS, *Analytical Biochemistry*, **287**, 234 – 242, 2000.

[24] Pampapathi VKM, *PhD Thesis University of London*, pp218 – 220, 1994.

Chapter 5

Light Module

5.1 Light within the immunosensor

In a fluorescence evanescent field immunosensor the output of the device depends on the excitation of fluorophores within the immunoassay element of the sensor. An accurate reading is one resulting from each bound fluorophore label, with no contribution from any of the unbound label. Two of the main factors that affect the resulting fluorescent output of the device are the evanescent field and scattering of light from the surface of the waveguide.

5.1.1 Evanescent field

An evanescent field is a time-varying electromagnetic field extending into a region where boundary conditions prevent it from propagating. The evanescent field decays exponentially with increased distance from the boundary. Light coupled into a waveguide causes an evanescent field to decay into the region on either side. In the case of an immunosensor this region contains the immunoassay that is immobilised on the upper surface of the waveguide, thus exciting those fluorophores that are bound near the surface (Figure 5.1).

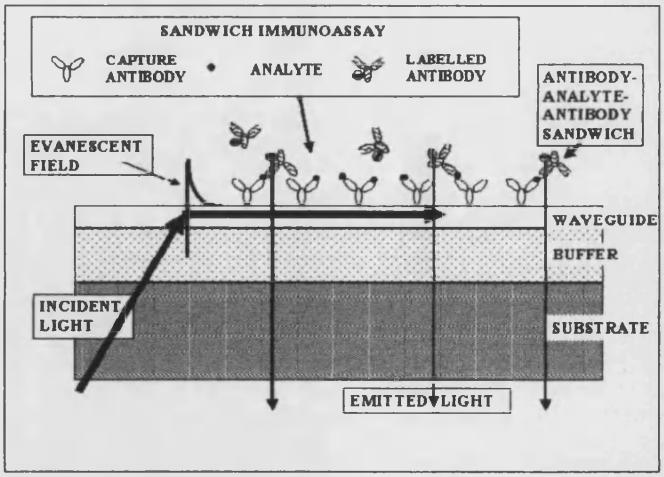

***Figure 5.1**: Light propagating in the waveguide causes an evanescent field to decay into the region above the waveguide that contains the immunoassay; thus exciting fluorophores bound within this field.*

In an evanescent field sensor the strength and depth of the field are crucial. Insufficient field depth may mean that some of the bound fluorophores are not excited whilst if the evanescent field penetrates too deeply unbound fluorophores may be excited. In either case the resulting reading from the device will be inaccurate. The incident light source and the coupling of this light into the waveguide are key factors in determining the evanescent field.

5.1.2 Coupling

The light module models the arrangement for the coupling of light into the waveguide and the resulting output fluorescence. Traditional methods of coupling into a waveguide, i.e. prism or grating coupling require phase matching, with the incident light being at a precise angle. One arrangement for an evanescent field immunosensor involves the capture antibody of the immunoassay immobilised onto a waveguide that has been deposited onto the lower glass surface of a capillary fill device (CFD). Coupling into the waveguide is achieved using a prism. The first light module, which models this arrangement, is referred to as Model A (Figure 5.2a).

The second light module, Model B (Figure 5.2b), involves the method of multilayer coupling devised by Pampapathi & Flanagan [1]. In this model coupling is achieved using a series of layers of appropriate thickness and refractive index, similar to the resonant mirror device.

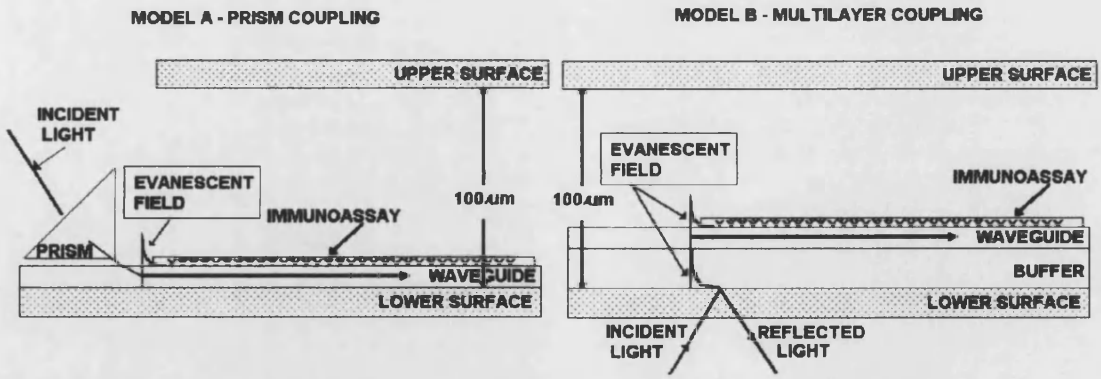

***Figure 5.2**: Two arrangements for coupling of light into the waveguide*
a) Model A - Light is coupled into the waveguide using a prism
b) Model B - Light is coupled through multiple layers c.f. resonant mirror

5.1.3 Scattering

In optical waveguides attenuation, i.e. loss of energy as the wave propagates along the waveguide is an important characteristic in determining the viability of the waveguide for the intended purpose. Loss can generally be attributed to three different mechanisms, absorption, radiation and scattering, with scattering being the predominant loss mechanism in dielectric waveguides [2].

In an evanescent field immunosensor based on a planar waveguide scattering of light from the top of the waveguide may cause unbound fluorophores in the cell beyond the evanescent field to be excited and thereby falsely produce a raised output signal. Thus scattering has been incorporated into the model. This will allow its effect on the output signal to be accurately studied for both Model A and Model B arrangements. The different approaches exemplified by these models than can be compared.

5.1.4 Modelling considerations

The objective of this aspect of the model is to calculate the amount of fluorescence that will be emitted as a result of the light incident on the sensor and the concentrations of the species within the immunoassay, i.e. the amount of label that is bound near the surface and the amount that is free in the solution within the cell. This module assumes that these concentrations are known. Thus the role of the light module is to

i) calculate the amount of light propagating in the waveguide;
ii) calculate the amount of light absorbed by the label both as a result of the evanescent field and of light scattered into the cell from the waveguide surface and
iii) determine the resulting fluorescence.

5.2 Model A – Prism coupling

The experimental set-up of Model A, illustrated by Figure 5.3, involves an indium phosphate waveguide which has been deposited onto the lower surface of a capillary fill device. The capture antibody has been immobilised onto the waveguide and the sample added to the space above the waveguide by means of capillary fill. The light source is a 0.2 mW Helium-Neon laser of wavelength 543.5 nm coupled into the waveguide by means of a prism. The CFD is masked to provide an observation length of 1 mm, this being the length from which output fluorescence will be detected [3].

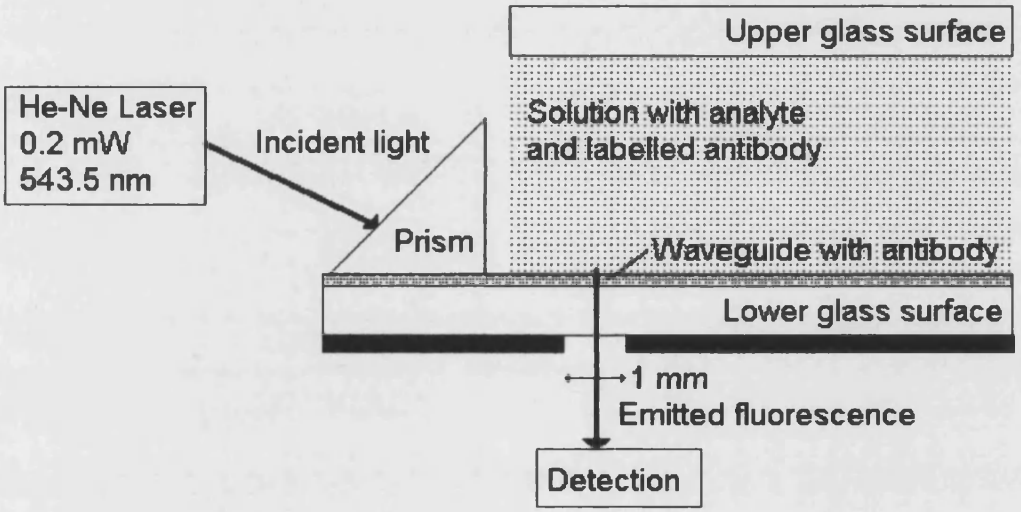

***Figure 5.3**: Experimental arrangement for an immunosensor with the light module modelled as Model A. Immunoassay takes place on the surface of an indium phosphate waveguide deposited onto the lower glass surface of a capillary fill device. Light is coupled into the waveguide via a prism.*

5.2.1 Light propagating in the waveguide

In order to determine the amount of light propagating in the waveguide the system was equated to a three-layer thin film dielectric slab waveguide and the standard equations for such a waveguide [4] outlined in Appendix D could then be applied. The equations and procedures detailed pertain to Transverse-Magnetic modes; however an analogous set of equations can be derived for Transverse-Electric mode propagation.

The characteristic equation for the waveguide is given by

$$\tan(bd) = \frac{b\left(\overline{p_0} + \overline{p_2}\right)}{b^2 - \overline{p_0}\,\overline{p_2}} \qquad (5.1)$$

where d is the thickness of the waveguide

$$\overline{p_0} = \frac{n_F^2}{n_S^2} p_0 \,.$$

$$\overline{p_2} = \frac{n_F^2}{n_C^2} p_2 \,.$$

$$b = \sqrt{\left((n_F k_0)^2 - \beta^2\right)}$$

$$p_0 = \sqrt{\left(\beta^2 - (n_S k_0)^2\right)}$$

$$p_2 = \sqrt{\left(\beta^2 - (n_C k_0)^2\right)}$$

$k_0 = \omega(\varepsilon_0 \mu_0)^{1/2} = \frac{\omega}{c}$ is the wave number in vacuum

c is the velocity of light in vacuum.

$\omega = 2\pi f/\lambda$ is the angular frequency of the light,

λ is the wavelength of the light,

ε_0 is the permittivity of free space,

μ_0 is the magnetic permeability of free space,

n is the refractive index of the medium,

subscripts S, F & C refer to substrate, film and cover respectively,

and β is the longitudinal phase constant of the propagating wave.

Since the waveguide confines the wave then the value of β must lie within the range [5]

$$k_0 n_S < \beta < k_0 n_F$$

Thus equation (5.1) can be solved iteratively to determine a value for β and hence b, p_0, p_2, etc.

The power propagating in the system is given by

$$P = \frac{W\beta}{4\omega\varepsilon_0 n_F^2}\left(1+\frac{\overline{p_2}^2}{b^2}\right)|A|^2 d_{eff}\eta \qquad (5.2)$$

where $d_{eff} = d + \dfrac{n_F^4 b^2 + n_S^4 \overline{p_0}^2}{n_S^4 \overline{p_0}\left(b^2+\overline{p_0}^2\right)} + \dfrac{n_F^4 b^2 + n_C^4 \overline{p_2}^2}{n_C^4 \overline{p_2}\left(b^2+\overline{p_2}^2\right)}$

is the effective thickness of the film due to Goos-Hænchen shift

W (>> d) is the width of waveguide in y-direction,

A is a constant,

η is the coupling efficiency,

with the other symbols are as defined above.

Once β has been determined, a value for A can be established by putting P equal to the incident power in equation (5.2). Values of A and β can then be used to determine the surface power density S at any value of x within the system by applying the equation

$$S(x) = \frac{\beta}{2\omega\varepsilon_0 n^2}|H_y(x)|^2 \qquad (5.3)$$

where

$$H_y(x) = \begin{cases} A\left\{\cos(bd)+\dfrac{\overline{p_2}}{b}\sin(bd)\right\}e^{p_0(x+d)} & x < -d \\ A\left\{\cos(bx)-\dfrac{\overline{p_2}}{b}\sin(bx)\right\} & -d \le x \le 0 \\ Ae^{-p_2 x} & 0 < x \end{cases}$$

Tiefenthaler & Lukosz [6] considered the electromagnetic fields within a four-layer sensor system where the thin antibody layer immobilised to the waveguide surface had a thickness much shorter than the wavelength of the light and showed that it was acceptable to treat this as a three-layer system with the thickness of the waveguide increased by the factor

$$\Delta d = \frac{n_A^2 - n_C^2}{n_F^2 - n_C^2} \left\{ \frac{\left(N/n_C\right)^2 + \left(N/n_A\right)^2 - 1}{\left(N/n_C\right)^2 + \left(N/n_F\right)^2 - 1} \right\}^{\rho} d_A \qquad (5.4)$$

where n is the refractive index of the medium,

$N = \frac{\beta}{k_0}$ is the effective refractive index of the system

$k_0 = \omega(\varepsilon_0 \mu_0)^{1/2} = \frac{\omega}{c}$ is the wave number in vacuum

c is the velocity of light in vacuum.

$\omega = 2\pi/\lambda$ is the angular frequency of the light,

β is the longitudinal phase constant of the propagating wave

d is the thickness of the layer

and subscripts denote layers as follows

S – substrate, F – film, C – cover and A – antibody layer.

5.2.2 Attenuation of light

Along the observation length in the sensor, light may be attenuated due to absorption by the bound label, absorption by the free label, scattering from the waveguide surface or absorption by the waveguide itself. In order to facilitate analysis of the sources of noise within the immunosensor it will be necessary to determine the contribution of each type of attenuation to the overall attenuation of light.

Consider a length L along which light is attenuated by two different factors a and b. Assume that the length is divided into segments of thickness Δz in which attenuation is due to either a or b and that segments attenuated by a and b occur alternately (see Figure 5.4).

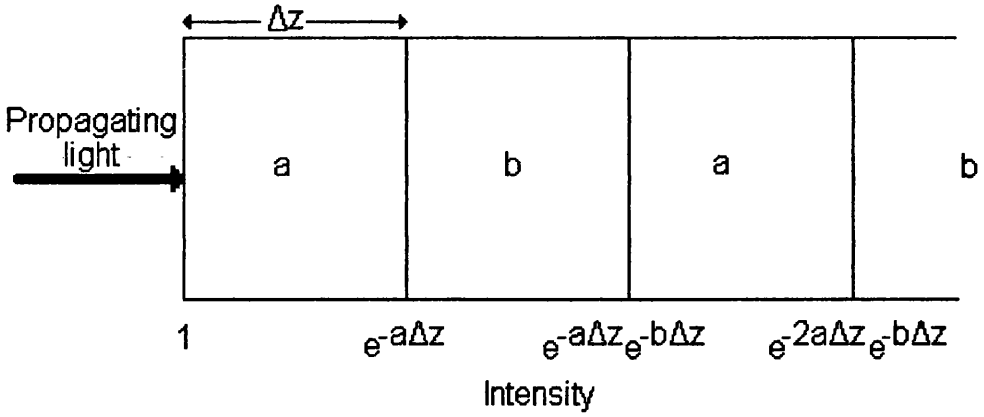

Figure 5.4: *Intensity of light propagating in an attenuating medium where the attenuation is due alternately to segments containing a and b*

Using Beer's absorption law

$$I(z) = I(0)e^{-\alpha z}$$

where I is intensity

z is distance

and α is the attenuation constant

Total light attenuated due to a is

$$I^{a}_{attenuated} = \left(1 - e^{-a\Delta z}\right) + e^{-a\Delta z}e^{-b\Delta z}\left(1 - e^{-a\Delta z}\right) + e^{-2a\Delta z}e^{-2b\Delta z}\left(1 - e^{-a\Delta z}\right) + \ldots$$

that is

$$I^{a}_{attenuated} = \left(1 - e^{-a\Delta z}\right)\sum_{i=0}^{N} e^{-i(a\Delta z + b\Delta z)}$$

Taking the sum of a geometric progression this becomes

$$I^{a}_{attenuated} = \left(1 - e^{-a\Delta z}\right)\left(\frac{1 - e^{-N(a\Delta z + b\Delta z)}}{1 - e^{-(a\Delta z + b\Delta z)}}\right)$$

which, noting the $N\Delta z = L$ and rearranging becomes

$$I^{a}_{attenuated} = \left(1 - e^{-L(a+b)}\right)\left(\frac{1 - e^{-a\Delta z}}{1 - e^{-(a+b)\Delta z}}\right)$$

Taking the limit as $\Delta z \to 0$

$$I^{a}_{attenuated} = \left(\frac{1-(1-a)}{1-(1-(a+b))}\right)\left(1 - e^{-L(a+b)}\right)$$

and thus the light attenuated due to a is

$$I^{a}_{attenuated} = \left(\frac{a}{a+b}\right)\left(1 - e^{-L(a+b)}\right) = \left(\frac{a}{a+b}\right) I^{Total}_{attenuated}$$

A similar argument leads to the fraction of light attenuated due to b

$$I^{b}_{attenuated} = \left(\frac{b}{a+b}\right) I^{Total}_{attenuated}$$

Thus, for light within the immunosensor

$$\begin{aligned}
P^{bound}_{att} &= \frac{g_1}{g_1+g_2+g_3+g_4} P^{Total}_{att} \\
P^{free}_{att} &= \frac{g_2}{g_1+g_2+g_3+g_4} P^{Total}_{att} \\
P^{scattered}_{att} &= \frac{g_3}{g_1+g_2+g_3+g_4} P^{Total}_{att} \\
P^{absorbed}_{att} &= \frac{g_4}{g_1+g_2+g_3+g_4} P^{Total}_{att}
\end{aligned} \qquad (5.5)$$

where P^{X}_{att} is the power attenuated due to X

$$P^{Total}_{att} = \left(1 - e^{-(g_1+g_2+g_3+g_4)}\right)P$$

P is the power at the start of the observation length

and g_i are attenuating factors as derived below.

5.2.2.1 Light absorbed by the fluorophore

Within the observation length light can be absorbed by fluorophores that have become bound close to the surface due to the immunoassay reactions and by those that are still free in the solution within the cell as illustrated by Figure 5.5.

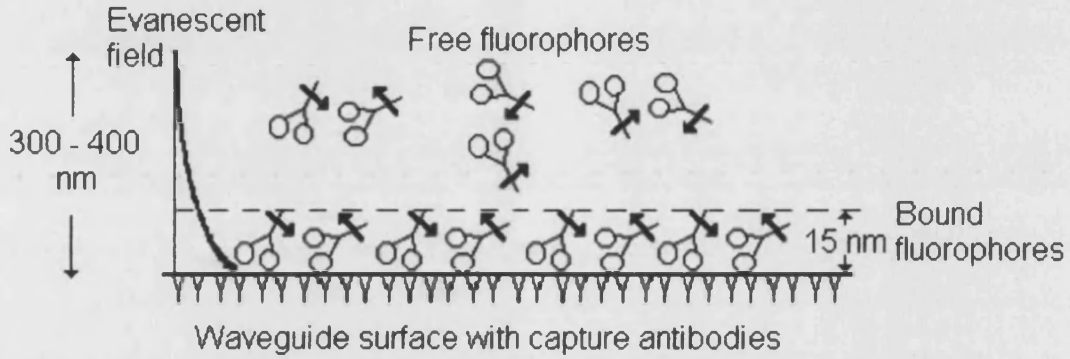

***Figure 5.5**: The bound and free fluorophore labels above the waveguide surface following immunoassay reactions where the capture antibody is immobilised onto the waveguide surface.*

Using Beer's law the amount of light absorbed across the observation length is

$$S_{absorbed} = S_0\{1 - \exp(-\varepsilon c_b L)\}$$

where ε is the extinction coefficient for the fluorophore (in M^{-1} m^{-1})

c_b is the concentration of the bound fluorophore (in M)

L is the observation length (in m)

and $S_0 = S(0)$ the surface power density calculated using equation (5.3).

However, S_0 refers to the power density at the waveguide surface and therefore does not take into account the decay of the evanescent field into the layer of bound fluorophores.

By equation (5.3)

$$S(x) = S_0 e^{-2p_2 x}$$

and so the total power absorbed by the layer of bound fluorophores is

$$P_{abs}^{bound} = S_0 W\{1 - \exp(-\varepsilon c_b L)\}\int_0^m e^{-2p_2 x} dx$$

$$= S_0 W\{1 - \exp(-\varepsilon c_b L)\}\frac{1}{2p_2}\{1 - \exp(-2p_2 m)\}$$

where multiplication by width W ensures that units are correct

and m is the thickness of the bound layer.

Assuming this to be the only source of attenuation i.e. $g_2 = g_3 = g_4 = 0$ in (5.5) above and equating $P_{abs}^{bound} = P_{att}^{bound}$ leads to

$$g_1 = -\ln\left[1 - \frac{S_0 W}{2p_2 P}\left(1 - e^{-\varepsilon c_b L}\right)\left(1 - e^{-2p_2 m}\right)\right] \qquad (5.6)$$

A similar argument to that used to establish the power absorbed by the bound fluorophores determines the power absorbed by the free fluorophores as

$$P_{free}^{absorbed} = S_0 W\{1 - \exp(-\varepsilon c_f L)\}\int_m^H e^{-2p_2 x} dx$$

$$= S_0 W\{1 - \exp(-\varepsilon c_f L)\}\frac{1}{2p_2}\{\exp(-2p_2 m) - \exp(-2p_2 H)\}$$

where c_f is the concentration of free fluorophore

and H is the height of the capillary fill cell.

and thus

$$g_2 = -\ln\left[1 - \frac{S_0 W}{2p_2 P}\left(1 - e^{-\varepsilon c_f L}\right)\left(e^{-2p_2 m} - e^{-2p_2 H}\right)\right] \qquad (5.7)$$

5.2.2.2 Scattering at the waveguide surface

Scattering of light from dielectric interfaces within waveguides is difficult to model. Extensive theories exist, for example, a sophisticated theory for scattering in symmetrical slab waveguides was developed by Marcuse [7]. This theory treats surface scattering as a form of radiation loss in which the irregularities in the surface couple energy into radiation modes above the surface. However there is little developed theory that allows easy simulation of multimode waveguides. Walter & Houghton [8] considered a monomode waveguide and developed the theory of Marcuse to produce a formula for the scattering of TE mode light from the surfaces of asymmetric waveguides as illustrated in Figure 5.6. A strong correlation between theoretical results from their model and experimentally achieved measurements supported the theory, thus making it ideal for application to a biosensor simulation.

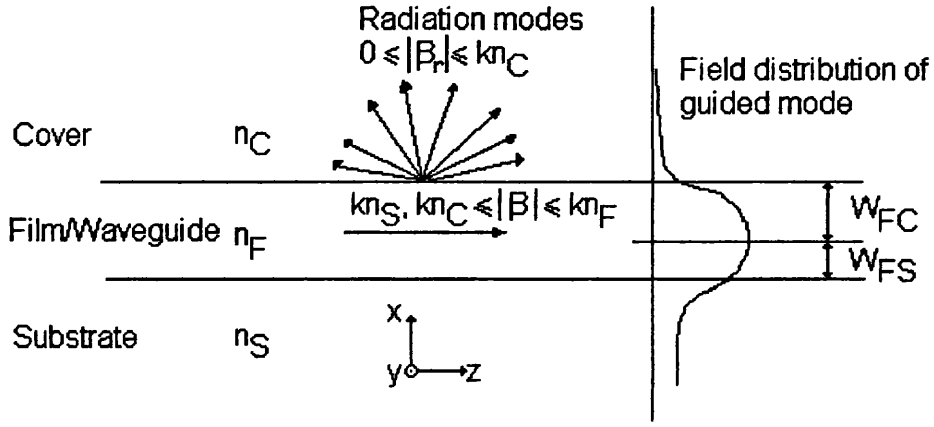

Walter & Houghton's formula:

$$\frac{\Delta P}{LP_T} = \frac{A^2}{B}\frac{\left\{\left(n_F^2 - n_C^2\right)k_0^2\cos(bW_{FC})\right\}^2}{\beta\pi W_{eq}} \times$$

$$2\int_{-k_0n_C}^{k_0n_C} \frac{r_C r_S^2}{(\beta-\beta_r)^2 + 1/B^2} \times \left[\right.$$

$$\frac{\cos^2(sW_{FC})}{r_S^2\left\{r_C^2\cos^2(sW_{FC}) + s^2\sin^2(sW_{FC})\right\} + r_C^2\left\{r_S^2\cos^2(sW_{FS}) + s^2\sin^2(sW_{FS})\right\}} +$$

$$\left. \frac{\sin^2(sW_{FC})}{r_S^2\left\{r_C^2\sin^2(sW_{FC}) + s^2\cos^2(sW_{FC})\right\} + r_C^2\left\{r_S^2\sin^2(sW_{FS}) + s^2\cos^2(sW_{FS})\right\}} \right] d\beta_r$$

Figure 5.6: *Guided and radiation modes of an asymmetrical planar optical waveguide (Diagram adapted from Figure 1 of Walter and Houghton [8]) with their formula for the calculation of power loss due to scattering at the Film-Cover interface for TE propagated light within the waveguide.*

Walter and Houghton [8] quote a formula that was derived for TE propagated light. Since the majority of the experimental work against which the current biosensor model is to be verified used TM propagated light it was necessary to adapt the formula accordingly. A similar procedure to that adopted by Walter and Houghton was used to produce the formula for calculating the amount of light lost through scattering at the surface of a dielectric waveguide for TM propagating light.

$$\frac{\Delta P}{LP_T} = \frac{A^2}{B}\frac{\left\{\left(n_F^2 - n_C^2\right)k_0^2\cos(bW_{FC})\right\}^2}{\beta\pi W_{eq}}\frac{\left(n_S^2 + n_C^2\right)}{n_F^2}\times$$

$$\int_{-k_0 n_C}^{k_0 n_C} \frac{r_C r_S^2}{(\beta-\beta_r)^2 + 1/B^2}\times\Bigg[$$

$$\frac{\cos^2(sW_{FC})}{r_S^2\left\{r_C^2\cos^2(sW_{FC}) + s^2\sin^2(sW_{FC})\right\} + r_C^2\left\{r_S^2\cos^2(sW_{FS}) + s^2\sin^2(sW_{FS})\right\}} +$$

$$\frac{\sin^2(sW_{FC})}{r_S^2\left\{r_C^2\sin^2(sW_{FC}) + s^2\cos^2(sW_{FC})\right\} + r_C^2\left\{r_S^2\sin^2(sW_{FS}) + s^2\cos^2(sW_{FS})\right\}}\Bigg]\mathrm{d}\beta_r$$

(5.8)

where ΔP is the change in power

P_T is the total power guided by the waveguide

L is the observation length

d is the thickness of the waveguide

$$b = \sqrt{\left((n_F k_0)^2 - \beta^2\right)}$$

$$p_0 = \sqrt{\left(\beta^2 - (n_S k_0)^2\right)}$$

$$p_2 = \sqrt{\left(\beta^2 - (n_C k_0)^2\right)}$$

$k_0 = \omega(\varepsilon_0\mu_0)^{1/2} = \frac{\omega}{c}$ is the wave number in vacuum

c is the velocity of light in vacuum.

$\omega = 2\pi c/\lambda$ is the angular frequency of the light,

λ is the wavelength of the light,

ε_0 is the permittivity of free space,

μ_0 is the magnetic permeability of free space,

n is the refractive index of the medium,

subscripts S, F & C refer to substrate, film and cover respectively,

β is the longitudinal phase constant of the propagating wave

$$W_{eq} = \frac{d}{n_F^2} + \frac{1}{n_S^2 p_0} + \frac{1}{n_C^2 p_2}$$

W_{FC} is the distance between the cover and the maximum of the propagating wave

W_{FS} is the distance between the substrate and the maximum of the propagating wave

$$s = \sqrt{(k_o n_F)^2 - \beta_r^2}$$
$$r_C = \sqrt{(k_o n_C)^2 - \beta_r^2}$$
$$r_S = \sqrt{(k_o n_S)^2 - \beta_r^2}$$

A is the roughness parameter as a length

and B is the correlation length of the surface profile.

The formula requires values for the roughness parameter i.e. a measure of the perturbations of the scattering surface and the correlation length i.e. the length over which these perturbations repeat. In an immunosensor perturbations at the surface of the waveguide will be primarily due to the immobilised capture antibody and biochemical complexes resulting from the immunoassay reactions. Sloper & Flanagan [3] have previously considered scattering of TE light at the surface of a waveguide within an evanescent field immunosensor and applied Walter & Houghton's formula to establish values for both the roughness parameter and correlation length, values that will apply for the TM light model currently being considered.

Application of equation (5.8) allows a value for ΔP, the power lost due to scattering to be calculated. Assuming that this is the only source of attenuation and equating to equation (5.5) gives

$$g_3 = -\ln\left(1 - \frac{\Delta P}{P}\right) \qquad (5.9)$$

5.2.2.3 Absorption in the waveguide

In developing the technique of using a thin film waveguide as the transducer for an immunosensor, Sloper & Flanagan conducted extensive investigations into the properties of the films being used [9]. Thus values for the absorption of the waveguide were available for the thin film waveguides being modelled. Thus

$$g_4 = \alpha_{abs} L \qquad (5.10)$$

where α_{abs} is the attenuation due to waveguide absorption.

The attenuation of light across the observation length can be calculated as

$$P_{att}^{Total} = \left(1 - e^{-(g_1+g_2+g_3+g_4)}\right)P$$

where P is the power at $\left(1 - e^{-(g_1+g_2+g_3+g_4)}\right)P$ ength

$$g_1 = -\ln\left[1 - \frac{S_0 W}{2p_2 P}\left(1 - e^{-\alpha_b L}\right)\left(1 - e^{-2p_2 m}\right)\right]$$

$$g_2 = -\ln\left[1 - \frac{S_0 W}{2p_2 P}\left(1 - e^{-\alpha_f L}\right)\left(e^{-2p_2 m} - e^{-2p_2 H}\right)\right]$$

$$g_3 = -\ln\left(1 - \frac{\Delta P}{P}\right)$$

$$g_4 = \alpha_{abs} L$$

and all other symbols are as defined during the derivation.

The proportion of the power lost due to each of the four possible causes of attenuation can be established using equation (5.5).

5.2.3 Fluorescence resulting from the model

Fluorophores are essentially coloured dyes that accept light energy at a given wavelength and re-emit it at a higher wavelength. Fluorescence occurs because the molecular structure of the fluorophore resonates or vibrates when excited by light at an appropriate wavelength. Excitation causes electrons to be raised to a higher energy state, which only exists for a short time (in the order of nanoseconds). The energy is then dissipated as electrons are transferred between the higher and lower energy state and as a result some of the excitation energy is emitted as fluorescence [10].

The amount of light absorbed by both the bound and free fluorophore above the waveguide is calculated using equations (5.5), (5.6) and (5.7). The fluorescence resulting from this absorbed light is found by multiplying by the quantum yield of the fluorophore, a factor that reflects the fact that not all of the energy absorbed by the fluorophore is emitted as fluorescence.

5.2.3.1 Fluorescence resulting from scattered light

The amount of scattered light that is absorbed by the fluorophores in the cell above the waveguide is dependent on the path of the scattered light through the layers of bound and then free fluorophores. The path length of the light will depend on the angle at which light is scattered. Since the calculation of the amount of scattered light involves an integral over the range of possible angles, the calculation of the path length and therefore the amount of the scattered light absorbed can be included within an adaptation of this integral.

Figure 5.7 shows the possible path lengths for light rays in a layer of height h.

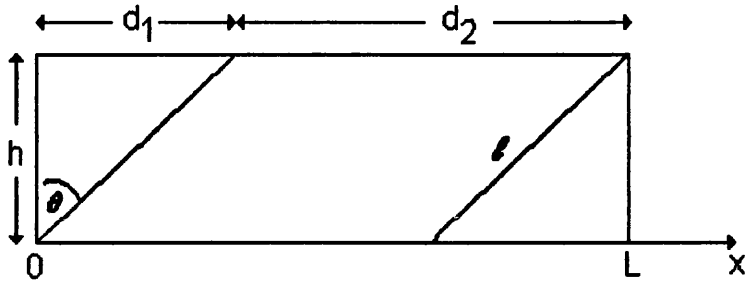

***Figure 5.7**: The path length (l) of light rays at angle θ in a layer of thickness h across an observation length L.*

The trigonometry of the layer dictates that

$$l = \frac{h}{\cos\theta}$$
$$d_1 = h\tan\theta$$
$$d_2 = L - h\tan\theta$$

The average path length of a ray is

$$\bar{l} = \begin{cases} l & 0 \le x \le d_2 \\ \frac{l}{2} & d_2 < x \le L \end{cases}$$

and therefore the weighted average is

$$\begin{aligned} \bar{L} &= \frac{ld_2 + \frac{l}{2}d_1}{L} \\ &= \frac{h}{L\cos\theta}\left[L - \frac{h\tan\theta}{2}\right] \end{aligned} \qquad (5.11)$$

Thus within the integration of equation (5.8) the value of the angle with the positive x-axis is calculated as

$$\varphi = \frac{\pi}{2} - \arcsin\left(\frac{\beta_r}{k_0 n_C}\right)$$

The angle with the normal is

$$\theta = \left| \frac{\pi}{2} - \varphi \right|$$

and $\bar{L}$ is calculated using equation (5.11), which by symmetry is valid for all angles.

The amount of scattered light absorbed by the bound layer is thus

$$F_{bound} = LP \int \frac{\Delta P}{LP}(\beta_r) \left\{ 1 - e^{-\alpha_b \bar{L}(\theta)} \right\} d\beta_r \qquad (5.12)$$

where $\frac{\Delta P}{LP}(\beta_r)$ is the integral function using equation (5.8)

and $\bar{L}(\theta)$ is the average length calculated using equation (5.11)

The amount of light absorbed by the solution layer is slightly more complex, as there will refraction at the interface between the bound layer and solution layer. The possibility that a particular ray does not reach the solution layer must also be taken into account. The possibility of total internal reflection at this interface was considered, but due to the nature of the interface i.e. bound antibodies, it was decided that the modelling of this interface would be too time consuming given the small impact on the resulting fluorescence of reflection at this point.

Thus scattered light absorbed by the free fluorophores is

$$F_{free} = LP \int \frac{\Delta P}{LP}(\beta_r) e^{-\alpha_b \bar{L}(\theta)} \left\{ 1 - e^{-\alpha_f \bar{L}(\theta')} \right\} d\beta_r \qquad (5.13)$$

where $\theta' = \arcsin\left(\frac{n_b \sin\theta}{n_f} \right)$

and n_b, n_f are the refractive indices of the bound and solution layers.

5.2.3.2 Calculation of fluorescence resulting from Model A

The calculation of fluorescence follows the stages shown.

i) use characteristic equation of waveguide (equation 5.1) to determine β;

ii) equate power propagating in the three-layer system (equation 5.2) with the input power and determine a value for the constant A;

iii) calculate waveguide surface power density (equation 5.3) using A;

iv) calculate the fraction of power scattered (equation 5.8);

v) calculate values for g_i using equations (5.6), (5.7), (5.9) & (5.10);

vi) calculate the amount of power absorbed by the bound and free label using equation (5.5);

vii) calculate amount of scattered power absorbed by fluorophores within the immunoassay using equations (5.12) & (5.13);

viii) add all absorbed powers and multiply by fluorophore quantum yield.

The physical parameters of the system that may impact on the resulting fluorescence are therefore:

i) input power;
ii) coupling efficiency;
iii) waveguide thickness;
iv) width of the cell;
v) height of the capillary fill cell and
vi) the observation length.

5.3 Model B – Multilayer coupling

The sensor employing multilayer coupling, modelled as Model B, involves a series of layers of appropriate thickness and refractive index. Coupling of light into the waveguide is achieved evanescently. Figure 5.8 illustrates the layers and the electric field within each layer resulting from light incident on the lower glass surface. Similarly to the resonant mirror device [11] at a particular angle of incidence, light coupled into the waveguide is at a maximum i.e. resonance is achieved. This resonance is reflected in the amount of emitted fluorescence resulting from a fluorophore labelled molecule involved in the immunoassay performed on the waveguide surface.

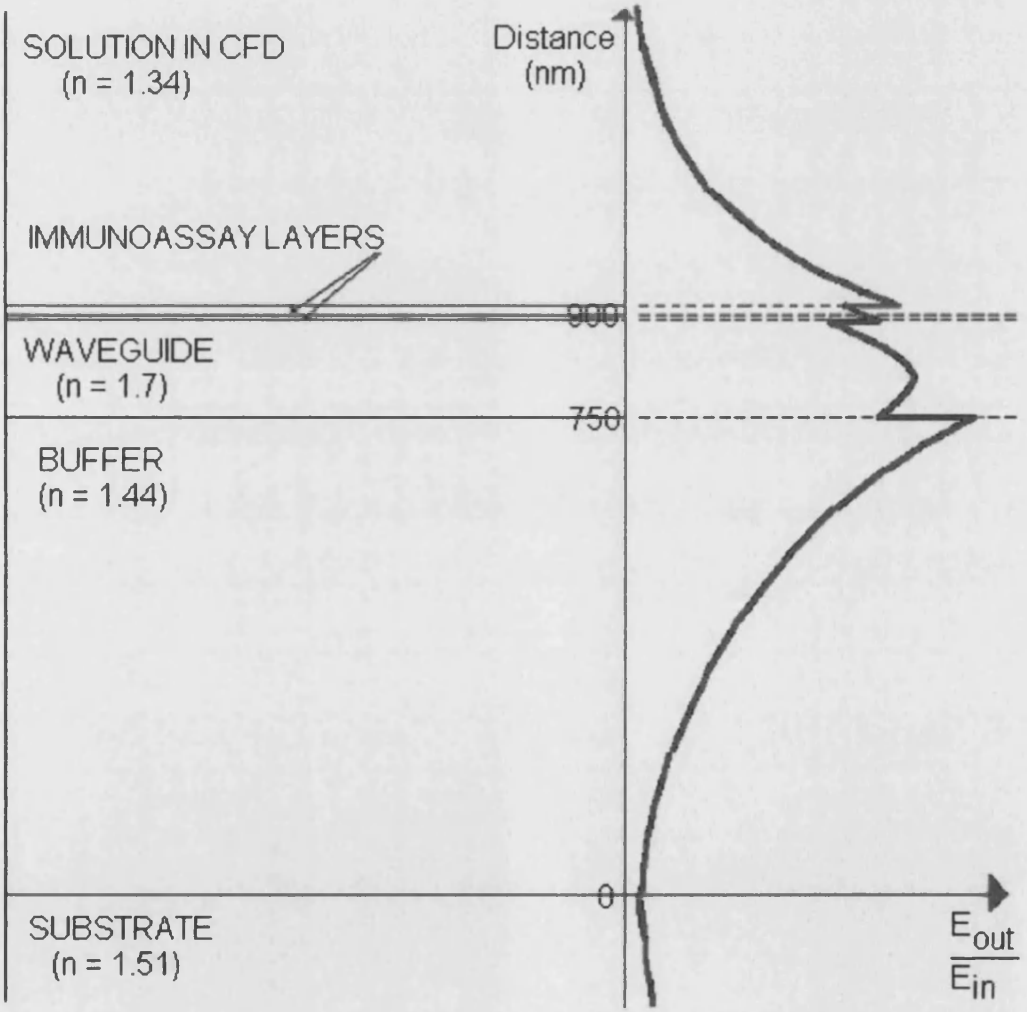

***Figure 5.8**: The layers used to achieve evanescent coupling into the waveguide in the multilayer coupled Model B immunosensor. The resulting electric field within each layer is also illustrated.*

Calculation of the emitted fluorescence follows a similar technique to that determined for Model A although the analysis of the electromagnetic field values differs. The resulting calculation will be dependent on the angle of incidence of the light, thus allowing a series of calculations to be performed for a range of angles, matching the angle scan used to determine resonance. The analysis given is for the TM mode of propagation, a similar set of results can be derived for the TE mode.

5.3.1 Electromagnetic field profile

Consider a series of layers with TM polarised light incident at the first interface (Figure 5.9). At each interface there will be an incident and a reflected component of light. Derivation of the fields in a multilayer system is a common technique in applied optics [12] and has not been repeated here.

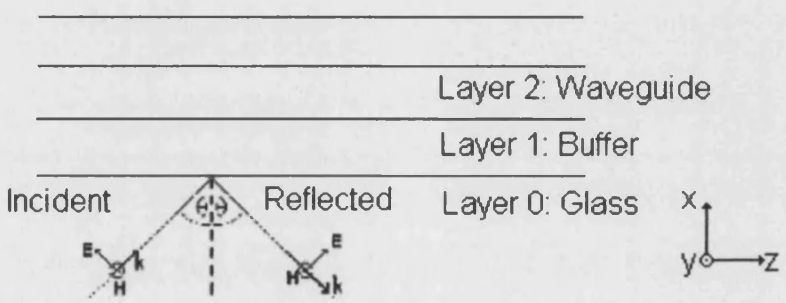

***Figure 5.9**: Light incident at the first interface in a multilayer system*

The fields in layer i can be written (following Appendix E)

$$\vec{E} = \left|\vec{A}_i\right|\left(\frac{k_z}{k_i},\ 0,\ -\frac{\alpha_i}{k_i}\right)e^{j\alpha_i x} + \left|\vec{B}_i\right|\left(\frac{k_z}{k_i},\ 0,\ \frac{\alpha_i}{k_i}\right)e^{-j\alpha_i x} \quad (5.14)$$

and

$$\vec{H} = \frac{n_i}{Z_0}\left|\vec{A}_i\right|(0,\ 1,\ 0)e^{j\alpha_i x} + \frac{n_i}{Z_0}\left|\vec{B}_i\right|(0,\ 1,\ 0)e^{-j\alpha_i x} \quad (5.15)$$

where $\left|\vec{A}_i\right|$ is the incident coefficient

$\left|\vec{B}_i\right|$ is the reflected coefficient

$$k_z = k_0 \sin\theta$$

$$k_i = \frac{\omega n_i}{c}$$

ω is the angular frequency of the light

c is the velocity of light in vacuum

n_i is the refractive index of layer i

$$\alpha_i = \sqrt{k_i^2 - k_z^2}$$

Z_0 is the characteristic impedance

and i denotes the layer.

At each interface boundary conditions can be applied, i.e. the fields parallel to the interface must be continuous. Thus the electric field in the z-direction and the magnetic field in the y-direction must be equal at each interface. Applying this to equations (5.14) and (5.15) leads to

$$|A_i|e^{j\alpha_i x}\left(-\frac{\alpha_i}{k_i}\right)+|B_i|e^{-j\alpha_i x}\left(\frac{\alpha_i}{k_i}\right)=|A_{i+1}|e^{j\alpha_{i+1}x}\left(-\frac{\alpha_{i+1}}{k_{i+1}}\right)+|B_{i+1}|e^{-j\alpha_{i+1}x}\left(\frac{\alpha_{i+1}}{k_{i+1}}\right)$$

and (5.16)

$$\frac{n_i}{Z_0}|A_i|e^{j\alpha_i x}+\frac{n_i}{Z_0}|B_i|e^{-j\alpha_i x}=\frac{n_{i+1}}{Z_0}|A_{i+1}|e^{j\alpha_{i+1}x}+\frac{n_{i+1}}{Z_0}|B_{i+1}|e^{-j\alpha_{i+1}x}$$

Making the assumptions that the coefficient of the incident light is normalised and that there is no reflected component in the final layer i.e.

$$|A_0| = 1$$

$$|B_{m-1}| = 0$$

implies that for m layers there are 2m-2 coefficients and a set of 2(m-1) linear equations from which the coefficients may be determined. Thus both the electric and magnetic fields can be established at any point within the multilayer for any given angle of incidence. Once the fields are known, equation (5.3) can be used to calculate the waveguide surface power density and the emitted fluorescence can be determined in the same manner as for Model A.

5.3.2 Laser Beam Divergence

The calculations used to determine the coefficients of the electromagnetic fields derived above are sensitive to the angle of incidence of the light and are scaled to the input power. A perfectly collimated beam of light is not a realistic possibility [13] and laser beams are found to be Gaussian in nature. Moreover, the incident area of the beam at large angles will be significantly larger than the beam area at normal incidence (Figure 5.10). Light incident at the extremes of this area may vary significantly in power and angle of incidence from light incident at the centre. The corresponding electromagnetic fields will vary and the fluorescence calculation will return different values. Thus the divergence of the beam was considered.

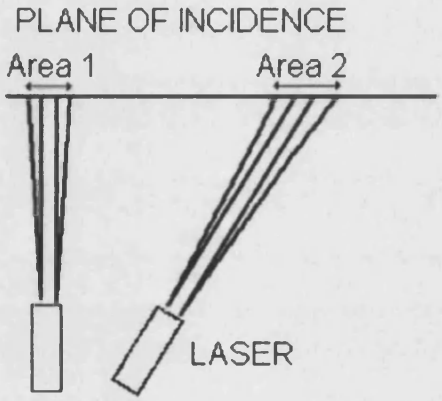

***Figure 5.10**: Area of incidence of a diverging laser beam incident on a plane at angles of incidence 0^o and 30^o illustrating that the area of incidence for 30^o incidence (area 2) is greater than that for incidence at 0^o (area 1).*

5.3.2.1 General laser beams

The wide variety of lasers currently available indicated that it would be difficult to find a simulation that would adequately model any laser. Thus it was decided to use the very general laser theory as a starting point in this model.

The variation in intensity from the centre of a laser beam diverges from a point at which the beam diameter is smallest, the beam waist w_0 [14]. The Rayleigh length is the distance from the waist at which the diameter of the beam has increased to $\sqrt{2}w_0$ and this length defines the Rayleigh range. Within this range the beam varies with a small divergence given by

$$\theta_{div} = \frac{4\lambda}{\pi w_0}$$

where λ is the wavelength of light

and w_0 is the beam waist.

The variation of the diameter with distance along the direction of propagation, x, is

$$w(x) = w_0\sqrt{1+\frac{x^2}{x_0^2}}$$

where x_0 is the Rayleigh length.

Within the Rayleigh range the beam is considered paraxial [15] and thus the paraxial solution to the wave equation for a light beam propagating in the x-direction [16] applies:

$$u = \Psi(x,\ y,\ z)e^{-j(wt-kx)}$$

with

$$\Psi = A\frac{w_0}{w(x)}\exp\left\{-\rho^2\left[\frac{1}{w(x)^2}-\frac{jk_0}{2R(x)}\right]-j\Phi(x)\right\} \quad (5.17)$$

where A is the normalisation constant

w_0 is the beam waist diameter

$$w(x) = w_0\sqrt{1+\frac{x^2}{x_0^2}}$$

$$\rho^2 = y^2 + z^2$$

$$R(x) = x\left(1+\frac{x_0^2}{x^2}\right)$$

$$\Phi(x) = \arctan\left(\frac{x}{x_0}\right)$$

$k = \frac{\omega n}{c}$ is the wave vector in medium with refractive index n

ω is the angular frequency of the light

c is the velocity of light in vacuum

n is the refractive index

and $x_0 = \frac{w_0^2 k_0}{2}$ is the Rayleigh length.

5.3.2.2 Application to the model

In order to include the beam divergence within the model it was assumed that the beam is composed of a bundle of rays that each follow a straight-line path. A two-dimensional array of incident field elements was created for a range of y and z values describing the normal incident area of the beam (Figure 5.11).

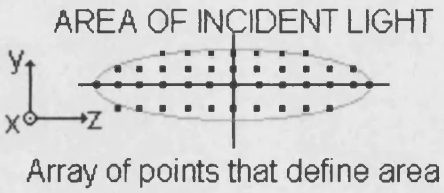

***Figure 5.11**: Illustrating the incident area of the light beam.*

Initially the values of the electric field were calculated using equation (5.17) for each pair of y, z values with A = 1. The surface power density is given by

$$S(x) = \frac{\beta}{2\omega\varepsilon_0 n^2}\left|H_y(x)\right|^2$$

Replacing H_y with $\frac{\omega\varepsilon_0 n^2}{\beta}E_x$ this becomes

$$S = \frac{n}{2Z_0}E_x^2$$

where n is refractive index

and Z_0 is the characteristic impedance.

The total power incident on the surface is thus

$$B^2 \frac{n}{2Z_0} \int_{y_{min}}^{y_{max}} \int_{z_{min}}^{z_{max}} E_x^2 dydz \qquad (5.18)$$

where B is a factor scaling the electric field according to the power of the incident light.

A two dimensional Gaussian Quadrature was used to perform the integration. Values of E_x were calculated using a bi-cubic spline interpolation from the two dimensional array of initial electric field values. Equating the result to the known incident power of the laser enabled a value for B, the scaling factor, to be determined and the array of electric field values can be scaled accordingly. This provided a symmetric array of electric field values that reflects the Gaussian variation within the total incident power normally incident on a surface.

In order to consider variation within the immunosensor the model may be incorporated into a Monte Carlo procedure and thus any calculations must be performed at optimum speed. The number of points that need to be included within the Gaussian Quadrature was investigated (Figure 5.12) and it was concluded that a 10 point Gaussian Quadrature would be sufficient to provide fast results whilst not compromising the accuracy of the calculation.

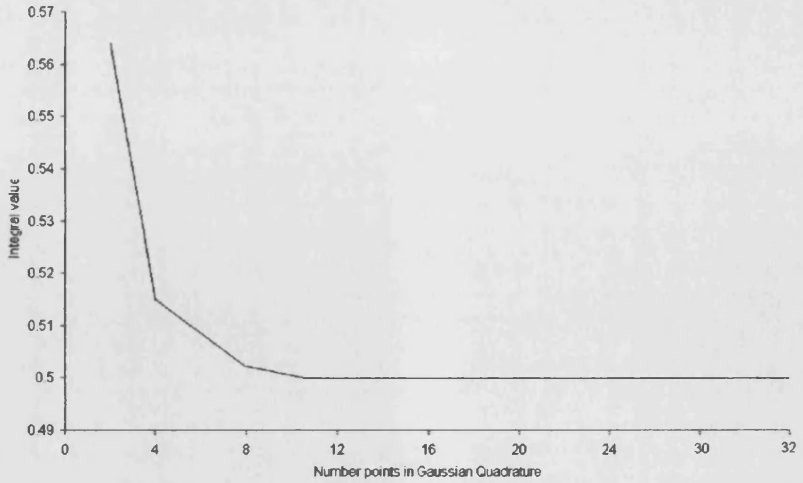

***Figure 5.12**: Value of the integral* $\int_{y\_min}^{y\_max} \int_{z\_min}^{z\_max} E_x dydz$ *calculated using a Gaussian Quadrature with varying number of points.*

A two dimensional array corresponding to the resulting angle of incidence for each of these rays was also determined by treating the laser as a point source. These values reflected the divergence of each ray from the normal and were subsequently used to adjust the angle of incidence in any power calculations.

At this point the arrays of electric field values and incident angles values reflect the divergence of the beam for normal incidence on a surface. Experiment showed that to interrogate a sensor based on a multilayer coupling technique the incident angle would need to range between 70° and 80° [1]. Thus the model must incorporate the spread of the incident area resulting from incidence at any angle within this range.

Since the propagation of light is within the x-plane, the expansion of the incident area caused by incidence at an angle occurs in the z-direction only. Assuming that the electric field associated with a particular ray before the beam is incident on the surface remains constant, the value of z relating to each ray was adjusted according to the projection of the beam onto the surface at the particular angle of incidence (see Figure 5.13 and Appendix F).

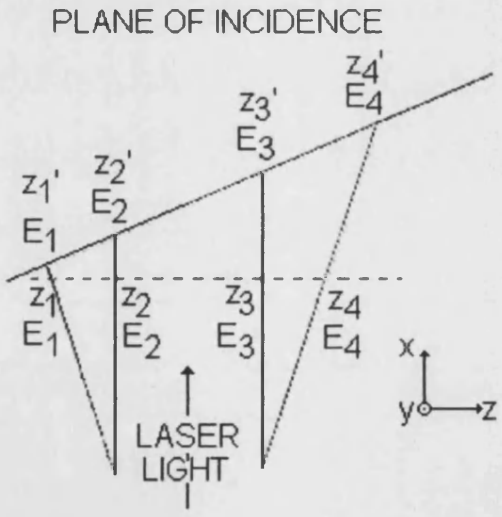

***Figure 5.13**: Projection of the values of the z distance onto the area of incidence. At normal incidence values z_i correspond to electric field values E_i. After incidence at an angle the electric field values remain the same but their corresponding z values have been adjusted according to the projection of the ray onto the surface.*

Within Model B any calculation of power at a particular point becomes a two-dimensional integration of the power resulting from each of the incident rays i.e.

$$P = \int_{y_{min}}^{y_{max}} \int_{z_{min}}^{z_{max}} P(y,z)dydz$$

The integration is performed using a two-dimensional Gaussian Quadrature. A bi-cubic spline interpolation of the electric field array with respect to the y and z arrays and a cubic spline interpolation of the divergence angle array with respect to the z array are used to provide an incident field coefficient and angle of incidence for the equations describing the multilayer system (5.16), which can be solved using an LU decomposition for the incident and reflected coefficients within each layer. The electric and magnetic fields and hence the power at the point in question can be then calculated and returned to the integration.

Thus, prior to the calculating the fluorescence resulting from the system, it is necessary to establish the precise electric field and angle of incidence at each point of incidence (Figure 5.14).

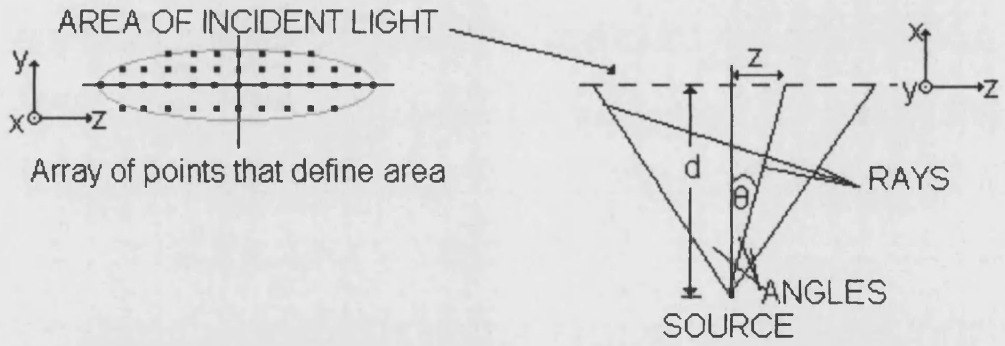

***Figure 5.14**: Illustration of the incident area subtended by a normally incident beam of light with divergence in the incident light beam.*

The steps necessary to establish the field and angles are

i) initialise a two-dimensional array of y and z values that define the area subtended by a normally incident light beam diverging from a point source;

ii) initialise an array of divergence angles relating to the z values in the area array i.e. $\theta = \arctan\left(\frac{z}{d}\right)$ in Figure 5.14;

iii) establish a two dimensional array of electric field values corresponding to each pair of y-z values using equation (5.17) and assuming A = 1

iv) calculate incident power using equation (5.18) and equate this to the known incident power to establish a value for A;

v) scale the electric field values accordingly;

vi) calculate the projection of the incident area resulting from incidence at the given angle and scale the z values to reflect the values within the new area.

The fluorescence emitted due to light incident at a particular angle is then calculated as detailed for Model A, replacing any power calculation with a two-dimensional integration as described above. Similarly to Model A, the physical parameters of the system that may impact on the resulting fluorescence are:

i) input power;

ii) coupling efficiency;

iii) waveguide thickness;

iv) width of the cell;

v) height of the capillary fill cell and

vi) the observation length.

5.4 Verification

Verification of the light module, i.e. ensuring that the output from the model reflects the output that would be achieved experimentally, is difficult to do analytically and will be best done by fitting results from the model to experimental results. However, it is possible to demonstrate that the equations used in the description of each model lead to physically real electric fields.

5.4.1 Model A – Prism coupling

Model A allows the electromagnetic fields in a three-layer system to be determined and used to calculate the power at any point in the system. The experimental arrangement simulated by this model (Figure 5.15) consisted of a substrate corresponding to the lower surface of the capillary fill cell which was constructed from Pilkington float glass with a refractive index of 1.5196.

The film was an indium phosphate waveguide with a layer of immobilised antibody on the surface, which had a thickness of 380.014 nm (being the deposited thickness, 380 nm, plus the adjustment due to Tiefenthaler & Lukosz [6] for a four-layer sensor i.e. equation (5.4)). The thin film waveguide had a refractive index of 1.6 [9].

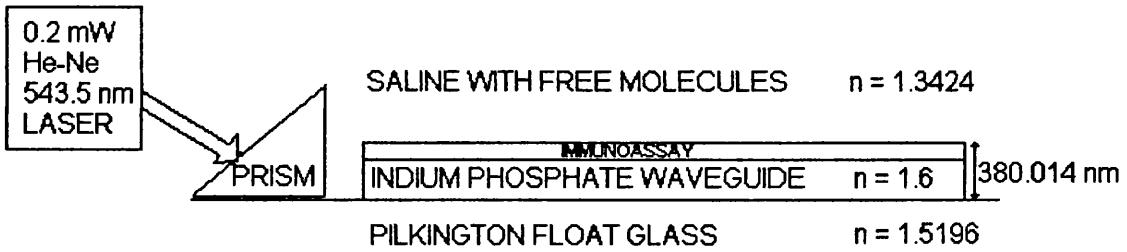

Figure 5.15: *Values used in Model A, prism coupling arrangement, to verify the electric and magnetic field values calculated by the model.*

The cover was a saline solution containing the analyte and the labelled antibody with a refractive index of 1.3424 calculated using the Clausius-Mossotti formula for refractive indices of compounds:

$$\frac{n_T^2-1}{n_T^2+2}V_T=\sum_{i=1}^{N}\frac{n_i^2-1}{n_i^2+2}V_i x_i$$

where n is refractive index,
V is molar volume,
x is mole fraction
the subscript T denotes the total compound
and subscript i refers to the each distinct component of which there are N [17].

The light source was a 0.2 mW Helium-Neon laser of wavelength 543.5 nm coupled into the waveguide by means of a prism, with an assumed coupling efficiency of 0.81, this being the maximum coupling efficiency achievable using a prism [18]. The width of the waveguide was,0 4 m and the observation length for resulting fluorescence was 1 mm.

The immunoassay layer was a sandwich assay for IgG with initial concentration values

$$[\text{analyte}]_0 = 20 \times 10^{-9}\ \text{M}$$

$$[\text{capture antibody}]_0 = 30.9 \times 10^{-9}\ \text{M}$$

$$[\text{labelled antibody}]_0 = 250 \times 10^{-9}\ \text{M}$$

and association constants

$$\text{capture – analyte}\quad K_C = 5.67 \times 10^{9}\ \text{M}^{-1}$$

$$\text{analyte – labelled antibody}\quad K_L = 1.52 \times 10^{10}\ \text{M}^{-1}.$$

The modified Markov approach described in Chapter 4 was used to determine that the resulting equilibrium concentrations of bound and free labelled antibody were

$$[\text{bound label}] = 2.99 \times 10^{-8}\ \text{M}$$

and

$$[\text{free label}] = 2.20 \times 10^{-7}\ \text{M}.$$

Figure 5.16 illustrates the electric and magnetic field profiles across the three-layer model resulting from the application of the three-layer system of equations to the Model A system described above. The fields correspond with those expected from a dielectric slab waveguide.

a) b)

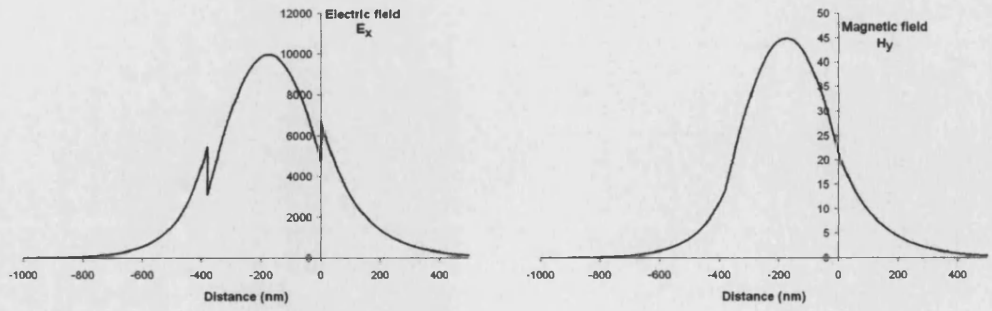

***Figure 5.16**: Plot of TM fields through the three-layers described by Model A*

a) Electric field (E_x)

b) Magnetic field (H_y)

5.4.2 Model B – Multilayer coupling

Model B modelled the fields through a multilayer system. Applying this to an immunoassay at a waveguide surface the model became a six-layer model as illustrated by Figure 5.7. The substrate was Pilkington float glass substrate with refractive index 1.5196, a 750 nm layer of buffer, refractive index 1.44 was placed above the glass and a thin film waveguide of iron phosphate, thickness 150 nm, refractive index 1.7 was deposited onto the buffer layer.

The exciting light was a 5 mW Helium-Neon laser of wavelength 632.8 nm. The width of the waveguide was 0 4 m and the observation length for resulting fluorescence was 1 mm.

The immunoassay, a sandwich assay for IgG as detailed above, was considered as a further three layers. The thickness of both the capture and bound layers were calculated by assuming that the molecules were spherical and hexagonally close packed at each surface as shown in Figure 5.17. The thickness of the capture layer was taken as the diameter of the capture antibody molecule and the thickness of the bound layer as the combined diameters of the analyte and labelled antibody. Thus for the sandwich assay for IgG, where the capture antibody is an anti-IgG antibody, the analyte is IgG and the labelled antibody is an allophycocyanin labelled anti-IgG antibody the thicknesses were 7 nm for the capture layer and 15 nm for the bound layer.

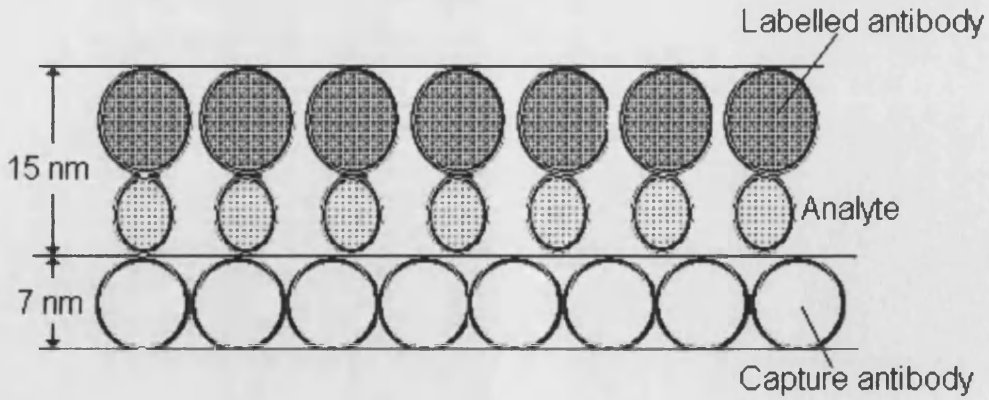

***Figure 5.17**: Layers representing the capture antibody and the bound analyte and label layer. Thickness of capture layer is the diameter of the capture antibody and the thickness of the bound layer is the combined diameters of the analyte and labelled molecule.*

The real parts of the refractive indices were calculated using the Clausius-Mossotti formula assuming the saline solution will have diffused into all gaps and that the refractive index of an antibody is 1.5 [19]. The imaginary parts of the refractive index relating to the presence of the absorbing label were calculated [20] using

$$n_{im} = \frac{c_l \varepsilon \lambda \ln(10)}{4\pi}$$

where n_{im} is the imaginary part of the refractive index

c_l is the concentration of the label

ε is the extinction coefficient of the label

and λ is the wavelength of the incident light.

The characteristics of the layers describing the system are shown in Table 5. 1.

Table 5. 1: Characteristics of the multilayer system used in Model B.

Layer	Thickness (nm)	Refractive Index Real part	Refractive Index Imaginary part
Glass	-	1.51958	-
Buffer	750	1.44	-
FePO4 waveguide	150	1.7	-
Capture antibody	7.14	1.3428	-
Bound layer	15.47	1.34239	0.000959
Solution	-	1.33284	1.45×10^{-6}

The calculated power at the waveguide surface resulting from application Model B across a range of angles is illustrated in Figure 5.18, demonstrating the existence of the resonant peak expected.

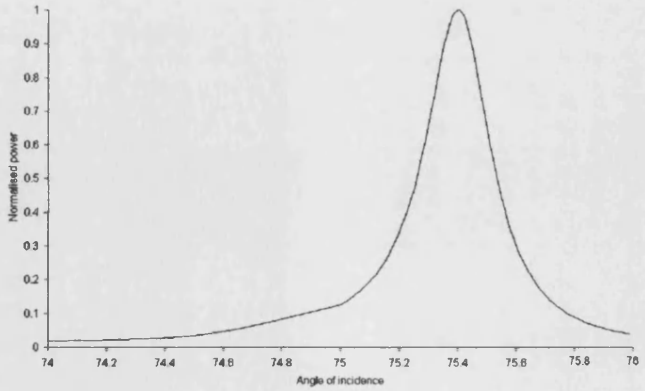

***Figure 5.18**: Normalised power at the waveguide surface calculated using Model B for a range of incident angles*

5.5 Comparison with experiment

A Nelder-Mead optimisation procedure incorporating the algorithm for determining the fluorescence resulting from Model B, the multilayer coupled model, was used to fit existing experimental data [21]. The detection module, i.e. the module that determines the output voltage resulting from the sensor, was also incorporated into the algorithm as the experimental data available recorded output voltage for a range of incident angles.

The experimental data was produced using an immunoassay for hCG. The values for the equilibrium concentrations of the biochemical species resulting from the immunoassay were determined using the modified Markov method described in Chapter 4. Initial concentration values for the assay were

$$[\text{analyte}]_0 = 24.2 \times 10^{-9}\ \text{M}$$
$$[\text{capture antibody}]_0 = 30.9 \times 10^{-9}\ \text{M}$$
$$[\text{labelled antibody}]_0 = 250 \times 10^{-9}\ \text{M}$$

with association constants

$$\text{capture} - \text{analyte}\ \ K_C = 2.2 \times 10^{9}\ \text{M}^{-1}$$
$$\text{analyte} - \text{labelled antibody}\ K_L = 4.1 \times 10^{10}\ \text{M}^{-1}.$$

The immunoassay module produced equilibrium concentrations leading to concentrations for bound and free labelled antibodies

$$[\text{bound labelled antibody}] = 4.76 \times 10\text{-}8\ \text{M}$$
$$[\text{free labelled antibody}] = 2.02 \times 10\text{-}7\ \text{M}$$

The optimisation assumed that the concentrations resulting from the immunoassay element of the model were fixed and thus the immunoassay element played no part in the optimisation procedure.

Previous studies of the multilayer coupling method have shown that the thickness of the waveguiding layer impacts on the angle of resonance [21]. The coupling factor determines the amount of power entering the system and thus will affect the output voltage achieved. Therefore initial fitting was performed with waveguide thickness and coupling factor as the variables. Figure 5.19 and Table 5.2 illustrate the results of this fitting, indicating that the experimental values used were valid.

Table 5.2: Values of factors determined using the algorithm for the multilayer coupled Model B with the detection module to fit experimental data for the output voltage from a multilayer coupled CFD containing an immunoassay for a range of incident angles.

Factor	Experimental value	Fitted value
Waveguide thickness	150 nm	148.24 nm
Coupling factor	1.0	0.97

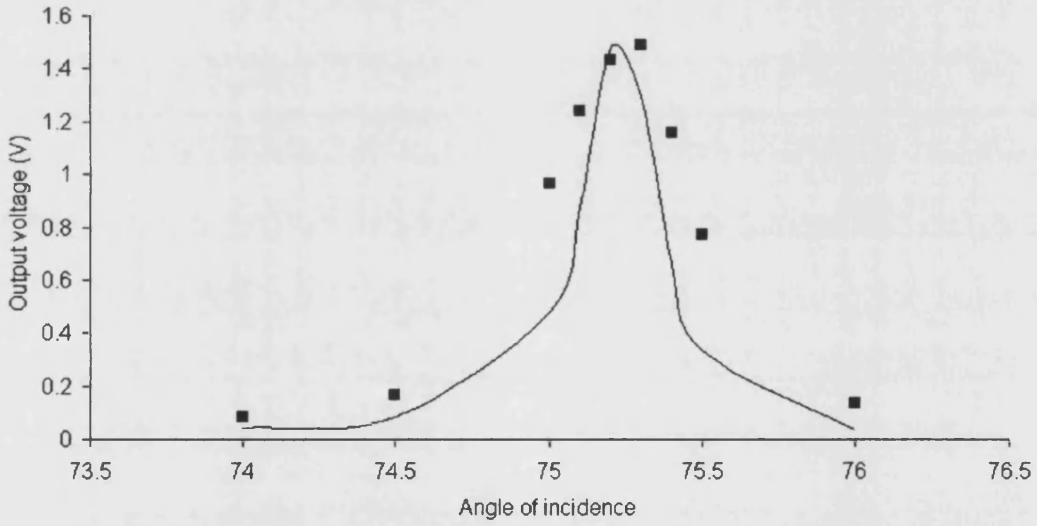

Figure 5.19: *Results of using the Model B algorithm with the detection module to fit data resulting from the detection of voltage output from an immunoassay performed on the surface of the multilayer coupled CFD.*
Squares – experimental data *Smooth line – fitted curve*

References

[1] Pampapathi VKM, *PhD Thesis University of London*, pp30 – 32, 1994.

[2] Hunsperger RG, *Integrated Optics Theory and Technology* (Berlin: Springer-Verlag Berlin Heidelberg) pp 74 – 77, 1995.

[3] Sloper AN & Flanagan MT, Scattering in planar surface waveguide immunosensors, *Sensors and Actuators*, **B, 11**, 537-542, 1993.

[4] Kriezis EE, Chrissoulidis DP & Papagiannakis AG, *Electromagnetics and Optics*, (Singapore: World Scientific Publishing Co. Pte. Ltd.), pp124 – 127, 1992.

[5] Yariv A, *Optical Electronics*, (NY: CBS College Publishing), pp 403-405, 1985.

[6] Tiefenthaler K & Lukosz W, Sensitivity of grating couplers as integrated-optical chemical sensors, *J. Optical Society of America B*, **6**, 209 – 220, 1989.

[7] Marcuse D, Mode Conversion Caused by Surface Imperfections of a Dielectric Slab Waveguide, *The Bell System Technical Journal*, **48**, 3187 – 3212, 1969.

[8] Walter DJ & Houghton J, Attenuation in thin film optical waveguides due to roughness-induced mode coupling, *Thin Solid Films*, **52**, 461 – 476, 1978.

[9] Sloper AN & Flanagan MT, Metal phosphate planar waveguides for biosensors, *Applied Optics*, **33**, 4230 – 4240, 1994.

[10] *Handbook of Fluorescent Probes and Research Products*, Available via the World Wide Web at http://www.probes.com/handbook/

[11] Cush R, Cronin JM, Stewart WJ, Maule CH, Molloy J & Goddard NJ, The resonant mirror: a novel optical biosensor for direct sensing of biomolecular interactions, *Biosensors & Bioelectronics*, **8**, 347-353, 1993.

[12] Born M & Wolf E, *Principles of Optics Electromagnetic Theory of Propagation, Interference and Diffraction of Light (Sixth edition)*, (Oxford, UK: Pergamon Press) pp 51 – 58, 1980.

[13] Silicon Sam's Technology Resource, Available via the World Wide Web at http://www.repairfaq.org/sam/

[14] O'Shea DC, *Elements of Modern Optical Design*, (USA: John Wiley & Sons, Inc.) pp 230 – 234, 1985.

[15] Varga P & Török P, The Gaussian wave solution of Maxwell's equations and the validity of scalar wave approximation, *Optics Communications*, **152**, 108 – 118, 1998.

[16] Mandel L & Wolf E, *Optical coherence and quantum optics*, (New York: Cambridge University Press), pp 267 – 271, 1995.

[17] The Clausius-Mossotti relation, Available via the World Wide Web at http://farside.ph.utexas.edu/teaching/jk1/lectures/node43.html

[18] Lee DL, Electromagnetic principles of integrated optics, (New York: John Wiley & Sons, Inc.), pp 42 – 47, 1986.

[19] Arwin H, Optical properties of thin layers of bovine serum albumin, gamma globulin and haemoglobin, *Applied Spectroscopy*, **40**, 313 – 318, 1986.

[20] Parton JE & Owen SJT, *Applied Electromagnetics*, (London: The Macmillan Press Ltd) pp 219 – 221, 1975.

[21] Pampapathi VKM, *PhD Thesis University of London*, pp218 – 220, 1994.

Chapter 6

Detection module

A fluorescence optical immunosensor involves three main elements, the immunoassay, the transducer, in this case the waveguide with prism coupling or the waveguide with multilayer coupling described previously, and the detection of the emitted fluorescence. The amount of fluorescence resulting from the sensor is small and therefore it is usual to use a device such as a photomultiplier tube (PMT) to amplify the signal into a detectable current or voltage.

6.1 Arrangement of detection system

Figure 6.1 shows the physical arrangement used to detect the fluorescence emitted from the capillary fill device. A collector lens, or arrangement of lenses, is used to focus the light through a longpass filter, a bandpass filter and onto the cathode of a PMT. The filters are used to limit the amount of stray light or breakthrough laser light reaching the PMT. Passing the output current from the PMT across a load resistor determines an output voltage.

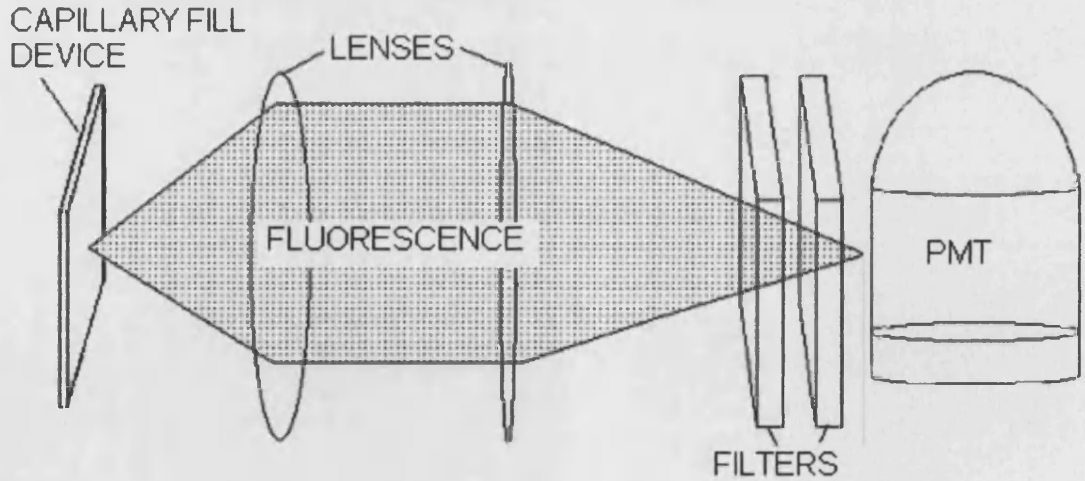

***Figure 6.1**: Arrangement of the system used to detect the emitted fluorescence. The fluorescence emitted from the CFD is focussed through a set of filters onto the cathode of a photomultiplier tube.*

6.1.1 Modelling considerations

The efficiency of a PMT depends on the wavelength of incident light, as do the emission of the fluorophore and the transmission of the filters. Thus any calculation of current resulting from the PMT must be undertaken for the range of wavelengths that will be present.

The objective of the detection module of the model is to calculate the voltage and associated noise resulting from the incidence of the emitted fluorescence onto the detection system described.

6.2 Model of detection system

Extensive literature exists detailing the modelling of photoemmissive events, including major contributions on extending theories to the modelling of a PMT [1]. However, the majority of these theories are at a level of complexity that does not lend itself to incorporation into the simulation being considered in this thesis. Their use of moment generating functions and saddle point calculations would lead to unacceptable computation times when included within an iterative procedure. It may also lead to over parameterisation of the model. Consequently, the less complex equations for output signal and noise current resulting from a PMT derived by Kingston [2] have been applied.

6.2.1 Photomultiplier Tube

A PMT contains a cathode, an anode and several intermediate dynodes within a high vacuum environment (Figure 6.2). The electric field applied to the dynodes accelerates the electrons released from the cathode towards the first dynode. The energy of the each incident electron causes the release of several electrons from the first dynode. These secondary electrons are then accelerated towards the second dynode where the process is repeated. The current resulting at the anode is a result of these multiplications and allows a tiny incident current to be magnified into a current large enough to be detected.

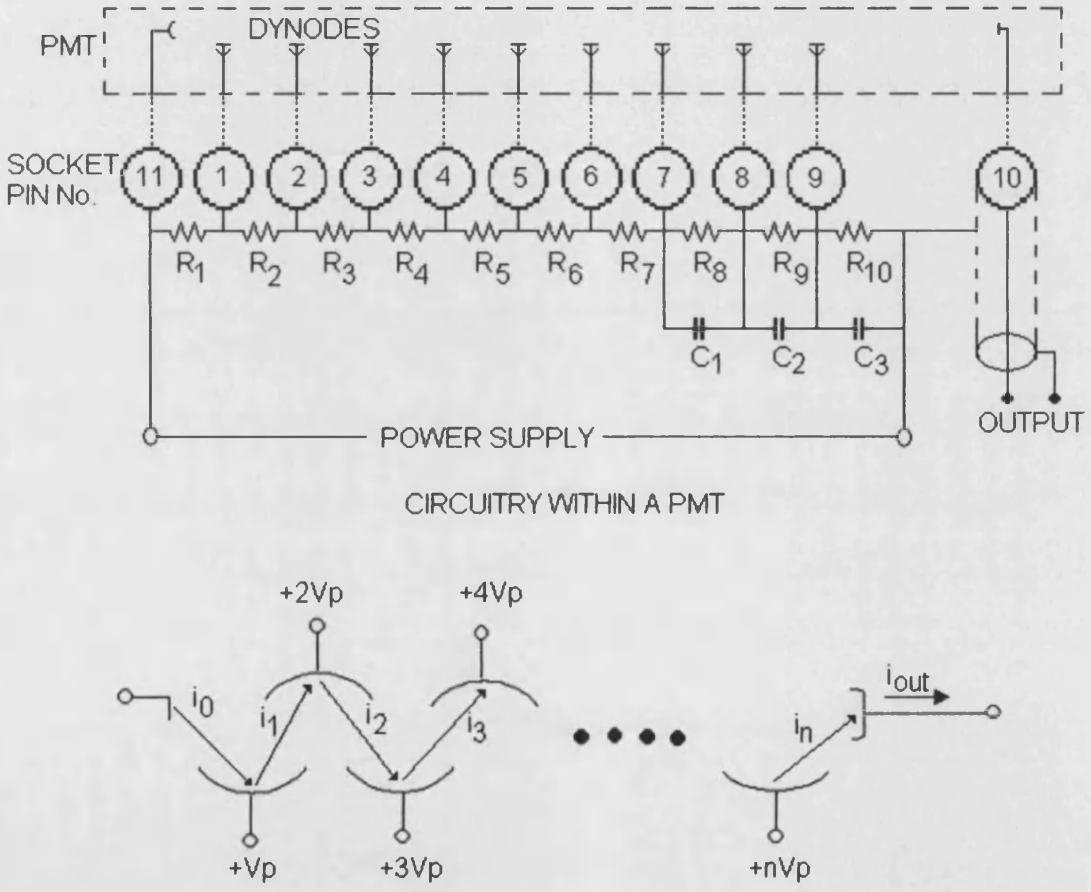

***Figure 6.2**: Highly schematic diagram illustrating the amplification of incident current by acceleration of electrons between successive dynodes within a photomultiplier tube.*

6.2.1.1 Kingston's derivation of signal current resulting from the PMT

The current incident on the dynode due to the signal only is

$$i_0 = \frac{\eta e P_s}{h\nu} \qquad (6.1)$$

where η is the efficiency of the cathode
e is the charge on an electron
P_s is the incident signal power
h is Planck's constant
and ν is the frequency of the incident light.

The mean-square current output from the PMT resulting from the signal is therefore

$$\overline{i_S^2} = G\left(\frac{\eta e P_s}{h\nu}\right)^2 \qquad (6.2)$$

where $G = m^{2n}$ is the power gain of the PMT
m is the average gain per dynode
and n is the number of dynodes.

6.2.1.2 Kingston's derivation for noise current resulting from the PMT

The mean-square noise current in a vacuum diode is

$$\overline{i_N^2} = 2eiB$$

where e is the charge on an electron
i is the incident current
and B is the bandwidth.

Defining P(k) as the probability of k secondary electrons being emitted by a particular dynode produces mean and mean-square values of k

$$\bar{k} = m = \sum_{k=0}^{\infty} kP(k) \qquad \text{and} \qquad \overline{k^2} = \sum_{k=0}^{\infty} k^2 P(k)$$

Thus for the first dynode of the PMT the mean-square noise current is

$$\overline{i_{N_1}^2} = 2ei_0B\overline{k^2}$$

and the excess noise produced by the current from the first dynode is

$$\left(\overline{i_{N_1}^2}\right)_{excess} = 2ei_0B\left(\overline{k^2} - m^2\right)$$

which at the output will be

$$\left(\overline{i_{N_1}^2}\right)_{out} = m^{2n-2}2ei_0B\left(\overline{k^2} - m^2\right)$$

since the current from the first dynode will be subject to a gain of $m^{2(n-1)}$.

Similarly the excess noise at the output due to the current from the second dynode will be

$$\left(\overline{i_{N_2}^2}\right)_{out} = m^{2n-4}2ei_0B\left(\overline{k^2} - m^2\right)$$

At the output the total excess noise is

$$\begin{aligned}\left(\overline{i_N^2}\right)_{out} &= 2ei_0B\left[m^{2n} + \left(\overline{k^2} - m^2\right)\sum_{i=1}^{n} m^{2n-2i}m^{i-1}\right] \\ &= 2ei_0Bm^{2n}\left[1 + \left(\overline{k^2} - m^2\right)\sum_{i=1}^{n} m^{-i-1}\right]\end{aligned}$$

Replacing the summation with $\frac{1}{m(m-1)}$ since $\sum_{i=0}^{n} x^{-i} = \frac{1}{1-x^{-1}}$ for n >> 1, the mean-square output noise current is

$$\left(\overline{i_N^2}\right)_{out} = 2ei_oBG\Gamma$$

where $G = m^{2n}$ is the power gain

and $\Gamma = \frac{\overline{k^2} - m}{m(m-1)}$ is the noise factor.

The probability distribution P(k) is considered to Poissonian for a PMT [2, 3] and thus

$$\overline{k^2} = m^2 + m$$

and the noise factor can be reduced to $\Gamma = \frac{m}{m-1}$.

However, the signal at the output will also contain a noise element due to any background power incident on the cathode and due to the dark current of the PMT itself. Thus the total noise signal at the output of the PMT, assuming the incident current given by equation (6.1) and a similar form for incident current resulting from background power, is

$$\overline{i_N^2} = \frac{2\eta\Gamma G e^2 B}{h\nu}\left[P_s + P_b + \left(\frac{h\nu i_d}{\eta e}\right)\right] + \frac{4k_B TB}{R} \qquad (6.3)$$

where η is the efficiency of the PMT

$\Gamma = \frac{m}{m-1}$ is the noise factor.

$G = m^{2n}$ is the power gain of the PMT

m is the average gain per dynode

n is the number of dynodes.

e is the charge on an electron

B is bandwidth

h is Planck's constant

ν is the frequency of the incident light.

P_s is the incident signal power

P_b is the incident background power

i_d is the dark current

and $\frac{4k_B TB}{R}$ is the shot noise associated with the electrical circuit

where k_B is Boltzmann's constant

T is the temperature

and R is the load resistance.

It should be noted that equation (6.3) differs slightly from the formula quoted in Kingston's book, which is dimensionally incorrect. However, the derivation is identical and it can only be assumed that the inaccuracy in the quoted formula is due to a type setting error.

6.2.1.3 Dark current

In the absence of any illumination a PMT will still produce a slight current, known as the dark current. This current is a result of thermionic emission from the cathode and is calculated according to the Richardson-Dushman equation [4], which relates the emission current to the work function and temperature of the cathode. Assuming that the work function and photoelectric threshold energy are equal; an assumption that is not totally accurate for the many materials used in electronics today as will be discussed later; the dark current is given by

$$i_d = 120T^2 Ae^{-\frac{h\nu_c}{k_B T}} \qquad (6.4)$$

where T is the temperature of the cathode
A is the area of the cathode in cm^2
h is Planck's constant
ν_c is the cut-off frequency of the PMT
and k_B is Boltzmann's constant.

6.2.1.4 Gain of the PMT

Hamamatsu [5] give the empirical formula for the average gain per diode, m, as

$$m = A\left(\frac{V}{n+1}\right)^{\alpha}$$

where V is the applied voltage
n is the number of dynodes
and A and α are constants dependent on the dynode material and geometry

The current gain across a PMT having n dynodes is therefore

$$\begin{aligned} \mu &= m^n \\ &= \frac{A^n}{(n+1)^{\alpha n}} V^{\alpha n} \\ &= KV^p \end{aligned}$$

where $K = \frac{A^n}{(n+1)^{\alpha n}}$

and $p = \alpha n$ are constants.

The logarithmic graph of voltage versus gain given by Hamamatsu for the R928 PMT device as used in the experimental arrangement of the immunosensor was used to determine values for K and p and therefore A and α. The average gain per diode could then be calculated as

$$m = 0.1691762\left(\frac{V}{n+1}\right)^{0.750561} \qquad (6.5)$$

6.2.2 Filters

Filters are used for isolating the band of light spectrum that is of interest [6]. A longpass filter allows light of longer wavelengths to be transmitted, whereas a bandpass filter passes a narrow region of wavelengths around a central wavelength. The filters used in the detection system will have a higher transmission at some wavelengths than at others. Values for the filter transmission as a function of frequency were determined from a typical transmission curve for the types of filter involved (Figure 6.3).

a) b)

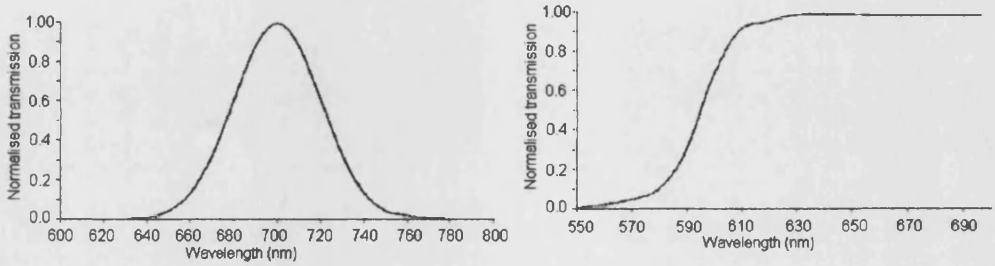

***Figure 6.3**: Transmission curves for filters*
a) bandpass filter at 700 ± 40 nm
b) longpass at 640 nm

6.2.3 Integration over frequency

Equations (6.2) and (6.3) both contain terms that are dependent on the frequency of the incident light. The fluorescence output from the capillary fill device may range over a number of frequencies with the emission of the fluorophore being dependent on the frequency. In order to account for the range of frequencies that may be present equations (6.2) and (6.3) are rewritten as

$$\overline{i_S^2} = Ge^2(P_F + P_B)^2$$

and (6.6)

$$\overline{i_N^2} = 2\Gamma Ge^2 B(P_F + P_B) + 2\Gamma GeBi_d + \frac{4k_B TB}{R}$$

where $$P_F = \frac{P_{fluor}}{h\nu_{exc}} \int_{\nu_1}^{\nu_2} emm(\nu)\eta(\nu)filter(\nu)d\nu$$

$$P_B = \frac{P_{break}}{h\nu_{exc}} \eta(\nu_{exc})filter(\nu_{exc})$$

P_{fluor} is the fluorescence output from the capillary fill cell

P_{break} is any laser light that has broken through the cell

ν_{exc} is the excitation frequency

emm(ν) is the normalised emission intensity of the fluorophore at ν

η(ν) is the PMT efficiency at ν

filter(ν) is the normalised filter transmission intensity at ν

and ν_1 and ν_2 determine the range of frequencies.

The emission spectrum for a fluorophore output is normally measured as a function of wavelength and must be converted to a function of frequency for the above calculation.

Given

$$\frac{\delta Q}{\delta \lambda} = KE_\lambda \qquad (6.7)$$

where Q is the energy of the fluorophore

K is a constant

λ is the wavelength

and E_λ are the emission values.

Let the emission value at the corresponding frequency ν be

$$I_\nu = \frac{\delta Q}{\delta \nu}$$

Since $c = \nu\lambda$

$$\frac{\delta Q}{\delta \lambda} = \frac{\delta Q}{\delta \nu}\frac{\delta \nu}{\delta \lambda} = -\frac{c}{\lambda^2}\frac{\delta Q}{\delta \nu} = -\frac{c}{\lambda^2} I_\nu$$

Putting this into equation (6.7) leads to

$$-\frac{c}{\lambda^2} I_\nu = KE_\lambda$$

Equation (6.6) must encompass the whole range of possible fluorescence, thus it requires

$$\int_{\nu_1}^{\nu_2} I_\nu d\nu = 1$$

Rewriting this in terms of λ leads to

$$K = \frac{1}{\int_{\lambda_1}^{\lambda_2} E_\lambda d\lambda}$$

and thus a conversion factor

$$I_\nu = -\frac{E_\lambda \lambda^2}{c\int_{\lambda_1}^{\lambda_2} E_\lambda d\lambda}$$

can be applied to the wavelength emission values to determine the appropriate values in terms of frequency.

6.2.4 Calculation of output voltage

The calculation of the output voltage and associated noise follows the following stages.

i) calculate fluorescence resulting from the light module;
ii) calculate the signal and associated noise current using equation (6.6);
iii) apply V = iR where V is voltage and R the load resistance.

The physical parameters of the detection system that may impact on the value of the output voltage are

i) the dynode voltage;
ii) the bandwidth and
iii) the resistance.

6.3 Verification

Implementation of the detection system requires that the code accurately calculates the values of the current and hence voltage determined as a result of using the PMT system to detect the fluorescence resulting from the capillary fill device. Any comparison with experimental data that includes the detection system will also need to include the fluorescence modelling and has been considered in Chapter 5. However, it is possible to verify some of the internal calculations of the detection system against data existing for the PMT device employed.

6.3.1 Dark current

Equation (6.4)

$$i_d = 120T^2 Ae^{-\frac{h\nu_c}{k_B T}}$$

calculates the dark current of the PMT device. The specification for the R928 Hamamatsu PMT gives values

$$A = 1.92 \text{ cm}^2$$

and

$$\nu_c = 3.33 \times 10^{-14} \text{ s}^{-1}$$

Equation (6.4) for T = 300 K gives the value $i_d = 1.439 \times 10^{-16}$ Amps whereas the specification quotes a typical dark current value of 3 nA. The disparity between these results warranted further investigation.

The Richardson-Dushman equation is based on the initial assumption that the work function and the photoelectric threshold energy of the cathode are equal. It is acknowledged that this assumption is not accurate for the materials currently used in electronics. Hamamatsu investigations have shown that dark current in a PMT is comprised, not only of thermionic emission, but also of ionisation of residual gases and leakage current from the glass stem base and socket [5]. The latter dominates when the operating voltage of the PMT is below 800 V, which is the case in this instance. There is, as yet, no theoretical development in relation to these other dark current sources. The closest research is the work of Kharin et al on melted pools of zirconium oxide [7] which unfortunately does not apply. Thus, given the disparity between theory and practice, for the model being considered, it was decided to use the Hamamatsu quoted figure for dark current $i_d = 3 \times 10^{-9}$ A.

6.3.2 Gain of the PMT

Equation (6.5) was derived for calculating the value of the gain per dynode within the PMT. Figure 6.4 illustrates the comparison between the gain calculated using this equation and the gain chart illustrated by the PMT specification, showing good agreement.

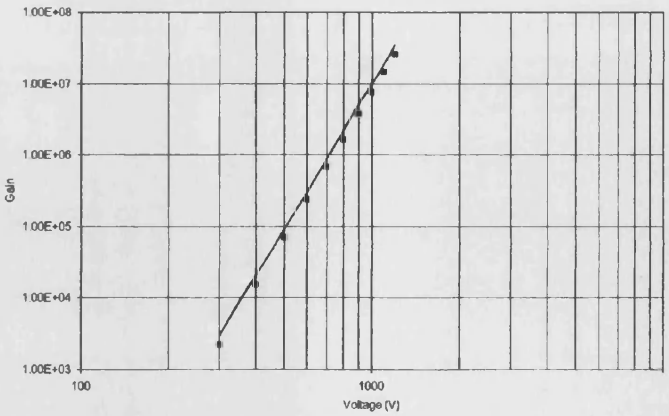

***Figure 6.4**: Current gain as a function of applied voltage.*
Squares - data points calculated using equation (6.5).
Smooth line - data specified for a R928 PMT

6.4 Calculation of sensitivity

"At such low levels of analyte even trace amounts of
interferents can become significant."

Foulds et al [8]

The accepted definition of sensitivity is the lowest detectable concentration of analyte distinguishable from measurements made with no analyte present. Figure 6.5 illustrates a typical calibration curve for a sandwich assay. Applying the definition of sensitivity to this figure the lowest concentration that can be determined from the graph occurs at an analyte concentration, s, such that the signal on the graph at the point s is equal to the signal at zero analyte plus the error in the zero analyte signal plus the error in the signal at s analyte i.e.

$$S_0 + N_0 + N_s = S_s$$

where S refers to the signal
N refers to the noise or error in the signal
the subscript refers to the analyte concentration

and s is the sensitivity.

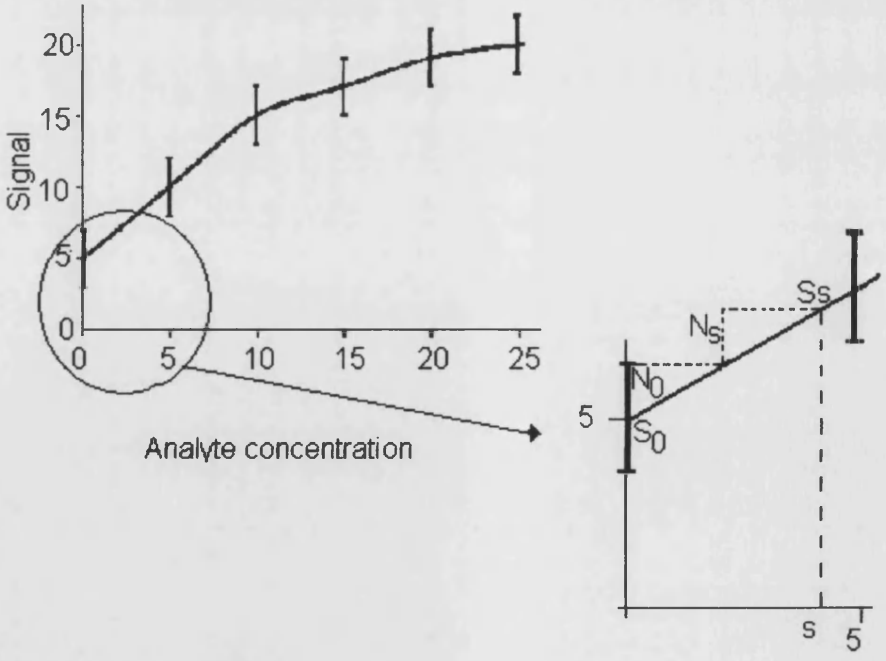

***Figure 6.5**: Calibration curve for a sandwich assay showing the calculation of the sensitivity (s) of the curve illustrated.*

The calibration curve resembles a cubic polynomial and fitting data to such a curve proved successful. Thus the sensitivity of a set of data from the immunosensor model was calculated by

i) fitting the output signal to a cubic polynomial S;

ii) fitting the noise signal to a cubic polynomial N;

iii) solving the equation $S(0)+N(0)+N(s)=S(s)$ for s > 0.

The solution of the equation was established using a bisection to locate the root and a Newton-Raphson procedure to determine an accurate value.

References

[1] Helstrom CW, *Elements of Signal Detection and Estimation*, (Englewood Cliffs, NJ: PTR Prentice Hall) pp 485 – 493, 1995.

[2] Kingston R. H. *Detection of Optical and Infrared Radiation* Vol 10 (Berlin: Springer-Verlag) pp 41 – 51, 1978.

[3] Teich MC, Matsuo K & Saleh BEA, Excess Noise Factors for Conventional and Superlattice Avalanche Photodiodes and Photomultiplier Tubes, *IEEE Journal of Quantum Electronics*, **QE-22**, 1184 – 1192, 1986.

[4] Dance JB, *Photoelectronic Devices*, (London: Iliffe Books Ltd) pp 62 – 87, 1969.

[5] Hamamatsu, *Photomultiplier Tubes Construction and Operating Characteristics*, Available via the World Wide Web at http://www.hpk.co.jp/Eng/products/etd/pmte/pmte.htm.

[6] O'Shea DC, *Elements of Modern Optical Design*, (USA: John Wiley & Sons, Inc.) pp 313 - 315, 1985.

[7] Kharin SN, Mukazhanov VN & Mokryshev AI, *Electrochemical Mechanism of Electron Emission in Electrical Contacts*, Available via the World Wide Web at http://www.met.kth.se/corr/icec2000/sessionC.htm

[8] Foulds NC, Frew JE & Green MJ, Immunoelectrodes In *Biosensors: A Practical Approach*, (Ed) Cass AEG, (Oxford UK: Oxford University Press), pp 97 – 124, 1990.

Chapter 7

Application of the model to the analysis of noise and variation within an immunosensor

Once each of the component modules had been fully implemented, tested and the results generated verified against experimental data, a full model of an evanescent field immunosensor was constructed and used to study some of the sources of noise and variation within the system. Time restrictions dictated that the results of the preliminary investigations discussed here were not pursued beyond the initial stages. However, the results demonstrate the range of investigations that can be undertaken using this type of model and the variety of information that can be accumulated.

7.1 Noise

Noise is a generic term that refers to any unwanted component of a signal [1]. In the case of the evanescent field immunosensors modelled here, noise refers to any part of the output voltage that does not result from fluorescence of the bound labelled molecule within the immunoassay. Noise or variation may occur within a sensor or the variation may be between different instances of the same sensor. The model allows sources of both within sensor and between sensor noise to be considered and the resulting effects on sensitivity to be determined.

7.1.1 Between sensor noise

A degree of variation may occur between instances of the same sensor and this is known as between sensor noise. These errors may produce a variation or error into the output voltage and therefore have an impact on the reproducibility and reliability of the sensitivity that can be achieved.

In the immunoassay element variation in the concentrations of the initial species added and the association constants will produce between variations in the amount of bound label. This variation may occur due to measurement of the concentration of the added

species or changes in the activity of the immobilised capture antibody. Previous fitting of experimental data (Section 4.6) showed that the values of the association constants could also be altered by immobilisation or labelling.

Within the light module both the physical dimensions of the system and the coupling and specifications of the power source may introduce between sensor error. The difference in value of the physical parameters of the system may be introduced due to manufacturing tolerance for example and variations in the incident power may occur in the progression from laboratory to field instrument. Similarly within the detector the applied voltage may impact on sensitivity. Table 7.1 lists the sources of between sensor noise, indicating those that have been considered in the current model of the immunosensor.

Table 7.1: Sources of "between sensor" noise indicating the appropriate module and whether the current model deals with the particular source

Module	Considered within project	Not considered as yet
Immunoassay	Concentrations	Cross reactivity
	Association constants	
Light	Beam divergence	Scattering*
	Coupling	
	Incident power	
	Physical dimensions	
Detection	Dynode voltage	

* has been considered as 'within sensor' noise

Given that the immunosensor model presented assumes a single immunoassay, i.e. one analyte, one capture antibody and one labelled molecule, cross-reactivity will not be a problem and need not be considered. However, future development of the model is likely to consider multianalyte detection. Obviously at this point cross-reactivity may become a significant source of noise and thus would be a vital factor to be included within the noise analysis.

7.1.2 Within sensor noise

Within sensor noise refers to variations in the output signal that occurs as a direct result of some element of the system. This may be due to electrical noise within the PMT or due to fluorescence excited by light scattering into the unbound labelled molecules. Noise resulting within the sensor is consistent for the sensor arrangement and may be difficult to eradicate. Thus, within sensor noise directly affects the sensitivity that can be achieved for a particular device. Table 7.2 lists the sources of within sensor noise, indicating those that have been considered in the current model of the immunosensor.

Table 7.2: Sources of "within sensor" noise indicating the appropriate module and whether the current model deals with the particular source

Module	Considered within project	Not considered as yet
Immunoassay		Non-specific binding
Light	Scattering	Stray ambient light
	Breakthrough laser light	
Detection	PMT noise	

The experimental data used to verify the model was generated using a system in which both non-specific binding and stray ambient light has been reduced to insignificant levels. Thus these factors were not a priority when determining the sources of noise to include within the original model. Further development of the model to encompass other systems would necessity their inclusion.

It should be noted that some of the physical parameters that define a sensor may also impact on the within sensor noise, for example the waveguide thickness is involved in the scattering calculation. Thus, there may be correlations between 'between sensor' and 'within sensor' noise. The current model has not considered this relationship as the possible complexity is beyond the scope of the preliminary investigations into noise.

7.2 Between sensor noise

7.2.1 Immunoassay concentrations and constants

It is difficult to exactly replicate a set of immunoassay conditions. Fitting the model to experimental data as outlined in section 4.6 showed that the manufacturer's values for the association constants of the reactions were altered by antibody immobilisation or the addition of a label. Immobilisation or labelling may also interfere with the active binding sites of the molecules and thus reduce the concentration available for reaction. It is therefore possible that there is a between sensor variation in the association constants and the initial concentrations of the capture and labelled species.

The modified Markov approach to simulating an immunoassay was incorporated into a Monte Carlo simulation to establish the variation in the output concentrations resulting from variations in the initial conditions. The assay was a sandwich assay for human chorionic gonadotrophin (hCG) with initial concentrations

$$[c]_0 = 30.9 \times 10^{-9}\ M$$
$$[l]_0 = 250 \times 10^{-9}\ M$$

and association constants

capture – analyte $K_C = 2.2 \times 10^{9}\ M^{-1}$

analyte – labelled antibody $K_L = 4.1 \times 10^{10}\ M^{-1}$.

The simulation assumed errors in the intrinsic association constants and initial concentrations and that there was no noise or errors associated with the remainder of the sensor. The number of simulations necessary to establish a reliable error is large and the runtime of the immunoassay module varies with the elapsed time assumed for the assay. Thus, a set of 100 simulations each allowing the assay module to run to an elapsed assay time of 1 minute was deemed sufficient to produce a realistic estimate of the mean and standard deviations involved.

The procedure was performed for a range of initial analyte concentrations. The Monte Carlo simulation produced means and standard deviations for the resulting bound and unbound label concentrations. These values were used within the remainder of the immunosensor model using Model B, the multilayer coupling model (characteristics described in Table 7.3); with exciting light provided by a 5 mW Helium-Neon laser of wavelength 632.8 nm, a waveguide width of .0 4 m and an observation length for resulting fluorescence of 1 mm.

Table 7.3: Characteristics of the multilayer system used in Model B.

	Thickness	Refractive Index	
Layer	**(nm)**	**Real part**	**Imaginary part**
Glass	-	1.51958	-
Buffer	750	1.44	-
$FePO_4$ waveguide	150	1.7	-
Capture antibody	7.14	1.3428	-
Bound layer	15.47	1.34239*	0.000959*
Solution	-	1.33284*	1.45×10^{-6}*

* Values dependent on concentrations

Examples of the calibration curves for the assay are illustrated by Figure 7.1 showing the errors in the output introduced by including errors within the immunoassay variables.

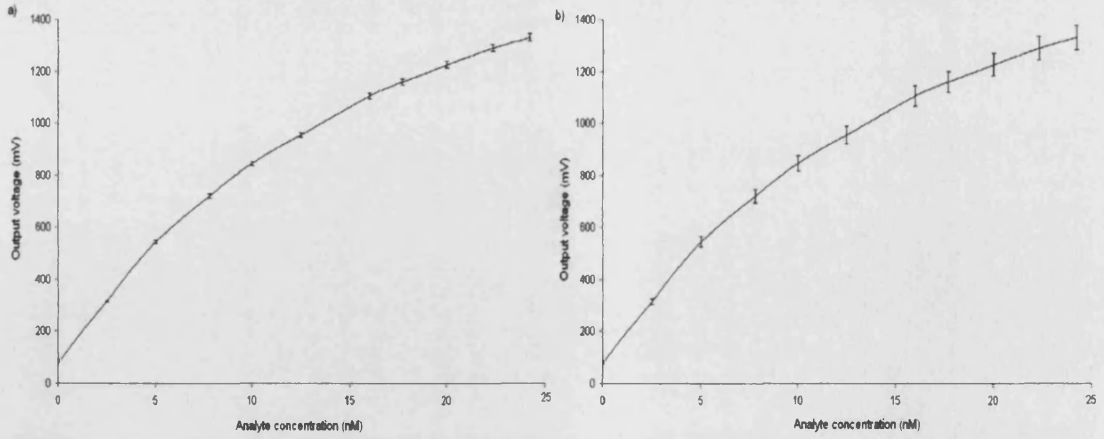

***Figure 7.1**: Output from the immunosensor model showing the errors in the output signal introduced by variations in the initial concentrations of species within the immunoassay determined using a Monte Carlo simulation*

a) 1% error in initial concentrations and 10% error in association constants

b) 10% error in initial concentrations and 10% error in association constants

The sensitivities, the lowest concentration of analyte that can be detected, of the resulting sensors are shown in Table 7.4 and Figure 7.2. The results demonstrate that increasing the amount of error in the assay concentrations has an effect on the sensitivity of the device. An increase in the percentage error in the concentrations from 1% to 5% decreases the sensitivity by 400%. However, further increasing the error in concentrations beyond 5% produces a slower decrease, a 25% decrease in sensitivity for each doubling of the percentage error.

Table 7.4: Sensitivities calculated for the immunosensor assuming variations in the parameters defining the immunoassay module (determined using a Monte Carlo simulation of the sandwich assay for hCG) with no errors or variations within the remainder of the sensor.

% error in Association constants	% error in Initial concentrations	Sensitivity x 10^{-11} M
10	1	1.103
10	5	4.024
10	10	5.040
10	20	6.377

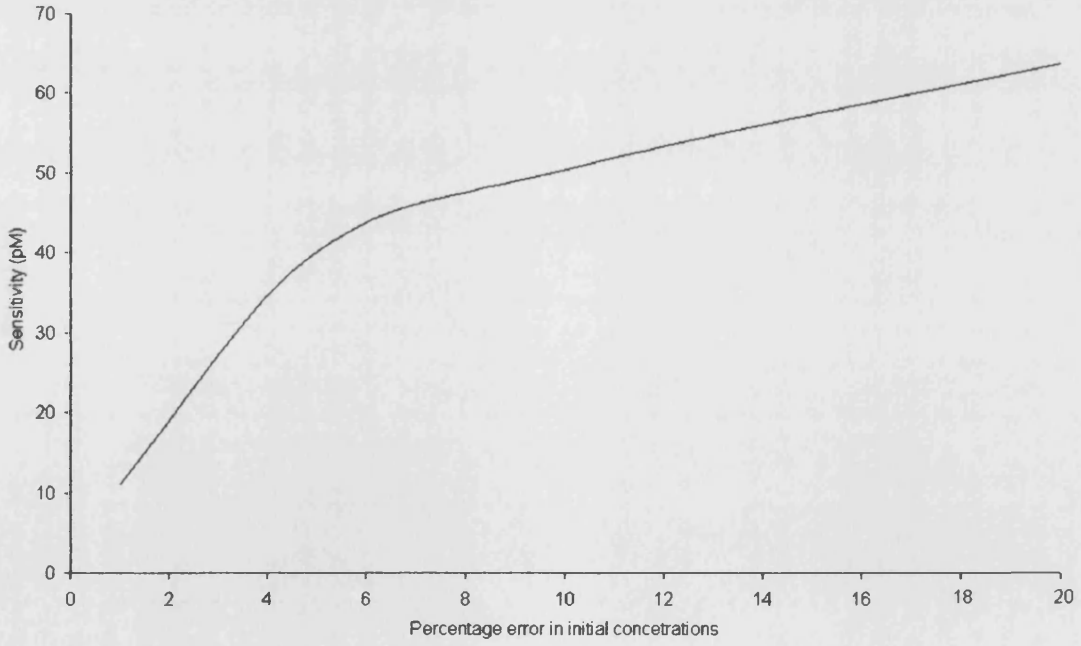

***Figure 7.2**: Sensitivity of the multilayer coupled CFD immunosensor containing a sandwich assay for hCG assuming a percentage error in the initial concentrations of the immunoassay module, a fixed 10% error in the association constants, and no variations within the remainder of the system.*

Errors of less than 1% in concentrations may be achievable by an expert but a viable biosensor will require no expert measurements and in the case of a CFD concentrations will be controlled by the physical dimensions of the device. However these results show that it is vital that the error in concentration be kept to a minimum if good sensitivity is to be achieved.

7.2.2 Physical parameters of Model A – Prism Coupling

The physical parameters of the Model A immunosensor (Figure 7.3) that may impact on the resulting fluorescence are:

i) input power;
ii) coupling efficiency;
iii) waveguide thickness;
iv) width of the cell;
v) observation length.

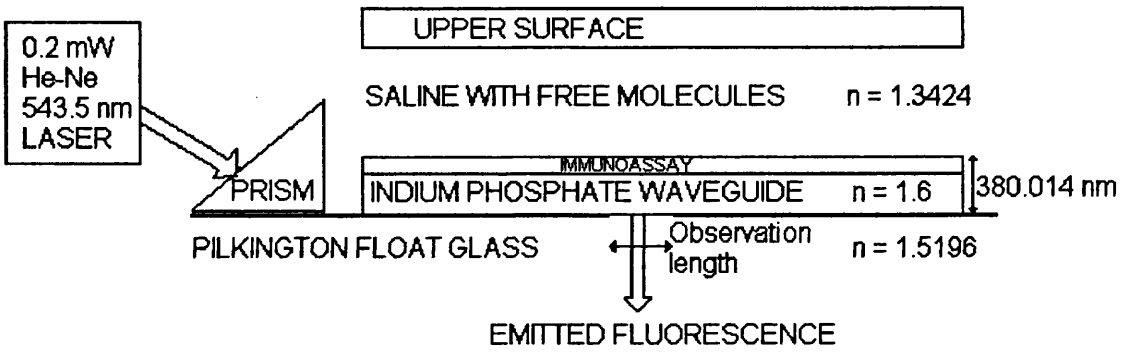

Figure 7.3: *Experimental arrangement for Model A, the prism coupled model illustrating the values for the physical parameters that may impact on the resulting fluorescence.*

A second Monte Carlo simulation was implemented. This procedure simulated output from the light module for variations in one of the physical parameters. The values of all other parameters were fixed, so the error in the output was due to variation in a single parameter only. The concentrations and variances of the species resulting from the immunoassay module were fixed as the values resulting from the Monte Carlo simulation of the immunoassay with a 1% error in initial concentrations described above.

The percentage error in the output signal of Model A, the prism-coupling model, with no errors in the physical parameters of the light module was determined as 0.96% (Table 7.5). Figure 7.4 illustrates the percentage errors resulting from the inclusion of a 1% error in each of the physical parameters listed.

Table 7.5: Percentage error in the output signal from a Model A (prism coupled) immunosensor caused by 1% error in the concentrations resulting from the immunoassay module with the addition of a 1% error in each of the physical parameters listed.

Parameter with 1% associated error	**% error in output signal**
Concentrations ONLY	0.96
+ Incident power	1.96
+ Coupling factor	1.97
+ Cell width	0.96
+ Observation length	1.88
+ Waveguide thickness	1.40

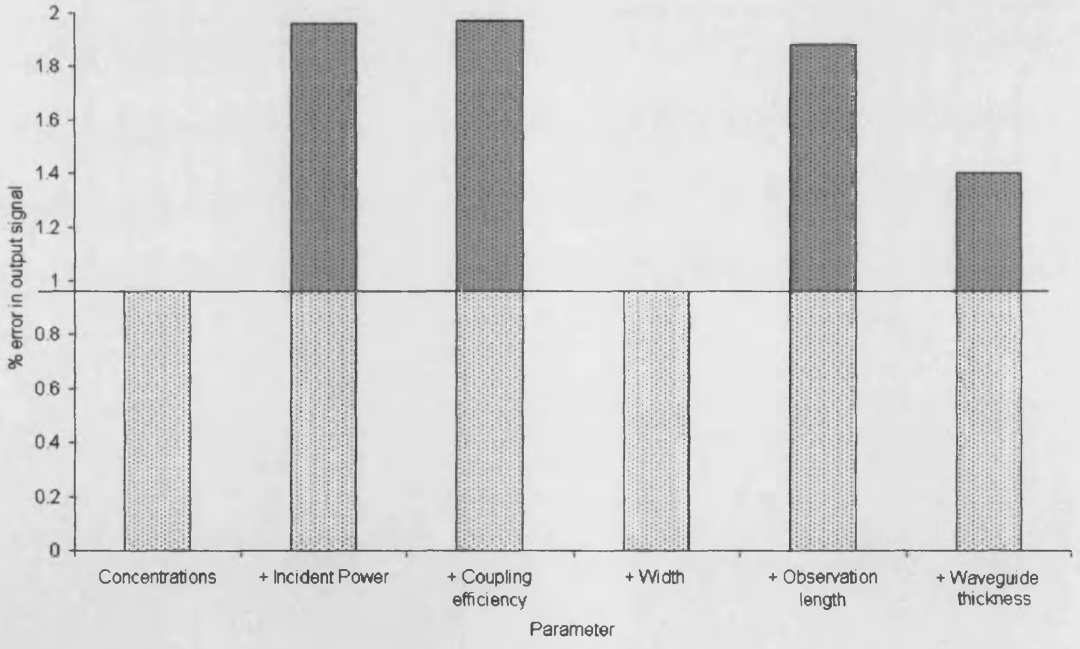

***Figure 7.4**: Percentage error in the output signal from a prism coupled immunosensor caused by 1% error in the immunoassay concentrations with the addition of a 1% error in each of the physical parameters listed determined using a Monte Carlo simulation. The lighter area below the line is the error due to variation in the concentrations of the immunoassay. The darker area above the line indicates the additional error resulting from error in the particular parameter.*

It can be seen that a 1% error in the incident power, the coupling efficiency and the observation length increased the error in the output signal by a similar percentage. However, a 1% error in the waveguide thickness had less effect and a 1% error in the width of the waveguide did not significantly increase the percentage error from that achieved with errors in the immunoassay only.

Analysis of this type is invaluable to a biosensor designer. The effect variation of the coupling efficiency and incident power demonstrate that the amount of light coupled into the waveguide is a crucial factor in the production of a sensitive device. In terms of the manufacture of the device the physical parameters of importance are the waveguide thickness and observation lengths.

Sloper & Flanagan [2] devised a spin coating technique that enabled them to deposit waveguides with accuracy in the deposited thickness of 3%. The Monte Carlo was adapted to allow variation in two of physical parameters and the impact of variation in both the waveguide thickness and the observation length on the output signal was determined (Figure 7.5). It can be seen that variations in the observation length produce a greater increase in output error than variations in the waveguide thickness.

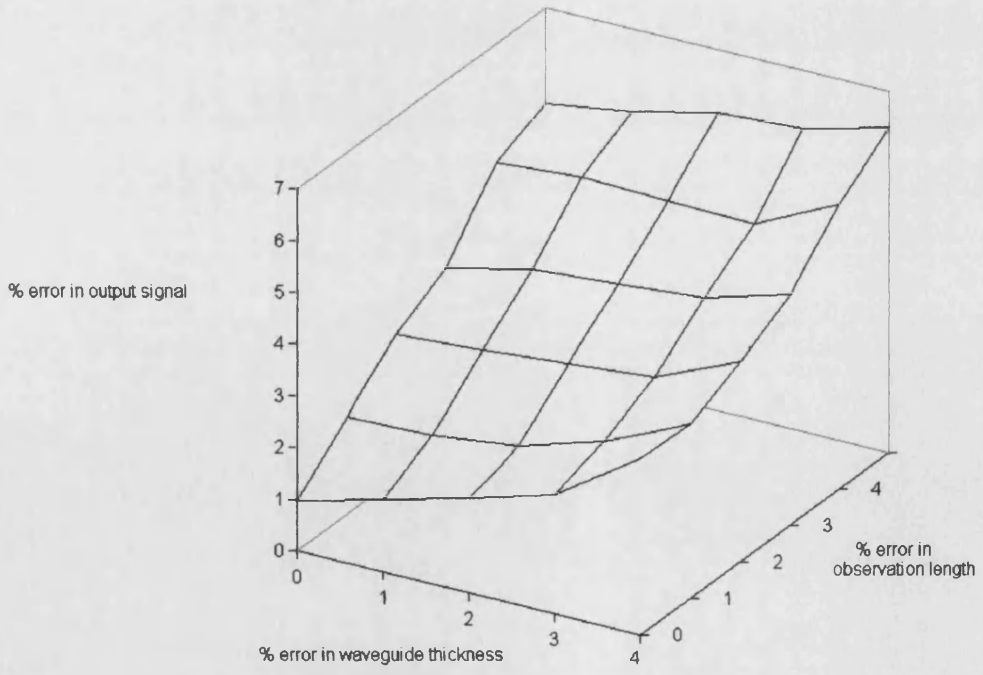

***Figure 7.5**: The percentage error in the output signal as a function of percentage errors in the waveguide thickness and observation length determined using a Monte Carlo simulation of the Model A (prism coupled) light module.*

7.2.3 Physical parameters Model B – Multilayer coupling

A similar analysis was made of the impact of errors within the physical parameters of the multilayer coupling model; Model B (layers and thicknesses as described in Table 7.3). The exciting light was a 5 mW Helium-Neon laser of wavelength 632.7 nm. The width of the waveguide was Ω 4 m and the observation length for resulting fluorescence was 1 mm.

A further Monte Carlo simulation was implemented to simulate output from the light module for variations in one of the physical parameters of Model B using values for the concentrations and variances of the species resulting from the Monte Carlo simulation of the immunoassay with a 1% error in initial concentrations previously discussed. Figure 7.6 illustrates the error in the output signal resulting from the separate inclusion of a 1% error in each of the parameters listed.

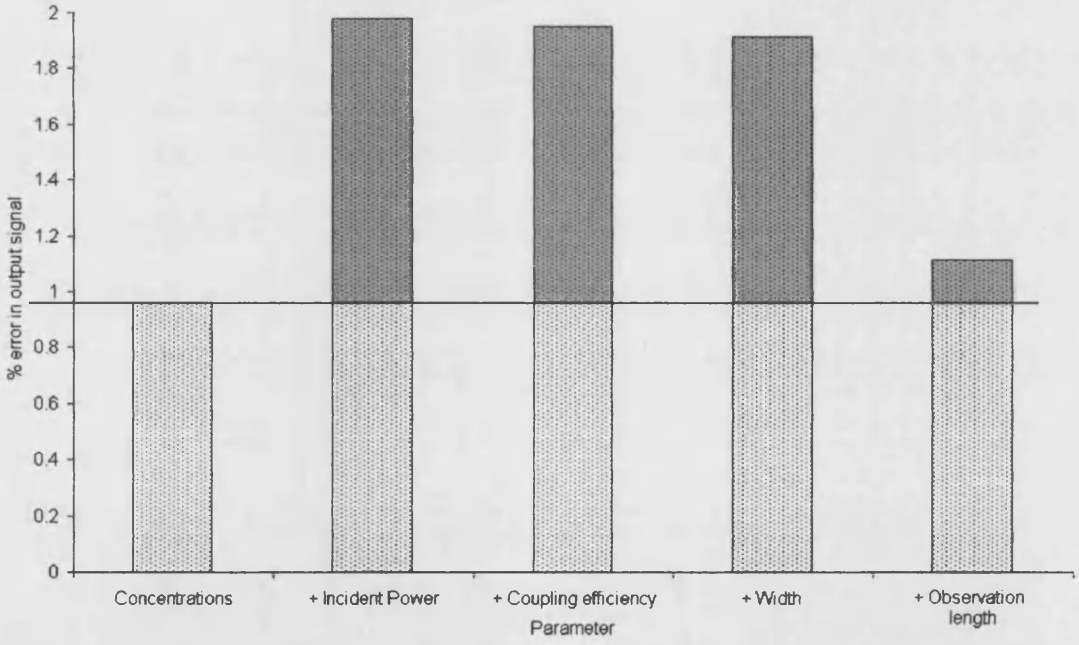

***Figure 7.6**: Percentage error in the output signal from a multilayer coupled immunosensor caused by 1% error in the immunoassay concentrations with the addition of a 1% error in each of the physical parameters listed determined using a Monte Carlo simulation.*
The lighter area below the line is the error due to variation in the concentrations of the immunoassay. The darker area above the line indicates the additional error resulting from error in the particular parameter.

Analysis of this type enables the comparison of the effect of the different parameters in Models A and B. It can be seen that variations in the incident power and coupling efficiency have a similar impact in both models but that the width of the waveguide becomes a significant factor in Model B, the multilayer coupling. The impact of the observation length is less significant in Model B than in the prism coupled Model A.

7.2.3.1 Noise in the resonance curve

Model B, the multilayer coupling device, involves performing an angle scan to determine the resonance point at which the signal is at its maximum value. Noise in the output signal produced by Model B may blur the point at which resonance occurs. A biosensor is unlikely to involve an angle scan, however if multilayer coupling is used the angle at which a light enters the system will effect the resulting output.

Figure 7.7 (overleaf) illustrates the resonance curve produced using the Model B model defined above. Figure 7.7a shows the error bars in the output resulting from a 1% error in the initial immunoassay concentrations only, whilst Figure 7.7b represents the output produced with the addition of a 1% error in the observation length. It can be seen that the introduction of an error does extend the range at which resonance may appear to occur, i.e. the point of maximum voltage minus the possible error in the signal.

Resonance curves were drawn for the addition of a 1% error in each of the parameters considered in section 7.2.3 above. Table 7.6 shows the range of angles whose output signals fall within the error margin of the maximum output, i.e. the range of angles that may appear to be the resonant angle.

Table 7.6: Range of angles within the error margin of the maximum voltage minus error in voltage for 1% errors in the parameters shown.

Parameter and error	Range of angles	Difference
1% error in immunoassay ONLY	75.38 – 75.41	0.03
+ 1% error in input power	75.37 - 75.42	0.05
+ 1% error in coupling efficiency	75.37 - 75.42	0.05
+ 1% error in width	75.37 - 75.42	0.05
+ 1% error in observation length	75.38 – 75.42	0.04

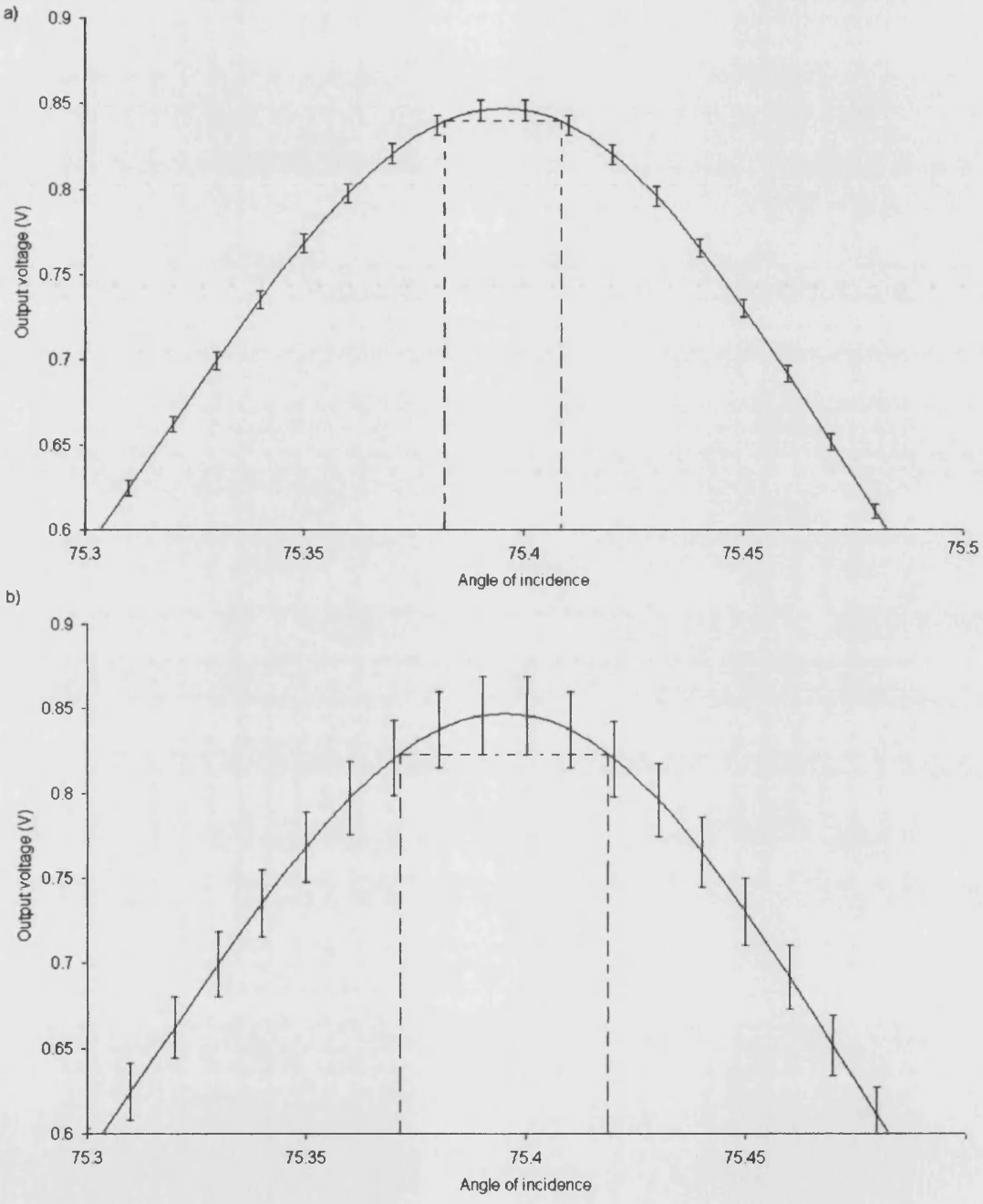

***Figure** 7.7: Output from the angle scan of the multilayer coupled device with error bars illustrating the error in the output signal at each point*

a) Errors in immunoassay ONLY

b) Errors in assay plus a 1% error in observation length

7.2.3.2 Waveguide thickness

Previous research has shown that the angle of resonance varies with the thickness of the deposited waveguide [3]. The Monte Carlo simulation used to determine the variation in the output caused by variations in the parameters illustrated by Figure 7.6 above assumed that the output signal was recorded at the known angle of resonance. Performing a Monte Carlo simulation with a 1% error in the waveguide thickness at a fixed angle returned an error in the output signal of 50%. This large variance is due to the fact that as the waveguide thickness varied within the simulation the angle at which the output signal was determined was no longer the resonant angle. Thus the mean and standard deviation of the output voltage calculated by the simulation were no longer realistic and waveguide thickness was not included in the comparison of the errors in the physical parameters (Figure 7.6).

Figure 7.8 shows the deviation of both the mean and standard deviation of the output voltage from the Monte Carlo simulation with increasing percentage errors in the waveguide thickness. It is clear that as the variations in the waveguide thickness increase the standard deviation of the output voltage become dominant. Therefore, if the waveguide thickness is not consistent, a multilayer coupled sensor using a fixed angle of incident light would not be viable.

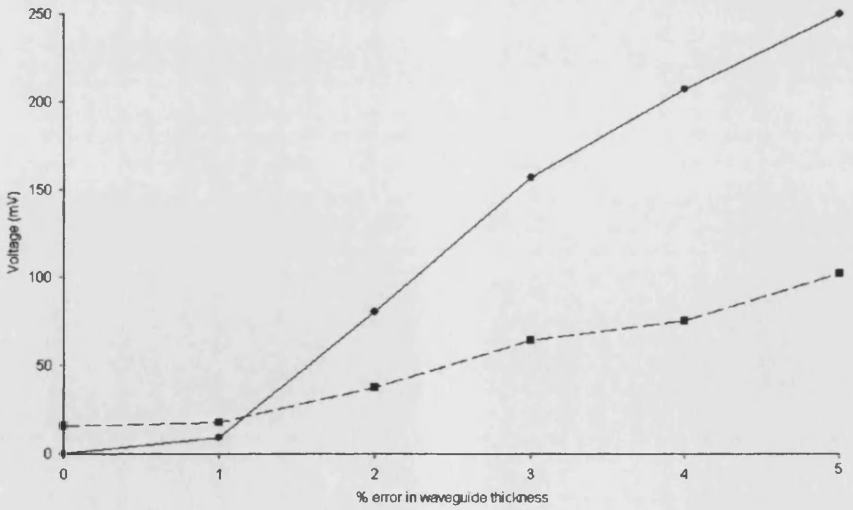

***Figure 7.8**: Variation in mean output voltage (dashed line ■) and standard deviation (smooth line ●) resulting from increasing percentage error in the waveguide thickness within a Monte Carlo simulation of a Model B (multilayer coupled) immunosensor assuming a fixed angle of incidence.*

The relationship between variation in the waveguide thickness and variation in the incident angle was investigated by adapting the Monte Carlo simulation to allow variations in these two parameters. Figure 7.9 shows the results of this simulation and illustrates that the relationship is non-linear. This confirms that if a multilayer coupled sensor is to be used waveguide thickness, incident angle and the trade-off between them need to be considered during the design process.

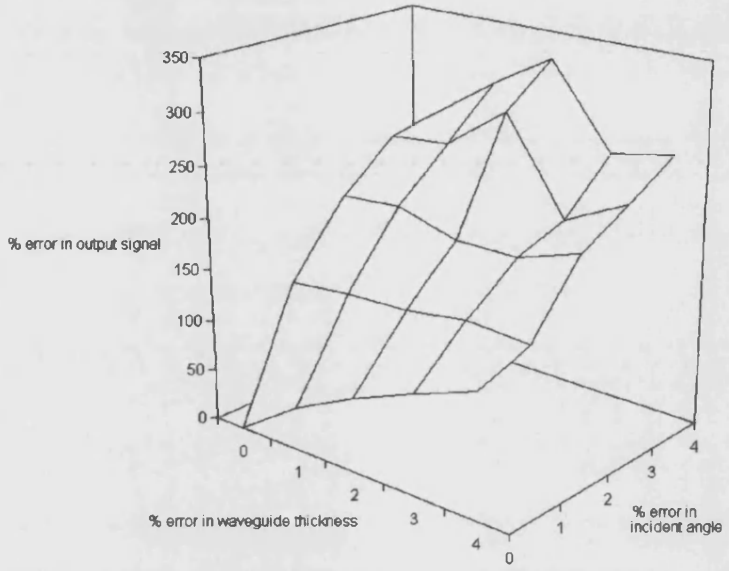

***Figure 7.9**: Percentage error in the output voltage of a Model B immunosensor as a function of percentage errors in the waveguide thickness and angle of incident light.*

7.2.3.3 Divergence in incident laser beam

Collimating optics would not be available within a small biosensor and thus the incident beam may diverge before it becomes incident on the sensing component. The impact of divergence in the incident beam on the resonance curve produced for the multilayer coupling device, Model B, was investigated. Resonance curves for the sandwich assay for 24.2 nM of hCG within a multilayer coupled CFD (as described in Section 7.2.1) were generated for a range of angles of divergence of the incident beam.

Figure 7.10 illustrates the incongruities between the values that parameterise the resonance curves resulting from the model for variations in the angle of divergence of the incident beam. Increasing the divergence of the beam significantly decreases the maximum output voltage. Given that the 24.2 nM of analyte used to generate these curves is a relatively high concentration then the impact of this reduction in output voltage for lower analyte concentrations and hence sensitivity is significant.

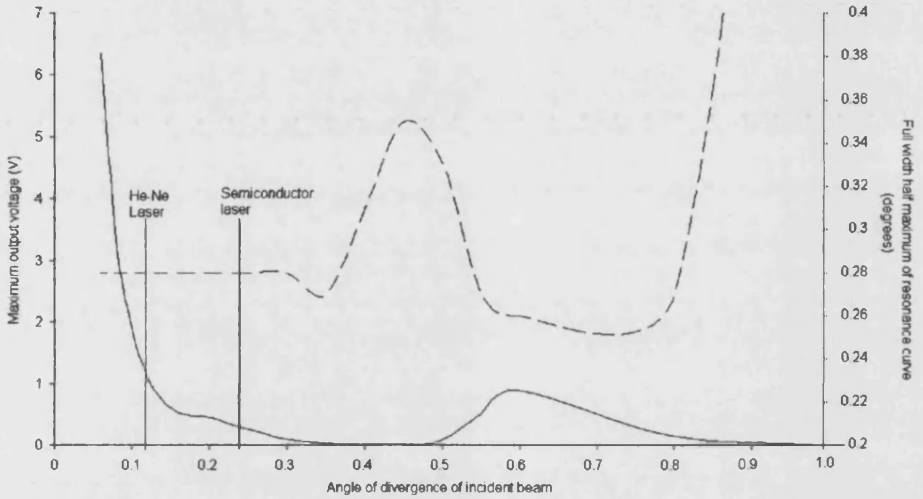

***Figure 7.10**: Variation in the maximum output voltage (smooth line) and the bandwidth (dashed line) of the resonance curve resulting from a sandwich assay performed within a multilayer coupled CFD.*
Typical values for a Helium-Neon and semiconductor laser are marked.

The bandwidth of the resulting curve varies dramatically with increasing angle of divergence. The "natural" bandwidth of the resonance curve is 0.28°, which remains constant until the divergence in incident beam exceeds this value. It then becomes erratic with a sharp increase followed by a decrease before the divergence reaches twice the "natural" bandwidth. At this point the maximum output voltage also peaks briefly. Once divergence has reached three times the "natural" bandwidth the curves produced no longer resemble a resonance curve.

The typical divergences of a Helium-Neon and a semiconductor laser are marked on the curve in Figure 7.10. It can be seen that whilst both fall within the region where the bandwidth of the resonance curve is constant, the maximum output voltage achievable using the semiconductor laser is about 50% of that achievable using the Helium-Neon laser.

7.2.4 Dynode voltage

Within the detection module one of the physical parameters that may vary between sensors is the dynode voltage applied to the PMT. A biosensor that is truly portable will not have the stable power supply that would be available under laboratory conditions and thus the impact on the sensitivity achieved with the inclusion of variation in the dynode voltage was considered.

A Monte Carlo simulation of the detection module was performed considering a 1% variation in the dynode voltage. Data transferred to this module was from the model with the sandwich assay for hCG performed within a multilayer coupled CFD (detailed in Section 7.2.1). This data included a 1% error in the initial concentrations but assumed that all other parameters were constant. Figure 7.11 shows the increased error and therefore reduced sensitivity with the inclusion of a 1% error associated with the dynode voltage.

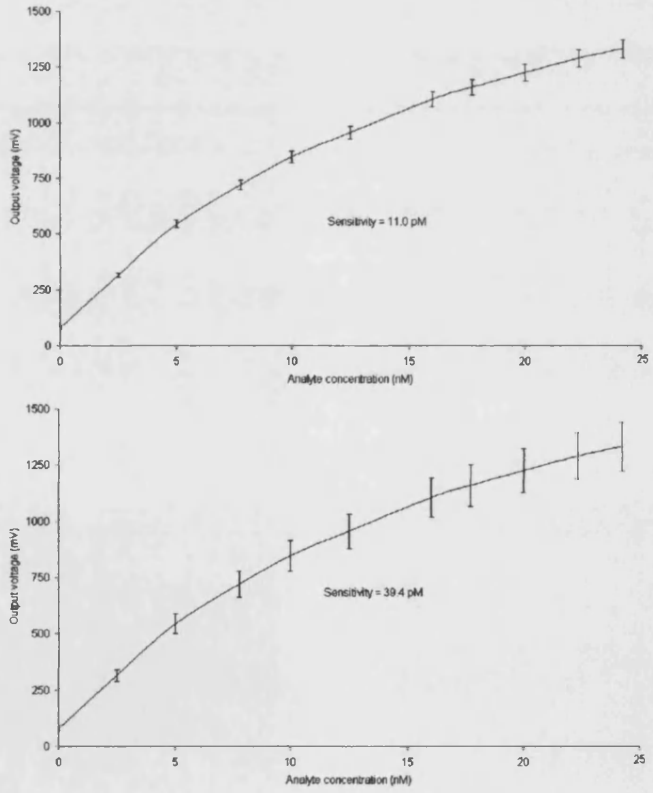

***Figure 7.11**: Output from the multilayer coupled immunosensor model containing a sandwich assay for hCG for*

a) Errors in immunoassay ONLY

b) Errors in assay plus a 1% error in dynode voltage

7.3 Within sensor noise

7.3.1 Scattering

The constitution of fluorescence resulting from the sensor can arise from both bound and unbound labelled molecule, excited by either the evanescent field or light scattered from the waveguide surface. Applying the definition of noise used here, any fluorescence that does not result from the bound label excited by the evanescent field is an unwanted part of the signal.

Concentrations for bound and unbound labelled molecule were determined for a 10 minute sandwich assay for IgG using the modified Markov approach. Initial concentrations were

$$[a]_0 = 20 \times 10^{-9} \text{ M}$$

$$[c]_0 = 30.9 \times 10^{-9} \text{ M}$$

$$[l]_0 = 250 \times 10^{-9} \text{ M}$$

with association constants

capture – analyte $K_C = 5.67 \times 10^9 \text{ M}^{-1}$

analyte – labelled antibody $K_L = 1.52 \times 10^{10} \text{ M}^{-1}$.

These concentrations were then used within both a Model A (Section 7.2.2) and a Model B (Section 7.2.3) arrangement and the resulting output analysed (Figure 7.12).

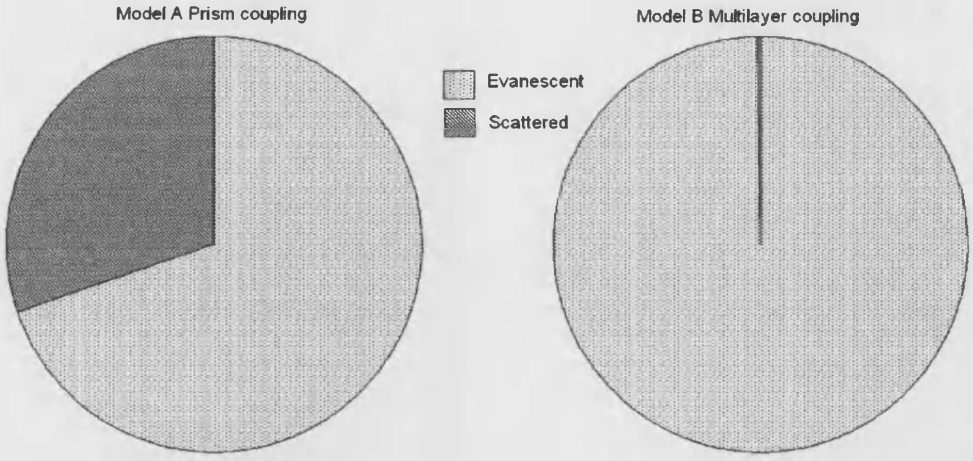

***Figure 7.12**: Percentage of fluorescence due to evanescent excitation and excitation due to scattered light for Model A – prism coupling and Model B – multilayer coupling*

The amount of fluorescence resulting from evanescent excitation and excitation due to scattered light for both the prism and the multilayer coupled sensors is shown in Figure 7.12 and indicates that scattered light contributes less to the output signal in the multilayer coupling device.

7.3.2 Breakthrough light

Breakthrough light, i.e. laser light that comes through the system and is incident at the photomultiplier tube cathode, adds an additional error to the output signal recorded by the sensor. The sandwich assay within the multilayer coupled CFD described above was used as the basis for analysing the impact of breakthrough light on the sensitivity of the device. Figure 7.13 illustrates the change in sensitivity of a device where an increasing amount of the laser light breakthroughs. It can be seen that the addition of breakthrough light lowers the sensitivity achieved, but that increasing the amount has little further impact. Since the breakthrough light will affect not only the output signal but also the PMT noise current, it seems likely that the increase in signal eliminates any further impact of the increased noise.

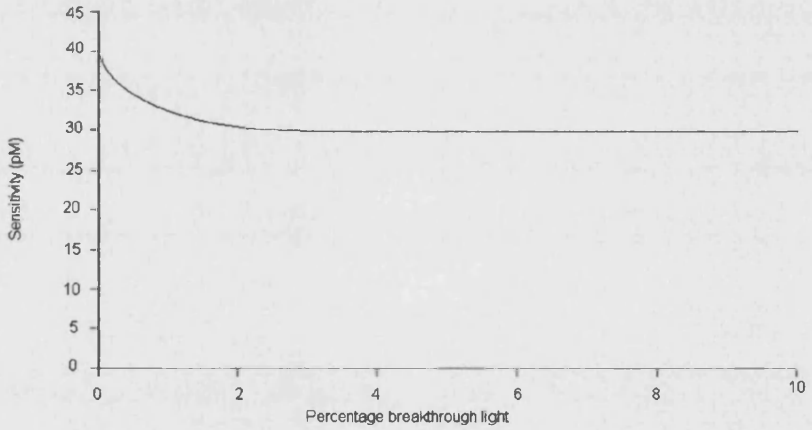

Figure 7.13: *Sensitivity of an immunosensor with increasing amount of "breakthrough" laser light incident at the detector.*

7.4 Summary

Noise within an immunosensor refers to any part of the output voltage that does not result from the fluorescence of the bound labelled element of the immunoassay component of the sensor. Errors may occur within a particular instance of a sensor or

between instances of the sensor and will affect the sensitivity and reliability of the resulting device. The model was used to consider the impact of various sources of noise and variation within the immunosensor.

7.4.1 Between sensor noise

Within the immunoassay between sensor errors may result from changes in the association constants of the reactions caused by labelling or immobilisation and differences in the initial concentrations caused by immobilisation and inaccurate measurement. Application of the model showed that errors in the immunoassay concentrations contribute to a lowering of the sensitivity of the device with a reduction in sensitivity by a factor of 4 on increasing the error from 5% to 10%. The rate of reduction slowed as errors increased with a reduction by a factor of 1.25 on increasing the error from 10% to 20%.

The physical parameters of the light module affected the error in the output to different degrees. In the prism-coupled model those that were most significant were identified as incident power/coupling efficiency and observation length. Waveguide thickness had a less significant effect. Comparing the effect of increasing the error in both the waveguide thickness and the observation length it could be seen that the more significant effect of the observation length remained dominant over the effect of variation in the waveguide thickness.

The multilayer coupled model was used to show that incident power/coupling efficiency and width were the most significant physical parameters in this arrangement. As this model uses an angle scan to establish the angle of resonance and therefore the maximum output voltage, it was used to demonstrate the fact that errors within the physical parameters of the model could cause noise within the resonance curve. The impact of waveguide thickness, which is directly related to the resonance angle, was investigated further and it was shown that errors in the waveguide thickness and angle of incident light have a serious impact on the sensitivity of the device.

Analysis of the impact of divergence within the incident beam demonstrated that increased divergence reduced the maximum output voltage and within certain parameters increased the bandwidth of the resonance curve. Increasing the divergence beyond 0.9° reduced the output to virtually zero with an undetermined bandwidth.

The model was used to show that the introduction of a 1% error in the dynode voltage of the PMT detector reduced the sensitivity achieved by a factor of 3.6.

7.4.2 Within sensor noise

Scattering at the waveguide surface was analysed and a profile of the scattered light was produced. It was shown that the contribution of scattered light to the detected fluorescence was negligible for the multilayer coupling model but amounted to 30.2% of the output for the prism coupled model.

Breakthrough light is laser light that comes through the capillary fill cell and becomes incident on the cathode of the PMT. The presence of breakthrough light lowered the sensitivity of the device but the effect stabilised for a breakthrough of 2%.

7.4.3 Potential of the model

The model can be used to study the impact on the output of a sensor for variations in a range of parameters. This enables a designer to identify which factors have the largest impact and to look at the trade-off in sensitivity that can be made between certain parameters. Studies of this type are difficult if not impossible to perform experimentally. Even if it were possible to vary the value of one parameter whilst maintaining the value of another, a comparison of the performance of two "runs" of the sensor may introduce between sensor noise from another source. Analysis of the composition of the resulting output, e.g. whether output results from the evanescent field or from scattered light could not be achieved experimentally. Thus, the model of the immunosensor adds a valuable tool to the resources available to anyone involved in biosensor design.

References

[1] O'Reilly JJ, *Telecommunication Principles*, 2nd edition, (London UK: Chapman & Hall) pp 23 - 25, 1989.

[2] Sloper AN & Flanagan MT, Metal phosphate planar waveguides for biosensors, *Applied Optics*, **33**, 4230-4240, 1994.

[3] Pampapathi VKM, *PhD Thesis University of London*, pp30 – 32, 1994.

Chapter 8

Application of the model to biosensor development

The potential of biosensors has been recognised since the early seventies and initially attracted a large research effort. Unfortunately success in the area has been limited and as a consequence the research effort has declined [1]. However despite a number of unresolved design issues, the potential for biosensors remains. The computer-based model of a biosensor described here has been developed in such a way as to facilitate its use in the research and development of biosensors and can be used to consider some of the issues that remain undecided in this arena.

8.1 Comparison of assay protocols

Initial immunoassay techniques, introduced by Yalow & Berson [2] and developed through the seventies used radio-isotope labels. Experimentally produced results indicated that the sandwich assay was more sensitive than the competitive assay and it is generally accepted that this was the case [3]. There was little theoretical evidence to support the hypothesis, but given that the factors limiting the performance of an assay were practical, Davies [4] reports that there was little incentive to resort to complex mathematics when experiments could achieve the desired result.

Ekins [5] disputed the lack of need for a theoretical model and produced several detailed theoretical examinations of the immunoassay, becoming acknowledged as a source of reliable, accurate theory in this area. Ekins applied his model to the radio-isotope labelled assays and verified that for this arrangement the sandwich assay proved more sensitive than the competitive assay.

However, a comparison of the sensitivity achieved using different assay protocols has not been repeated for the fluorescent techniques used in immunoassays today or for the different formats employed by biosensors. Unfortunately the amount of experimental data relating to biosensors is insufficient to allow the comparison to be made

experimentally or to directly apply the theory developed by Ekins. However the model developed here was used to produce a theoretical comparison between competitive and sandwich assay protocols within an evanescent field immunosensor.

8.1.1 Application of the model to the comparison of assay protocols

The modified Markov approach was applied to simulate a competitive assay for the protein IgG for a range of initial analyte concentrations. Other initial concentrations for the assay were

$$[c]_0 = 30.9 \times 10^{-9}\ M$$

$$[l]_0 = 45 \times 10^{-9}\ M$$

and the association constants were

capture – analyte $K_C = 5.67 \times 10^9\ M^{-1}$

capture – labelled analyte $K_L = 2.63 \times 10^8\ M^{-1}$.

The resulting concentrations were determined for elapsed times of 1, 2, 5 and 10 minutes from the addition of the analyte. These values were then used to determine the output voltage assuming that the assay were being performed within a CFD with multilayer coupling (layers and thicknesses as described in Table 8.1). The exciting light was a 5 mW Helium-Neon laser of wavelength 632.8 nm. The width of the waveguide was 0.4 m and the observation length for resulting fluorescence was 1 mm.

Table 8.1: Characteristics of the multilayer system used in Model B.

	Thickness	Refractive Index	
Layer	**(nm)**	**Real part**	**Imaginary part**
Glass	-	1.51958	-
Buffer	750	1.44	-
FePO4 waveguide	150	1.7	-
Capture antibody	7.14	1.3428	-
Bound layer	15.47	1.34239*	0.000959*
Solution	-	1.33284*	1.45×10^{-6}*

* Values dependent on concentrations

The immunoassay module of the model was replaced with a sandwich assay for IgG. The initial labelled antibody concentration for the sandwich assay was

$$[l]_0 = 250 \times 10^{-9}\ M$$

and the association constant for the analyte - labelled antibody reaction

$$K_L = 1.52 \times 10^{10}\ M^{-1}$$

whilst all other parameters of the model remained identical to those described above. Concentrations and the resulting output voltages were again determined at elapsed times of 1, 2, 5 and 10 minutes from addition of the analyte.

Table 8.2 shows the resulting sensitivities for both the competitive and sandwich assays at each elapsed time and clearly demonstrates that, even with the potentially different sources of noise presented within the evanescent field immunosensor modelled here, the sandwich assay still produces a more sensitive device.

Table 8.2: Sensitivity calculated after elapsed time from addition of analyte shown for both a sandwich and competitive assay for IgG.

	Sensitivity calculated after elapsed time (pM)			
	1 min	**2 min**	**5 min**	**10 min**
Competitive ($Sens_C$)	23100	14800	11500	10500
Sandwich ($Sens_S$)	140	80	30	30
Difference Factor $Sens_C/Sens_S$	165	180	410	397

8.2 Transient response

Ideally a biosensor would be available for use in a doctor's surgery, ambulance or even at home. Laboratory immunoassay techniques that involve removing any unbound molecules prior to measurement, allow the immunoassay reactions to come to equilibrium before the washing step. In some assays this may take in excess of 10 minutes, not a reasonable time for a test to be performed during a routine visit to a doctor. A viable biosensor should return a result in 2 – 3 minutes. The time taken for the result to be determined is therefore a crucial design factor [6]. The biosensor modelled provides the ideal vehicle with which to undertake studies of the sensitivity of

an immunosensor during the transient phase of the immunoassay, i.e. results recorded before the reactions have come to equilibrium (as seen in Table 8.2). The nature of the model also allows further analysis of the resulting output.

Visualising comparisons of assay protocols at different elapsed times across a range of analyte values proved difficult. The most satisfactory method found is illustrated by Figure 8.1 (overleaf) which shows calibration curves for both the competitive and sandwich assays for IgG described above. Noting the difference in scale on the y axis it is immediately obvious that the sandwich assay produces the more sensitive device.

8.2.1 Competitive assay

Figure 8.1a illustrates the calibration curves for the competitive assay for IgG at different elapsed times from the addition of the analyte. It is clear that after an elapsed time of 1 minute the gradient and the amount of noise do not produce a curve from which a small amount of analyte could be determined. Also, at this elapsed time the difference in the output between a sample with no analyte and one with 25 nM of analyte (~200 ± 90mV) has a large percentage error (45%) compared to the difference as the elapsed time of the assay increases (~650 ± 75 mV, 11.5% error, for a 10 minute assay).

8.2.2 Sandwich assay

Figure 8.1b shows the resulting calibration curves for the sandwich assay for IgG, demonstrating that with a sandwich assay the difference in output voltage between a sample with no analyte and one with analyte present greatly exceeds the differences produced with a competitive assay. For example, the presence of 25 nM analyte in a sandwich assay sample produces a difference in output voltage of ~1200 ± 120 mV from a sample with no analyte after 1 minute of elapsed time compared with a difference of 200 mV for equivalent analyte concentrations in a competitive assay. The percentage error (i.e. noise) in the output signal for the sandwich assay is 10%, more than double the 4% error in the output signal for the competitive assay. However, the lower voltages produced by the sandwich assay lessens the impact of this noise on the resulting sensitivity.

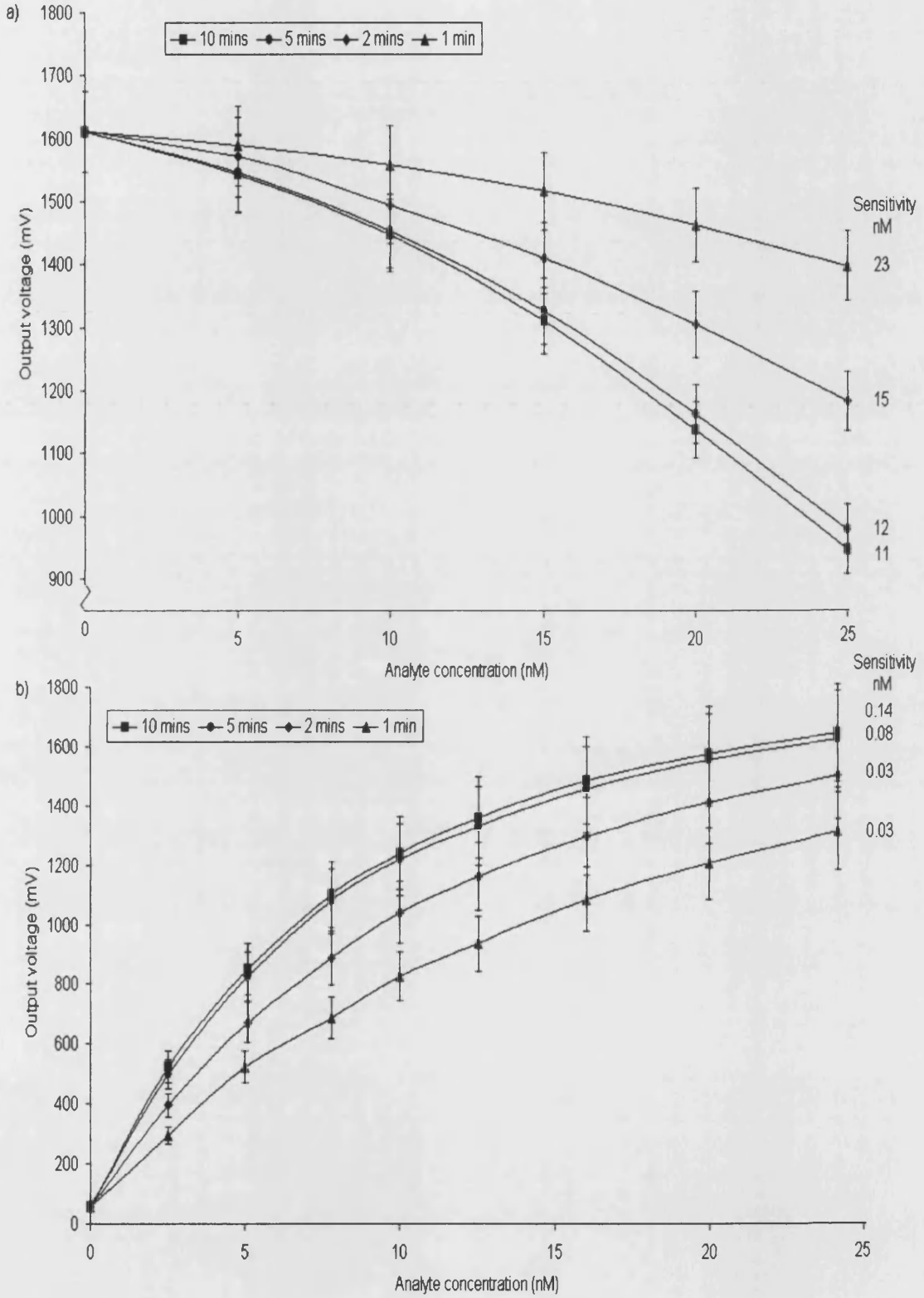

Figure 8.1: *Calibration curves produced using a simulation of assays for IgG within a multilayer coupled CFD at different elapsed times from the addition of the analyte. 1 minute (triangles); 2 minutes (diamonds); 5 minutes (circles); 10 minutes (squares).*
a) competitive assay
b) sandwich assay

8.2.3 Sensitivity as a function of elapsed time

Ultimately the sensitivity that can be achieved dictates the superiority of any particular biosensor arrangement. Figure 8.2 illustrates the sensitivities of both the competitive and sandwich assays described above. It is clear that the immunosensor is at its most sensitive once the immunoassay has come to equilibrium. In the particular case illustrated it takes approximately 5 minutes for the competitive assay and 8 minutes for the sandwich assay to reach equilibrium. It can be seen from Figure 8.2 that measurements taken at half the equilibrium time would not greatly reduce the sensitivity achieved, although for the sandwich assay this has still not reached the desired time of 2 – 3 minutes. However, the ability to make these comparisons at various elapsed times from the introduction of the analyte is an additional benefit of the model. Ekin's work in this area was restricted to comparison of results established once the assay had reached equilibrium.

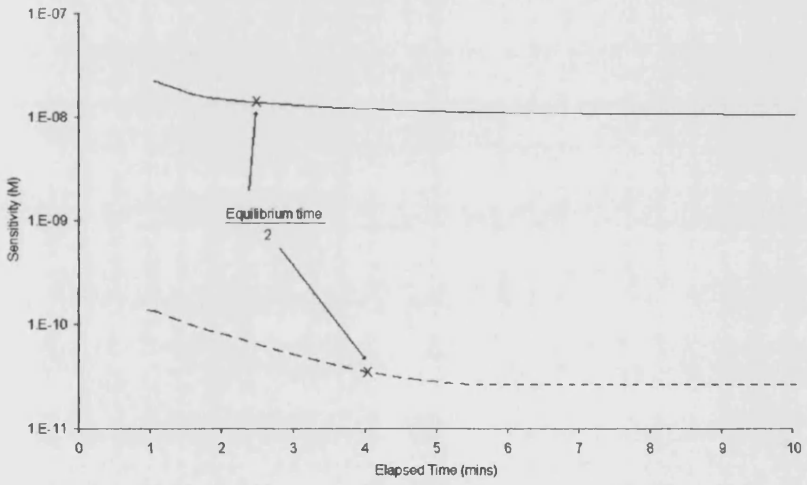

***Figure 8.2**: Sensitivity of a competitive (smooth line) and sandwich assay (dashed line) for IgG as a function of elapsed time from the addition of analyte determined using a simulation of the assays within a multilayer coupled capillary fill device.*

8.3 Scattering in planar waveguide sensors

Optical immunosensors in which the evanescent field interrogates the immunoassay offer a means of producing a sensor which eliminates the washing step used in standard immunoassay techniques, thus providing a more user-friendly interface. Planar waveguides [7] have been used as the transducer in evanescent field fluorescence

immunosensors. However, it has been suggested that scattering of light at the waveguide surface may contribute to noise in the output signal by exciting unbound fluorescent labels and thus decrease the sensitivity of the device [8]. The modular design of the model allows data from a particular aspect of the model to be determined independently of the remainder of the model. Thus it can be used to facilitate the analysis of the impact of a particular phenomenon, e.g. scattering at the waveguide surface, on the sensitivity of the sensor under investigation.

8.3.1 Scattering in the model

Scattering of light from dielectric interfaces is a difficult phenomenon to simulate. However, the theory developed from that of Walter & Houghton [9] (outlined in detail in Section 5.2.2.2) allows the proportion of light scattered from the surface of a monomode waveguide to be incorporated within the model. As the experimental work of this group is based on monomode waveguides the use of this element of the model to further analyse the profile of the scattered light and its contribution to the resulting output signal was beneficial.

8.3.2 Profile of scattered light

The formula (Equation (5.8))

$$\frac{\Delta P}{LP_T} = \frac{A^2}{B}\frac{\left\{\left(n_F^2 - n_C^2\right)k_0^2\cos(bW_{FC})\right\}^2}{\beta\pi W_{eq}}\frac{\left(n_S^2 + n_C^2\right)}{n_F^2}\times \int_{-k_0 n_C}^{k_0 n_C}\frac{r_C r_S^2}{(\beta-\beta_r)^2 + 1/B^2}\times\left[\frac{\cos^2(sW_{FC})}{r_S^2\left\{r_C^2\cos^2(sW_{FC}) + s^2\sin^2(sW_{FC})\right\} + r_C^2\left\{r_S^2\cos^2(sW_{FS}) + s^2\sin^2(sW_{FS})\right\}} + \frac{\sin^2(sW_{FC})}{r_S^2\left\{r_C^2\sin^2(sW_{FC}) + s^2\cos^2(sW_{FC})\right\} + r_C^2\left\{r_S^2\sin^2(sW_{FS}) + s^2\cos^2(sW_{FS})\right\}}\right]d\beta_r \tag{8.1}$$

calculates the proportion of propagated light that is scattered from the surface of a planar waveguide.

The formula involves integration over the range of radiation modes i.e. $[-k_0n_C, k_0n_C]$. It is obvious, considering Figure 8.3, that this range of constants is equivalent to the range of angles at which the light is scattered.

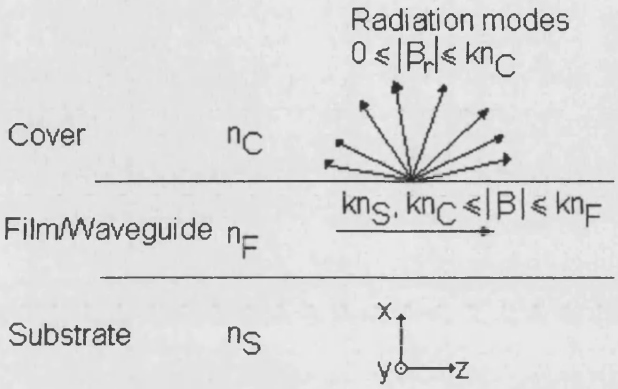

***Figure 8.3**: Radiation modes of an asymmetrical planar optical waveguide (Diagram adapted from Figure 1 of Walter and Houghton [9])*

The integration from formula (8.1) was performed for a number of small steps and the contribution of each to the whole integral enabled a profile of the scattered light to be determined. Figure 8.4 illustrates the normalised values of the integral function and the resulting profile of the scattered light, which shows that the majority of the light is scattered forward with a peak at approximately 20°.

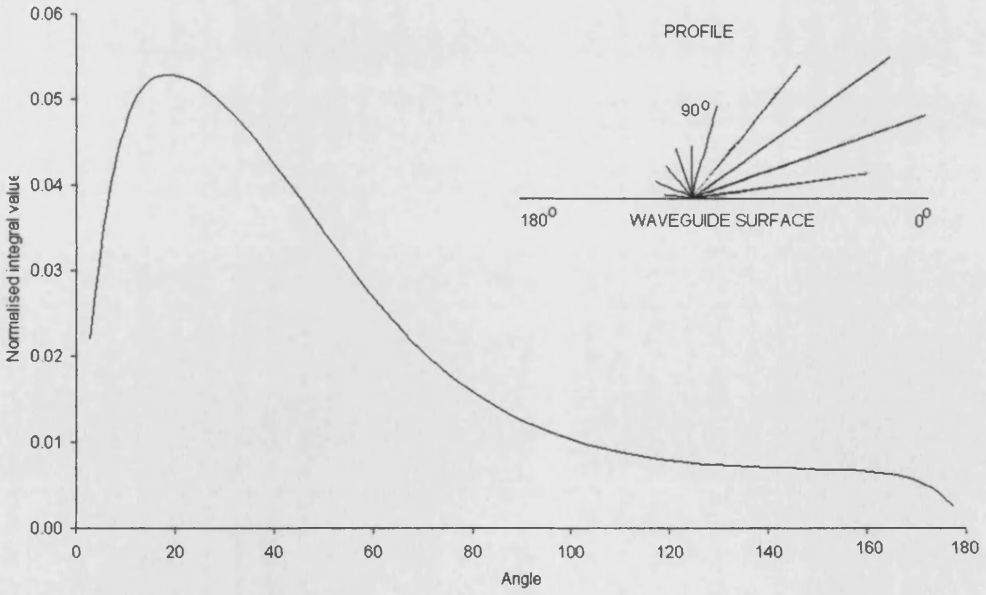

***Figure 8.4**: Normalised value of the integral of equation (8.1) as a function of angle of scatter. Profile of the light scattered at the waveguide surface where the length of line indicates the percentage of light scattered in the corresponding direction.*

In the capillary fill device any light within the cell that has not been absorbed by a fluorophore may reflect from the upper surface and potentially excite further unwanted fluorescence (Figure 8.5). An observation length of 1mm is used to limit the amount of fluorescence detected and thus limit the impact of reflected light on the signal. The profile of the scattered light determined using the model indicates that the peak of the scattered light occurs at 20°. Considering the geometry of the cell it can be determined that at this angle the scattered light will be reflected 0.3 mm (100μm/tan 20°) beyond the point of scattering and thus may contribute to the detected signal in an observation length of 1 mm. Such analysis, that is determination of the amount of reflected light and its impact on the output fluorescence, is virtually impossible to do experimentally and yet calculating the amount of scattered light that may be reflected within the observation length has obvious consequences for the physical design of the sensor.

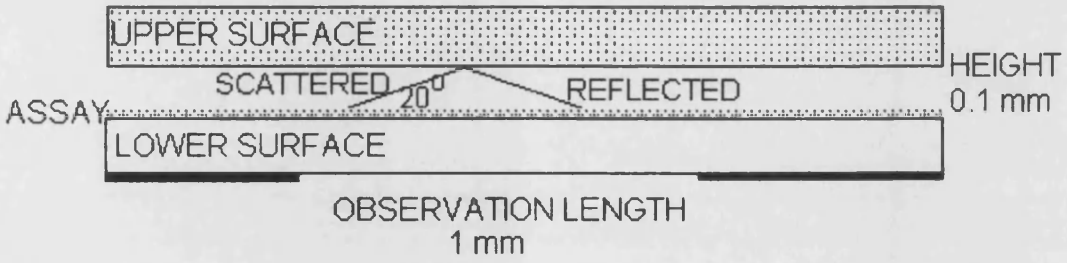

***Figure 8.5**: Scale drawing of capillary fill cell illustrating the reflection of scattered light at the upper surface and the observation length used to limit unwanted fluorescence being detected.*

8.3.3 Constitution of resulting fluorescence

The fluorescence excited and detected at the output of an immunosensor can arise from two sources, the bound labelled molecule near the surface of the waveguide and any unbound labelled molecules free in the solution within the capillary fill cell. Excitation can occur due to the evanescent field or due to light scattered from the waveguide surface. The output for the 10 minute sandwich assay for IgG described above (section 8.1.1) was analysed in order to determine the percentage of the fluorescence resulting from the different sources.

Table 8.3 illustrates the results of the analysis and shows that for this particular configuration (multilayer coupling) less than 0.5% of the total signal is due to fluorescence excited by scattered light but that the evanescent field is such that 2.5 % of the fluorescence results from evanescent excitation of unbound label.

Table 8.3: Analysis of the origins of the output signal from the immunosensor model involving a sandwich assay and a multilayer-coupled CFD.

Excitation source	Label	Percentage of output
Evanescent field	Bound	97.15
	Unbound	2.50
Scattered light	Bound	0.01
	Unbound	0.34

8.4 Application to a reverse symmetry waveguide

Horvath et al. [10] recently published an article detailing their analysis of a reverse symmetry waveguide, a waveguide where the refractive index of the substrate layer is lower than that of the cover layer (Figure 8.6), in which they suggested that this configuration would have a potential application as a biosensor. They demonstrated that the change in refractive index that could be detected in the cover layer of a reverse symmetry waveguide was superior to that that can be detected in the cover layer of a normal waveguide, i.e. one in which the refractive index of the cover is greater than that of the substrate.

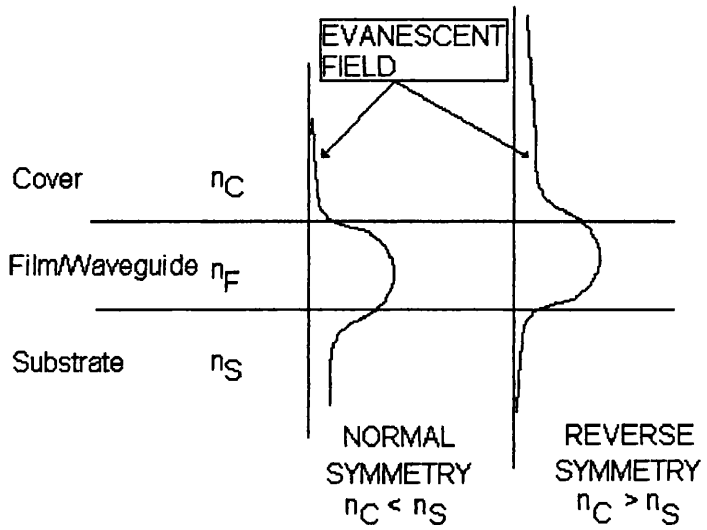

Figure 8.6: *Evanescent field profile in normal and reverse symmetry waveguides*

8.4.1 Application of the model

Although Horvath et al did not consider fluorescence evanescent field sensors they suggest sensors as one of the applications of their theory and the argument that the increased penetration depth of the evanescent field would be beneficial may apply to the optical immunosensors considered in this project. In order to consider the effect of a reverse symmetry waveguide the Model A - prism coupling module was used to simulate the output from a sensor in which the immunoassay is performed on the surface of a reverse symmetry waveguide (Figure 8.7).

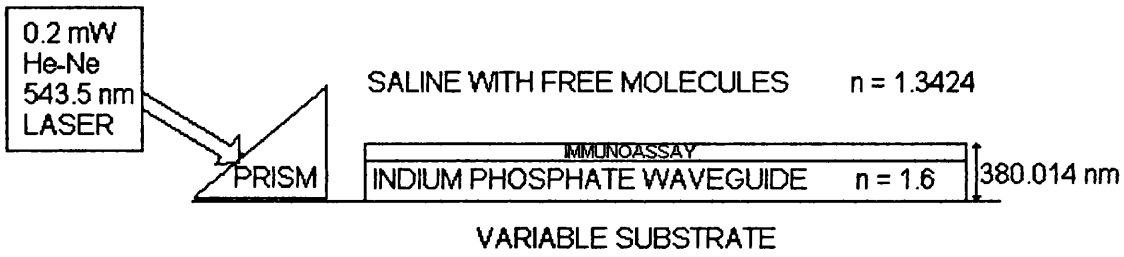

Figure 8.7: *Values used in Model A to consider reverse symmetry waveguides.*

The film was an indium phosphate waveguide with a layer of immobilised antibody on the surface, which had a thickness of 380.014 nm (being the deposited thickness, 380 nm, plus the adjustment due to Tiefenthaler & Lukosz [11] for a four-layer sensor i.e. equation (5.4)). The thin film waveguide had a refractive index of 1.6 [12].

The cover was a saline solution containing the analyte and the labelled antibody with a refractive index of 1.3424 calculated using the Clausius-Mossotti formula [13] for refractive indices of compounds. The immunoassay was a sandwich assay for IgG as described above. The light source was a 0.2 mW Helium-Neon laser of wavelength 543.5 nm coupled into the waveguide by means of a prism, with an assumed coupling efficiency of 0.81, this being the maximum coupling efficiency achievable using a prism [14]. The width of the waveguide was 0.4 m and the observation length for resulting fluorescence was 1 mm.

Figure 8.8 shows the output from the immunosensor where the waveguide substrate is either air, a low refractive index polymer or glass and demonstrates that the reverse symmetry waveguide would indeed enhance the signal. However, the corresponding sensitivities (Table 8.4) are of a similar order, indicating that the noise within the signal is also enhanced by use of the reverse symmetry waveguide.

Table 8.4 Waveguide substrates and the sensitivity achieved using these configurations within the prism coupling model.

Substrate		Refractive index	Sensitivity
Glass	(Normal symmetry)	1.5	7.71×10^{-11} M
Polymer	(Reverse symmetry)	1.2	8.27×10^{-11} M
Air	(Reverse symmetry)	1.0	8.43×10^{-11} M

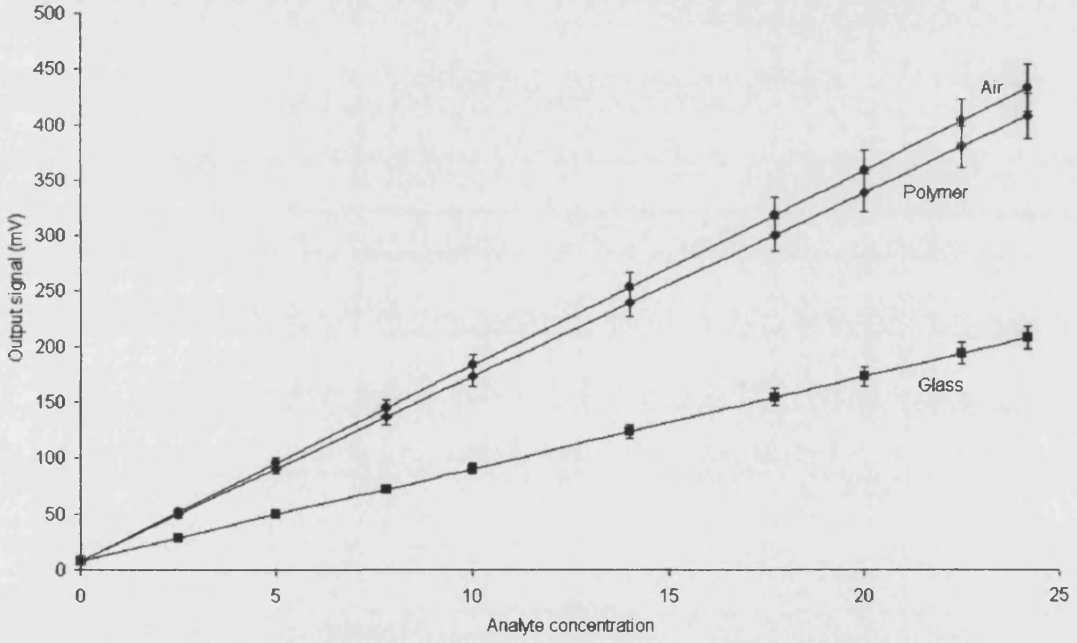

Figure 8.8: *Output voltage determined using the model of a prism coupled immunosensor for a waveguide with different substrates Air (■) Polymer (♦) Glass (●)*

It is possible that a reverse symmetry waveguide may produce a more sensitive device in the context of the larger scale gas sensor. However the application of the detailed model presented in this project showed that this was not necessarily the case for biosensors, thus demonstrating one of the potential pitfalls of extrapolating from chemical sensing to biosensing without thorough investigation.

References

[1] Baird CL & Myszka DG, Current and emerging commercial optical biosensors, *Journal of Molecular Recognition*, **14**, 261-268, 2001.

[2] Yalow RS & Berson SA, Assay of plasma insulin in human subjects by immunological methods, *Nature*, **184**, 1648-1649, 1959.

[3] Edwards R, Radiolabelled immunoassay In *Principles and Practice of Immunoassay* Eds Price CP & Newman DJ, (NY: Stockton Press) pp 265 - 294, 1991.

[4] Davies C, Introduction to Immunoassay Principles in *The Immunoassay Handbook*, Wild D (Ed) (London UK: Nature Publishing Group) pp 3 – 40, 2001.

[5] Ekins R, Immunoassay design and optimisation In *Principles and Practice of Immunoassay* Eds Price CP & Newman DJ, (NY: Stockton Press) pp 96-153, 1991.

[6] Robinson GA, Optical immunosensing systems – meeting the market needs, *Biosensors & Bioelectronics*, **6**, 183 – 191, 1991.

[7] Ligler FS, Breimer M, Golden JP, Nivens DA, Dodson JP, Green TM, Haders DP & Sadik OA, Integrating Waveguide Biosensor, *Anal. Chem.*, **74**, 713-719, 2002.

[8] Sloper AN & Flanagan MT, Scattering in planar surface waveguide immunosensors, *Sensors and Actuators*, **B11**, 537 – 542, 1993.

[9] Walter DJ & Houghton J, Attenuation in thin film optical waveguides due to roughness-induced mode coupling, *Thin Solid Films*, **52**, 461 – 476, 1978.

[10] Horvath R, Lindvold LR & Larsen NB, Reverse symmetry waveguides: theory and fabrication, *Applied Physics B*, **74**, 383 – 393, 2002.

[11] Tiefenthaler K & Lukosz W, Sensitivity of grating couplers as integrated-optical chemical sensors, *J. Optical Society of America B*, **6**, 209 – 220, 1989.

[12] Sloper AN & Flanagan MT, Metal phosphate planar waveguides for biosensors, *Applied Optics*, **33**, 4230 – 4240, 1994.

[13] The Clausius-Mossotti relation, Available via the World Wide Web at http://farside.ph.utexas.edu/teaching/jk1/lectures/node43.html

[14] Lee DL, Electromagnetic principles of integrated optics, (New York: John Wiley & Sons, Inc.), pp 42 – 47, 1986.

Chapter 9

Application of the model as a design tool

Early computer models of biosensors received only limited application, which Ekins [1] ascribed to the experimentalists reluctance to dissect their assay systems in order to identify the sources of error. However the author of this thesis would suggest that the increase in computing power over the last decade has significantly facilitated the development of this project and that lack of computing power was a major deterrent to early modelling.

The implementation of the model presented here provides the facility to perform a number of evaluations of the immunosensor being modelled, such as comparison of protocols, optimisation and data analysis, which would be beneficial to research and thus feature in a design tool for biosensors. This chapter outlines the application of these features and demonstrates their benefit to a biosensor design strategy. The use of the model in this fashion would allow a designer to identify key experiments and thus eliminate some of the routine experimental work involved in biosensor development.

9.1 Comparison of different protocols

The model was developed to enable the comparison of different protocols within the immunosensor system. The modular nature of the model allows one component of the model to be replaced with another variant of the same component, and the difference in resulting output and sensitivity to be compared. Experimentally such comparison is difficult to achieve. Between sensor noise, discussed in Chapter 7, means that it is virtually impossible to guarantee that any differences observed between two instances of a sensor result only from a single changed component.

Figure 9.1 illustrates the modules within the model and lists some of the possible variants for each module. Not all of the variants listed have been modelled but a complete design tool would allow any combination of protocols to be simulated and compared.

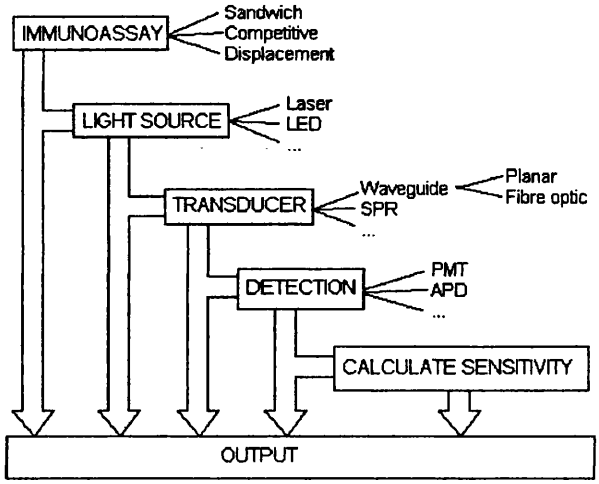

Figure 9.1: *(Repeat of Figure 3.3) The blocks denote each module representing a component of the sensor, with the module variants listed to the right.*

9.1.1 Assay protocols

The assay protocol employed within a sensor is a critical design factor, and as such was discussed at length in chapter 8. Comparisons of a competitive and a sandwich assay were made at both equilibrium and during the transient phase of the assay and the sandwich assay proved superior in both instances.

9.1.2 Coupling techniques

In biosensors, components other than the immunoassay may play a significant role in decreasing the sensitivity of the device and therefore become important considerations. Coupling of light becomes an issue in many applications of optics [2]. In an optical immunosensor coupling of light plays a major role in producing a detectable output signal that can be used to determine the amount of analyte in a sample. In any particular arrangement the design involves compromises between the amount of light that is coupled into the system and the practicality of the arrangement.

Development of the capillary fill device (CFD) on which the model is based involved a progression of techniques that refined the coupling of light to produce the most viable arrangement. Initially the CFD developed by Professor Shanks at Unilever used the lower glass surface as a collecting waveguide rather than an exciting waveguide. The cell was flood illuminated from below (Figure 9.3a). Emission close to the lower surface, i.e. within what would be the evanescent field of a wave guided in a multimode planar waveguide, will according to reciprocity be coupled into the waveguide provided emission is at the appropriate angle. Thus a small amount of the fluorescence emitted is coupled into the lower glass surface and the possibility of using a slit to distinguish between this and any stray light that has become coupled into the waveguide was explored.

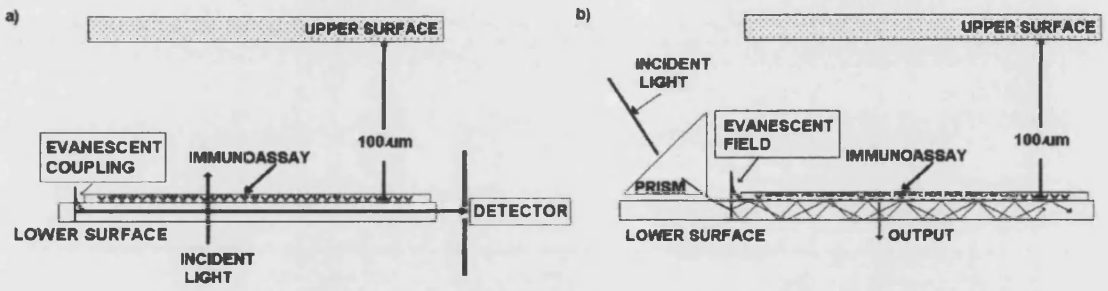

***Figure 9.3**: Initial arrangement of capillary fill device*
a) Light shone into cell and resulting fluorescence coupled into lower glass surface
b) Light coupled into lower glass surface and resulting fluorescence excited by evanescent field

Upon acquisition of the CFD patent Sereno approached the UCL group with a view to adapting the technique to include coupling via a prism into the lower glass surface of the cell (Figure 9.3b). Fluorescence was then excited by the resulting evanescent field [3], thus eliminating a percentage of the unwanted signal. However the width of the lower glass surface of the cell produced multimode coupling of the light and the resulting fluorescence was weak.

Flanagan with the support of Sereno examined alternative techniques in part use of the lower surface to produce evanescent excitation. At this point the method of depositing a thin film waveguide onto the lower surface was developed [4]. Coupling into this waveguide, whilst more difficult to achieve, produced a single propagation mode which resulted in a stronger evanescent field and greater output signal.

The compromise between the ease of coupling light into the sensor and the overall design is not restricted to the capillary fill device. It is a design consideration for any optical immunosensor. Sensors with the immunoassay element immobilised on an adiabatically tapered optical fibres [5] have attempted to address the issue of coupling. This design allows easy coupling from the multimode fibre into the tapered region which supports only a single mode of propagating light. However, the resulting sensor is extremely fragile and once again a compromise has been made between sensor design and the coupling of light into the sensor.

In considering the arrangement in Figure 9.3b Flanagan has examined both grating coupling [4] and base plate coupling as alternatives to the prism coupling shown. It is clear that coupling is a major design issue in any optical immunosensor. Thus a biosensor design tool would need to allow the simulation and comparison of different coupling arrangements.

9.1.2.1 Application of the model to the comparison of coupling protocols

The light component of the model deals with the coupling and propagation of light into the system. Two different experimental arrangements were modelled (Figure 9.4); Model A involving prism coupling and Model B involving the multilayer coupling technique devised by Pampapathi [6]. This enabled a direct comparison between these two coupling techniques to be made.

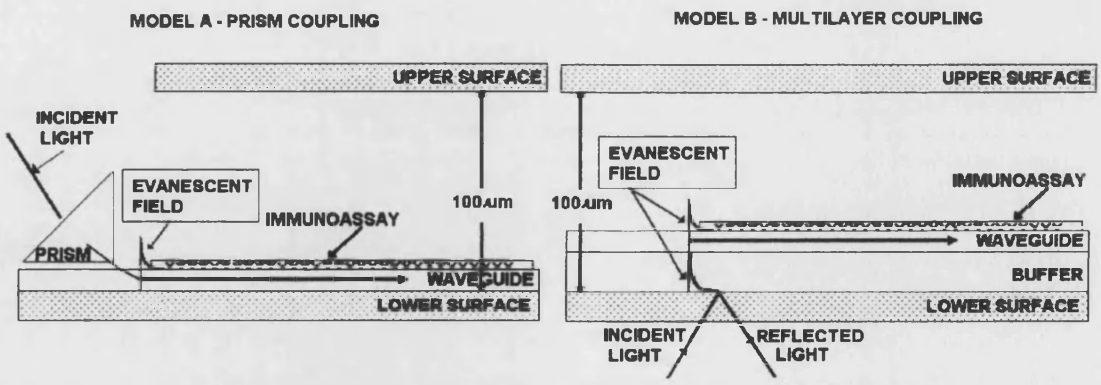

***Figure 9.4**: Two arrangements for coupling of light into the waveguide*
Model A - Light is coupled into the waveguide using a prism
Model B - Light is coupled through multiple layers c.f. resonant mirror

The concentrations resulting from the sandwich assay for IgG described in section 8.1.1 were used within both a Model A and a Model B arrangement with exciting light provided by a 5 mW Helium-Neon laser of wavelength 632.8 nm, a waveguide width of .0 4 m and an observation length for resulting fluorescence of 1 mm. Figure 9.5 shows the calibration curves produced for the sandwich assay using these two different arrangements. The straight line produced for Model A, the prism coupling model is due to the fact that this model does not perform an angle scan to establish the best coupling, a reflection of the difficulty of performing such a scan experimentally for a prism coupled sensor. The less pronounced curve for Model B (the multilayer coupling) than those seen in Chapter 8, is due to the fact that the angle of incidence of the exciting light was fixed; as would be the case in a portable sensor; and thus the output will not have been at resonance for all of the readings.

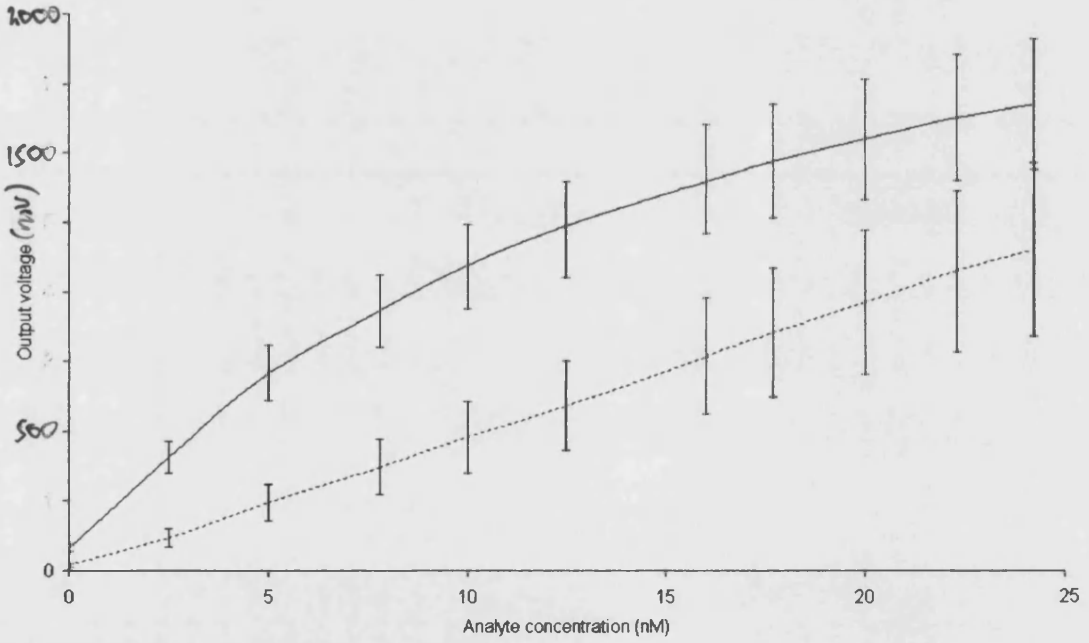

***Figure 9.5**: Calibration curves for a sandwich immunoassay for IgG placed into two different immunosensor system models. Model A (dashed line) involves coupling using a prism whilst Model B (smooth line) involves coupling through a thin film multilayer.*

The calculated sensitivities (Table 9.1) demonstrate that changing the coupling technique did not produce a significant change in the sensitivity of the device. This application of the model was a genuine use of the model as a design tool. The multilayer coupling technique was devised as an adaptation of prism coupling that would be easier to achieve using external instrumentation. Coupling with a prism involves evanescent coupling through the very thin layer of air between the prism and the waveguide and consequently requires the angle of incidence to be highly accurate [2]. In the multilayer coupling into the waveguide also occurs evanescently, through the buffer layer, but is not so dependent on the angle of incidence. Theoretically it was impossible to determine whether this ease of coupling reduced the sensitivity of the resulting device and between sensor noise issues meant experimental comparison was invalid. Thus the model provided the only accurate means of making this assessment.

Table 9.1: Sensitivities of a sandwich assay calculated using different experimental arrangements of the light propagation module

Model	Sensitivity
A Prism coupling	26.9 pM
B Multilayer coupling	15.9 pM

9.2 Optimisation of an immunosensor

The model presented provides the ideal vehicle for the optimisation of immunosensor performance. A single parameter can be varied, whilst the remainder of the system remains identical – a situation that is difficult to achieve experimentally. Thus the effect on sensitivity of a single parameter can be studied and used to optimise the performance of the sensor.

9.2.1 Amount of labelled complex

Ekins applied his modelling to the optimisation of biosensors and in particular the immunoassay element. He used his experimental data to produce precision profiles that could be used to identify the optimal characteristics of an immunoassay. This approach was adopted by the few practitioners that considered modelling an asset in the development of immunoassays [7].

Ekins determined that the amount of labelled complex used within an immunoassay effects the resulting sensitivity to such an extent that he used the terms 'excess reagent' and 'limited reagent' assays to categorise types of immunoassay. The model was used to consider the optimisation of an immunoassay with reference to the amount of labelled molecule, exemplified for the competitive assay for IgG with initial concentrations

$$[c]_0 = 30.9 \times 10^{-9}\ M$$

and association constants

$$\text{capture} - \text{analyte}\ \ K_C = 5.67 \times 10^{9}\ M^{-1}$$

$$\text{capture} - \text{labelled analyte}\ \ K_L = 2.63 \times 10^{8}\ M^{-1}.$$

The modified Markov method was used to determine the resulting concentrations for an elapsed time of 10 minutes from addition of sample for a range of initial analyte concentrations. These values were then used to determine the output voltage assuming that the assay was being performed within a CFD with multilayer coupling (layers and thicknesses previously described in Table 8.1). The exciting light was a 5 mW Helium-Neon laser of wavelength 632.8 nm. The width of the waveguide was 0.4 m and the observation length for resulting fluorescence was 1 mm.

In a competitive assay the labelled analyte competes with the unknown quantity of analyte for the binding sites on the capture antibody surface. If the amount of unbound labelled analyte is too small the output signal will reach a maximum value and no longer indicate the amount of analyte present. However, if the amount is too large the labelled analyte will dominate the competitive reaction and the output signal may not be proportional to the amount of analyte present.

The model was used to calculate the sensitivity resulting from a range of initial labelled analyte concentrations with a view to finding the optimum concentration for the assay concerned. Figure 9.6 illustrates the results and shows that for this particular assay the optimum concentration of labelled analyte is approximately 40 nM.

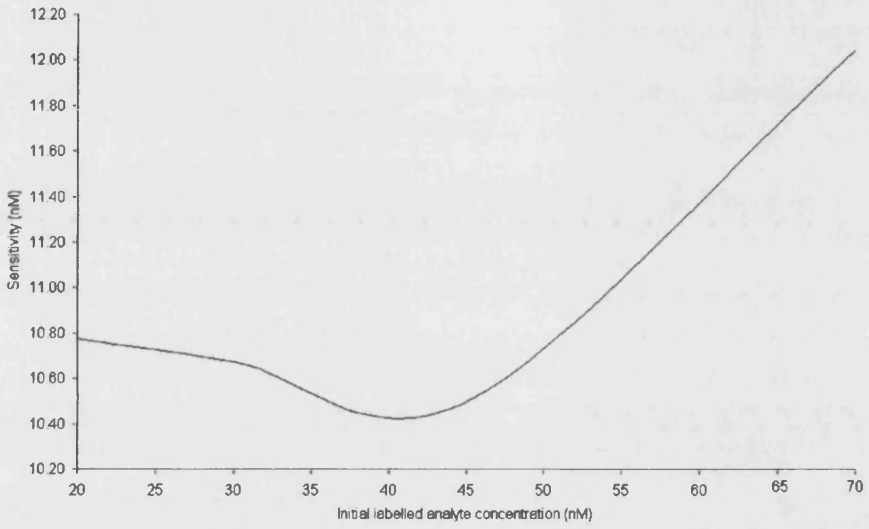

***Figure 9.6**: Sensitivity of an immunosensor containing a competitive assay for IgG as a function of the amount of initial labelled analyte within the immunoassay.*

Figure 9.7 shows the precision profiles, corresponding to those employed by Ekins, produced using the data obtained from the model illustrating the result determined using the Figure 9.6, i.e. that a 40 nM initial concentration of labelled analyte produces the optimal assay.

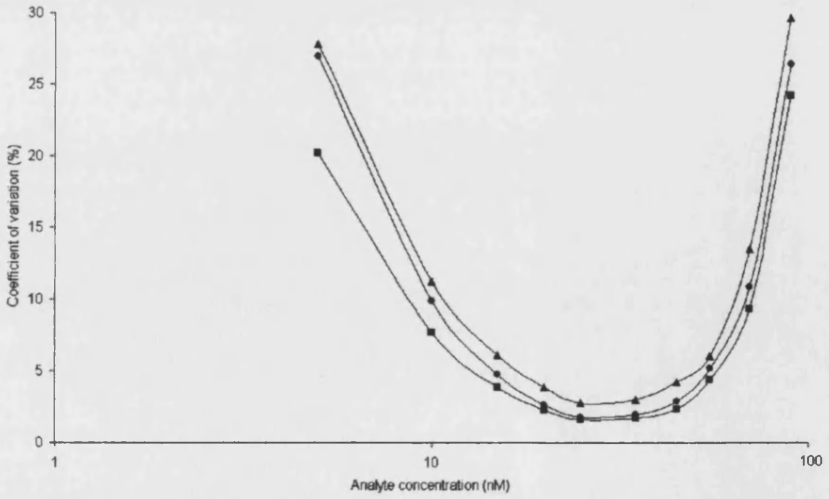

***Figure 9.7**: Precision profiles following Ekins determined using the model for the competitive assay for IgG with initial concentration of labelled analyte 20 nM (●), 40 nM (■) and 70 nM (▲).*

It should be noted that each data point on Ekins profiles was the result of a large number of repetitions of each experiments, repetitions intended to eliminate the effect of any variations not under consideration. The model presented in this thesis can be used as a faster means of identifying optimal values for many of the parameters involved and thus establish guidelines for subsequent experimental investigation.

9.2.2 Dynode voltage of the PMT

Most applications in opto-electronics use avalanche photodiodes or semiconductor detection devices. Nevertheless, the progressive miniaturisation of the PMT [8] and the low light levels emitted by the fluorophores mean that the PMT is still a serious contender for the detection element of a biosensor. However, an immunosensor that is to be used on location may not have the stable high voltage power supply available in a laboratory environment. The multilayer coupled sensor containing a sandwich assay for hCG as previously described was used to investigate the effect of reducing the dynode voltage of the PMT. Figure 9.8 shows that there is little effect on the sensitivity until below 300 V where PMT noise becomes dominant.

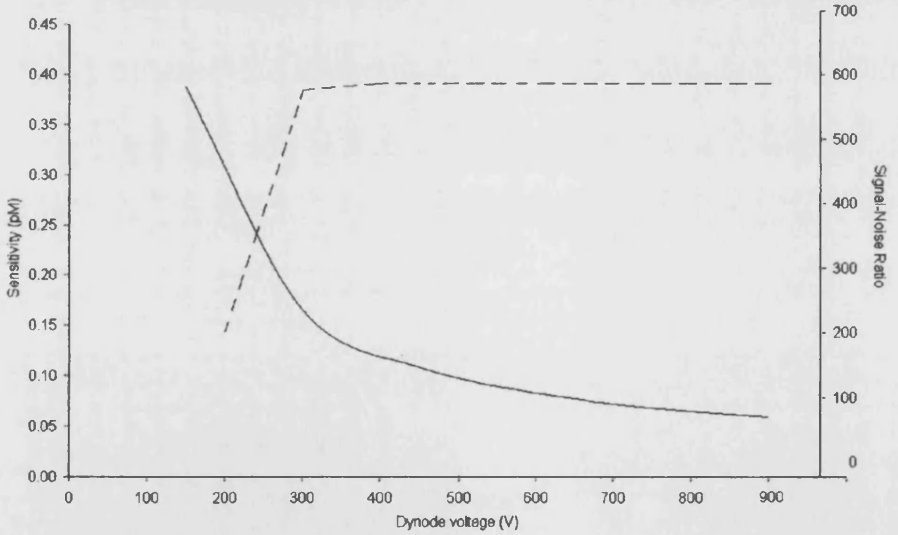

***Figure 9.8**: The sensitivity of a multilayer coupled immunosensor containing a sandwich assay for hCG as a function of the dynode voltage of the PMT used to detect the fluorescence (smooth line) with the signal to noise ratio of the PMT (dashed line).*

The output signal and noise current resulting from the photomultiplier were calculated according to equation (6.6), i.e.

$$\overline{i_S^2} = Ge^2(P_F + P_B)^2$$

and

$$\overline{i_N^2} = 2\Gamma Ge^2 B(P_F + P_B) + 2\Gamma GeBi_d + \frac{4k_B TB}{R}$$

where variables are defined in Section 6.2.1. The signal to noise ratio for the PMT is thus

$$\left(\frac{S}{N}\right) = \frac{\overline{i_s^2}}{\overline{i_n^2}}$$

which was calculated as a function of dynode voltage and superimposed on Figure 9.8, confirming that below 300 V noise dominates the PMT. However, as dynode voltage increases beyond this point the signal to noise ratio remains constant whereas the sensor become gradually more sensitive, indicating that the dynode voltage alone cannot be used to optimise an immunosensor; as would be expected given the multiple noise sources within the system.

9.3 Data Analysis

Sensitivity, that is the lowest detectable concentration of an analyte distinguishable from measurements made with no analyte present, is of prime importance in determining the viability of a biosensor, as limited sensitivity has been a major block to the commercialisation of many biosensor applications. A design tool should allow the calculation of sensitivity in addition to the analysis of the key aspects of the simulated sensor determining that sensitivity. The modular nature of the model presented allows data from any part of the model to be analysed independently. This facilitates the comparison of different protocols, not only in terms of the sensitivity of the resulting device, but also in terms of the sources of noise contributing to the resulting sensitivity.

Chapter 7 presented an analysis of noise within an immunosensor and employed a variety of visualisation techniques to illustrate the results; line graphs, 2D "nets", bar charts and pie charts. Each technique was chosen as the appropriate means to

accurately represent the data involved. However, in a design tool, there are applications in which the user may not be sufficiently familiar with a particular protocol to be concerned with accurately determined values but need a means of easily identifying problematic areas. After consideration of the data and different visualisation techniques a means of representing the data as a series of pie charts illustrating the relative impact of noise sources was devised (Figure 9.9). This allows the user to instantly identify the major sources of noise at a particular instant.

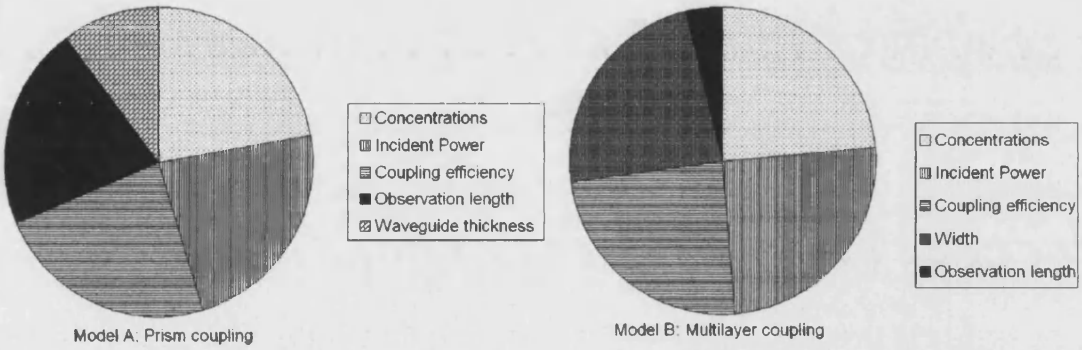

***Figure 9.9**: Relative proportions of the noise sources within the signal of the Model A (prism coupling) and Model B (multilayer coupling) immunosensor for the determination of IgG where the immunoassay has been allowed to reach equilibrium.*

Figure 9.9, representing a snapshot of an assay, illustrates the fact that impact of errors within the observation length is much more significant in Model A than in Model B. A good design tool should provide a user with the means to make such instant comparisons as well as the ability to analyse the numerical data in detail.

9.4 Summary

The application of the model to a number of features of a computer aided biosensor design tool has been demonstrated. The comparison of different protocols was illustrated using a comparison of assays and a comparison of coupling techniques. This comparison confirmed that the sandwich assay proves more sensitive than the competitive assay in a fluorescent evanescent field immunosensor. It also demonstrated that the multilayer coupling technique did not produce a significantly more sensitive device than the prism coupled device.

Ekins [1] advocated the use of modelling to facilitate the optimisation of a biosensor. Two examples, optimisation of the amount of labelled complex in a competitive assay and optimisation of the dynode voltage of the PMT within the detection element of the sensor, were illustrated here to demonstrate the range of parameters that can be optimised with ease using the model presented.

Whilst repeated experiments could have been used to both compare protocols and perform optimisation, the model was free from sources of noise that may occur between experiments and thus provided a more accurate as well as a quicker, cheaper means of doing the comparisons.

The use of the model for data analysis was considered and it has been demonstrated that the model could be used to produce data from parts of the sensor independently (Chapters 7 & 8) as well as being used to produce a measure of the sensitivity of the sensor modelled. Presentation of data as a visual means of identifying problematic areas within the model was illustrated.

It should be noted that the design of a biosensor is dictated by available instrumentation and thus the results that can be achieved are to some extent constrained by the limitations of the instrumentation chosen. The value of a design tool such as the model described here is that it can be used to perform initial comparisons and data analysis and thus provide the biosensor developer with an indication of the most productive direction in which to pursue the necessary experimental research.

References

[1] Ekins R, Immunoassay design and optimisation **In** *Principles and Practice of Immunoassay* Eds Price C. P. and Newman D. J. (NY: Stockton Press) pp 96-153, 1991.

[2] Lee DL, Electromagnetic principles of integrated optics, (New York: John Wiley & Sons, Inc.), pp 42 – 47, 1986.

[3] Robinson GA, Attridge JW, Deacon JK & Whitely SC, The fluorescent capillary fill device, *Sensors and Actuators*, **B11**, 235-238, 1993.

[4] Sloper AN & Flanagan MT, Metal phosphate planar waveguides for biosensors, *Applied Optics*, **33**, 4230 – 4240, 1994.

[5] Ogert RA, Brown, JE, Singh SR, Shriver-Lake LC & Ligler FS, Detection of Clostridium botulinum toxin A using a fiber optic-based biosensor, *Analytical Biochemistry,* **205**, 306-312, 1992.

[6] Pampapathi VKM, *PhD Thesis University of London*, pp30 – 32, 1994.

[7] Baker TS, Abbott SR, Daniel SG & Wright JF, Immunoradiometric assays **In** *Alternate Immunoassays* (Ed) Collins WP (UK: Chichester, John Wiley & Sons) pp 59 – 76, 1985.

[8] Hamamatsu, *Photomultiplier Tubes Construction and Operating Characteristics*, Available via the World Wide Web at http://www.hpk.co.jp/Eng/products/etd/pmte/pmte.htm.

Chapter 10

Application of the model to the investigation of the effect of a humectant layer

10.1 Humectant layer

The humectant layer is a layer deposited over the immobilised capture antibody in order to preserve it. Once the solution containing the analyte has been added the humectant dissolves, leaving the capture antibody available for binding. Several materials have been used as humectants. Protein sugar combinations were once common, for example, sucrose-casein. More recently it has been found that single sugars, e.g. trehalose or sucrose, are just as effective. Trehalose now appears to be the most effective. However, as the experimental data used to verify the model produced here was generated using an immunoassay with sucrose as the humectant, the initial modelling has considered the effective of a sucrose humectant layer.

The impact of the humectant layer on the sensitivity of the device is a matter of some debate. The sucrose layer dissolves in approximately 13 seconds (Figure 10.1 reproduced from Section 4.5.3.1) but it has been reported that the presence of a humectant layer can cause perturbations during and in some cases beyond the first minute of the assay [1]. This may indicate that the dissolution model is too simplistic or that the early masking of the surface has a prolonged effect on the kinetics.

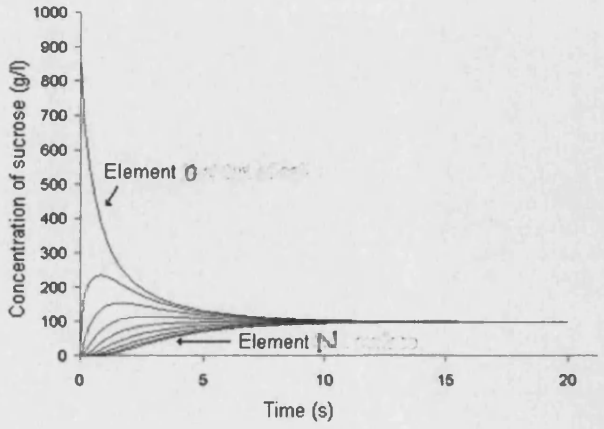

Figure 10.1: *(Repeat of Figure 4.15) Diffusion of the humectant through the capillary fill cell. Different lines relate to different elements within the finite element analysis.*

A humectant is necessary if a device is to have a realistic shelf life [2], but any impact on the timescale with which a result can be achieved must be resolved if the aim of a outcome within 2 minutes is to be achieved. Consequently, the model was used to produce a detailed examination of the effect of the humectant layer on the immunoassay and the sensitivity of the resulting sensor.

10.2 Effect of humectant on sensitivity

10.2.1 Application of the model

The modified Markov method was applied to the sandwich assay for hCG both with and without a humectant layer for a range of initial analyte concentrations. Other initial concentrations for the assay were

$$[c]_0 = 30.9 \times 10^{-9}\ M$$

$$[l]_0 = 250 \times 10^{-9}\ M$$

and the association constants were

capture – analyte $K_C = 2.2 \times 10^9\ M^{-1}$

analyte – labelled antibody $K_L = 4.1 \times 10^{10}\ M^{-1}$.

The output voltages were determined using the resulting concentrations assuming that the assay was being performed within a CFD with multilayer coupling (layers and thicknesses as described in Table 10.1). The exciting light was a 5 mW Helium-Neon laser of wavelength 632.8 nm. The width of the waveguide was 0.4 m and the observation length for resulting fluorescence was 1 mm.

Table 10.1: Characteristics of the multilayer coupling system.

Layer	Thickness (nm)	Refractive Index Real part	Refractive Index Imaginary part
Glass	-	1.51958	-
Buffer	750	1.44	-
FePO4 waveguide	150	1.7	-
Capture antibody	7.14	1.3428	-
Bound layer	15.47	1.34239*	0.000959*
Solution	-	1.33284*	1.45×10^{-6}*

* Values dependent on concentrations

10.2.2 Calibration curves

Figure 10.2 illustrates the resulting calibration curves for the device with and without humectant layer determined at an elapsed time of 1 minute from addition of the analyte. It is interesting to note that the assay with a humectant layer produces higher output voltages than the assay without humectant. The calculated sensitivities of 139.6 pM with the humectant layer and 171.1 pM without showed that the device without the humectant layer was slightly more sensitive, a result that is difficult to explain intuitively given that the sucrose diffuses to an equilibrium within 15 seconds from the addition of the sample.

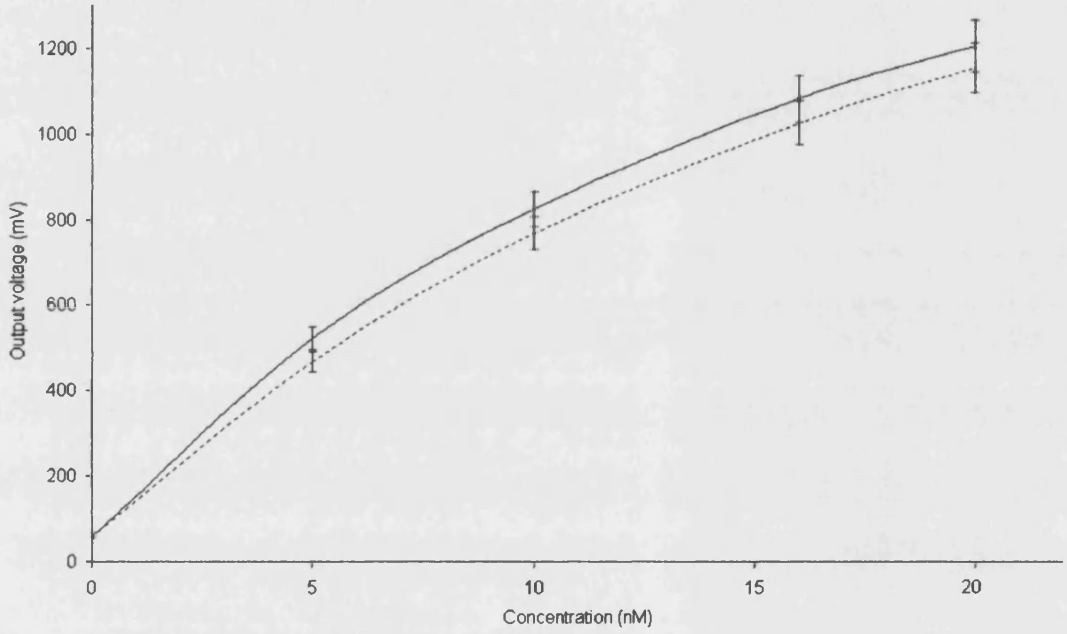

***Figure 10.2**: Calibration curves for a sandwich assay for hCG performed within a capillary fill cell with multilayer coupling produced at an elapsed time of 1 minute with a humectant layer (smooth line) and without a humectant layer (dashed line).*

10.2.3 Sensitivity

The sensitivity of the device with and without humectant was calculated for very short periods of elapsed time (Table 10.2). At an elapsed time of just 15 seconds the device with the humectant layer proved more sensitive. However by 30 seconds this had changed and the device without humectant was superior, remaining more sensitive until 5 minutes where the difference in sensitivities between the device with and without humectant was no longer significant.

Table 10.2: Sensitivities of immunosensor with and without a humectant layer

Elapsed time	**Sensitivity**		
	+ humectant layer (+h)	**- humectant layer (-h)**	**Difference (+h) – (-h)**
15 seconds	289.3 pM	262.4 pM	26.9
30 seconds	216.1 pM	246.9 pM	-30.8
1 minute	139.6 pM	171.1 pM	-31.5
2 minutes	78.6 pM	93.7 pM	-15.1

Investigation of the layers above the waveguide showed that the presence of the humectant layer reduced the penetration depth of the evanescent field by less than 2 nm, not sufficient to significantly alter the resulting output voltage. The variations in the sensitivities indicated that the amount of bound label was perturbed by the addition of the humectant layer. Thus, a comparison was made between the transient response of the immunoassay reactions in the presence of a humectant layer and the response when no humectant layer was present.

10.3 Analysis of transient response

10.3.1 Bound labelled antibody

The complexity and structure of the model are such that it is possible to output data at various points within a module. Thus it was possible to consider the amount of labelled antibody that had become bound at the surface as the assay progressed for both the device with and without a humectant layer. Figure 10.3 illustrates the results and shows that the amount of label bound was greater for the device with no humectant layer in the early stages of the assay, which is consistent with what was expected. However, between approximately 1 and 4 minutes the concentration of bound label was greater for the device with a humectant layer. Subsequently the amount bound for a device with no humectant layer become dominant, reaching an equilibrium value consistent with the increased concentration of labelled antibody within the cell in absence of a humectant layer i.e. the concentration occupying the additional volume left available by this absence.

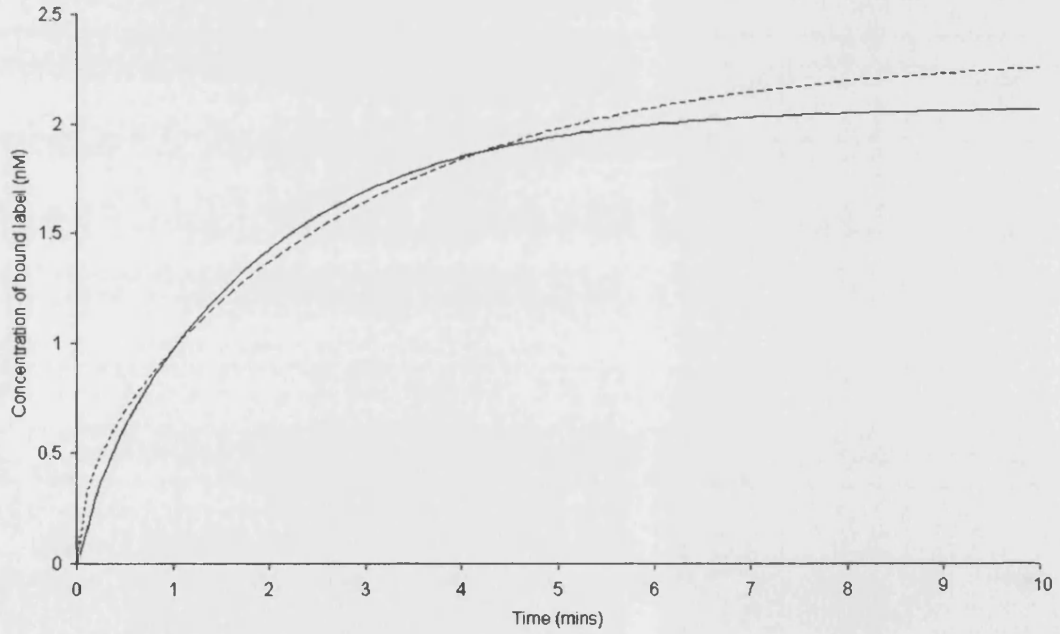

Figure 10.3: *Concentration of bound labelled antibody as a function of the elapsed time from the addition of the sample for a sandwich assay for hCG performed within a capillary fill cell with a humectant layer (smooth line) and without a humectant layer (dashed line).*

This phenomenon immediately suggests that within the complex network of reactions that occur during a sandwich immunoassay there are steps in which transiently a kinetically controlled species may appear which with time decays as the true thermodynamic equilibrium is established.

10.3.1.1 Kinetic and thermodynamic control

Kinetic and thermodynamic control are well illustrated in many organic reactions. Figure 10.4 illustrates the example of the bromination of a diene [3] with the corresponding energies for the two alternate products. This shows that at low temperatures the reaction is under kinetic control forming the products in the ratio 81:19, whilst at room temperature thermodynamic control produces 56% of the more stable form of the product.

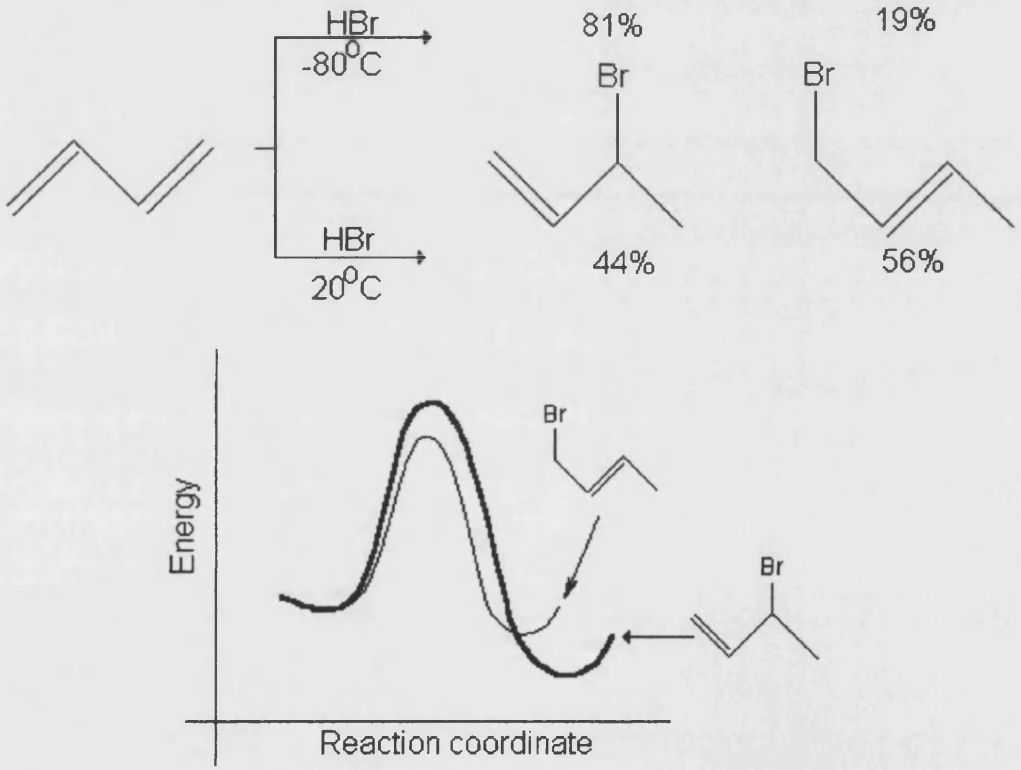

***Figure 10.4**: Distribution of products depending on temperature for the bromination of a diene with the energy diagram for the two alternatives shown*

10.3.2 Species within the sandwich assay

There are several routes to many of the species in the sandwich assay (Figure 10.5) and it is very possible that such a kinetically controlled situation may occur. The addition of the humectant will increase the viscosity of the solution and this may selectively alter the reaction rates in a similar manner to the change in temperature in the simple example above. However, the complexity of the sandwich assay, as illustrated by Figure 10.5, and the fact that the diffusing humectant will have a continuous effect on the viscosity indicate that it may not be particularly easy to identify such kinetic control steps.

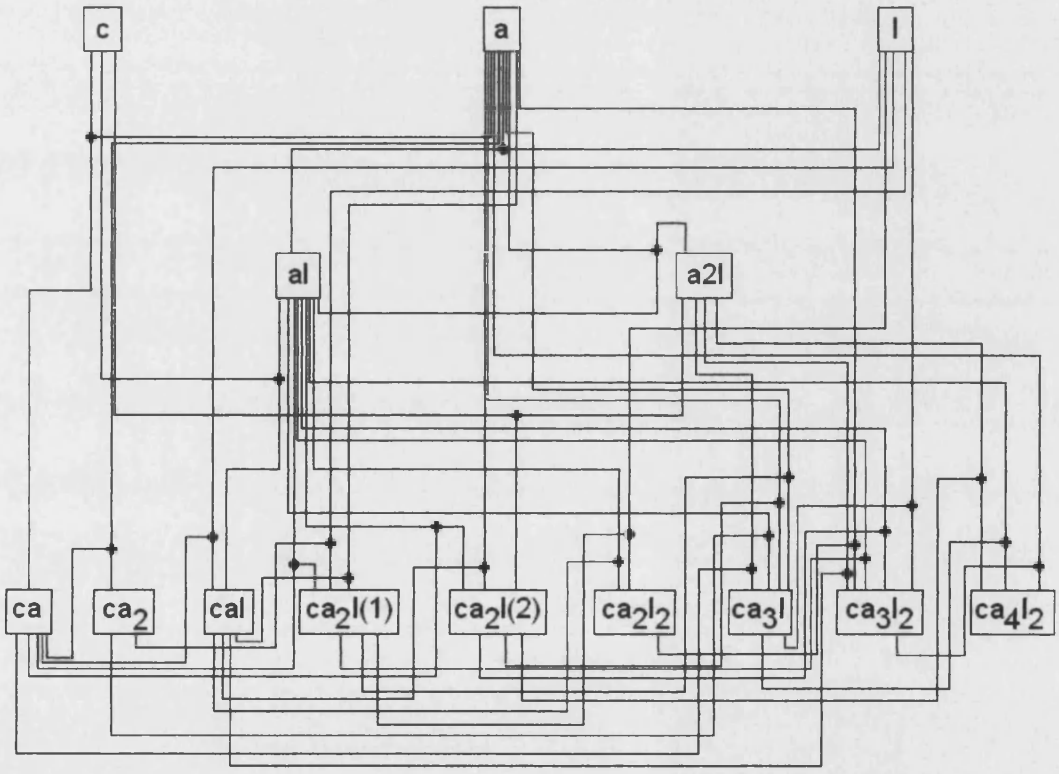

***Figure 10.5**: A network diagram illustrating the species that may occur during a sandwich assay and the possible interactions between them. All species that may occur within the sandwich assay are shown in boxes. The lines indicate reaction pathways and the nodes (dots) indicate the combination of two species.*
c – capture antibody; a – analyte; l – labelled antibody.

10.3.2.1 Initial reactions

In order to begin the analysis the initial stages of the assay were considered. Within the bulk of the solution, i.e. at a distance from the capture antibody at the surface, the reactions occurring between the analyte, a, and the labelled antibody, l, are:

$$a + l \rightleftarrows al$$

$$al + a \rightleftarrows a_2l$$

Thus within the first few seconds after addition of the sample the capture antibody, c, in the absence of a humectant layer will 'see' predominantly a and l, whilst in the presence of a humectant the first species that the capture antibody will 'see' are al and a_2l. Therefore the initial reactions occurring to bind l at the surface will be

$$c + a \rightleftarrows ca$$

$$ca + l \rightleftarrows cal$$

in the absence of a humectant layer and

$$c + al \rightleftarrows cal$$

$$c + a_2l \rightleftarrows ca_2l(2)$$

when the humectant layer is present. Consequently the build up of ca, cal and $ca_2l(2)$ in the early stages of the assay were examined and are illustrated in Figure 10.6 (overleaf). In all cases the build up is initially greater in the absence of a humectant layer, which is as expected, although the cross over to the situation where the concentration is greater when the humectant layer is present occurs at different times i.e. about 55 seconds for ca, 60 seconds for cal but only 12 seconds for $ca_2l(2)$.

The shape of the transience of each species is clearly different with and without humectant. At about 7 seconds species $ca_2l(2)$ begins to deplete when there is no humectant, however the presence of the humectant delays the beginning of the depleting reactions which then occur at a reduced rate. In both species ca and cal there is a change in the rate at about 7 seconds in the absence of humectant, suggesting that a subsequent reaction begins to affect the production of the species in this case; a reaction that is prohibited in the case when the humectant layer is present. It is therefore likely that the perturbing step is in an intermediate species.

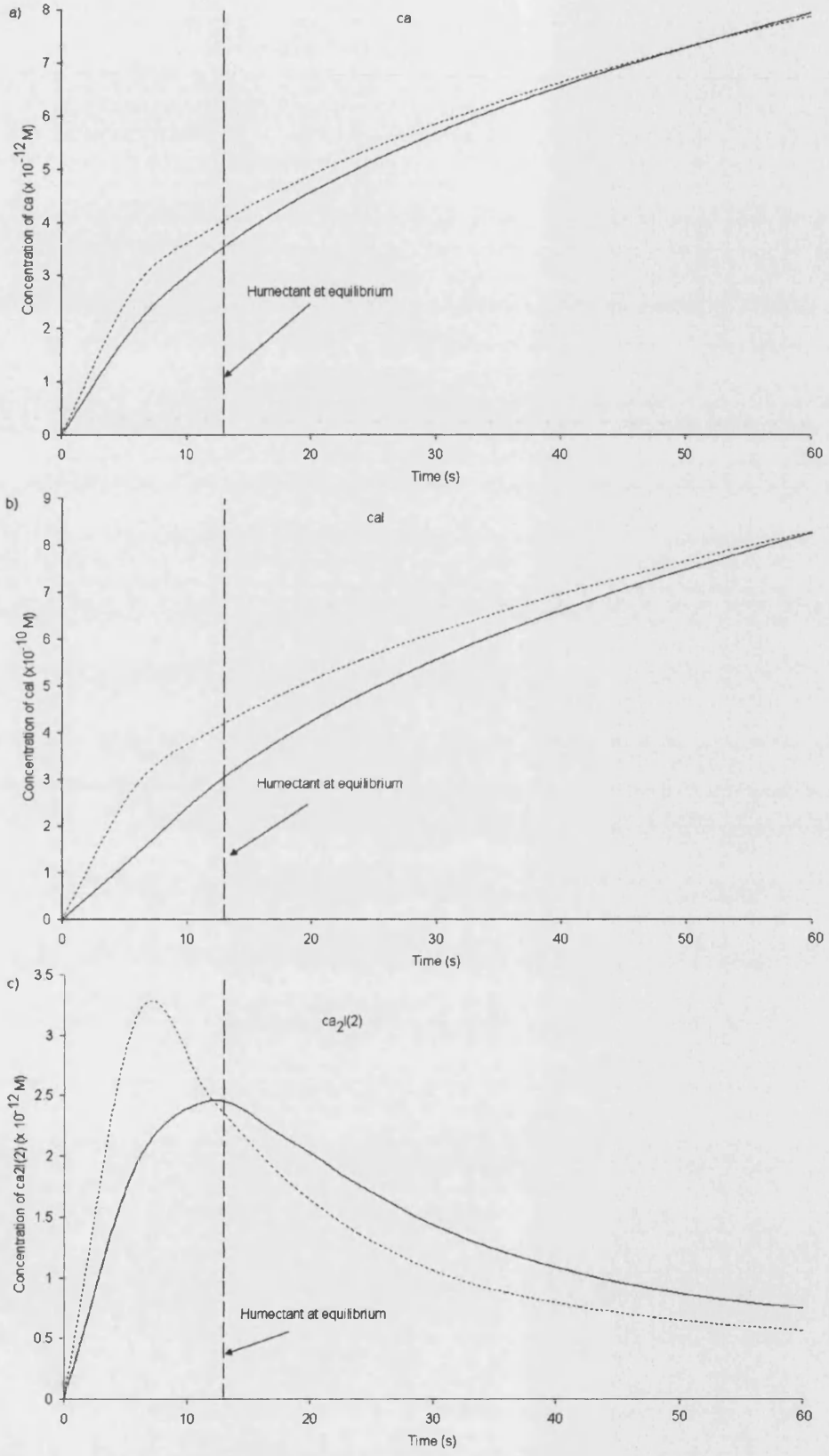

***Figure 10.6**: Concentration of species as a function of elapsed time from the addition of sample with a humectant layer (smooth line) and without a humectant layer (dashed line). a) ca b) cal c) $ca_2l(2)$*

10.3.2.2 Intermediate species

The bound label concentration consists predominantly of cal (70%) and ca_2l_2 (15%). Examination of the transient concentrations of the species that deplete cal and ca_2l_2 suggested ca_3l and ca_3l_2 as the species likely to cause the perturbation (Figure 10.7). In both cases the initial production of the species is delayed slightly by the presence of the humectant. However, the decay and subsequent reformation experienced in the absence of humectant is significantly perturbed by the presence of a humectant layer.

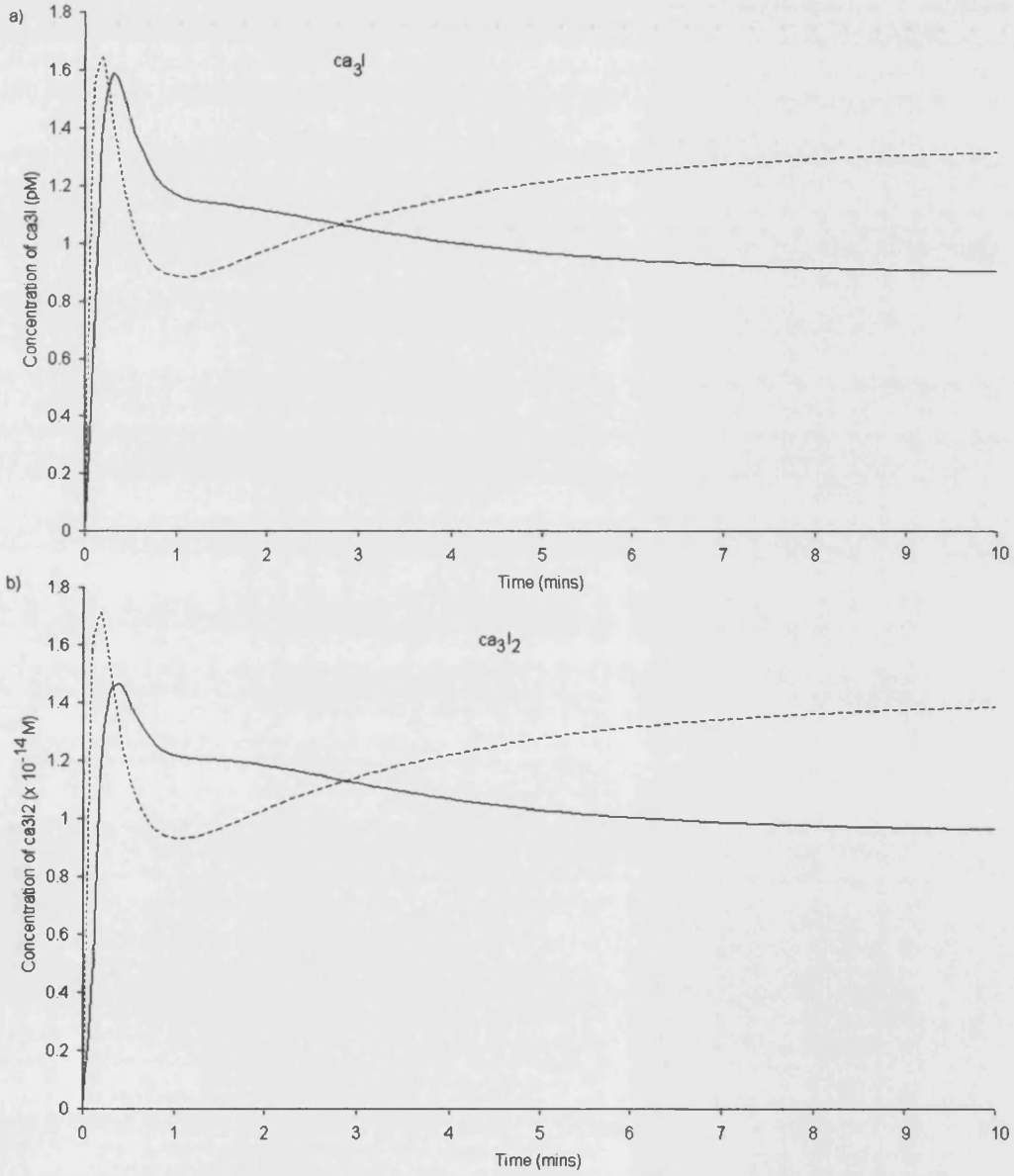

Figure 10.7: *Concentration of species as a function of elapsed time from the addition of sample with a humectant layer (smooth line) and without a humectant layer (dashed line).* *a) ca_3l* *b) ca_3l_2*

Very early work reported by Sereno & Flanagan [4] on CFD immunosensors commonly showed an overall response not dissimilar to that shown in Figure 10.7. An example of the transient response of a sandwich assay for hCG is illustrated by Figure 10.8. The major difference between these early experiments and those on which the simulation presented here is based is the fluorescent label used. In this early work the fluorescent label was XRITC, a small dye, whilst later experiments used allophycocyanin (APC), a large protein. The latter is expected to cause strong steric hindrance, as was demonstrated in the fitting of the model to experimental data described in Section 4.6. Fitting to an immunoassay for hCG determined the steric hindrance factor between the analyte and the APC labelled antibody as 1.0 i.e. total steric hindrance. A consequence of such hindrance is that the pathways that lead to the formation of ca_3l and ca_3l_2 will not be dominant. However in the case of the early work, where the label was a small dye, steric hindrance is likely to be significantly smaller and thus such pathways will play a more significant role in establishing the equilibrium of the assay.

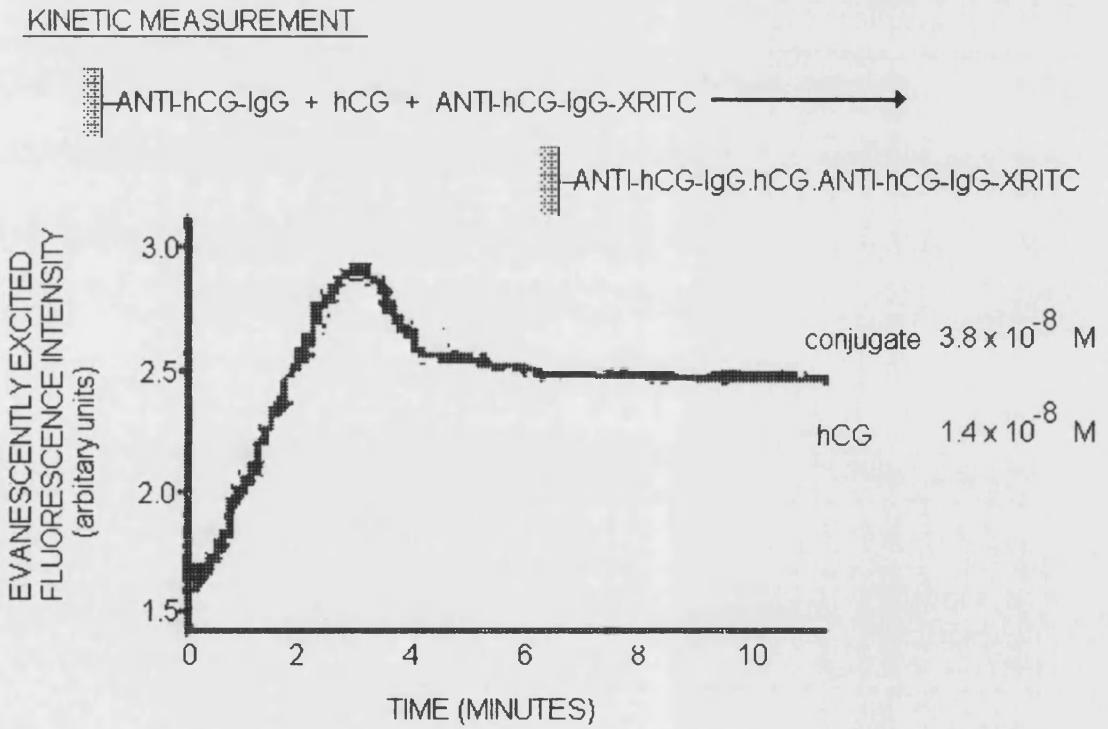

Figure 10.8: *Kinetic response for a sandwich assay for hCG (Reproduced from [4])*

10.3.3 Further analysis

The analysis performed indicates the likelihood of a kinetically controlled species contributing to the difference in the build up of the bound label on the surface between an assay with a humectant layer and one without and suggests candidate species. Such analysis, using results that cannot be produced experimentally, demonstrates the advantage of this type of modelling. However, in order to further pursue the cause of the differences shown, the model presented requires the addition of a module that will calculate the correlations between each pair of species and thus facilitate further statistical analysis.

References

[1] Private communication between GA Robinson (Sereno Diagnostics Ltd.) and MT Flanagan.

[2] Robinson GA, Optical immunosensing systems – meeting the market needs, *Biosensors & Bioelectronics*, **6**, 183 – 191, 1991.

[3] Addition of HX to Dienes, Available via the World Wide Web at http://library.tedankara.k.12.tr/carey/ch10-4-1.html

[4] Unpublished work of Deacon JK & Flanagan MT.

Chapter 11

Discussion

11.1 Biosensor design

Biosensors have only succeeded in a very narrow medical niche, i.e. blood sugar monitoring in diabetics [1]. Several factors affect the viability of biosensor design: sensitivity; reproducibility; calibration and compliance with regulatory authorities; practicality and cost of the mass production of a part disposable device and ease of use. The complexity and interplay of these factors has contributed to the lack of progress in this field. Noise within the sensor and monitoring elements, non-specific binding contributions and the reproducibility of biomolecular immobilisations all contribute to this failing. In particular, the reduction of a standard bioassay procedure to a pseudo-reagentless small sensor has often been made at the expense of the required sensitivity.

The underlying aim of this project was to develop a computer model of an evanescent field immunosensor, which could be used to study the various design criteria and analyse data generated from the model in order to facilitate the future development of biosensors. In order to achieve this aim the three main objectives of the project were defined as being

i) to model the components of an evanescent field immunosensor;
ii) to implement a full model and use it to study the sensor implemented and
iii) to demonstrate the potential of the model as a design tool.

11.2 Overview of model

11.2.1 Modules

The model was implemented as a series of modules, each representing one aspect of the sensor, i.e. immunoassay; propagation of light and detection. This allowed each component to be tested independently and provided the potential for analysis of data from within a particular element of the sensor. The modules could be linked together to

produce a model of the whole sensor. This approach greatly facilitated the comparison of different protocols within the sensor as a single module could be replaced with an alternative variant of the component, whilst the remainder of the system remained the same.

The model presented was based on the evanescent field immunosensors previously developed by the UCL group for which experimental data was available. This facilitated the testing and verification of the model.

The immunoassay module determines the concentrations of the biochemical species within the immunoassay that takes place on the surface of the waveguide within the capillary fill device (CFD). These concentrations allow the amount of the fluorophore that is bound at the surface and the amount that is free in the solution within the cell to be calculated. Two variants of the immunoassay, sandwich and competitive assay are presented.

The light module calculates the amount of fluorescence excited when laser light is incident on a CFD containing an immunoassay in which one of the species has been labelled with a fluorophore. Two different models are presented; one in which coupling into the waveguide on the lower glass surface of the CFD is achieved using traditional prism coupling and the other in which the coupling is via a series of base layers of appropriate thickness and refractive index.

The detection module converts the fluorescence output from the CFD into a detectable voltage and calculates its associated noise. The experimental system modelled focuses the output fluorescence through two filters onto the cathode of a photomultiplier tube (PMT). The current resulting from the PMT is detected as a voltage across a resistor.

11.2.2 Implementation

The modules presented can be linked together to form a complete simulation of an evanescent field immunosensor or used independently to study the particular aspect of the sensor. Prior to the commencement of this project no complete model of an

evanescent field immunosensor has been developed, although within the lifetime of this project Holt et al [2] acknowledged the potential benefit of simulation to biosensor design and produced a limited model of a continuous flow displacement immunosensor.

Several aspects of the model are based on standard well established mathematical models of the components involved. The calculation of the laser output within the Rayleigh range [3] is one such example. However, the ideal portable biosensor may not have a stable light source or collimating optics and thus the facility to study the impact of beam divergence on the sensor would be an advantage. In order to fully encompass the effect of the beam divergence, particularly on the multilayer coupling system, it was necessary to produce a profile of the incident angle and electric fields which could be used as part of an integration to determine the response of the system to an incident light beam. The inclusion of beam divergence as a variable produced a sophisticated model of the incident light that allowed the impact of beam divergence to be analysed, an analysis as yet unreported within the biosensor community.

The model for the output and associated noise from a PMT was based on Kingston's derivation [4], with a minor correction of what was considered to be a type setting error. However, investigation showed that modern materials and fabrication processes mean that the assumptions made by the Richardson-Dushman formula for the calculation of dark current are no longer valid [5] and thus the Hamamatsu quoted figure was used. Although this component of the model is quite simplistic, even the most complex of biosensor models previously reported (Holt et al [2]) neglected any modelling of the detection element of their system

The fluorescence output from the model was calculated by determining the power at the waveguide surface following either prism (Model A) or multilayer (Model B) coupling and determining the percentage reduction by any of the possible means of attenuation e.g. absorption by the bound label, absorption by the free label, scattering from the waveguide surface or absorption by the waveguide itself. The amount of light absorbed by either bound or free label was then used to determine the output fluorescence. In order to apply the standard calculation of the surface power density of a dielectric

waveguide to the sensor it was necessary to adapt the formula to take into account that the arrangement could be considered to be a four-layer system with a very thin sensing layer. Tiefenthaler & Lukosz [6] had previously considered this adaptation in the context of sensors but focussed their modelling on the resulting surface power density and did not extend their model to include other components of the sensor.

It is acknowledged that scattering at the surface of a waveguide in an evanescent field immunosensor may have an impact on the resulting sensitivity of the device [7]. However it is often neglected when considering sources of noise within an optical biosensor. Modelling the scattering of light from dielectric interfaces within waveguides is difficult. The inclusion of scattering in the model presented here involved the adaptation of the theory developed by Walter & Houghton [8] for the scattering of TE mode light from the surfaces of asymmetric monomode waveguides to produce a formula that would be applicable to the TM model light used in the experimental models on which the simulation is based. Thus, the contribution of scattered light to the fluorescence output can be calculated and the resulting impact on sensitivity of the immunosensor determined. Inclusion of scattering also facilitates the analysis of the scattered light, i.e. amount and direction, and the physical design of the sensor can be evaluated accordingly.

Ekins' [9] early modelling established that the signal to noise ratio was the dominant factor affecting the sensitivity of the device. However, the complexity and interplay of the factors that determine the output and associated noise within a biosensor are such that the model presented here is the first simulation of an immunosensor that includes the possible sources of noise; e.g. scattering of light, PMT noise; and that has been developed in a style that allows Monte Carlo procedures to be applied to different components of the model in order to establish the impact of variations in the physical parameters that define the system.

Although several authors have acknowledged the potential of modelling to immunoassay and biosensor research [2, 9, 10, 11] the tendency in any such modelling is to simplify the assay. The immunoassay module presented here represents a significant advance on any previous analysis of an immunoassay or indeed of any set of complex multiple equilibria.

11.3 Aspects of the model

11.3.1 Immunoassay

Traditionally attempts to model immunoassay reactions have been very simplistic. Initially the Scatchard plot, a method commonly used to characterise molecular binding events throughout biology [12], was used to plot the ratio of bound to unbound analyte against the bound analyte to produce a straight line from which the association constant could be determined. However, if the capture antibody is bivalent, a more complex Scatchard plot is obtained which requires non-linear regression in order to extract the value of any constants (Figure 11.1). It is clear that the complexity of the sandwich assay is such that it would be difficult to produces Scatchard plots for the assay that could be easily analysed.

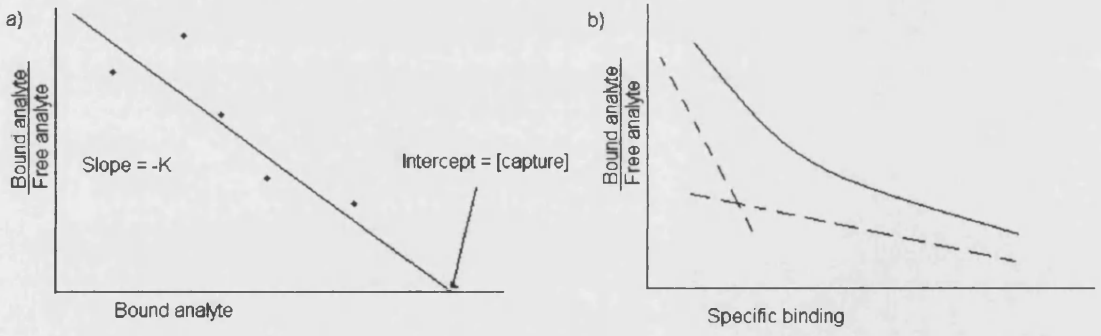

Figure 11.1: *Scatchard plots for analyte binding to an antibody*

a) Monovalent antibody

b) Bivalent antibo dy (dashed lines represent the binding for each site whilst the smooth line is the curve produced by applying the formula for the Scatchard plot)

The Sips plot developed the methodology of plotting binding data and using the resulting graphs to determine constants relating to the reactions. Figure 11.2 shows a number of variants of the Sips plot that can be again be used to calculate association constants. However, any early research with antibodies used antibodies that were polyclonal, i.e. their affinity with a particular antigen was not constant. Attempts were made to approximate this variation by formulating a distribution of the affinities of the antibody and Pauling et al [13] developed the mathematically tractable Sipsian distribution, based on the logarithmic Sips plot. This enabled an average value for the association constant and its distribution to be determined, however this is still insufficient data for a full analysis of the immunoassay.

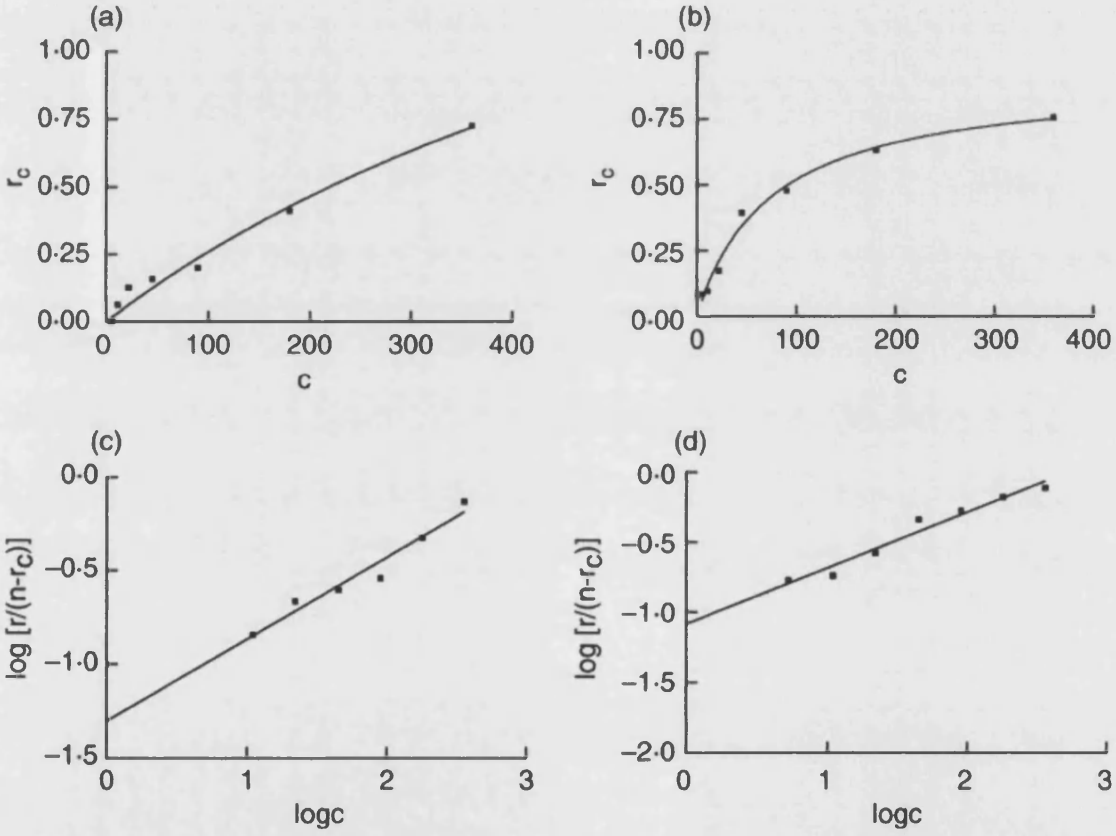

***Figure 11.2**: Sips plots for an immunoassay taken from Dougan et al [14]*
r – number of antigen binding sites
r_c – number bound antigen per antibody
c – molar concentration of free antigen
n – valency of the antibody

Other early modelling techniques that advanced the techniques illustrated above include the four parameter log-logistic (4PL) and the logit-log method [15], both of which use regression techniques to fit to the calibration curve of the immunoassay. However, these methods are fits to arbitrary functions and thus the estimated parameters cannot be related to the underlying physical constants, e.g. association constants.

Thus, the analysis potential of these methods is limited. One of the aims of this project was to model the full complexity of the immunoassay so that the model could be applied to considering issues such as the impact of variations within the immunoassay itself, the possibility of producing measurements from the immunosensor during the transient phase of the immunoassay reactions and performing a full analysis of the effect of a humectant layer on the reactions. Obviously the methods discussed above would not facilitate this level of analysis and therefore it was necessary to determine an alternative means of modelling the immunoassay.

Initial literature searching established that there were a number of computer programs available for studying multiple equilibrium amongst which were RAMESES [16], HySS [17], and ES4EC [18]. These, along with several others, were reviewed. The common feature of these models was their application to titrations, allowing the inclusion of pH as an additional variable within the set of simultaneous equations that described the reactions and the mass conservation of the system being modelled. The simultaneous equations were solved using classic regression techniques, in two cases the method of Newton Raphson, a method that was considered and discarded when applying regression techniques to the immunoassay equations due to the tendency for this procedure to become trapped within a false minimum. It is possible that the over parameterisation introduced by the inclusion of pH as an additional variable produced search pathways that were less complex. [illegible] pH is not a factor in an immunoassay.

In addition these programs solved reactions for their equilibrium concentrations, an inevitability if one is using a regression technique and thus could not easily be adapted for the more rigorous kinetic analysis required. The complexity of the examples illustrated

was minor compared with the complexity of a sandwich immunoassay and it was concluded that the systems being modelled were well conditioned and were thus suitable for regression procedures.

The initial modelling of the immunoassay presented here did follow the approaches outlined in the publications mentioned above i.e. applying optimisation techniques to the equilibrium equations describing the assay and investigating the performance of a range of classic regression procedures in addition to the "intelligent" genetic algorithm and simulated annealing techniques. Some analysis of the search surfaces produced by this approach revealed the complexity of the assay, even in two dimensions. The comparison of the different approaches implemented enabled the appropriate procedure for inclusion within an iterative calculation to be made. However, whilst optimisation was being applied to the immunoassay further investigation, with a view to modelling the transient response of the assay, was being undertaken.

The technique developed by Too et al [19] and Antia & Lee [20] for solving the chemical concentrations in continuous flow reactors provided a viable solution. Their approach was applied to the rate equations describing the assay reactions and used to produce an modified Markov chain that could be solved for the concentration values at any given time from the addition of the analyte. Thus this approach allowed both the transient and equilibrium concentrations of the immunoassay to be calculated.

It has been suggested that Markov chains could be used to solve sets of differential equations [21]. This application provides an example where a Markov chain is used to solve a set of differential equations. As part of the verification process the transient data produced by the modified Markov method was compared with that produced using a fourth order Runge-Kutta technique [22]; a standard method for solving sets of differential equations. The data from the two methods was found to be in total agreement, although the Markov approach was significantly faster in terms of computation time. Analysis of the implementation of the modified Markov approach indicated that it was essentially a zero order Runge-Kutta. It is therefore possible that the adaptive steps employed by procedures such as Runge-Kutta, which evolved to

facilitate computations, are no longer necessary given the vast improvement in computer performance over the last decades.

11.3.2 Aspects of a design tool

In order to demonstrate the potential for this type of modelling to become part of a biosensor design tool, the model was used to compare different protocols within the sensor arrangement. At the time when Ekins demonstrated the superiority of the sandwich assay over the competitive assay in radioimmunoassay [9] lack of computing power hindered the development of a totally theoretical model and his models were derived from a large number of experiments. The ease and speed with which the superiority of the sandwich assay over the competitive assay for an optical immunosensor was established highlights the advancement of computer performance over the last decades. This advancement supports the benefits of developing the type of model presented here.

The model was used to compare the two types of coupling implemented, Model A prism coupling and Model B multilayer coupling. The multilayer coupling technique had been developed experimentally as it proved easier to construct and use the instrumentation necessary. However, experimentally there was no way to determine whether this ease of coupling affected the sensitivity of the resulting device, as in any experimental work such a comparison could introduce between sensor errors that may bias the result. Using the model it was possible to demonstrate that there was no significant change in the sensitivity of the immunosensor when prism coupling was replaced with multilayer coupling, thus establishing that the ease of this method of coupling was not detrimental to the device.

It has been noted that performing repeated experiments with an immunosensor may introduce between sensor noise that biases any comparison between results and that one of the benefits of the model is that a single parameter can be changed whilst the remainder of the system remains identical. This allows the model to be used to optimise the value for any of the physical parameters that define the sensor, another potential function of a design tool.

Parameter estimation using data fitting techniques is an established means of determining values for parameters that cannot be determined experimentally. Immobilisation of the capture antibody in the immunoassay and the labelling of a second molecule can cause alterations to the value of the association constants and the steric hindrance that may occur once the assay has began. Once immobilisation or labelling has occurred it is impossible to determine the new values. The immunoassay module of the model presented encompasses the full complexity of both a competitive and a sandwich assay and thus provides the basis for parameter estimation of those values that can not be determined experimentally.

11.3.3 Aspects of biosensor development

Ideally a biosensor will produce a result in 2 minutes. Thus it will be necessary for the sensor to perform measurements before the immunoassay has reached equilibrium. The immunoassay module of the model presented allows a full analysis of the transient response of the assay from the time of the addition of sample. Thus it was possible, using the model, to determine the sensitivity of a immunosensor as a function of the elapsed time from the addition of sample and thus provide information regarding the elapsed time necessary to produce results at the required sensitivity.

Another design factor that is a cause of debate is the use of a humectant layer, deposited onto the immobilised capture antibody in order to preserve it and thus produce a device with a realistic shelf life. The model was applied to the comparison of a sensor with and without a humectant layer, producing results that could not be intuitively explained. The full complexity of the immunoassay module facilitated the preliminary analysis of the effects of the humectant layer on the build up of the different species within the assay, establishing that initially the amount of bound label was greater without a humectant layer than in the presence of a humectant but that this trend reversed for a period before being re-established. This suggested the existence of a kinetically controlled intermediate species and the analysis of the composition of the bound label, an analysis that is only possible with a full theoretical model of the immunoassay, identified two possible candidates.

11.4 Project in current context

Modelling of evanescent field immunosensors is not a well established area of research. Early computer models of biosensors received only limited application [9]. It has been suggested that this lack of exploitation of computer models is due to the fact that such models are complex, do not easily take into account common features of assays or information on assay parameters and thus do not reflect reality [11]. The potential benefit of modelling to biosensor design is beginning to be recognised and Holt et al [2] produced a model of a continuous flow displacement immunosensor that was used to optimise certain parameters. However, the immunoassay element of their model was a gross simplification of this aspect of the sensor. The model presented in this thesis has modelled an evanescent field immunosensor with a more complex analysis of the immunoassay element than any model previously published. Table 11.1 indicates both the strengths and limitations of the resulting model.

Table 11.1: Strengths and limitations of the model presented

	Strengths	**Limitations**
Immunoassay module	Equilibrium data available	Non specific binding not yet included
	Kinetic data available	Fitting to kinetic data not yet available
	Two immunoassay modules implemented	
	Diffusion within the cell considered	Horizontal transport of molecules within cell not yet included
Light module	Two coupling methods implemented Scattering at waveguide considered Divergence of incident beam considered	Only one light source implemented
Detection module	Algorithm for calculating sensitivity	Only one detection module implemented
Overall model	Modular nature	No user interface as yet

Non-specific binding (nsb) within an immunoassay i.e. the binding of the analyte or label to the surface without binding to a capture antibody can be a major source of unwanted signal in many assays. Initially nsb was not included within the assay module as the added complexity slowed the development; modelling the complexity of the immunoassay being one of the most difficult aspects within the project. Verification of the assay data without nsb was valid, since the experimental data used was generated using a system in which nsb had been reduced to an insignificant level. However, now a technique for modelling the complexity of the assay has been produced it would be a trivial exercise to include non-specific binding within the immunoassay module and, given the importance of nsb in immunoassays in general, an essential one.

Attempts to fit transient data from an immunoassay using the modified Markov approach within an optimisation procedure were initially abandoned due to the unacceptable computation times involved. The excessive computation times relate to the fact that the time interval, Δt, used in the immunoassay module is calculated to be small enough so that when the free species arrive at the capture antibody surface the reactions that occur are within the physical constraints of the system. This value is then used as the time step throughout the entire model, i.e. for both the reactions and the diffusion. Since the diffusion rates are slower than the reaction rates, the value for Δt is smaller than necessary within the majority of the cell. It is common practice in these types of situations to allow the value of Δt to vary. However for the purposes of this model it was decided that the development of other aspects of the sensor was a more critical use of the author's time. At this stage this adaptation could be made to the immunoassay module and would greatly facilitate the application of the model to the fitting of kinetic data.

Inclusion of the horizontal transport of molecules within the cell is not trivial. The present model considered only one analyte and one label. The experimental aim of the UCL group, along with many others, is to produce multi-analyte sensors. In this case different capture antibodies would be immobilised onto different areas of the lower surface of the capillary fill device. The corresponding labelled antibody would be inkjet printed onto the upper surface opposite. The sample may then contain several analytes that will each react with the appropriate antibodies. The FDA requirement for a

commercial biosensor is that internal calibration is necessary, calibration that may be achieved by including a separate calibration channel within the sensor [23]. Preliminary experiments on such systems indicated that in this type of device cross-talk will be a serious problem. There are procedures for extending a one dimensional finite element approach to two dimensions. It is clear that the complex dynamics of the capillary fill device will need to be incorporated in such a model if the benefits of the model presented are to be extended to the consideration of multi-analyte devices.

The model as it stands does not benefit from the type of graphical user interface common to many applications these days. However the classes implemented to describe each component of the sensor provide a suitable platform from which such an interface may easily be constructed.

11.5 Conclusion

It was stated in the introduction that 'The complexity and interactions of the factors affecting the practicality of a biosensor have hindered their development in the traditional experimental environment.' and the development of the model presented would provide the basis for a design tool that could facilitate biosensor research and development.

Evanescent field sensors were initially proposed as a means of drawing a precise distinction between the bound and unbound label present in the immunoassay [24]. The analysis of the scattering at the waveguide surface presented in this thesis, analysis that could only be achieved with a computer model, demonstrated that the distinction is not as precise as expected, vital information for the future development of evanescent field immunosensors.

References

[1] Medisense, Medisense Facts, Available via the World Wide Web at http://www.medisense.co.uk/pages/medisensefacts.cfm

[2] Holt DB, Kusterbeck AW & Ligler FS, Continuous Flow Displacement Immunosensors: A Computational Study, *Analytical Biochemistry*, **287**, 234-242, 2000.

[3] O'Shea DC, *Elements of Modern Optical Design*, (USA: John Wiley & Sons, Inc.) pp 230 – 234, 1985.

[4] Kingston R. H. *Detection of Optical and Infrared Radiation* Vol 10 (Berlin: Springer-Verlag) pp 41 – 51, 1978.

[5] Hamamatsu, *Photomultiplier Tubes Construction and Operating Characteristics*, Available via the World Wide Web at http://www.hpk.co.jp/Eng/products/etd/pmte/pmte.htm

[6] Tiefenthaler K & Lukosz W, Sensitivity of grating couplers as integrated-optical chemical sensors, *J. Optical Society of America B*, **6**, 209 – 220, 1989.

[7] Sloper AN & Flanagan MT, Scattering in planar surface waveguide immunosensors, *Sensors and Actuators*, **B, 11**, 537-542, 1993.

[8] Walter DJ & Houghton J, Attenuation in thin film optical waveguides due to roughness-induced mode coupling, *Thin Solid Films*, **52**, 461 – 476, 1978.

[9] Ekins R, Immunoassay design and optimisation In *Principles and Practice of Immunoassay* Eds Price CP & Newman DJ, (NY: Stockton Press) pp 96-153, 1991.

[10] Flanagan MT, Tattam FG & Green NM, *Immunochemistry*, **15**, 261-267, 1978.

[11] Ezan E & Grassi J Optimization In *Immunoassays* Ed. Gosling JP, (Oxford: Oxford University Press) pp 187 - 210, 2000.

[12] Forde A & Coley J Choosing and characterizing antibodies In *Immunoassays* Ed. Gosling JP, (Oxford: Oxford University Press) pp 62 - 67, 2000.

[13] Pauling L, Pressman D & Grosberg AL, *Journal of the American Chemical Society*, **66**, 784 – 792, 1944.

[14] Dougan T, Levy JB, Salama A, George AJT & Pusey CD, Characterization of autoantibodies from patients with Goodpasture's disease using a resonant mirror biosensor, *Clinical & Experimental Immunology*, **128**, 555-561, 2002.

[15] Nix B & Wild D Data Processing In *Immunoassays* Ed. Gosling JP, (Oxford: Oxford University Press) pp 240 - 247, 2000.

[16] Leung VW-H, Darvell BW & Chan AP-C, A rapid algorithm for the solution of the equations of multiple equilibrium systems – RAMESES, *Talanta*, **35**, 713 – 718, 1988.

[17] Alderighi L, Gans P, Ienco A, Peters D, Sabatini A & Vacca A, Hyperquad simulation and specification (HySS): a utility program for the investigation of equilibria involving soluble and partially soluble species, *Coordination Chemistry Reviews*, **184**, 311-318, 1999.

[18] DeRobertis A, DeStefano C, Sammartano S & Rigano C, The calculation of equilibrium concentrations in large multimetal/multiligand systems, *Analytica Chimica Acta*, **191**, 385-398, 1986.

[19] Too JR, Fan LT & Nassar R, *Computers and Chemical Engineering*, **7**, 1-12, 1983.

[20] Antia FD & Lee S, *Chemical Engineering Science*, **40**, 1969 – 1971, 1985.

[21] Kurtz TG, *Journal of Applied Probability*, **7**, 49-58, 1970.

[22] Runge-Kutta Method, Available via the World Wide Web at http://mathworld.wolfram.com/Runge-KuttaMethod.html

[23] Private communication between MT Flanagan and the Food and Drug Administration.

[24] Kronick MN & Little AW, *Bull. Am. Phys. Soc.*, **18**, 782 – 790, 1973.

Appendix A

A.1 Finite element analysis of diffusion

Fick's 1st Law of Diffusion

$$J(x,t) = -D\frac{\delta C(x,t)}{dx}$$

where J is the flux
D is the diffusion coefficient
C is the concentration
x is distance
and t is time.

Recasting this becomes

$$J(x,t) = \lim_{\Delta x \to 0} -D\frac{\{C(x+\Delta x,t) - C(x,t)\}}{\Delta x}$$

The finite element technique assumes that Δx can be made small enough to allow the limit to be

$$J(x,t) = -D\frac{\{C(x+\Delta x,t) - C(x,t)\}}{\Delta x}$$

or

$$J(x,t) = -\frac{D}{\Delta x}\left\{C\left(x+\frac{\Delta x}{2},t\right) - C\left(x-\frac{\Delta x}{2},t\right)\right\} \qquad \text{(A.1)}$$

Fick's 2nd Law of Diffusion

$$-\frac{dC(x,t)}{dt} = \frac{dJ(x,t)}{dx}$$

written in it's finite difference form becomes

$$-\frac{C(x,t+\Delta t)-C(x,t)}{\Delta t} = \frac{J\left(x+\frac{\Delta x}{2},t\right)-J\left(x-\frac{\Delta x}{2},t\right)}{\Delta x}$$

Substituting for J(x,t) from (A.1) this becomes

$$C(x,t+\Delta t) = C(x,t)+\frac{D\Delta t}{(\Delta x)^2}\{C(x+\Delta x,t)-2C(x,t)+C(x-\Delta x,t)\}$$

A successive application of this formula allows the concentration in a particular element to be calculated for each time period.

Appendix B

B.1 Diffusion limited rate constants

Fick's 1st Law of Diffusion

$$J_i = -D_i \nabla C_i \qquad \text{(B.1)}$$

where J_i is the flux

D is the diffusion coefficient

∇C is the concentration gradient

and i refers to the particular molecule.

If the gradient is spherically symmetrical (B.1) becomes

$$J_i = -D_i \frac{dC_i}{dr} \qquad \text{(B.2)}$$

Consider a reaction between spherical molecules A and B with reaction rate K

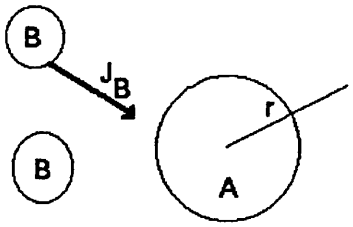

***Figure B.1**: Spherical molecules A and B. B is diffusing towards A.*

$$A + B \xrightarrow{K} AB$$

Assume

1) when A & B are in contact they react
2) B is diffusing towards A
3) r is the distance from A
4) neither molecule is charged

The rate of diffusion of B towards A is

$$-[A]4\pi r^2 pfJ_B$$

where p is the proportional of the sphere that is surrounded by B
f is the fraction of the surface that might bind with B

and the flux is derived from equation (B.2) as

$$J_B = -(D_A + D_B)\frac{d[B]_r}{dr} \qquad \text{(B.3)}$$

where $D_A + D_B$ takes account of the motion of both molecules
and $[B]_r$ is the concentration of B at a distance r from A.

The total rate of reaction is

$$-\frac{d[B]}{dt} = K[A][B]$$

which in the diffusion limited case is equal to the diffusion rate

$$-\frac{d[B]}{dt} = K[A][B] = -[A]4\pi r^2 pfJ_B$$

Substituting (B.3)

$$K[B] = 4\pi r^2 pf(D_A + D_B)\frac{d[B]_r}{dr}$$

rearranging

$$\frac{dr}{r^2} = \frac{4\pi pf(D_A + D_B)}{K[B]} d[B]_r$$

Integrating from R (the radius of contact of A & B) to ∞

$$\int_R^\infty \frac{dr}{r^2} = \frac{4\pi pf(D_A + D_B)}{K[B]} \int_R^\infty d[B]_r$$
$$\frac{1}{R} = \frac{4\pi pf(D_A + D_B)}{K[B]} ([B]_\infty - [B]_R) \qquad \text{(B.4)}$$

Noting that as $r \to \infty$ $[B]_\infty \to [B]$ equation (B.4) becomes

$$[B]_R = [B]\left(1 - \frac{K}{4\pi Rpf(D_A + D_B)}\right) \qquad \text{(B.5)}$$

Assume that A and B in contact react with rate K_R

i.e.

$$-\frac{d[B]}{dt} = K[A][B] = K_R[A][B]_R$$

Substituting (B.5) and eliminating [A][B]

$$K = K_R\left(1 - \frac{K}{4\pi Rpf(D_A + D_B)}\right)$$
$$K = \frac{4\pi Rpf(D_A + D_B)}{1 + \frac{4\pi Rpf(D_A + D_B)}{K_R}}$$
$$K = \frac{K_D}{1 + \frac{K_D}{K_R}} \qquad \text{(B.6)}$$

where $K_D = 4\pi Rpf(D_A + D_B)$

Examination of (B.6) shows that

$$K \leq K_D$$

and thus K_D is the maximum rate constant applicable i.e. the diffusion limited rate constant.

Note on units:

The units of K_D derived above are $[\text{Length}]^3\ [\text{molecule}]^{-1}\ [\text{sec}]^{-1}$
To convert to $M^{-1}\ s^{-1}$ multiply the above formula by $1000 * N_{Avagadro}$

Thus the diffusion limited rate constant for the reaction is

$$K_D = 4\pi Rpf(D_A + D_B)N_A \times 1000$$

B.2 Statistical allocation of association constant value

Given a set of chemical reactions

$$c + a \rightleftarrows ca$$
$$ca + a \rightleftarrows ca2$$

where the intrinsic association constant for c-a bond is K_c and c is bivalent.

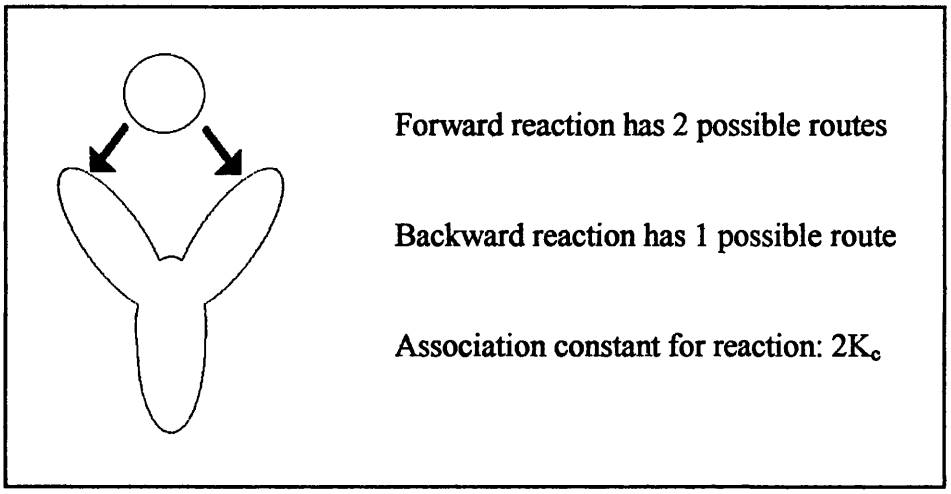

***Figure B.2**: Reaction: c + a ⇄ ca*

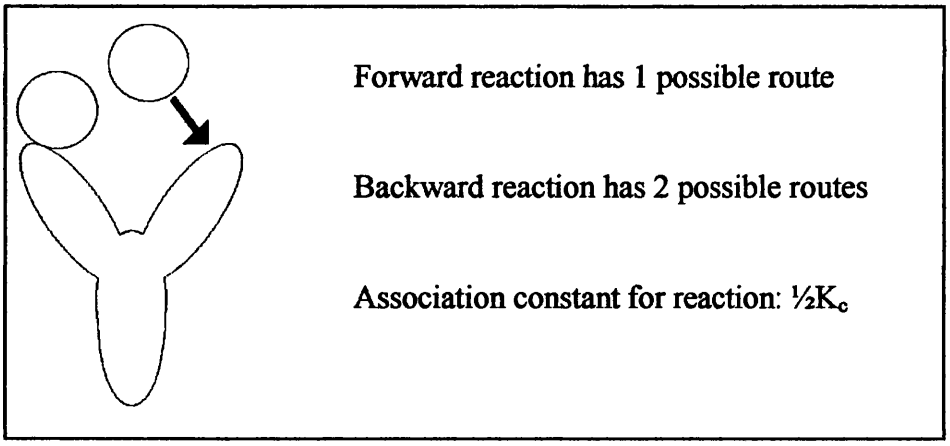

***Figure B.3**: Reaction: ca + a ⇄ ca2*

Appendix C

C.1 Analytical solution of the transient response of a single chemical reaction

Consider the reaction

$$a + b \underset{k_b}{\overset{k_f}{\rightleftharpoons}} c$$

where k_f is the forward rate constant

and k_b is the backward rate constant

The association constant for the reaction is given by

$$K = \frac{k_f}{k_b} \qquad \text{(C.1)}$$

Assume that at time t = 0

concentration of a is $[a]_0$

concentration of b is $[b]_0$

concentration of c is 0

and that at time t

concentration of c is [c]

concentration of a is $[a] = [a]_0 - [c]$

concentration of b is $[b] = [b]_0 - [c]$

The rate of change of [c] is given by

$$\frac{d[c]}{dt} = k_f[a][b] - k_b[c]$$

Substituting for [a] and [b]

$$\frac{d[c]}{dt} = k_f([a]_0 - [c])([b]_0 - [c]) - k_b[c]$$
$$\frac{d[c]}{dt} = k_f[a]_0[b]_0 - (k_f[a]_0 + k_f[b]_0 + k_b)[c] + k_f[c]^2$$

Dividing by k_b and substituting (C.1) this becomes

$$\frac{1}{k_b}\frac{d[c]}{dt} = K[a]_0[b]_0 - (K[a]_0 + K[b]_0 + 1)[c] + K[c]^2$$

Making the substitutions

$\beta = -(K[a]_0 + K[b]_0 + 1)$

$\gamma = K[a]_0[b]_0$

and rearranging leads to

$$k_b dt = \frac{d[c]}{K[c]^2 + \beta[c] + \gamma}$$

Integrating this becomes

$$k_b qt = \ln\left(\frac{2K[c] + \beta - q}{2K[c] + \beta + q}\right) + C \qquad \text{(C.2)}$$

where $q = \sqrt{(\beta^2 - 4K\gamma)}$

and C is a constant

Using the assumption that at t = 0, [c] = 0

$$C = \ln\left(\frac{\beta + q}{\beta - q}\right)$$

Substituting into (C.2) and rearranging leads to the equation for the concentration of c and thus the concentration of a and b, at any time t:

$$[c] = \frac{(\beta+q)(\beta-q)\left(1-e^{-k_b q t}\right)}{2K\left((\beta+q)e^{-k_b q t}-\beta+q\right)} \qquad \text{(C.3)}$$

$$[a] = [a]_0 - [c]$$

$$[b] = [b]_0 - [c]$$

where $\beta = -(K[a]_0 + K[b]_0 + 1)$

$$q = \sqrt{(\beta^2 - 4K\gamma)}$$

and $\gamma = K[a]_0[b]_0$

Appendix D

D.1 Maxwell's equations for light propagating within a waveguide

Maxwell's equations for a perfect dielectric (i.e. $\varepsilon = n^2\varepsilon_0$, $\mu = \mu_0$ and $\sigma = 0$) are

$$\nabla \times \vec{E} = -j\omega\mu_0 \vec{H} \qquad \text{(D.1)}$$

$$\nabla \times \vec{H} = j\omega\varepsilon_0 n^2 \vec{E} \qquad \text{(D.2)}$$

where E represents the electric field vector,
H the magnetic field vector,
$j = \sqrt{-1}$
μ_0 is the magnetic permeability of free space,
ε_0 is the permittivity of free space,
n is the refractive index of the medium
and ω is the angular frequency of the guided light.

For a slab waveguide, unconfined in the y-direction, the field components for a wave propagating along the waveguide in the z-direction can be expressed as

$$F(x,y,z;t) = F_0(x)e^{j(wt-\beta z)}$$

where x, y & z are the spatial coordinates,
t is time
and β is the longitudinal phase constant.

Suppressing the exponential component and expanding Maxwell's equations for fields of this form produces the following equations:

$$\left.\begin{aligned} \beta E_{0y} &= -\omega\mu_0 H_{0x} \\ j\beta E_{0x} + \frac{dE_{0z}}{dx} &= j\omega\mu_0 H_{0y} \\ \frac{dE_{0y}}{dx} &= -j\omega\mu_0 H_{0z} \end{aligned}\right\} \text{from Equation (D.1)}$$

$$\left.\begin{aligned} \beta H_{0y} &= \omega\varepsilon_0 n^2 E_{0x} \\ j\beta H_{0x} + \frac{dH_{0z}}{dx} &= -j\omega\varepsilon_0 n^2 E_{0y} \\ \frac{dH_{0y}}{dx} &= j\omega\varepsilon_0 n^2 E_{0z} \end{aligned}\right\} \text{from Equation (D.2)}$$

Inspection of these equations shows that they can be divided into two groups each representing either the Transverse-Electric (TE) or Transverse-Magnetic (TM) mode of propagation.

TE modes are described by

$$\frac{dE_{0y}}{dx} = -j\omega\mu_0 H_{0z}$$

$$j\beta H_{0x} + \frac{dH_{0z}}{dx} = -j\omega\varepsilon_0 n^2 E_{0y}$$

$$\beta E_{0y} = -\omega\mu_0 H_{0x}$$

and TM by

$$j\beta E_{0x} + \frac{dE_{0z}}{dx} = j\omega\mu_0 H_{0y} \qquad \text{(D.3)}$$

$$\beta H_{0y} = \omega\varepsilon_0 n^2 E_{0x} \qquad \text{(D.4)}$$

$$\frac{dH_{0y}}{dx} = j\omega\varepsilon_0 n^2 E_{0z} \qquad \text{(D.5)}$$

The following derivation of the fields and resulting power has been confined to the TM mode, however analogous equations may be derived for TE propagating waves.

Rearranging, equation (D.5) becomes

$$E_{0z} = \frac{-j}{\omega\varepsilon_0 n^2}\frac{dH_{0y}}{dx} \qquad \text{(D.6)}$$

and equation (D.4) becomes

$$E_{0x} = \frac{\beta}{\omega\varepsilon_0 n^2}H_{0y} \qquad \text{(D.7)}$$

Substituting equations (D.6) and (D.7) into equation (D.3) gives

$$\frac{\beta^2}{\omega\varepsilon_0 n^2}H_{0y} - \frac{1}{\omega\varepsilon_0 n^2}\frac{d^2H_{0y}}{dx^2} = \omega\mu_0 H_{0y}$$

which becomes

$$\left\{\frac{d^2}{dx^2} + \left[(nk_0)^2 - \beta^2\right]\right\}H_{0y} = 0 \qquad \text{(D.8)}$$

where $k_0 = \omega(\varepsilon_0\mu_0)^{1/2} = \frac{\omega}{c}$ is the wave number in vacuum

and c is the velocity of light in vacuum.

D.2 Fields in a dielectric thin film waveguide

In the three layer dielectric slab waveguide illustrated in Figure D.1 equation (D.8) should represent a standing wave in the film and an evanescent wave in the substrate and cover regions.

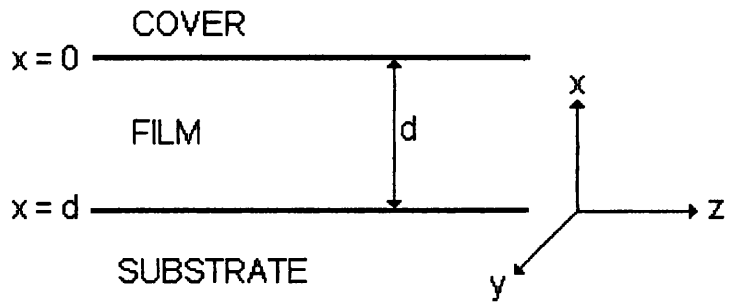

***Figure D.1**: Dielectric slab waveguide*

Establishing fields that represent the appropriate type of waveform and using the continuity of H_{0y} across the substrate-film and film-cover boundaries the magnetic field in the y-direction is given by

$$H_{0y}^{S}(x) = \{A\cos(bd) - B\sin(bd)\}e^{p_0(x+d)} \qquad x < -d$$

$$H_{0y}^{F}(x) = A\cos(bx) + B\sin(bx) \qquad -d \le x \le 0$$

$$H_{0y}^{C}(x) = Ae^{-p_2 x} \qquad 0 < x$$

where S, F & C denote the substrate, film and cover respectively,
A & B are constants,
d is the thickness of the film

$b = \sqrt{\left((n_F k_0)^2 - \beta^2\right)}$ is the transverse phase constant in the film

and $p_0 = \sqrt{\left(\beta^2 - (n_S k_0)^2\right)}$

$p_2 = \sqrt{\left(\beta^2 - (n_C k_0)^2\right)}$ are the transverse attenuation constants in the substrate and cover respectively.

Applying equation (D.6) produces the equations for the electric field in the z-direction, namely

$$E_{0z}^{S}(x) = \frac{-j}{\omega\varepsilon_0 n_S^2} p_0 H_{0y}^{S}(x) \qquad x < -d$$

$$E_{0z}^{F}(x) = \frac{-j}{\omega\varepsilon_0 n_F^2}\{-bA\sin(bx) + bB\cos(bx)\} \qquad -d \le x \le 0$$

$$E_{0z}^{C}(x) = \frac{-j}{\omega\varepsilon_0 n_C^2}(-p_2) H_{0y}^{C}(x) \qquad 0 < x$$

Continuity of E_z across the film-cover boundary

$$E_{0z}^{F}(0) = E_{0z}^{C}(0)$$

implies

$$\frac{-j}{\omega\varepsilon_0 n_F^2} bB = \frac{-j}{\omega\varepsilon_0 n_C^2}(-p_2)A$$

which leads to

$$B = -\frac{\overline{p_2}}{b}A \qquad \text{(D.9)}$$

where $\overline{p_2} = \frac{n_F^2}{n_C^2} p_2$.

Continuity of E_z across the film-substrate boundary

$$E_{0z}^{F}(-d) = E_{0z}^{S}(-d)$$

implies

$$\frac{-j}{\omega\varepsilon_0 n_F^2}\{bA\sin(bd) + bB\cos(bd)\} = \frac{-j}{\omega\varepsilon_0 n_S^2} p_0 \{A\cos(bd) - B\sin(bd)\}$$

which leads to

$$\sin(bd)\left\{\frac{bA}{n_F^2} + \frac{p_0 B}{n_S^2}\right\} = \cos(bd)\left\{\frac{p_0 A}{n_s^2} - \frac{bB}{n_F^2}\right\}$$

Substituting equation (D.9) and rearranging leads to

$$\tan(bd) = \frac{b\left(\overline{p_0} + \overline{p_2}\right)}{b^2 - \overline{p_0}\,\overline{p_2}} \qquad \text{(D.10)}$$

where $\overline{p_0} = \frac{n_F^2}{n_S^2} p_0$.

Equation 10 is the characteristic equation of the waveguide and can be used to determine the value of β.

D.3 Guided power within the waveguide

The guided power in the waveguide is given by

$$P = W \int_{-\infty}^{\infty} S_z dx \qquad \text{(D.11)}$$

where W (>> d) is the width in the y-direction

and S_z is the longtitudinal component of the Poynting vector

$$\vec{S} = \frac{1}{2}\mathrm{Re}\left|\vec{E} \times \overline{H^*}\right|$$

For a TM wave

$$S_z = \frac{1}{2}\mathrm{Re}\left(E_x H_y^*\right)$$

Substituting for E_x from equation (D.7)

$$S_z = \frac{\beta}{2\omega\varepsilon_0 n^2}\left|H_y\right|^2$$

Thus equation (D.11) becomes

$$P = \frac{W\beta}{2\omega\varepsilon_0}\left\{\frac{1}{n_S^2}\int_{-\infty}^{-d}\left|H_y^S\right|^2 dx + \frac{1}{n_F^2}\int_{-d}^{0}\left|H_y^F\right|^2 dx + \frac{1}{n_C^2}\int_{0}^{\infty}\left|H_y^C\right|^2 dx\right\}$$

i.e.

$$P = \frac{W\beta}{4\omega\varepsilon_0 n_F^2}\left(1+\frac{\overline{p_2}^2}{b^2}\right)|A|^2 d_{eff} \qquad \text{(D.12)}$$

where $$d_{eff} = d + \frac{n_F^4 b^2 + n_S^4 \overline{p_0}^2}{n_S^4 \overline{p_0}\left(b^2 + \overline{p_0}^2\right)} + \frac{n_F^4 b^2 + n_C^4 \overline{p_2}^2}{n_C^4 \overline{p_2}\left(b^2 + \overline{p_2}^2\right)}$$

is the effective thickness of the film resulting from the small penetration of the guided wave into the medium on either side. The value of A can be calculated from equation (D.12) if the total power in the system is known and thus the field and hence the power at any value of x can be determined.

Appendix E

E.1 Electromagnetic field equations

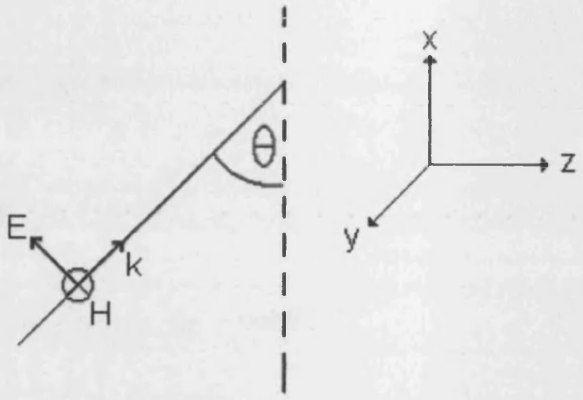

***Figure E.1**: Transverse-Magnetic field with propagation vector k*

Consider the transverse magnetic wave with propagation vector k as illustrated by Figure E.1. The propagation vector k can be written

$$\vec{k} = (k_x,\ 0,\ k_z) \qquad \text{(E.1)}$$

where $k_z = k \sin\theta$

$$k = \frac{\omega n}{c}$$

ω is the angular frequency of the light

c is the velocity of light in vacuum

n is the refractive index of the propagation medium

and $k_x = \sqrt{k^2 - k_z^2} \quad (= \alpha)$

The electric field vector can be written

$$\vec{E} = Ee^{j(k \bullet r - \omega t)}$$

Expanding this becomes

$$\vec{E} = Ee^{-j\omega t}e^{jk_z z}e^{jk_x x}$$

Confining the direction of interest to the x direction this can be written as

$$\vec{E} = \vec{A}e^{j\alpha x}$$

Expanding this vector

$$\vec{E} = \left|\vec{A}\right|(\sin\theta,\ 0,\ -\cos\theta)e^{j\alpha x} \qquad \text{(E.2)}$$

Noting that $\sin\theta = \frac{k_z}{k}$ and $\cos\theta = \frac{\alpha}{k}$ equation (E.2) can be rewritten as

$$\vec{E} = \left|\vec{A}\right|\left(\frac{k_z}{k},\ 0,\ -\frac{\alpha}{k}\right)e^{j\alpha x} \qquad \text{(E.3)}$$

Maxwell's equations imply

$$\vec{H} = \frac{1}{\omega\mu}\vec{k}\times\vec{E}$$

Substituting equations (E.1) and (E.2) this becomes

$$\vec{H} = \frac{n}{Z_0}\left|\vec{A}\right|(0,\ 1,\ 0)e^{j\alpha x} \qquad \text{(E.4)}$$

where $Z_0 = \sqrt{\frac{\mu_0}{\varepsilon_0}}$ is the characteristic impedance

Appendix F

F.1 Projection of a beam incident at an angle

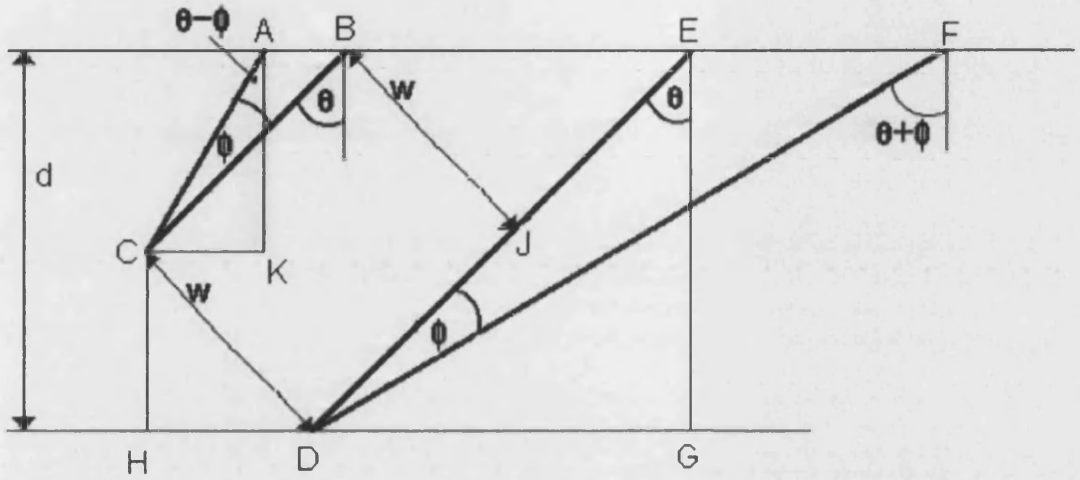

NOTE: Exaggerated scale (w<<d)

Figure F.1: *Projection of a beam of light of width w with angle of divergence* ϕ *incident at an angle* θ *on a surface AF at a distance d from the source of the light beam*

Applying the sine rule to triangle DEF

$$\frac{|EF|}{\sin\phi} = \frac{|DE|}{\sin\left(\frac{\pi}{2} - \theta - \phi\right)} = \frac{|DE|}{\cos(\theta + \phi)} \tag{F.1}$$

In the right angle triangle DEG

$$|DE| = \frac{d}{\cos\theta} \tag{F.2}$$

Combining (F.1) and (F.2) gives

$$|EF| = \frac{d\sin\phi}{\cos\theta\cos(\theta + \phi)} \tag{F.3}$$

Applying the sine rule to triangle ABC:

$$\frac{|AB|}{\sin\phi} = \frac{|AC|}{\sin\left(\frac{\pi}{2}-\theta\right)} = \frac{|AC|}{\cos\theta} \qquad \text{(F.4)}$$

In the right angle triangle CDH

$$|CH| = w\sin\theta$$

In the right angle triangle ACK

$$|AC| = \frac{|AK|}{\sin(\theta-\phi)} = \frac{d-|CH|}{\sin(\theta-\phi)} = \frac{d-w\sin\theta}{\sin(\theta-\phi)} \qquad \text{(F.5)}$$

Combining (F.4) and (F.5) gives

$$|AB| = \frac{|AC|\sin\phi}{\cos\theta} = \frac{(d-w\sin\theta)\sin\phi}{\sin(\theta-\phi)\cos\theta} \qquad \text{(F.6)}$$

In right angle triangle BEJ

$$|BE| = \frac{w}{\cos\theta} \qquad \text{(F.7)}$$

Thus the total length subtended by the beam on the interface, from (F.3), (F.6) and (F.7) is

$$|AB|+|BE|+|EF| = \frac{(d-w\sin\theta)\sin\phi}{\sin(\theta-\phi)\cos\theta} + \frac{w}{\cos\theta} + \frac{d\sin\phi}{\cos\theta\cos(\theta+\phi)}$$

Appendix G

G.1 Publications resulting from this work

Refereed journal papers

Keating S M & Flanagan M T, *Physiological Measurement*, **22**, 1 – 10, 2001.

Refereed conferences

Keating S M, O'Reilly J J & Flanagan M T, Proceedings of the International Conference on Mathematical and Engineering Techniques in Medicine and Biological Sciences, 25 – 28 June 2001, Las Vegas, 2001.

Non-refereed conferences

Keating S M, O'Reilly J J & Flanagan M T, Proceedings of the Third Conference on Postgraduate Research in Electronics, Photonics, Communications and Software, 9 –11 April 2001, Keele University, 91 – 92, 2001.